

DEVELOPMENT OF MODELING TECHNIQUES FOR A GENERATION IV GAS
FAST REACTOR

A Thesis

by

ANDREW STEVEN DERCHER

Submitted to the Office of Graduate Studies of
Texas A&M University
in partial fulfillment of the requirements for the degree of

MASTER OF SCIENCE

August 2011

Major Subject: Nuclear Engineering

Development of Modeling Techniques for a Generation IV Gas Fast Reactor

Copyright 2011 Andrew Steven Dercher

DEVELOPMENT OF MODELING TECHNIQUES FOR A GENERATION IV GAS
FAST REACTOR

A Thesis

by

ANDREW STEVEN DERCHER

Submitted to the Office of Graduate Studies of
Texas A&M University
in partial fulfillment of the requirements for the degree of

MASTER OF SCIENCE

Approved by:

Chair of Committee,	Karen Vierow
Committee Members,	Pavel Tsvetkov
	Devesh Ranjan
	Sunil Chirayath
Head of Department,	Raymond Juzaitis

August 2011

Major Subject: Nuclear Engineering

ABSTRACT

Development of Modeling Techniques for a Generation IV Gas Fast Reactor.

(August 2011)

Andrew Steven Dercher, B.S., The Pennsylvania State University

Chair of Advisory Committee: Dr. Karen Vierow

Worldwide, multiple countries are investing a great deal of time and energy towards developing a new class of technologically advanced nuclear reactors. These new reactors have come to be known as the Generation IV (Gen IV) class of nuclear reactors. Similarly to the other designs, the Gas Fast Reactor (GFR) has many advantages, such as electricity production at high efficiency, hydrogen production, minor actinide burning capabilities, etc. However, there are currently no immediate plans to build a GFR due to uncertainties regarding safety issues.

The study conducted herein contains input techniques for the development of new neutronic and thermal hydraulic input decks for the United States (US) Department of Energy (DOE) GFR design. The Monte Carlo N-Particle (MCNP) and MELCOR codes are used to model neutronic and thermal hydraulic characteristics, respectively. These codes are used with the intention of gaining further insight into GFR design and steady state operating characteristics of the US DOE GFR.

Descriptions of inputs for all input decks, along with the results of the execution of both input decks can be found in this thesis. Although many alterations are made to

original design specifications, results found in this thesis support the design modifications that have been made. Results suggest that steady-state operation of the GFR is a plausible possibility, given the right conditions. The lack of design criteria for both the reflector and borated shield regions imposes a necessity of invention upon all those who seek to clarify design criteria for the US DOE GFR. Furthermore, resulting temperature profiles for the fuel, cladding and coolant give rise to the possibility of the design of a system, based on thermionic principles, that converts core thermal energy directly to electricity. Such a system is envisioned to provide electricity to a decay heat removal system and possibly increase plant efficiency.

To my family, for all of their love and support

ACKNOWLEDGEMENTS

I would like to thank Professor Karen Vierow for her help and advice throughout the course of this endeavor. I would also like to thank all those who are a part of the Laboratory for Nuclear Heat Transfer Systems. In particular, I would like to thank Brad Beeny for his help with MELCOR-related issues. His help is deeply appreciated. Matthew Solom's help with establishing more efficient ways to run MCNP is also deeply appreciated along with Patrick McDermott's advice on MCNP-related issues.

Furthermore, I would also like to thank the members of my thesis committee: Professors Karen Vierow, Pavel Tsvetkov, Devesh Ranjan, and Sunil Chirayath. Their help is deeply appreciated.

I would also like to thank the MELCOR code developers at Sandia National Laboratories. Their efforts in locating difficult bugs in my input were instrumental towards the completion of the MELCOR input deck. In addition, I would like to thank James Corson for his advice on MELCOR-related issues. Furthermore, Dr. Chirayath's help with creating an MCNP input deck was vital towards the development of the MCNP input deck used for this endeavor.

Above all, I would like to thank my parents, David and SuEllen Dercher, and my girlfriend Rachel Ginchansky. Their love and support has truly helped me through this endeavor.

NOMENCLATURE

ANL	Argonne National Laboratory
CB	Core Barrel
CEA	Commissariat à l'énergie atomique (French Atomic Energy Commission)
CO ₂	Carbon Dioxide
CRDM	Control Rod Drive Mechanism
CRGT	Control Rod Guide Tube
DC	Downcomer
DCHRS	Decay Heat Removal System
DOE	Department of Energy
GA	General Atomics
GBR-4	Gas Breeder Reactor-4
GCFR	Gas-Cooled Fast Reactor
Gen IV	Generation IV
GFR	Gas Fast Reactor
He	Helium
KWU	Kraftwerks Union
LBS	Lower Borated Shield
LCP	Lower Core Plate
LFR	Lead-Cooled Fast Reactor

LOCA	Loss of Coolant Accident
LOFA	Loss of Flow Accident
LWR	Light Water Reactor
MCNP	Monte Carlo N-Particle
MSR	Molten Salt Reactor
MWe	Megawatts Electric
MWt	Megawatts Thermal
RPV	Reactor Pressure Vessel
SCWR	Super Critical Water Reactor
SiC	Silicon Carbide
SFR	Sodium-Cooled Fast Reactor
TMI	Three Mile Island
UBS	Upper Borated Shield
UO ₂	Uranium Dioxide
US	United States
(U,TRU)C	Uranium-Transuranic Carbide
VHTR	Very High Temperature Reactor
Zr ₃ Si ₂	Zirconium Silicide

TABLE OF CONTENTS

	Page
ABSTRACT	iii
DEDICATION	v
ACKNOWLEDGEMENTS	vi
NOMENCLATURE.....	vii
TABLE OF CONTENTS	ix
LIST OF FIGURES.....	xii
LIST OF TABLES	xvi
1. INTRODUCTION.....	1
1.1 Objectives.....	3
1.2 Significance of Work.....	3
1.3 Thesis Overview.....	4
2. GAS FAST REACTOR (GFR) OVERVIEW.....	7
2.1 History.....	8
2.2 GFR Core Design.....	10
2.3 Thermal Hydraulic Research on the GFR	13
2.3.1 Experiments Concerning the GFR	13
2.3.2 Computational Analysis of the GFR	13
3. TECHNICAL APPROACH.....	15
4. MCNP OVERVIEW	17
4.1 Code Overview.....	18
4.2 Code Architecture	18
4.2.1 Cell Card Overview.....	19
4.2.2 Surface Card Overview	20

	Page
4.2.3 Data Card Overview	20
5. MELCOR OVERVIEW	23
5.1 Code Overview	24
5.2 Code Architecture	25
5.2.1 COR Package Overview.....	26
5.2.2 CVH and FL Package Overview	28
5.2.3 HS Package Overview.....	30
6. MCNP CALCULATIONS	32
6.1 Modeling Approach.....	33
6.1.1 Fuel Assemblies	35
6.1.2 Control/Shutdown Assemblies	40
6.1.3 Reflector Assemblies.....	43
6.1.4 Borated Shield Assemblies.....	44
6.2 Input Description.....	46
6.2.1 Surface Card Input	47
6.2.2 Material Card Input	53
6.2.3 Cell Card Input	59
6.2.4 Assembly Layouts	67
6.3 Results	77
6.3.1 Analysis of US DOE GFR Reactor Kinetics	80
6.3.2 Axial Meshing Results	83
6.3.3 Radial Meshing Results.....	85
6.3.4 Three-Dimensional Normalized Flux Distribution	87
6.4 MCNP Conclusions.....	88
7. MELCOR CALCULATIONS.....	91
7.1 Modeling Approach.....	92
7.1.1 Reactor Pressure Vessel (RPV).....	93
7.1.2 Core Barrel (CB)	94
7.1.3 Reactor Vessel Lower Head.....	94
7.1.4 Lower Core Plate (LCP).....	94
7.1.5 Assembly Lower Nozzles.....	95
7.1.6 Reactor Vessel Upper Head	95
7.2 Input Description.....	96
7.2.1 COR Input	98
7.2.2 CVH Input	118
7.2.3 FL Input.....	121

	Page
7.2.4 HS Input	126
7.2.5 MP Input.....	129
7.2.6 TF Input.....	130
7.2.7 CF Input.....	130
7.2.8 NCG Input	132
7.3 Results	132
7.3.1 Coolant Pressure Drop	133
7.3.2 Coolant Temperature Changes	140
7.3.3 Coolant Velocity Observations	145
7.3.4 Fuel Temperature Results.....	155
7.3.5 Clad Temperature Results	161
7.3.6 Canning Temperature Results	164
7.3.7 Fuel-Clad-Coolant Temperature Profile.....	168
7.4 MELCOR Conclusions	169
8. CONCLUSIONS AND FUTURE WORK	172
8.1 MCNP Models.....	172
8.2 MELCOR Techniques.....	174
8.3 Thermionic Modeling Considerations.....	176
REFERENCES.....	181
APPENDIX A	185
APPENDIX B	189
APPENDIX C	214
VITA	291

LIST OF FIGURES

FIGURE	Page
2.1 2400MWt GFR Core Layout.....	11
2.2 2400MWt GFR Fuel Assembly Design	12
6.1 1/6 th Core Loading Pattern	38
6.2 Hexagonal Structure for Fuel Rod Meshing and Core.....	49
6.3 Hexagonal Structure for Control Rod Support Cans and Assemblies.....	53
6.4 Signs for Hexagonal Structure of Fuel Rod Mesh and Core.....	60
6.5 Signs for Hexagonal Structure of Control Rod Cans and Assemblies.....	60
6.6 20 w/o Enriched Fuel Assembly	65
6.7 Empty Plenum Region for All Fuel Rods in a Fuel Assembly	68
6.8 Close-up View of Empty Plenum Region of a Fuel Rod	69
6.9 Reflector Region for All Fuel Rods in a Fuel Assembly	70
6.10 Close-up View of Reflector Region in a Fuel Rod	70
6.11 Close-up View of Gap Between Reflector and Clad in a Fuel Rod.....	71
6.12 Fuel Region for All Fuel Rods in a Fuel Assembly	71
6.13 Close-up View of Fuel Region in a Fuel Rod	72
6.14 Close-up View of Gap Between Fuel and Clad in a Fuel Rod.....	72
6.15 Control/Shutdown Assembly Layout at Fuel Elevation.....	73
6.16 Close-up View of Control Rod in Control/Shutdown Assembly.....	74
6.17 Reflector Assembly	75

FIGURE	Page
6.18 Close-up View of Reflector Rod in a Reflector Assembly	75
6.19 Borated Shield Assembly	76
6.20 Close-up View of a Borated Shield Rod	76
6.21 Gap Between Boron Carbide and Tungsten Cladding	77
6.22 Normalized Axial Neutron Flux Profile.....	84
6.23 Normalized Radial Neutron Flux Profile	86
6.24 3D Plot of Relative Normalized Neutron Flux Distribution	88
7.1 MELCOR Input Nodalization Diagram	97
7.2 Identification of Assembly Canister Parameters	105
7.3 Pressure Drop Along Core	134
7.4 Pressure Drop Through Channel Side of Ring 1	135
7.5 Pressure Drop Through Channel Side of Ring 5.....	136
7.6 Pressure Drop Through Channel Side of Ring 7	136
7.7 Pressure Drop Through Bypass Side of Ring 1.....	137
7.8 Pressure Drop Through Bypass Side of Ring 5.....	137
7.9 Pressure Drop Through Bypass Side of Ring 7.....	138
7.10 Channel Pressure Drop Across Core in Radial Direction	139
7.11 Coolant Temperature Rise on Channel Side of Ring 1	141
7.12 Coolant Temperature Rise on Channel Side of Ring 5	141
7.13 Coolant Temperature Rise on Channel Side of Ring 7	142
7.14 Coolant Temperature Rise on Bypass Side of Ring 1	142

FIGURE	Page
7.15 Coolant Temperature Rise on Bypass Side of Ring 5	143
7.16 Coolant Temperature Rise on Bypass Side of Ring 7	143
7.17 Channel Temperature Difference Observed in Radial Direction	144
7.18 Bypass Temperature Difference Observed in Radial Direction	144
7.19 Coolant Velocity Through Channel Side of Ring 1	146
7.20 Coolant Velocity Through Channel Side of Ring 5	147
7.21 Coolant Velocity Through Channel Side of Ring 7	147
7.22 Coolant Velocity Through Bypass Side of Ring 1	148
7.23 Coolant Velocity Through Bypass Side of Ring 5	148
7.24 Coolant Velocity Through Bypass Side of Ring 7	149
7.25 Channel Coolant Velocity Variations with Radial Direction	149
7.26 Bypass Coolant Velocity Variations in Radial Direction	150
7.27 Velocity in Horizontal Flow Paths Between Ring 1 and Ring 2	151
7.28 Velocity in Horizontal Flow Paths Between Ring 5 and Ring 6	151
7.29 Flow Acceleration Through Channel Side of Bottom of Rings 1 and 7	153
7.30 Axial Fuel Temperature Variation in Ring 1	156
7.31 Axial Fuel Temperature Variation in Ring 5	157
7.32 Radial Fuel Temperature Variation Across Active Core	157
7.33 MELCOR Nodalization Diagram with Fuel and Coolant Temperatures ...	160
7.34 Cladding Temperature Along Core in Ring 1	161
7.35 Cladding Temperature Along Core in Ring 5	162

FIGURE	Page
7.36 Radial Cladding Temperature Profile at Middle Elevation.....	162
7.37 MELCOR Nodalization Diagram with Cladding and Coolant Temperatures	163
7.38 Canning Temperature Along Core in Ring 1	165
7.39 Canning Temperature Along Core in Ring 5	165
7.40 Canning Temperature Variations in Radial Direction at Middle Elevation.....	166
7.41 MELCOR Nodalization Diagram with Canning and Coolant Temperatures	167
7.42 Temperature Profile in Center of Active Core	168
8.1 Illustration of Thermionic Principles	178
8.2 Illustration of Thermionic Principles Applied to a Fuel Rod.....	179

LIST OF TABLES

TABLE	Page
6.1 Fuel Assembly Design Characteristics.....	40
6.2 Control/Shutdown Assembly Design Characteristics	42
6.3 Reflector Assembly Design Characteristics	44
6.4 Borated Shield Assembly Design Characteristics	46
6.5 Key GFR Neutronic Data.....	79
6.6 Reactor Kinetics Parameters (All Neutrons).....	80
6.7 Reactor Kinetics Parameters (Prompt Neutrons Only)	81
6.8 Effective Delayed Neutron Fraction Results.....	82
6.9 Normalized Axial Neutron Flux Data	83
6.10 Normalized Radial Neutron Flux Data.....	85
7.1 Key Thermal Hydraulic Data	133

1. INTRODUCTION

An ever-present energy crisis exists that must be solved in order to provide the world with an adequate and sustainable supply of energy. A handful of countries have undertaken the task of finding a viable solution to the energy crisis. While energy sources, such as coal and oil, provide much of the world's energy, they are accompanied by harmful side effects that pollute the environment. Furthermore, they are not renewable energy sources and are guaranteed to eventually be totally consumed. Renewable energy sources, such as wind and solar power, present possible solutions to our increasing demand for electricity; however, their electrical output per amount of space utilized is too small to be considered as a viable solution to our energy needs. Furthermore, they cannot be used as a base load for US electricity requirements.

Perhaps the best solution to our electricity needs can be found within the nuclear engineering discipline. Nuclear reactors provide only 16% of the world's electricity supply [1]. Although nuclear reactors have proven to be an excellent source of energy, a handful of accidents have slowed progress towards the development of an enlarged worldwide nuclear reactor fleet. Accidents such as the core meltdown at Three Mile Island (TMI) and the radioactivity releases at Chernobyl and Fukushima have led to increased concerns about the safety of currently operating and possible future nuclear reactors. Due to the harmful biological effects caused by excessive radiation exposure, one can understand why people are concerned about mankind's ability to safely operate

This thesis follows the style of International Journal of Heat and Mass Transfer.

a device that could potentially release vast amounts of radiation to the public. In addition to concerns about possible accident scenarios leading to the release of radiation, concerns have also risen due to the need to store nuclear waste expended from nuclear reactor sites. Nuclear waste is also seen as a large source of radiation and can have harmful effects on our environment as well.

Along with technological advances in the nuclear industry that have been created in order to increase plant life and plant safety, a new class of nuclear reactors is being considered in order to meet the world's ever-growing energy demands. This class of new reactors has been termed as the Gen IV class of nuclear reactors. These new reactors are being tailored to meet various demands, such as increased plant safety, better fuel utilization, minimization of waste storage requirements, production of process heat for hydrogen production, proliferation resistance, and increased plant efficiency. Of these new proposed reactor designs, the GFR may present the best opportunity for the nuclear industry to meet the majority of the demands listed above. While the GFR presents an attractive solution as a nuclear reactor design that could possibly help meet the world's energy needs, there are still various problems associated with the design that present safety concerns. Perhaps the primary concern is the ability of the reactor to be properly shut down during certain postulated accident conditions. Due to a high thermal power density during operation, the GFR creates a large amount of decay heat. During hypothetical accident conditions, such as a loss of coolant accident (LOCA) or loss of flow accident (LOFA), the reactor could be at risk of overheating and experiencing meltdown. This thesis is an investigation into the development of modeling techniques

for GFR operating scenarios that may lend further insight into GFR conditions prior to various accident scenarios.

1.1 Objectives

The objectives of this thesis are:

- To advance neutronic modeling techniques for the GFR
- To advance thermal hydraulic modeling techniques for the GFR
- To extend current applications of the MELCOR code

1.2 Significance of Work

Presently, there is no definitive solution as to how the GFR may be cooled during a LOFA. With large thermal power densities during operation, a significant amount of decay heat is still present in the GFR core even after a reactor SCRAM is completed. In order to be able to safely operate any nuclear reactor, various countermeasures to accident scenarios must be available in order to safely shutdown the reactor, as well as protect the public from any possible increased radiation exposure. The development of a decay heat removal system for the GFR is a crucial step towards ensuring that the GFR can be safely shut down in the event of a LOFA in addition to ensuring that the public health can be protected during this particular accident scenario.

Prior to developing a decay heat removal system, adequate neutronic and thermal hydraulic models of the GFR must be established. While the US DOE has used codes such as REBUS and DIFF3D in order to model GFR neutronic characteristics, they have not used the MCNP code. While REBUS and DIFF3D are deterministic codes, MCNP is a Monte Carlo code and may offer further insight into GFR neutronic characteristics.

Furthermore, MELCOR has not been used in order to model GFR thermal hydraulic characteristics. Initial thermal hydraulic studies performed by the DOE were performed with RELAP. MELCOR is a thermal hydraulic and reactor safety code that uses a control volume approach, unlike other reactor safety codes, such as RELAP, which use a component based approach [2]. In addition, the flexibility of MELCOR allows for definition of materials and components not normally found in light water reactors. Thus, a model of the GFR in MELCOR may offer further insight into GFR thermal hydraulic characteristics.

In addition to furthering the development of modeling techniques for the GFR, this project will also advance the current application range of the MELCOR code. Initially, MELCOR was designed to model accident scenarios for a Light Water Reactor (LWR) [2]. Recently, advancements in code development have allowed MELCOR users to model gas-cooled reactors as well. However, MELCOR is still intended to be used as a code for thermal reactors. Thus, a GFR model in MELCOR will allow users to observe how MELCOR can handle a fast reactor. In addition, the GFR contains materials not normally seen in MELCOR models. Thus, this investigation will lend further insight into how different materials are treated in MELCOR. Overall, this project will advance our knowledge of the capabilities of MELCOR.

1.3 Thesis Overview

Section 1 of this thesis has been reserved for outlining the tasks accomplished by this investigation in addition to the significance of the thesis itself. Section 2 consists of an analysis of old and current GFR designs. It contains the progression of the

development of a gas-cooled nuclear reactor with a fast neutron spectrum in addition to some of the design characteristics relevant to this thesis. In addition, various physics aspects governing the operation of the GFR are discussed. Due to incomplete aspects of the US DOE GFR design report, proposals for certain design modifications are also presented in Section 2.

Section 3 provides the technical approach used throughout the course of this project. Included in this section are explanations as to which codes are used to model certain physical phenomena, as well as how the information extracted from each code output is used. Section 4 contains an explanation of the physical principles governing the MCNP code. Section 5 of this document contains an explanation of the physical principles governing the MELCOR code.

An explanation of how the MCNP code is used in order to create models for this particular project can be found in Section 6, along with results, and a discussion of the results, obtained from execution of the MCNP models. Section 7 contains an explanation as to how the MELCOR code is used in order to develop inputs for this project. Results from execution of the MELCOR inputs, as well as a discussion of those results, can also be found in this Section.

Finally, Section 8 contains a discussion of future work that could be performed in order to advance this project and further improve upon GFR modeling techniques. To conclude, suggestions for future work with regard to thermionic modeling of decay heat removal systems is mentioned in addition to a discussion of the conversion of thermal

energy into electrical energy for other purposes relevant to reactor operation and efficiency.

2. GAS FAST REACTOR (GFR) OVERVIEW

The GFR is a fast neutron spectrum, helium (He)-cooled nuclear reactor. Two reactor thermal powers, namely 600 Megawatts thermal (MWt) and 2400 MWt, are being considered as appropriate operating powers for the GFR [3]. This thesis will focus on the 2400 MWt design. Furthermore, direct cycle and indirect cycle coolant systems utilizing He and carbon dioxide (CO₂) have been considered as heat removal systems [4,5,6,7,8,9,10,11,12]. This thesis will focus on a direct cycle He-cooled GFR. Operating temperatures for the GFR range from 490°C, at the reactor core inlet, to 850°C, at the reactor core outlet [3]. One more important aspect of the GFR considered in this paper is the fact that it is a pin-design reactor. The GFR core consists of fuel pins, similar to those seen in an LWR, contained within hexagonal cans. One difference in fuel pin design is the fact that the GFR contains uranium-transuranic carbide ((U,TRU)C) fuel while LWR fuel is uranium dioxide (UO₂) [3]. Another difference is the fact that while LWR fuel is contained within zircalloy cladding, GFR fuel is contained within silicon carbide (SiC) cladding [3]. Furthermore, LWR fuel is molded into a solid cylindrical pellet; however, GFR fuel is molded into an annular cylindrical pellet [3]. Along with the US, France has also undertaken the task of designing a GFR. However, their design consists of a reactor core containing plate fuel [9].

Although the GFR has many design characteristics that make it unique relative to all other reactor designs, it is classified as a Gen IV reactor along with the Very High Temperature Reactor (VHTR), the Sodium-cooled Fast Reactor (SFR), the Super

Critical Water Reactor (SCWR), the Lead-cooled Fast Reactor (LFR), and the Molten Salt Reactor (MSR). Along with the five other GenIV reactors, the GFR has been conceived to meet increasing energy demands and exhibit features such as proliferation resistance, process heat production, minor actinide burning capabilities, and increased plant efficiency.

2.1 History

While the GFR is considered a Gen IV reactor design, its origins extend back to 1962 when it was first conceived by General Atomics (GA). Initially, the GFR was labeled as the Gas-cooled Fast Reactor (GCFR). Two designs were considered, namely, a 300 Megawatt electric (MWe) design and a 1000 MWe design. A great deal of concern was placed on the ability to properly cool the reactor. Coolants considered for the GFR design included He and CO₂. During the early stages of the design process, there was universal recognition that these gases had poor heat transfer characteristics and low thermal inertia. Two notable methods to induce a greater degree of heat transfer were introduced in order to obtain a viable solution to cooling the reactor core. First, fuel surface roughening was envisioned as an adequate measure to take in order to increase the heat transfer surface area, thus passing more heat to the coolant. Second, core coolant flow reversal was seen as another method that could increase core cooling. Until 1978, studies concerning gas-cooled fast reactors were based on downward coolant flow through the reactor core. However, in 1979 upward coolant flow was seen as a more viable solution to core heat removal due to the incorporation of cooling by means of natural convection during a loss of forced cooling circulation accident. Although

upward He flow could provide a greater degree of core cooling during a loss of forced cooling circulation accident, fuel rod surface roughening induces greater frictional losses along the length of the core, thus increasing core pressure drop, an undesired effect. Increased core pressure drop places more stress on supporting mechanical systems in addition to reducing the heat capacity of the coolant, thus reducing the coolant's ability to remove heat from the core. Eventually, the primary focus of reactor core heat removal was placed on decay heat removal during loss of forced circulation accident scenarios [13].

Gaining international recognition, the GCFR attracted the efforts of other countries around the world. Between the 1960's and 1980's, research performed by GA was accompanied by research efforts from European countries such as Germany and Switzerland [13]. The European community collaborated to work on the Gas Breeder Reactor-4 (GBR-4), while the German Kraftwerks Union (KWU) performed some of its own design efforts [13]. In order to remedy LOFA scenarios, active safety systems were investigated. Ideas ranged from steam driven turbines for powering circulators to electric powered blowers. Emergency power supply was also investigated, as diesel generators and compressed air came under consideration for powering backup safety systems [13]. However, with the accident at TMI Unit 2 occurring in the spring of 1979, passive safety systems became the forefront of loss of flow accident mitigation efforts [13]. GCFR programs were canceled prior to an investigation of passive safety systems for GCFR designs.

With the recent development of a worldwide effort to pursue a Gen IV advanced reactor design program, interest in finding a passive solution to GFR decay heat removal has resurfaced over the last decade. Primary participants in GFR technology development consist of the US DOE and the Commissariat à l'énergie atomique (CEA). While both organizations have been tackling many design aspects of the GFR, a definitive solution for passive decay heat removal still does not exist. The primary focus of this thesis is an investigation into GFR modeling techniques that will lend further insight into GFR operating characteristics.

2.2 GFR Core Design

Prior to delving into GFR modeling techniques, it is important to become familiar with the reactor core design characteristics. An understanding of the reactor core design allows one to better understand the MCNP and MELCOR models used to simulate GFR conditions during operation. While the reactor core is characterized by the different assemblies that make up its design, three major regions can be observed, namely, the active core, reflector, and borated shield regions, as shown in Figure 2.1. The active core produces the thermal energy carried by the coolant from the core to the gas turbine. A reflector region surrounds the active core in order to reflect neutrons that leak from the core back into the core. Located at the periphery of the reactor core is a borated shield region designed for the purpose of capturing neutrons that leak beyond the reflector region. In order to create this three-region core, ten different types of assemblies are used. Details concerning the design aspects for all assemblies are scarce due to the lack of development of the GFR design. The design description of the fuel

assemblies provided by the US DOE provides some details as to how a GFR fuel assembly must be constructed. Thus, other assemblies must be modeled in a similar fashion to the fuel assemblies with obvious corrections for materials and rod dimensions. Details for the design of all reactor assemblies will be provided later in this thesis. Figure 2.2 provides an outline of a fuel assembly.

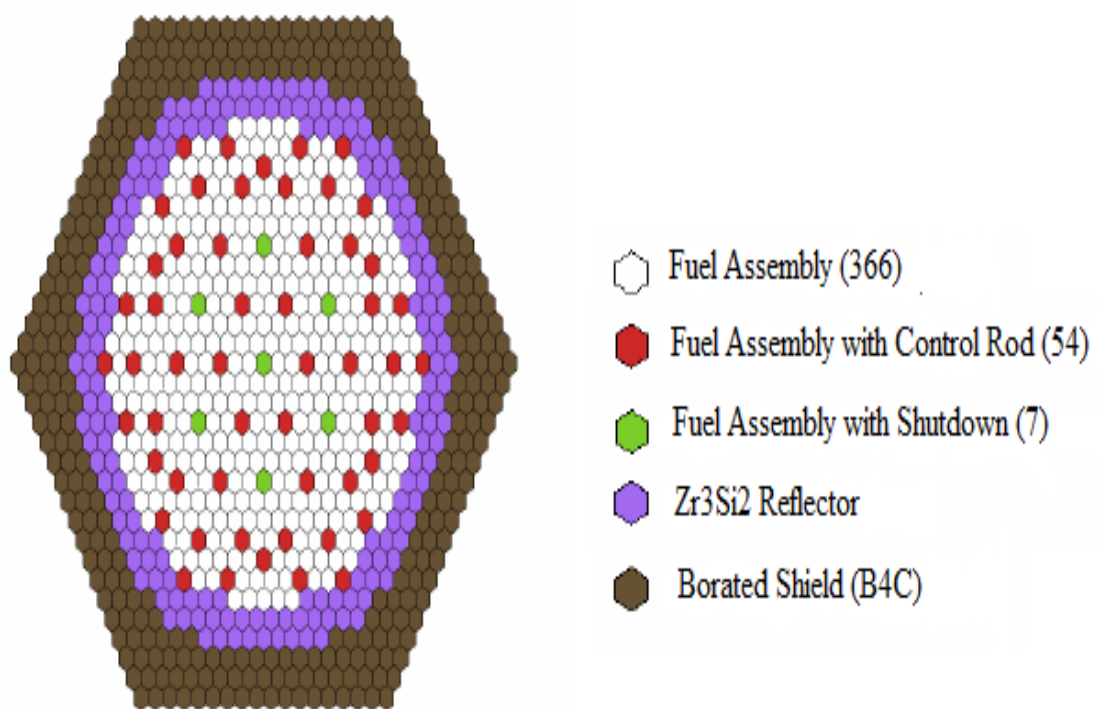


Figure 2.1: 2400MWt GFR Core Layout [3]

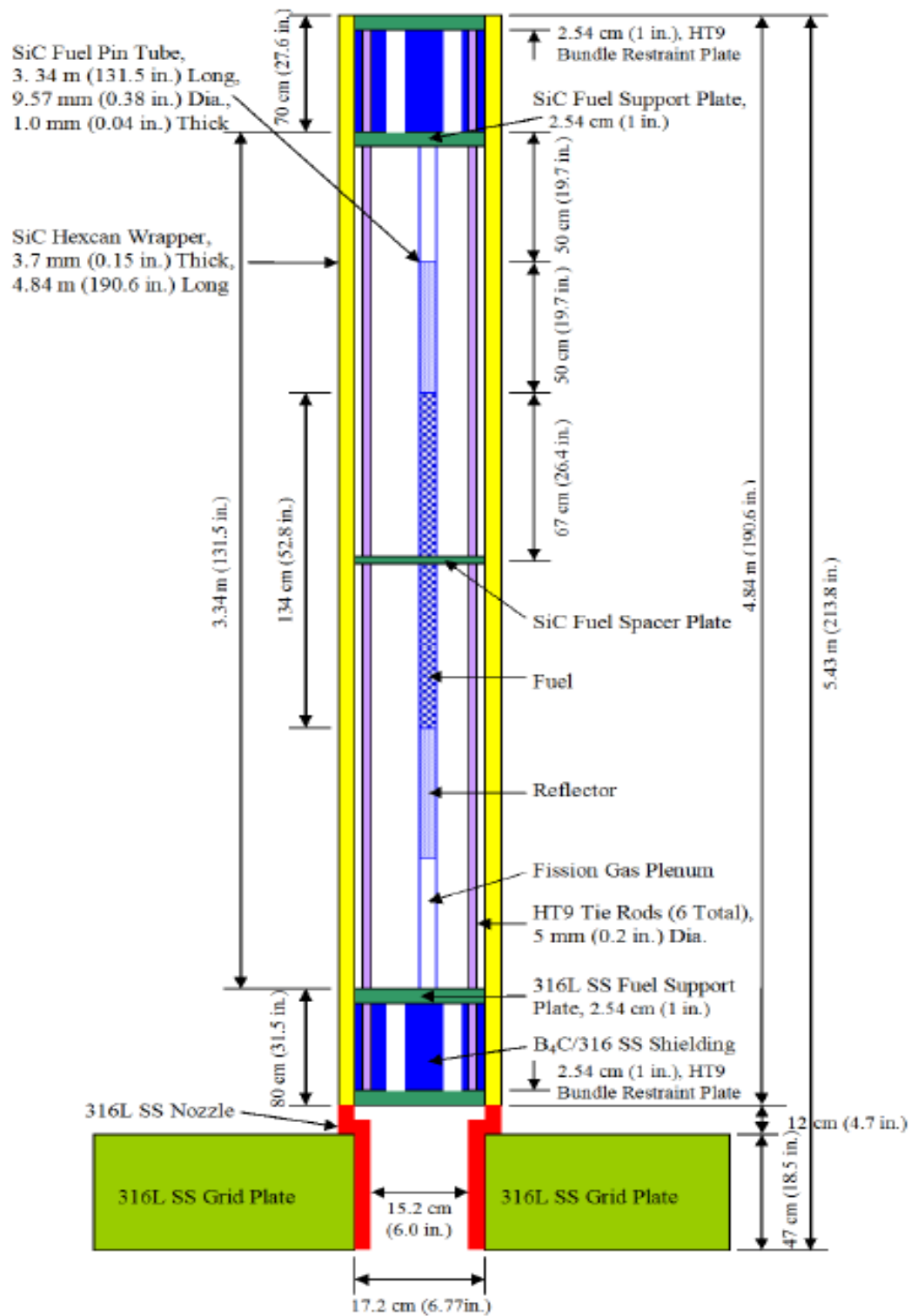


Figure 2.2: 2400MWt GFR Fuel Assembly Design [3]

2.3 Thermal Hydraulic Research on the GFR

Currently, there is some ongoing research regarding the thermal hydraulics of a GFR. However, the majority of these studies are conducted by European institutions, such as the CEA and Paul Scherrer Institute. Furthermore, the studies that are currently being conducted on a GFR design are with respect to a plate fuel design as opposed to a pin core design. Thus, results concerning the thermal hydraulic design of the American GFR design may slightly differ with respect to the thermal hydraulic design aspects of the CEA thermal hydraulic design. Variations in results will occur due to unequal hydraulic diameters that are a consequence of the differences observed between the two core designs. Results may also vary due to how heat is distributed in the US DOE GFR relative to the CEA GFR. Differences in heat distribution may occur due to the inconsistencies in the core geometries between the two designs.

2.3.1 Experiments Concerning the GFR

To date, no experimental data concerning the design of a Gen IV GFR design exists. All data obtained regarding a 2400 MWt design is computational. The next subsection discusses computer codes that have been used in order to obtain information regarding a 2400 MWt GFR design.

2.3.2 Computational Analysis of the GFR

Computer codes that have been used in order to evaluate the thermal hydraulic characteristics of possible GFR designs include the CATHARE and ATHENA codes [9]. The US DOE has used RELAP in order to simulate GFR thermal hydraulic operating and accident conditions [3]. However, their analysis was performed while taking the

600 MWt design into consideration as opposed to the 2400 MWt design. While gas-cooled thermal reactor analysis has been performed with MELCOR, there has been no gas-cooled fast reactor analysis with MELCOR. Thus, this thesis will lend further insight into how the MELCOR code can be used to analyze the thermal hydraulic characteristics of a gas-cooled reactor with a fast neutron spectrum. Information regarding thermal hydraulic modeling techniques of the US DOE GFR will prove crucial towards the development of modeling techniques and assessment of GFR accident scenarios.

3. TECHNICAL APPROACH

Ultimately, the intention of this investigation is to develop a MELCOR model of a GFR operating in steady state conditions in order to understand possible GFR operating scenarios prior to a possible LOFA caused by station blackout. Such a model will prove pivotal towards understanding reactor conditions that will have a significant impact on safety concerns in the event that this particular accident occurs. To begin the investigation, a model of the GFR is made in MCNP according to US DOE design specifications. The MCNP model is needed in order to obtain a neutron flux profile throughout the reactor core. Then, with a known flux profile, the normalized radial and axial power distributions are calculated. A power distribution is necessary in order to properly develop a model of the GFR in MELCOR. After calculating the radial and axial power profiles for the GFR, this data is then implemented into MELCOR. Next, the MELCOR model is created according to DOE design specifications. A MELCOR model of the GFR is required in order to obtain axial and radial temperature distributions in the GFR reactor core. With knowledge of varying temperature distributions prior to a variety of postulated scenarios, one may be able to gain a better understanding of how to design a decay heat removal system needed for heat removal during accident scenarios.

Because this document is concerned with developing modeling techniques for the purpose of improving reactor safety, special attention is placed upon temperature distributions during steady state conditions. Furthermore, it is assumed that these temperatures have a significant impact on accident scenarios, such as a LOFA. A

discussion on how thermal energy may be converted to electrical energy in order to power a passive decay heat removal system is included in the closing section.

4. MCNP OVERVIEW

Prior to an explanation as to how an input deck for MCNP is constructed, it is important to understand how the code works. The MCNP code is based off of the Monte Carlo method for statistically determining the transport of neutrons. Within the code, different individual events that may take place are simulated in a sequence. Probability distributions governing each of the possible events are sampled in order to describe all phenomena together. The sampling process occurs through the selection of random numbers. Once a neutron is born, it is tracked throughout space. Neutrons are tracked over the course of their life until their death, which may occur due to absorption or escape. Known transport data is used in order to sample probability distributions that determine what will happen to a neutron over the course of its life [14].

In order to further understand what may happen to a neutron over the course of its life, one may look at the different events that may take place. Such events include neutron scatter along with photon production, fission along with photon production, neutron capture, neutron leakage, photon scatter, photon leakage, and photon capture. These events may or may not occur in the order listed. The MCNP code uses ones and zeros in order to determine whether an event does or does not occur. The probability that a one or zero will be selected for a particular event is based on probability distributions obtained from known transport phenomena [14].

4.1 Code Overview

An MCNP input deck is made of one input file. When executed, the input file creates an output file that may contain varying pieces of information. Information contained within an output file is dependent on the tallies and print tables chosen by the user in the input deck. Tallies represent the type of statistical analysis the code performs upon the information in the deck that is specified by the user. Information that can be extracted from an MCNP output includes particle current, particle flux and energy deposition. With the appropriate tally selection, the user can extract the flux distribution from the MCNP output, which ultimately allows one to calculate how power is distributed throughout the reactor core being modeled [14].

4.2 Code Architecture

MCNP is allocated into sections composed of particular card types. Card types relevant to this particular thesis include:

- Title Card: Contains information about the problem modeled by the user.
- Cell Card: Contains information regarding the shape and material content of physical space.
- Surface Card: Contains information regarding the geometry of structures in the core, such as fuel rods, assembly cans, and spacing between assemblies.
- Data Card: Contains information regarding the criticality calculation source and materials cards. Tallies are also classified as a particular type of data card along with material cards.

All of the cards mentioned above can be combined in order to design a reactor core. The following subsections elaborate on the details of the mentioned cards and how they can be used in order to create an input deck. There is no discussion regarding the Title cards since they are only used in order to specify the problem and do not provide reactor core information necessary for running an input deck.

4.2.1 Cell Card Overview

Following the construction of the Title card, cell cards are established in order to define shapes and materials present in the input deck. First, each cell card present in an input deck must be associated with a number. The number of a cell card is the first entry on a line for a particular cell card. Following the number of the cell card is the material number for that particular card. Materials are defined later in the input deck; however, they are called upon in the section containing the cell cards in order to provide material specifications for the cell being created. Next, the user must specify the cell material density. Then, the surface numbers for the cell card must be specified by the user in order to give the cell a particular shape. Furthermore, the surface numbers allow the user to specify the location of multiple materials within one cell card. Finally, an optional specification of cell parameters may be input by the user as the final entry for a particular cell card. A cell parameter includes the importance the user places on specific particles, such as a neutron or photon. If importance is placed on a particle, then the MCNP code tracks that particular type of particle. However, if importance is not placed on a particular type of particle, then it is ignored by MCNP [15].

4.2.2 Surface Card Overview

Surface cards are needed in order to provide the cell cards with geometric specifications. The surface cards must be input after all of the cell cards have been defined by the user. When constructing surface cards, the first entry that must be input is the number with which the surface card is associated. Next, the surface mnemonic must be input. Surface mnemonics describe the actual geometric shape being input. Options for a shape of a surface include planes, cylinders, spheres, etc. Finally, the dimensions of the surface are placed at the end of the line for a surface card [15].

4.2.3 Data Card Overview

Although there are many different types of data cards available in the MCNP code, only the ones that are relevant to this thesis are mentioned in this subsection. Relevant data cards include the kcode card, ksrc card, material cards, card for the type of tally chosen by the user, and the print cards. Both the kcode and ksrc cards refer to the criticality calculations occurring in the input deck. The material cards are used for construction of an actual material that is used in the cell cards, and the tally card chosen by the user is dependent upon his/her preference for certain statistical data desired from the calculation. The print cards allow the user to select the type of information he/she would like to extract following execution of the input deck.

Statistical accuracy from a particular MCNP input deck is largely dependent upon the kcode data card because it allows the user to specify how many particles he/she would like to use. A greater amount of particles ensures a greater degree of precision up to a certain point. However, a greater amount of particles also ensures a larger amount

of computational time. It is up to the user to decide how much statistical precision he/she would like to sacrifice in order to decrease computation time. In order to establish the kcode card, the user must first input "kcode". Then, the number of neutrons per cycle is specified followed by an initial guess of keff, the effective eigenvalue that determines how close the reactor is to criticality. Next, the number of cycles to be skipped before gathering data on keff is input followed by the total number of cycles that the user would like to run. A certain number of cycles must be skipped due to statistical fluctuations that may appear in the first few cycles [15].

Because fuel is present throughout much of the reactor core, there are many possible locations where the fission process can be initiated. While the user has the option to input multiple fission source points into the code, he/she must list at least one source point in a location where fuel is present. Construction of the ksrc card begins with the word "ksrc", and is further established with x, y, and z coordinates of the source [15].

Although information concerning material properties is first found in the section containing cell cards, actual material properties are not found until the material cards located in the data card section of the MCNP input deck. The user must input a number that is associated with the particular material being input. Next, the user must input the atomic number of an isotope that makes up part of the material followed by the atomic mass of that particular material. A period is placed after the mass number along with the cross section library used for the material being identified. If multiple isotopes combine

to form a particular material, then all of the atomic numbers and masses of those isotopes must be input by the user [15].

While there is a lot of valuable information that can be extracted from an MCNP input deck, it is up to the user to select the appropriate tally for the information that he/she desires. Furthermore, when selecting a tally, the user can also specify the types of particles that he/she would like to track, such as neutrons and photons. After applying the desired tally and print tables, the user can end the input deck and run the calculation. Print tables are selected according to information the user desires to view following execution of the input deck. While there are many more data cards that can be discussed, only the ones relevant to this thesis have been discussed in this subsection.

5. MELCOR OVERVIEW

While this thesis primarily focuses on gas-cooled fast reactor modeling, one should note that MELCOR was originally designed in order to model thermal LWR nuclear power plants. Recent extensions have enabled analysis of gas-cooled thermal reactors. MELCOR is also designed to handle a wide variety of severe accidents and allows the user to determine the various consequences of a severe accident, such as rapid pressure changes and large temperature increases. Initially, MELCOR was seen as a parametric code with respect to modeling complex physical processes. This was due to a desire for quick code execution along with a lack of understanding of reactor physics. However, due to advancements in technology allowing for reductions in uncertainty, along with increased user expectations, MELCOR has been developed into a code that is now best estimate in nature. Some aspects of MELCOR still remain parametric in nature due to certain physical phenomena that are accompanied by a high degree of uncertainty relative to simpler physical phenomena [2].

Although other reactor safety codes, such as SCDAP/RELAP, allow a reactor safety analyst to develop a model of a reactor using components already built into the reactor safety code, MELCOR allows the user much more freedom in that MELCOR is based off of a “control volume” approach. MELCOR does not allow the user to piece together reactor components. Rather, it allows the user to specify conditions within independent control volumes that may represent different areas located within and around the reactor core. While this feature of MELCOR makes it more difficult for the

user to actually see reactor components, it provides the user with a greater degree of freedom in the sense that he/she may specify varying conditions within and around the reactor core that may simulate different components or other properties. Thus, the user is not restricted to working with built-in pumps or valves that may only simulate a restricted amount of conditions. In addition, the “control volume” approach removes the restriction of a specific nodalization required from the user. Thus, the user has more freedom to define either very small or very large control volumes, depending on whether the user prefers a more accurate description of physical phenomena, or decreased computation time, respectively. Upon further evaluation, one may deduce that MELCOR allows the user to specify his/her own nodalization scheme rather than working with one already built into the code.

5.1 Code Overview

Comprising the MELCOR code are two executables, MELGEN and MELCOR. The MELGEN executable processes and checks the code input. Furthermore, it creates a diagnostic file including error and warning messages and a restart file that contains the initial and boundary conditions necessary for the actual calculation. The MELCOR executable reads the restart file along with other user input and advances the calculation in time. Then, MELCOR writes the output to both text and plot files. The plot file is known as a PTF file, and it generates plots using an excel plug-in or a plotting tool, such as AcGrace. Diagnostic and message files containing error and warning messages are also created by the MELCOR executable [2].

5.2 Code Architecture

MELCOR and MELGEN are composed of modules known as packages.

MELCOR packages relevant to the GFR analysis conducted for this thesis include:

- Control Functions (CF): Evaluates control functions defined by the user and applies them in order to control various characteristics of the calculation, such as maintaining constant conditions in a source and sink, establishing mass flow rates and velocities, etc.
- Core Behavior (COR): Evaluates the behavior of the fuel along with other core and lower plenum structures. Evaluations may be conducted up to and through bottom head failure and release of core material to the containment.
- Control Volume Hydrodynamics (CVH): Evaluates the flow of mass and energy between control volumes together with the FL package to be mentioned later in this section.
- Executive (EXEC): Controls execution of the MELGEN and MELCOR executables.
- Flow Paths (FL): Models the flow rates of liquids and gases between control volumes together with the CVH package.
- Heat Structures (HS): Models the thermal response of heat structures and mass, as well as the heat transfer between heat structures and control volumes.
- Material Properties (MP): Evaluates the physical properties for all packages excluding H₂O and NCG.

- Noncondensable Gas Equation of State (NCG): Evaluates the properties of noncondensable gas mixtures.
- Tabular Functions (TF): Evaluates user-selected tabular functions in order to control various characteristics of the calculation, such as mass and energy sources [2].

All of the packages mentioned above supply the necessary information in order for MELCOR to carry out a calculation. General explanations of four of the packages mentioned are given in Subsections 5.2.1 through 5.2.3. The four packages discussed in these subsections are selected due to their content and the large volume of information they hold relative to the packages not selected for further explanation.

5.2.1 COR Package Overview

In order to understand many of the physical processes occurring within the reactor core, the user must utilize the MELCOR COR package in order to create a model of the core. Different physical processes that can be modeled include heat generation within the fuel and other core and lower plenum structures. Furthermore, heat transfer, and chemical interaction between various reactor core and lower plenum structures can also be modeled with the core package. During a severe accident, such as when core and reactor vessel melting take place, the COR package can assist the user in evaluating how material relocation occurs within and beyond the reactor core. In general, the MELCOR COR package calculates the thermal response of the core and lower plenum structures.

Construction of the reactor core and lower head must evolve from the appropriate allocation of axial levels and radial rings. Axial levels are sequenced from the bottom of

the core to the top of the core, while radial rings are sequenced from the core centerline outward. By creating a multitude of axial levels and radial rings, the core and lower plenum eventually become divided into core cells. Materials contained within the core cells are specified by the user and include fuel, cladding, canning, control poisons, etc. All core cells must be coupled with a control volume created within the CVH package [16].

Although the majority of modeling with the COR package is dependent upon user preference for specifying certain reactor conditions, there are default options built into the MELCOR COR package that allow the user to choose a reactor type that can provide certain default conditions. Such default reactor types include a Pressurized Water Reactor (PWR), a Boiling Water Reactor (BWR), a Pebble Bed Reactor (PBR), and a Prismatic Reactor (PMR). Each default reactor type sets specific default conditions, such as geometric parameters concerning fuel and cladding size, and the location at which the control blades enter the core. Later in this thesis, a detailed explanation will be provided for the reasons as to why a BWR reactor type is chosen for the MELCOR COR package of this thesis. Due to the lack of a GFR option built into the MELCOR COR package, a setting with default specifications for a GFR could not be selected [16].

While some geometric parameters are provided in default settings, others must be specified by the user. Geometric specifications that must be input by the user include surface areas for structures, such as fuel, cladding, canning, control rod guide tubes, and the rods housing the control poisons. Other geometric specifications that must be input

by the user include the geometry of the lower head and lower plenum. Specifications for the amount of mass contained within each core cell must be input by the user as well [16].

5.2.2 CVH and FL Package Overview

Unlike many other reactor thermal hydraulic codes, such as MAAP [17], which model the movement of mass and energy through specific reactor components, MELCOR uses a control volume-flow path approach to model the movement of mass and energy through space. The user can model the movement of liquid or gas between control volumes in order to represent the medium which is gaining thermal energy from the fission processes taking place in the fuel. Each control volume represents a volume of space containing mass and energy, while each flow path connecting control volumes represents the paths between control volumes through which mass and energy can move. Control volumes, along with flow paths are used to model how thermal energy is passed to the coolant and taken away from the core structures [2].

As stated earlier, MELCOR is designed to allow the user to create a specific nodalization scheme rather than piecing together reactor components already built into the code. This was done with the intention of creating an environment that allows the user to simplify sensitivity studies as well as allow for more detailed studies that could be compared to other specialized codes [2].

In order to define the state of each control volume, the user must specify all hydrodynamic conditions within a control volume. Such specifications include the type of coolant present, as well as the pressure and temperature of the coolant.

Hydrodynamic materials are separated into two independent fields, pool and atmosphere. The user may interpret these two fields as the coolant material being separated due to gravity; however, conditions are really dependent upon user specification. Both the pool and atmosphere for a control volume are given a temperature value; however, only one pressure is needed for a single control volume. Other conditions, such as elevation, number of segments, and coolant velocity must also be specified in order to appropriately model a control volume. Control volumes are associated with core cells and heat structures in order to provide a medium to which those structures may pass thermal energy.

Control volumes alone cannot fully describe hydrodynamic conditions throughout the reactor. Flow paths must be used to connect control volumes in order to allow a path for the coolant to move when it is being advanced from one control volume to another. The user must specify conditions for the flow paths, such as orientation, flow restrictions, the number of segments, etc. Obviously, a greater number of segments allow for a more accurate calculation; however, computational time will certainly increase. Other specifications, such as hydraulic diameter and flow path segment length are required as well. As calculations are being run, MELCOR solves conservation of mass, momentum and energy equations in order to provide the user with the details of the hydrodynamic processes taking place through the flow paths and within the control volumes. While solving the governing equations for the CVH and FL packages, MELCOR uses information already provided by the user in the CVH and FL packages. However, MELCOR also uses information from other packages, such as the COR and

HS packages since there may be heat sources or sinks present within calculations for those packages. Thus, the thermal energy transferred between control volumes is dependent upon thermal energy created or dissipated within other structures.

5.2.3 HS Package Overview

The MELCOR HS package calculates heat conduction within intact solid structures as well as heat transfer across the boundary surfaces of those particular structures. Solid structures that may be treated within the HS package include vessel internal walls, containment structures, piping, etc. While in reality, the solid structures are three-dimensional, a heat structure is represented by one-dimensional heat conduction with boundary conditions at each of its surfaces [17].

As with control volumes and flow paths, heat structures require certain user-specified input in order to provide a description suitable for calculation. Within the HS package, the user must define the elevation, orientation and material properties of all heat structures. Furthermore, each heat structure must be divided into nodes which may or may not be made of different materials. The nodes of the heat structure do not need to be equally spaced. If a convective boundary condition is specified by the user, then the entire boundary surface must fit within its boundary volume. In other words, the bottom surface of the heat structure cannot extend below the bottom elevation of the bottom of its associated control volume. In addition, the top surface may not exceed the elevation of the top of the control volume to which the heat structure is associated [2].

Previously, in Subsection 5.2.2, it was mentioned that calculations done within those packages are partially dependent upon data originating from the HS package.

Evidence of this transfer of information between these packages is showcased by the fact that during boiling, radiative heat transfer from the surface of a heat structure to a pool volume is calculated. This calculation may also take place between a heat structure and an atmosphere if water vapor or carbon dioxide is present within the atmosphere. Thus, one can see how the HS package can calculate the amount of heat being delivered to a control volume. This same principle applies for the calculation of mass transfer as well. Liquid vapor may form on the surface of a heat structure and eventually become entrained within the coolant flow path [2].

6. MCNP CALCULATIONS

Prior to the development of a MELCOR input deck representative of the GFR, an MCNP deck is created in order to obtain the normalized neutron flux distribution in the GFR active core. With the assumption that the power profile follows the neutron flux profile in the active core, the flux distribution obtained in MCNP is normalized and then used in the MELCOR input deck. A description of how the normalized power profile is integrated into the MELCOR input deck will be discussed in the following subsection.

Initial neutronics calculations for the US DOE GFR design were performed using the DIFF3D and REBUS codes, deterministic neutronics modeling codes. A relative power distribution was not given in the most recent design document. However, it seems as if the codes were used in order to determine where fuel assemblies with varying enrichments needed to be placed in order to create an appropriate power profile for the GFR. Rather than using the DIFF3D and REBUS codes to determine the flux profile throughout the active core region, MCNP is used for this project. The decision to use MCNP is made in order to lend a different type of neutronics modeling technique to the GFR design effort. While DIFF3D and REBUS are deterministic modeling codes, MCNP is a Monte Carlo code, which applies Monte Carlo statistics in order to determine neutron motion.

Because MCNP has not been used to obtain a flux profile from the US DOE GFR, this section mainly focuses on modeling techniques for the GFR with MCNP. During the modeling effort, various incomplete design aspects were encountered. In the

next subsections, as the modeling approach and MCNP input are explained, measures taken to complete insufficient design data are also discussed. Other adjustments to design criteria that do not pertain to incomplete design aspects are also explained.

6.1 Modeling Approach

The main purpose for the development of these particular MCNP decks is to advance neutronic modeling techniques for the US DOE GFR. However, the reader must also keep in mind that these decks are also necessary for creating a neutron flux profile that can be used in the COR package of the MELCOR input deck. There are two MCNP input decks that have been created and that are similar in all aspects except for one, the meshing scheme used to determine the neutron flux profile. In the input file named `ftn3.inp`, the active core is split into 5 radial rings of equal width. These 5 rings are meant to correspond with the 5 radial rings that represent the radial rings in the MELCOR input deck. The height at which the 5 rings have been placed is at half of the active core length. Within the other input file, `ftnA3.inp`, the active core is split in 10 axial regions, with all regions having the same height. The axial regions are divided at the halfway point between the center and edge of the radial boundary of the active core. All other input, such as the input for cell cards, surface cards, and all data cards not relating to the meshing scheme are exactly the same.

Along with a description of how the GFR core is modeled are descriptions of each of the assemblies as they were initially designed. Some assembly types lack details required to fully construct them. Thus, some inferences regarding their design are made based upon how other assemblies with a full description are designed. While there are

five different types of fuel assemblies, they are geometrically the same. The assemblies only differ due to their fuel enrichments. Therefore, only one subsection exists for the description of the fuel assembly design. Similarly, there are 3 types of control/shutdown assemblies that are all geometrically the same and only differ due to variations in fuel enrichments. Control material boron-10 enrichments vary as well between control/shutdown assemblies; however, a conclusion on boron-10 enrichments for control poisons for each control/shutdown assembly has not yet been reached. Alterations to original design specifications of various boron-10 enrichments found within the boron carbide control rod poison must be made in order to insure that the reactor can be operated safely and placed in a subcritical state. Assemblies not found within the active core include reflector assemblies and borated shield assemblies. Many details regarding the design of these assemblies are not given by the US DOE. Therefore, certain inferences regarding their possible design are made for the sake of completing the MCNP input deck. Although the majority of assumptions lie within the following subsections, some general assumptions may be stated as:

- The Reactor Pressure Vessel (RPV), core barrel (CB), lower head, lower core plate (LCP), assembly nozzles and upper head are not modeled. They are considered negligible for neutronics calculations.
- Although design specifications require that the canning for the borated shield rods be comprised of tungsten, they are modeled with silicon carbide. This is due to a MELCOR code restriction that is discussed in the following section.
- 2.5 million particles are simulated.

- No control/shutdown rods are inserted.
- No core material relocates at any time during the simulation.

6.1.1 Fuel Assemblies

Contained within the active core region of the GFR are 366 fuel assemblies. Two possible interpretations as to how many fuel pins are present in a fuel assembly are available. There are multiple places in the DOE design report that claim there are 271 fuel pins present in a fuel assembly [3]. However, Figure 2.2 of this document shows that there are also 6 tie rods present in a fuel assembly. There are two possible ways in which one could accommodate the 6 tie rods. First, 6 fuel rods could be removed from the fuel assembly and replaced with 6 tie rods. Geometrically, this is a realistic possibility since the tie rod diameter is listed at 5mm, 4.57 mm smaller than a fuel rod diameter. However, it was decided that having the maximum amount of fuel rods present in a fuel assembly is appropriate for the MCNP input deck. This decision is a result of the fact that having the maximum amount of fuel rods in an assembly presents the most limiting case in terms of assessing a severe accident scenario since more heat is delivered to the coolant when more fuel is present. Second, the fuel pitch could be decreased in order to accommodate the tie rods at each of the 6 corners of the hexagonal assembly can. This action is not taken due to concerns that placing the fuel rods too close together may cause them to interact after undergoing large amounts of irradiation that could potentially induce large amounts of fuel rod swelling. Prevention of interaction between fuel rods is a necessity in order to reduce fuel rod stress as well as

maintain fuel rod integrity. Thus, it is decided to model all fuel assemblies with 271 fuel rods only.

Although no consensus has been reached as to the type of fuel that will be used in the GFR, (U,TRU)C has been selected for use during this analysis. However, prior to discussing the fueled region of the pin, fuel pin description should begin at the bottom of the fuel pin. Starting at the bottom of the fuel pin, an empty plenum region is reserved for thermal expansion of fuel and reflector material. Furthermore, the empty plenum provides a gap to where fission gases may accumulate rather than cause increased stress on the cladding of the fuel pin. The plenum region extends 0.5 m up the length of the fuel pin until the reflector region of the fuel pin is encountered [3].

Design specifications indicate that the reflector material is made of zirconium silicide (Zr_3Si_2). Zr_3Si_2 is not commercially available, and there is not a large amount of data about the material. However, studies have been conducted which prove that the material can withstand high temperatures. This particular property, along with a high elastic scattering cross section, makes Zr_3Si_2 a good reflecting material. The rod reflector region extends 0.5 m above the empty plenum region until the active fuel region is encountered.

Accounting for the nuclear material producing thermal energy, an annular region of (U,TRU)C extends for a length of 1.34 m above the reflector region mentioned in the previous paragraph. Fuel enrichments range between 14.8% and 20%, where the percentages represent the amount of fissile TRU material present within the fuel. All uranium present within the fuel is considered to be natural uranium. The fuel

enrichment in one particular assembly is constant both along the length of the fuel region in a pin as well as for each fuel pin contained within one assembly. While only five different enrichments are specified for the GFR core design, one must keep in mind that this specification is only for a first batch loading. Depending on minor actinide burning capabilities, as well as other possible nuclear fuels that could potentially be used for the GFR, other fuel enrichments may be used in the future. Determination of other possible enrichments and fuel options is beyond the scope of this thesis.

Extending above the active fuel region is a repetition of the two regions below the fuel region beginning with the reflector region and ending with the empty plenum region. As is the case below the fuel region, both the reflector and empty plenum regions are listed at 0.5 meters. Holding the fuel, reflector and empty plenum regions in one pin is the SiC cladding. SiC is chosen as the cladding due to its ability to operate at high temperatures. Fixing the position of the fuel pins are fuel support plates located just above and below the top and bottom of the fuel pins, respectively. The fuel support plate located below the fuel pins is made of stainless steel. However, the fuel support plate above the fuel pins is made of SiC. Above and below the fuel support plates just mentioned are borated shield regions. These shields act as neutron absorbers that can capture neutrons and stop them from leaking out of the core. The lower borated shield (LBS) and upper borated shield (UBS) regions are comprised of stainless steel rods packed with boron carbide. Below the lower borated shield region and above the upper borated shield region are stainless steel plates for increased support. Initially, the highest support plate was designed to be made of HT9 steel. However, due to uncertainties in

Further specifics regarding the dimensions of the fuel assemblies will be mentioned in the subsections regarding the MCNP input. The MCNP input does not contain information regarding the nozzle at the bottom of each assembly nor any aspects of the LCP below all assemblies. The decision is made to leave out such details due to the assumption that neutronics considerations pertaining to the nozzle and LCP are considered negligible. Once neutrons have encountered the LBS, or possibly have leaked beyond, the probability that they make their way back into the core and affect the neutron flux profile is very small. Nozzle and LCP dimensions will be discussed during the modeling techniques subsection of the next section. Due to the nozzle's impact on flow characteristics and the LCP's impact on conduction, their impact will be felt in MELCOR.

For simplification, it is assumed that the bottom of a fuel pin is connected with the bottom of an assembly as it is modeled earlier in this subsection. Thus, the bottom of the fuel pin is now considered to be at the lowest point of the stainless steel support plate that is below the borated shield. Another simplifying assumption is that all support plates are grids that have cylindrical pegs on which the remainder of the fuel rods rests. These pegs have the same circumference as the fuel rods themselves. Furthermore, the UBS and LBS are considered to be a collection of rods that are the same in number and circumference as the fuel rods. Such assumptions are made in order to simplify MCNP input. Major design characteristics associated with a fuel assembly design are presented in Table 6.1. The reader should note that the assembly pitch, can thickness and flat-to-flat distance are the same for all assemblies present throughout the entire core.

Table 6.1: Fuel Assembly Design Characteristics

Parameter	Value (cm)
Inner Fuel Radius	1.510E-01
Outer Fuel and Reflector Radius	3.685E-01
Gas Gap Thickness	1.000E-02
Cladding Thickness	1.000E-01
Pin Radius	4.785E-01
Upper and Lower Plenum Length	5.000E+01
Upper and Lower Reflector Length	5.000E+01
Active Fuel Length	1.340E+02
Flat-to-Flat Distance	2.150E+01
Can Thickness	2.300E-01
Pin Pitch	1.256E+00
Assembly Pitch	2.220E+01

6.1.2 Control/ Shutdown Assemblies

Control and shutdown assemblies are constructed in the same manner as fuel assemblies. While there is no specification as to why they have different names, one may surmise that their names differ due to their location in the core. Just as a PWR has different control rod banks, perhaps control and shutdown assemblies have different functions. Due to their names, it seems like the control assemblies are used for fine power control during operation, whereas the shutdown assemblies may only be used to shut down the reactor core.

While control and shutdown assemblies may contain neutron absorbing material when rods are inserted into the core, one must note that they also contain fuel rods. Both control and shutdown assemblies contain 234 fuel rods along with space for one control rod [3]. The fuel rods contained within control and shutdown assemblies are of the same

design as those seen in fuel assemblies, and their enrichments can vary from assembly to assembly as well. Located in the middle of both the control and shutdown assemblies is a gap where a control rod may be inserted during operation. Control rods are made of a boron carbide powder packed into SiC cladding. Although the material contained within a fuel rod remains separated from the cladding by a gas gap, the boron carbide is in direct contact with its cladding. Although not specified in the design document, it is assumed that the control rod is, at the very least, as tall as the entire core. Another interesting feature of the control and shutdown assemblies is that they each have a hexagonal can surrounding the gap reserved for control rod insertion and withdrawal. One could consider this hexagonal can to be analogous to a control rod guide tube (CRGT) seen in a PWR.

Although no design specifications went into detail regarding how the fuel rods and control rods are held in place in control and shutdown assemblies, the assumption is made that upper and lower fuel support plates, similar to those used in a fuel assembly, are used to hold the fuel rods in place. Once again the lower fuel support plate located just under the fuel rods is made of stainless steel, while the upper fuel support plate is made of SiC. The major difference between the support plates used in the control/shutdown assemblies and the fuel assemblies is that the control/shutdown assembly support plates have a large central gap in them in order to account for the space needed for control rod insertion and withdrawal. It is also assumed that control rods are held in place by a control rod drive mechanism (CRDM) used for the control rod. Because the control rods are driven into the core from underneath the core, one can

assume that the CRDM may be similar to that of a BWR CRDM. Thus, the control rod is held in place by an index tube. Another assumption made is that the LBS and UBS, similar to the ones seen in the fuel assemblies, are present below and above the lower and upper fuel support plates, respectively. The major difference between the borated shields in the different assembly types is that the borated shields in the control/shutdown assemblies contain a large central gap that allows for control rod insertion and withdrawal. Furthermore, as seen in the fuel assemblies, stainless steel support plates lie above the UBS and below the LBS. Finally, the entire assembly is encased within a hexagonal SiC can of the same dimensions as the can surrounding the fuel assemblies.

Again, greater detail regarding the dimensions of the control/shutdown assemblies will be given along with the MCNP input description. Also, details regarding the inlet nozzle for the control/shutdown assemblies are reserved for the discussion on MELCOR modeling techniques. The inlet nozzle is assumed to have negligible impact on neutronics considerations relative to MCNP input. Two main design characteristics concerning the control/shutdown assemblies are presented in Table 6.2. Details concerning the design characteristics of a fuel rod present in a control/shutdown assembly can be found in Table 6.1 since the fuel rods present in a control/shutdown assembly are of the same design as those found in a fuel assembly.

Table 6.2: Control/Shutdown Assembly Design Characteristics

Parameter	Value (cm)
Inner Can Flat-to-Flat Distance	7.240E+00
Inner Can Thickness	2.300E-01

6.1.3 Reflector Assemblies

In Subsection 6.1.1, a reflector region comprised of Zr_3Si_2 was described as being located above and below the active fuel in a fuel pin. However, there was no mention of a reflector region in the radial direction of the core. Just beyond the active core region, in the outward radial direction, is a reflector region also comprised of Zr_3Si_2 material. Its purpose is, also, to reflect neutrons back into the core. Reflector assemblies contain no fuel rods and no cladding support for the Zr_3Si_2 rods encased within a reflector assembly. Due to the lack of design specifications for the reflector assemblies, some assumptions are made in order to provide a basic description of this particular type of assembly. However, an in-depth design description regarding the dimensions of a reflector assembly will be given along with the MCNP input for a reflector assembly.

While the dimensions for the hexagonal can surrounding the reflector rods are of the same dimensions as the cans surrounding the fuel, control, and shutdown assemblies, only 19 reflector rods are contained within each reflector assembly. The reflector rods are made of Zr_3Si_2 , and are assumed to extend the same length as a fuel pin. One can assume that upper and lower support plates, hold the reflector rods in place. Similar to the fuel assembly design, a SiC support plate is assumed to lie above the reflector rods, while a stainless steel support plate is assumed to lie below the reflector rods. Furthermore, a borated shield layer can be assumed over the upper support plate and below the lower support plate. Another important assumption is that stainless steel support plates lay above the UBS and below the LBS. Axial dimensions of the support plates are equivalent to those seen for the fuel and control/shutdown assemblies. Radial

dimensions are adjusted to the radii of the reflector rods. Finally, the hexagonal can surrounding the reflector assemblies is made of the same material as the reflector rods themselves, namely, Zr_3Si_2 .

As is the case with the fuel and control/shutdown assemblies, the lower nozzle and LCP specifics that relate to the reflector assemblies will be mentioned during the discussion of MELCOR modeling techniques. Their characteristics are assumed to be unimportant with respect to neutronics considerations for the reflector assemblies. Important design characteristics concerning the construction of a reflector assembly may be found in Table 6.3.

Table 6.3: Reflector Assembly Design Characteristics

Parameter	Value (cm)
Rod Radius	2.005E+00
Rod Length	3.340E+02
Rod Pitch	4.664E+00

6.1.4 Borated Shield Assemblies

Comprising the outermost region of the GFR core are the borated shield assemblies. The purpose of the borated shield is to prevent neutrons from leaking out of the core in the outward radial direction. Prevention of neutron leakage helps to slow the process of RPV embrittlement, as well as, helps protect the plant workers and public from radiation poisoning. Assumptions regarding design specifications for the borated

shield assemblies needed to be made due to a lack of design data for the borated shield assemblies.

Once again the dimensions of the hexagonal can surrounding the borated shield assembly are considered to equal those of the hexagonal can surrounding the fuel, control/shutdown, and reflector assemblies. Similar to the reflector assemblies surrounding the active core, the borated shield assemblies contain 19 rods that extend the same length as a fuel pin. However, the rods in these particular assemblies are made with boron carbide in order to capture leaking neutrons. As assumed for the reflector rods, the borated shield assemblies also contain lower support plates below the shield rods and upper support plates above the shield rods. Once again the upper support plate above the shield rods is made of SiC, while the lower support plate is made of stainless steel. In order to maintain consistency above and below the core, a borated shield is assumed to exist above and below the upper and lower support plates, respectively. Above the UBS and below the LBS lie additional stainless steel plates for added support. Support plate and shield rod dimensions are equivalent to those seen for the reflector assemblies. Perhaps one of the most interesting features of the borated shield assemblies is the cladding and canning material. Design specifications indicate borated shield assemblies are to consist of boron carbide packed into tungsten rods surrounded by a can made of tungsten. While expensive, tungsten has the ability to withstand very high temperatures, such as those predicted for the GFR. However, due to MELCOR code restraints, the canning is assumed to be made of silicon carbide. Design characteristics concerning the construction of a borated shield assembly are presented in Table 6.4.

Table 6.4: Borated Shield Assembly Design Characteristics

Parameter	Value (cm)
Boron Carbide Radius	1.895E+00
Gas Gap Thickness	1.000E-02
Cladding Thickness	1.000E-01
Rod Radius	2.005E+00
Rod Length	3.340E+02
Rod Pitch	4.664E+00

6.2 Input Description

Included within this subsection is a description of the MCNP input along with additional details regarding reactor dimensions and geometry calculations. The input describes the reactor dimensions and material makeup of the reactor core. Furthermore, the input contains information regarding a fission source which allows the user to begin the calculation. MCNP input accounts for information ranging from the lowest stainless steel support plate to the highest stainless steel support plate in all assemblies. In addition, the input also accounts for information ranging from the center of the core to the outermost point of the borated shield. Design specifications regarding the CB, RPV boundary, lower head, LCP, lower nozzles, and upper head are not taken into consideration until MELCOR input is discussed.

When constructing an MCNP input deck, the user must list all of the cell cards at the beginning of the input deck. However, the cell cards are very hard to construct prior to realizing the boundaries within which the cells may be constructed. Furthermore, it is important for the user to understand the materials with which he/she can fill the cell

cards. The surface cards are discussed first, in Subsection 6.2.1, in order to provide the reader with an understanding of the geometry off of which the cell cards are based. Then, the material cards are discussed in order to provide the reader with an understanding of which materials are used to fill the various cell cards present in the MCNP input deck. Following a discussion of the input for the surface and material cards, a description of how the materials are placed within certain geometric boundaries makes up the subsection for the description of cell card input data. Finally, a discussion of the remaining data cards concludes the discussion of the MCNP input for the GFR. Although, material cards are classified as a type of data card, the description of the material input is discussed prior to and separate from the other data cards in order to provide the reader with an appropriate development scheme for the MCNP input deck.

6.2.1 Surface Card Input

Perhaps one of the most important parameters necessary in order to create a fuel rod is the geometric information. While the actual fuel rods are created using cell cards, the user must first have an understanding of where the fuel rod material exists in space. The same philosophy applies to all other structures present in the input deck, such as control rods, reflector rods, borated shield rods, assemblies, etc. This subsection indicates available geometric boundaries in which material may be placed in order to develop different structures.

While there are many different types of geometric boundaries, such as circles, planes, spheres, etc, perhaps it is easiest to begin with a discussion of circles pertinent for this MCNP input development. Prior to assigning a surface identifier, the user must

assign a number to the surface being described. The “cz” surface identifier is followed by a value that describes the bounding radius of a circle. For example, the first radius input in the surface card section of the MCNP input is meant to serve as a border for the outside of the annular region inside the fuel that is meant to be filled with helium. Because the region is circular and has a radius of 0.151 [cm], the surface is constructed by first assigning a number to the surface and following it with the “cz” designation and 0.1510. All distances in MCNP are measured in centimeters. No axial range is assigned to the circular boundary since it assumed to be infinite, thus creating an infinite cylinder. Materials can be bounded within certain axial levels within a cylinder through the use of planar surface cards.

Surface cards intended for bounding material between various elevations in space are given the “pz” designation and can be considered infinite in the x and y directions. However, when another surface, such as a circle, bounds the x and y direction, such as is the case with a fuel rod, the plane no longer needs to be seen as being infinite in the x and y directions. As with all other surface cards, planar surface cards also have a numerical identifier. Furthermore a number that designates the elevation of the plane in the z-direction follows the “pz” designation. For example, the bottom of the lower fuel rod empty plenum region is considered to be located at elevation zero. Thus, the surface card is first given a numerical identifier followed by the “pz” designation and 0.0000. Other elevations are listed in Appendix B.

Although all geometric shapes considered in MCNP are equally important, the shape that can be found most frequently in the MCNP input deck associated with this

project is the hexagon. Hexagonal shapes needed to be constructed for a multitude of reasons. For example, a hexagonal mesh needed to be constructed in order to properly space the fuel rods present in a fuel assembly. Furthermore, hexagonal shapes are necessary for describing the can surrounding a control rod, the can surrounding an assembly, and the overall shape of the entire core. However, there is no pre-constructed hexagonal shape that exists in MCNP. Thus, hexagonal structures must be formed through the use of equations for various types of planes. Two examples are given. First, Figure 6.2 shows an example of the hexagonal array that must be constructed in order to establish a meshing scheme for the fuel rods. A meshing scheme is needed for the fuel rods in order to ensure that they are appropriately allocated in space.

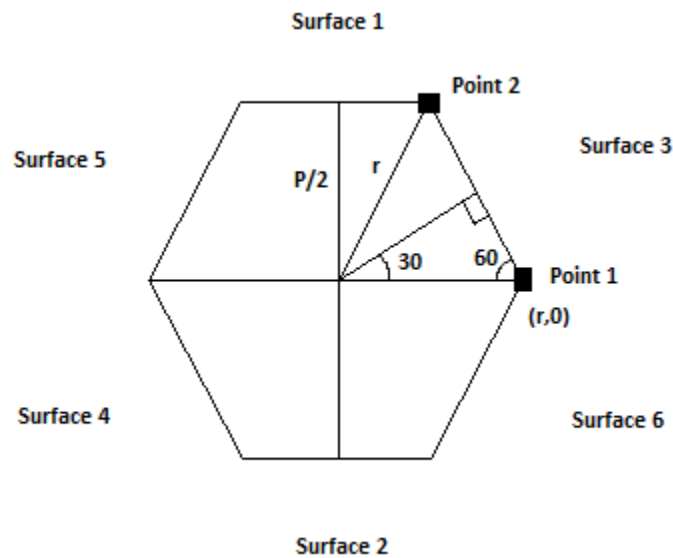


Figure 6.2: Hexagonal Structure for Fuel Rod Meshing and Core

Surfaces 1 and 2 are initially considered infinite in the x and z directions until they become bounded by surfaces 3,4,5, and 6. However, the y location of surfaces 1 and 2 are given defined distances from the central location inside of the hexagon of Figure 6.2. As can be seen from Figure 6.2, the distance of surfaces 1 and 2 from the center of the hexagon is equal to the hexagon's pitch divided by 2. The pitch is defined as the distance between the centers of two hexagons that are attached to one another. The concept of hexagonal lattice sites attached to each other becomes important when observing how these lattice sites form the foundation for the locations of the rods in the core assemblies. Surfaces 1 and 2 are identified by the "py" type. While these surfaces are considered simple plane surfaces normal to the y-axis, surfaces 3, 4, 5, and 6 are considered general surfaces that require more geometric interpretation in order to establish. Perhaps it is prudent to begin with surface 3 in order to lay a foundation for the construction of a general plane surface. Looking at Figure 6.2, one can see that one can obtain the value of r in terms of the pitch through equation 6.1. When solving for r , one finds that its value is equal to $\frac{P}{\sqrt{3}}$. Furthermore, it is also important to recognize points 1 and 2 that are highlighted in Figure 6.1. The x and y coordinates of point 1

$$\frac{\frac{P}{2}}{r} = \frac{\sqrt{3}}{2} \quad (6.1)$$

and the y coordinate of point 2 are easily defined; however, the x coordinate of point 2 must be found through the use of the Pythagorean Theorem as is shown in equation 6.2. Equation 6.3 shows the x location for point 2, which is necessary for finding the slope of the line between points 1 and 2. Using equations 6.1 through 6.3, one can find an

$$r^2 = x^2 + \left(\frac{P}{2}\right)^2 \quad (6.2)$$

$$x = \sqrt{r^2 - \left(\frac{P}{2}\right)^2} \quad (6.3)$$

equation for the slope of the line between points 1 and 2. Using equation 6.1 to solve for

$$m = \frac{\frac{P}{2} - 0}{\sqrt{r^2 - \left(\frac{P}{2}\right)^2} - r} \quad (6.4)$$

the value of half of the pitch in terms of r , one can rearrange equation 6.4 into equation 6.5 seen below in order to find the slope of the line between point 1 and point 2. After

$$m = \frac{r * \frac{\sqrt{3}}{2}}{\sqrt{r^2 - \frac{3}{4}r^2} - r} \quad (6.5)$$

manipulating terms in equation 6.5, one can find that the slope is equal to $-\sqrt{3}$. After identifying the slope of the line used to connect points 1 and 2, one can establish an equation for the line between those two points. Beginning with the basic equation for a line, equation 6.6 marks the starting point towards finding an equation for line. While solving for this line equation, the reader must keep in mind that this line ultimately represents a general plane that exists in space. After solving equation 5, the slope was determined:

$$y = mx + b \quad (6.6)$$

Applying this value to equation 6.6, one obtains:

$$y = -\sqrt{3}x + b \quad (6.7)$$

In order to solve for b in equation 6.7, one can plug the coordinates of point 1 into the equation and solve for b . Upon performing this task, one can find the equation of the line between points 1 and 2 to be:

$$y = -\sqrt{3}x + \sqrt{3}r \quad (6.8)$$

Although the equation of the line has now been found, this equation must be placed into a different format in order for MCNP to interpret it properly. MCNP must see equation 6.8 in the form:

$$Ax + By + Cz = D, \text{ where } A = -m \text{ and } D = \sqrt{3}r \quad (6.9)$$

Taking equation 6.9 into account, one can establish the equation of the line as:

$$\sqrt{3}x + 1y + 0z = \sqrt{3}r \quad (6.10)$$

Using equation 6.1 to find the value of r as $\frac{P}{\sqrt{3}}$, one can see that equation 10 becomes:

$$\sqrt{3}x + 1y + 0z = P \quad (6.11)$$

The coefficients in the equation are clearly seen as $A = \sqrt{3}$, $B = 1$, $C = 0$, and $D = P$. The zero value for the C coefficient does not need to be entered into MCNP. Thus, when defining the surface for a general plane, the numerical surface identifier is entered first followed by the letter “p” and the coefficients for the equation of the plane in the order that they appear in equation 6.11. The procedure described between equations 6.1 through 6.9 can be applied to all general surfaces in Figure 6.1 in order to create the remainder of the hexagon. Figure 6.1 also applies to the overall shape of the entire core.

As mentioned in the preceding paragraph, there are two types of hexagonal structures that exist in the MCNP deck that require attention. The second type of

hexagon may be found in Figure 6.3. This particular type of hexagon represents the hexagonal geometry used to define a layer of the can that provides support for the control rod in the control/shutdown assemblies. This same type of geometry is also used for all assembly types. Surfaces 1 and 2 in Figure 6.3 are represented by the “px” surface type, and the number that follows the surface type identifier is equal to half the distance of the pitch. Surfaces 3, 4, 5 and 6 are all general planes, whose equations can be found through the same process as was used for finding the equation of surface 3 in Figure 6.2.

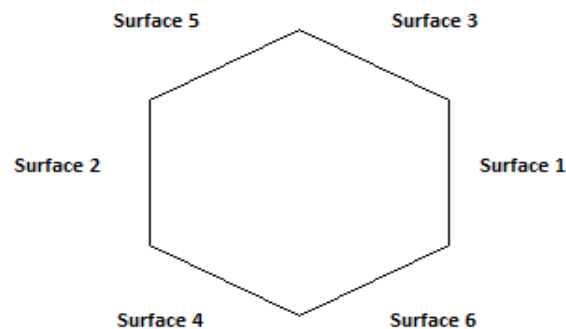


Figure 6.3: Hexagonal Structure for Control Rod Support Cans and Assemblies

6.2.2 Material Card Input

The establishment of surfaces in MCNP lays the foundation for the construction of the cell cards needed to create actual core structures. However, prior to constructing core structures, one must be able to identify the materials which are used in order to fill

the surfaces that outline the core structures. This subsection provides the reader with information regarding the establishment of various materials and their compositions within the MCNP input deck. Also, included in this subsection is information regarding the temperatures at which the cross sections of the materials must be taken. Because material cross sections are temperature dependent, the appropriate material cross section libraries are chosen based on GFR temperatures.

Prior to describing how the material cards are input into the MCNP input deck, it is important for the reader to understand how to calculate various isotopic compositions that comprise a particular material. This is particularly important when entering data into MCNP since either the atomic or weight percentage must be placed next to the mnemonic for a particular material data card. A description of how to calculate the isotopic abundance of uranium-235 and uranium-238 is shown in order to present the reader with the method of how to calculate the abundance of various isotopes of an element. All other isotopes present in the material card section can be found using a similar method. It was chosen to show how to calculate the abundance of the different uranium isotopes because they seem to be the hardest to isolate due to the fact that they are mixed with carbon and multiple transuranic isotopes present within the fuel. The reader must also note that while the fuel is considered a (U,TRU)C based fuel, it is mostly made of uranium and plutonium carbide. Other trace elements include Am-242m, Cm-243, and Cm-245. However, their contribution to the fuel mixture is so small that material properties, such as density, are assumed to be those of uranium-plutonium

carbide. All isotopic compositions can be found in the table referring to the material data cards in Appendix B.

Although the material data cards are not necessarily related to a particular amount of mass, the percentages of uranium-235 and uranium-238 were found by applying the methodology found within this subsection to one fuel rod. Beginning with the fact that the fuel present in a fuel rod is annular, the area of actual fuel material was found first using the inner radius (r_i) and outer radius (r_o) of the annular fuel. After obtaining the area of the annular fuel pellet, the volume is found using equation

$$A_{fuel} = \pi(r_o^2 - r_i^2) \quad (6.12)$$

6.13 below, where h_{fuel} is the height of the fuel. Next, the density (ρ_{fuel}) was

$$V_{fuel} = A_{fuel} * h_{fuel} \quad (6.13)$$

multiplied by the volume in order to obtain the amount of fuel in one rod.

$$m_{fuel} = V_{fuel} * \rho_{fuel} \quad (6.14)$$

The value of the mass of fuel present in one fuel rod in the reactor core will become important later in the overall calculation for this subsection. It is now necessary to momentarily depart from equations 6.12 through 6.14 in order to further understand the amount of the different types of uranium present within the fuel. It was assumed that the uranium present in the fuel is natural uranium. Thus, it is composed of 99.3 w/o uranium-238 and 0.7 w/o uranium-235. Taking these values into account, the molecular weight of the uranium fuel was found by taking the reciprocal of equation 6.15. In equation 6.15, w/o($^{238}_{92}\text{U}$) represents the weight percentage of uranium-238 present in

the fuel, and $w/o(^{235}_{92}\text{U})$ represents the weight percentage of uranium-235 present in the fuel. In addition, $M(^{238}_{92}\text{U})$ represents the molecular weight of uranium-238, and $M(^{235}_{92}\text{U})$ represents the molecular weight of uranium-235. Next, it is

$$\frac{1}{M(\text{U})} = \frac{w/o(^{238}_{92}\text{U})}{M(^{238}_{92}\text{U})} + \frac{w/o(^{235}_{92}\text{U})}{M(^{235}_{92}\text{U})} \quad (6.15)$$

necessary to find the molecular weight of the transuranic component of the fuel. After much deliberation and many trial runs in MCNP, it was determined that the transuranic composition should be comprised of 95 w/o plutonium-239, 3 w/o plutonium-241, 1 w/o Americium-242m, 0.5 w/o Curium-243, and 0.5 w/o Curium-245. Equation 6.16 shows how the molecular weight of the transuranic portion of the fuel is computed. Taking the reciprocal of the left side of equation 6.16 allows one to obtain the molecular weight of the transuranic component of the fuel. All terms found in equation 6.16 have the same representation for their respective elements as can be found from the terms in equation 6.15. The next step is to determine the molecular mass of the combination of the

$$\frac{1}{M(\text{TRU})} = \frac{w/o(^{239}_{94}\text{Pu})}{M(^{239}_{94}\text{Pu})} + \frac{w/o(^{241}_{94}\text{Pu})}{M(^{241}_{94}\text{Pu})} + \frac{w/o(^{242\text{m}}_{95}\text{Am})}{M(^{242\text{m}}_{95}\text{Am})} + \frac{w/o(^{243}_{96}\text{Cm})}{M(^{243}_{96}\text{Cm})} + \frac{w/o(^{245}_{96}\text{Cm})}{M(^{245}_{96}\text{Cm})} \quad (6.16)$$

uranium and transuranic component of the carbide fuel. This is found by taking the reciprocal of equation 6.17. Then, the mass of carbon can be added in order to determine the molecular mass of the actual fuel. After performing the calculation to find the molecular weight of the fuel, the mass of the (U,TRU) component was found using

$$\frac{1}{M(\text{U,TRU})} = \frac{w/o(\text{U})}{M(\text{U})} + \frac{w/o(\text{TRU})}{M(\text{TRU})} \quad (6.17)$$

$$M((U,TRU)C)=M(U,TRU)+M(C) \quad (6.18)$$

equation 6.19. Then, equation 6.20 is used in order to find the mass of uranium present in the fuel. Now that the mass of the uranium component of the fuel is known, it is quite

$$kg(U,TRU)=m_{fuel} * \left(\frac{M(U,TRU)}{M((U,TRU)C)} \right) \quad (6.19)$$

$$kg(U)=w/o(U)*kg(U,TRU) \quad (6.20)$$

simple to obtain the mass of each type of uranium present in the fuel since the weight percentages of uranium-235 and uranium-238 are known. These calculations can be found in equations 6.21 and 6.22, respectively. After obtaining the mass of both of the uranium components, they can be divided by the total mass of fuel in a fuel rod in order to determine the percentage in which they exist in a fuel element. These calculations can be found in equations 6.23 and 6.24, respectively. These equations can be applied to all fuel of a particular enrichment throughout the entire active core. The total weight percentages in equation 6.23 and 24 differ from the weight percentages used in equations

$$kg({}_{92}^{235}U)=w/o({}_{92}^{235}U)*kg(U) \quad (6.21)$$

$$kg({}_{92}^{238}U)=w/o({}_{92}^{238}U)*kg(U) \quad (6.22)$$

$$\text{Total } w/o({}_{92}^{235}U)=\frac{kg({}_{92}^{235}U)}{m_{fuel}} \quad (6.23)$$

$$\text{Total } w/o({}_{92}^{238}U)=\frac{kg({}_{92}^{238}U)}{m_{fuel}} \quad (6.24)$$

6.21 and 6.22 in the sense that the percentages used in equations 6.21 and 6.22 represent the weight percentages of uranium-235 and uranium-238, respectively, in the uranium component of the fuel, while the percentages in equations 6.23 and 6.24 represent the

amount of uranium-235 and uranium-238 in the overall fuel mixture, respectively [18,19].

Although the preceding paragraph discussed a calculation for finding the amount of different types of uranium present within the overall fuel mixture, the same methodology can be applied for finding other isotopes that comprise another mixture, such as the amount of iron present in stainless steel. Because finding the isotopic abundance for all of the elements and mixtures used in the GFR core is not the focus of this thesis, they are not all discussed. It seems wise to show how to calculate the weight percentage of the different uranium isotopes in the fuel mixture since those are the hardest isotopes to isolate due to the fact that they are part of a couple of different mixtures.

Entering the weight percentages in MCNP is only one of two methods for defining the amount of a particular isotope in a material. If the atom percentages of an isotope in a mixture are known, they can be entered into MCNP instead of the weight percentages. Weight percentages are entered as negative values, while atom percentages are entered as positive values. All isotope percentages must add to one for any material; however, if they do not, then MCNP normalizes all of the percentages to unity.

To conclude this subsection, it is important to mention how a material card is actually entered into MCNP. First, the material identifier is entered as “m” with an attached numerical identifier for a material. Then, a string of numbers representative of a particular isotope is entered. For example, the uranium-235 isotope is entered as 92235. Then, the isotope identifier is followed by a period along with the extension for

the cross section library used to analyze the isotope. A list of all of the isotopes, along with their cross section libraries is in Appendix B.

6.2.3 Cell Card Input

With the knowledge of how to construct the surface and material cards, cell card construction can now be shown. The basic driving concept behind the construction of a fuel rod is that materials are bounded between different surfaces created in the surface card input section. A collection of multiple materials placed between specific surfaces can lead to the construction of a fuel pin, a fuel assembly, and even an entire core, if done properly. Perhaps it is best to begin with a description of how a cell card is constructed. First, a numerical identifier is assigned to all cell cards. Following the cell card numerical identifier is the numerical identifier for the material that is being used in the cell. Next, the atom density of the material is listed. The units of atom density are in [atoms/barn-cm]. Then, the surface cards are used to pinpoint the location of the material in the cell. When a negative sign is placed before a numerical surface identifier, it signifies that the material lies inside the surface if the surface is a circle or below the surface if the surface is a plane of the “pz” type. Assigning signs to the planes that comprise the hexagons discussed in Subsection 6.2.1 is slightly more complicated. However, Figures 6.4 and 6.5 show how to assign material to a particular location within a hexagonal structure.

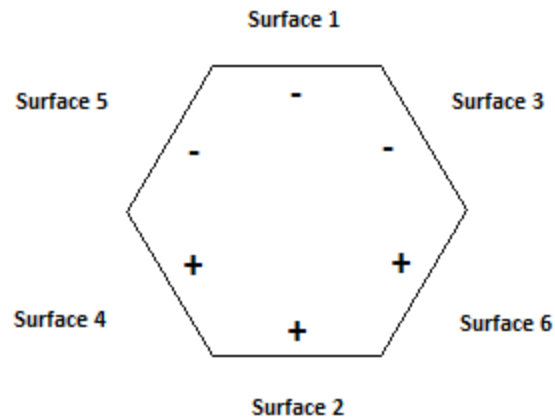


Figure 6.4: Signs for Hexagonal Structure of Fuel Rod Mesh and Core

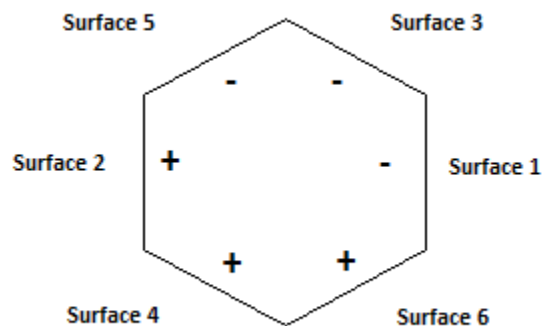


Figure 6.5: Signs for Hexagonal Structure of Control Rod Cans and Assemblies

In figures 6.4 and 6.5, the signs indicate the signs that must accompany the surfaces to which they are attached in order to be able to assign a material inside that particular surface. The opposite sign is used when a material is assigned outside of a surface. This concept is important when assigning the location of materials that

accompany a fuel assembly. While all of the fuel rods are assigned within the hexagonal assembly, helium gas is assigned outside of the assemblies. After assigning surfaces to the cell card, the universe card is assigned to it. The universe card is very important because it has the ability to combine multiple cell cards. This is particularly useful during the construction of a fuel pin when multiple cell cards must be held together in order to form a fuel rod. The universe command is also important when creating assemblies and the entire core. Finally, the last command on the line for a cell card is the importance command. This command is needed in order to identify the particles being tracked within the cell during the MCNP calculation. All cells, except for the outermost hexagonal layer that marks the boundary for the entire core, carry a neutron importance of one. In other words, only neutrons are being tracked throughout the MCNP calculation.

In order to provide the reader with a better understanding of how the cell cards are constructed for the MCNP input deck, a couple of examples are discussed for the remainder of this subsection. Actual numbers pertaining to density numbers, surface numbers, and other numbers that are present on a cell card command line are listed in Appendix B. They are not listed here since the reader must look in the appendices in order to understand which numbers represent specific material cards, surfaces, etc. The remainder of this subsection simply discusses how the commands are used in order to create a few selected structures. Perhaps it is prudent to begin with what could be considered the simplest structure in terms of cell card development, the reflector rod. Beginning at the bottom of the assembly, with the stainless steel support plate below the

lower borated shield, the cell card is given a number along with the material number representing stainless steel, its density, its location, its universe, and the neutron importance inside the cell. The location of the material is inside the radial boundary that is representative of the radius of the reflector rod. Thus, a negative sign is assigned to the surface that represents the radius of the reflector rod. Furthermore, the plane below which the material exists is listed along with a negative sign that is representative of the fact that the material is below a particular axial elevation. While the steel plate is also above the plane boundary that represents the bottom of the assembly, this boundary is not taken into account until an entire assembly is constructed. The concept of not entering this boundary until full assembly construction will be discussed later in this subsection when it is shown how to construct a full assembly.

Although other materials located in the rod are bounded between different axial elevations, they are all bounded within the same radius. However, one must pay special attention to the construction of both the lower and upper borated shields due to the fact that there is a boron carbide layer packed within a stainless steel tube. Keeping this in mind, a different radius is assigned to the boron carbide material in both the lower and upper borated shields. Furthermore, a different cell card is created for each of the different material layers. Beginning with the cell card for the boron carbide, all of the identifiers are entered in the same manner as the cell card for the stainless steel portion of the rod. All input values on the cell card differ from those on the stainless steel input card discussed in the preceding paragraph, except for the universe and neutron importance cards. The universe card must remain the same because the boron carbide is

considered to be part of the reflector rod just as the stainless steel layer previously discussed. Also, the neutron importance remains the same since all MCNP cells carry the same neutron importance except for the outer layer of the core. Perhaps the most important difference to note is the surface card identifiers. Because the boron carbide rests inside of a layer of stainless steel, the radial boundary to which it is bound is smaller than radial boundary for the outermost layer of the reflector rod. Furthermore, it is bound between two planar surface cards. Thus, the surface cards entered for this cell card include the surface associated with the radius of the boron carbide accompanied with a negative sign, as well as the planar surface cards with the upper surface card accompanied by a negative sign. The cell cards representing the stainless steel layer surrounding the boron carbide obviously have different material entries; however, the planar surface card identifiers remain the same. The most important difference to note is the fact that the stainless steel is located outside of the radial surface identifier for the boron carbide, but inside of the surface identifier for the radial boundary of the outermost point of the reflector rod. After entering the cell cards that define the lower borated shield region of a reflector rod, another layer of stainless steel is placed above the borated shield region of the reflector rod. The remainder of the rod is constructed following the same MCNP modeling principles discussed regarding the construction of the lower borated shield region. However, due to the simplicity of the reflector rod, only one radius needs to be taken into consideration until the upper borated shield region of the rod is reached. Because the neutron reflecting portion of the rod, which comprises the majority of a reflector rod, is only made of neutron reflecting material, only the

outermost radius is taken into consideration. The upper borated shield region of the rod is constructed in the same manner as the lower borated shield region of the rod.

While other rod types found within the reactor are of a much more complicated construction, they are modeled in MCNP in the same manner as the simple reflector rod. The major idea to note is that more cell cards are required for the other rods since they contain more materials as well as more surface card identifiers used to pinpoint the location of those materials in a specific rod type. Further discussion of other rod type construction is unnecessary since they all follow the same process. However, for the benefit of the reader Appendix B provides the reader with all of the MCNP input information required to describe how the MCNP input deck is constructed.

In addition to the establishment of different types of rod structures in the MCNP input deck, the reader must also be familiar with how the rods are grouped to form assemblies, as well as how the assemblies are grouped together in order to form the entire reactor core. In Subsection 6.2.1, a description was given as to how a hexagonal structure can be created in MCNP. Now, it is appropriate to describe how a cell card is used in order to fill a hexagonal structure. Repetitive hexagonal lattices occupy larger hexagonal structures that are used as the canning structure for an entire assembly, regardless of assembly type. Then, the hexagonal lattice inside of the assembly boundary is filled with rods. Just as each assembly contains a hexagonal lattice allowing for available sites where the rods may be placed, the entire core contains hexagonal lattice sites where all of the assemblies may be placed. The following paragraph provides an explanation as to how cell cards may be used in order to create an assembly.

the SiC hexagonal can, as well as the axial distance between the bottom and top of the assembly. This region is filled with universe 99, which is shown in cell 502. All material bounded within this particular hexagonal outline belongs to universe 1, which is eventually used in the overall core layout to be explained in the following paragraph. As is the case with all other cells bounded within the core boundary, the neutron importance of this cell is set to 1. Cell 502 provides information regarding a hexagonal component that is repeated in a lattice in order to occupy the space that is contained within the inner layer of the assembly can. The hexagon is filled with helium with the given atom density. The surfaces which form the hexagon are also listed in this cell card. The lat=2 command denotes that the hexagon is repeated in a lattice that is specifically for hexagonal structures. Then, the universe which was used for the fill command in cell 501 is designated along with the neutron importance for this cell. On the next line of code, a fill command is used in order to allocate the lattice in space. A row of 21 cells exists in both the x and y directions. Then, the hexagonal structure created by numbers on the following 21 lines outlines the layout of the fuel assembly. When the letter R is attached to a particular number, the reader should consider the previous number as being repeated the amount of times of the number attached to the letter R. The next cell, cell 503, contains information regarding the SiC used to construct the assembly can. The numerical identifier for SiC is accompanied by its atom density. Then, the surface cards that create the outer layer of the hexagonal can are placed in parentheses followed by the surface cards that create the inner layer for the assembly can. Next, the axial locations of the bottom and top of the assembly are input, respectively. Because this cell card

identifies a structure that is part of the entire assembly that is to be placed in the core, it is associated with universe 1 and a neutron importance of 1. Finally, cell 504 is created as an area of space occupied by helium that lies outside of the assembly can. This area also belongs to universe 1 and also holds a neutron importance of 1.

While all of the assembly types in the GFR core have specific characteristics that make them different from each other, they are all constructed in the same manner as the 20 w/o enriched fuel assembly discussed in the preceding paragraph. In addition, the core is also constructed in the same manner. However, the hexagonal lattice that lies within the core boundary is filled with assemblies that already hold their respective rod types. Just as the 20 w/o enriched fuel assembly fuel pin locations were filled with the universe identifiers for a particular type of pin, the GFR core is filled with the universe identifiers that identify particular assembly types. One can see how the universe command is a very powerful organizational tool that allows the user to combine multiple structures. The inputs used in order to create all of the assemblies and the overall core are shown in Appendix B along with all other MCNP input. While all other MCNP input is organized in a tabular format, MCNP input for all assemblies is left in its original format in order so that the reader could gain a better understanding of how the input “shape” lends further insight into the input deck.

6.2.4 Assembly Layouts

Although all other subsections in Subsection 6.2 adequately outline a method for construction of structures in MCNP, it seems advisable to present the reader with a picture description of the different types of assemblies. The four assembly types shown

in this subsection include a fuel assembly, a control/shutdown assembly, a reflector assembly, and a borated shield assembly. While there are multiple fuel assemblies with different enrichments, they have the same layout. This concept is also true for the control/shutdown assemblies. Therefore, only one fuel assembly type and one control/shutdown assembly type are shown.

Beginning with the fuel assembly, one may first observe that there are three main regions observed, namely the rod plenum region, rod reflector region, and the fuel region. Following each figure that shows a specific region is a closer view of the rod characteristics for that particular region of the rod. For example, Figure 6.7 shows how the empty plenum region is observed for all of the rods seen in a fuel assembly. Then, Figure 6.8 shows a close-up of the plenum region of a fuel rod. The dark yellow region

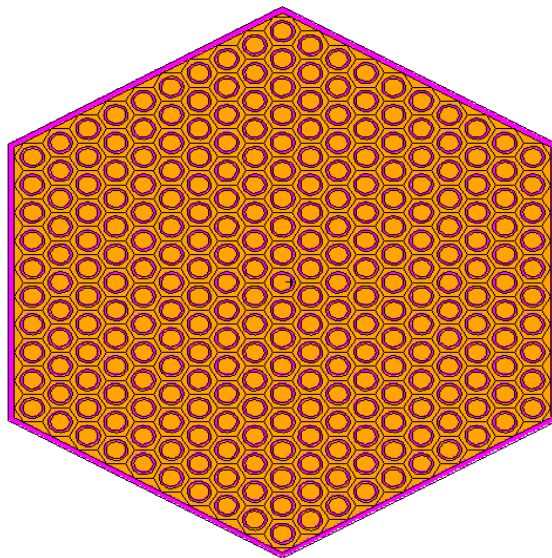


Figure 6.7: Empty Plenum Region for All Fuel Rods in a Fuel Assembly

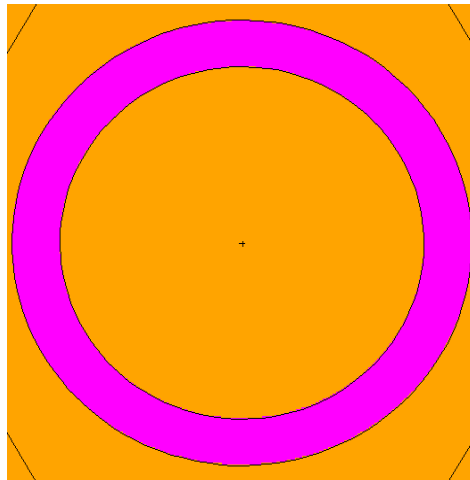


Figure 6.8: Close-up View of Empty Plenum Region of a Fuel Rod

in Figures 6.7 and 6.8 represents helium coolant. Furthermore, the purple regions are made of SiC. Therefore, one can see how the SiC serves as the can material as well as the cladding material. Next, the reader may observe the reflector region in a fuel assembly and fuel rod in Figures 6.9 through 6.11. The dark yellow and purple colors still represent the helium and SiC, respectively, while the light pink region represents the reflector material. One can notice that the gap shown in Figure 6.11 contains helium.

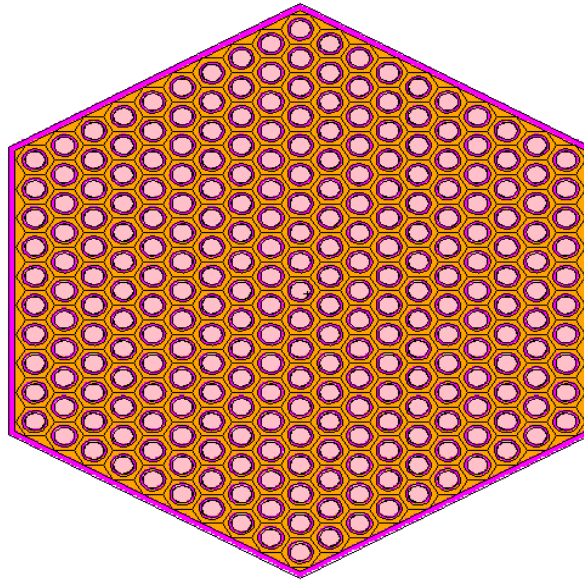


Figure 6.9: Reflector Region for All Fuel Rods in a Fuel Assembly

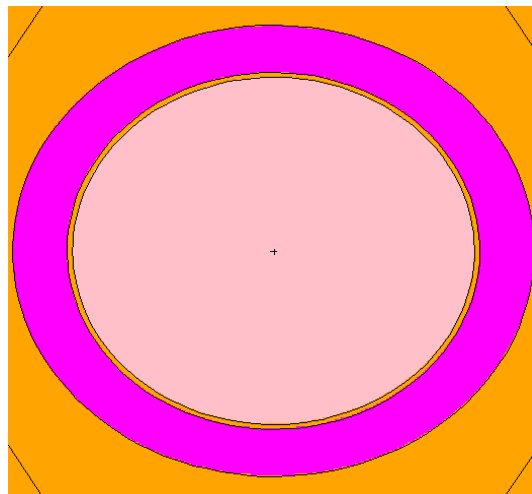


Figure 6.10: Close-up View of Reflector Region in a Fuel Rod

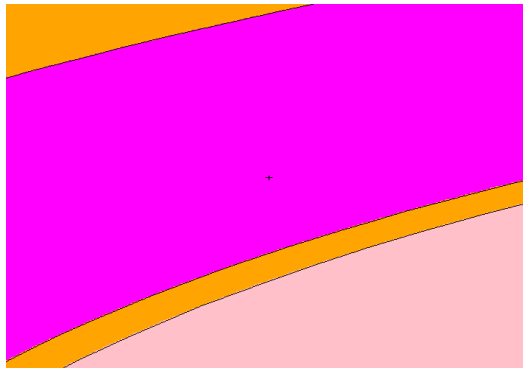


Figure 6.11: Close-up View of Gap Between Reflector and Clad in a Fuel Rod

This gap is there intentionally in order to allow for swelling of the reflector material during operation. Figures 6.12 through 6.14 provide the reader with a description of the fuel region of the assembly and fuel rods. All colors previously used represent the same materials. The red regions represent the fuel. The reader should note the annulus in the center of the fuel regions.

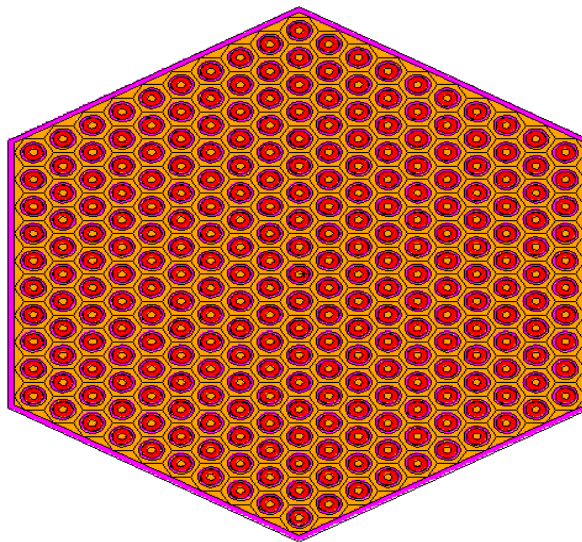


Figure 6.12: Fuel Region for All Fuel Rods in a Fuel Assembly

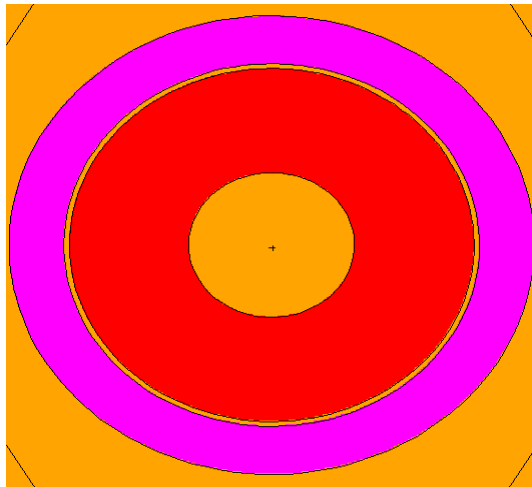


Figure 6.13: Close-up View of Fuel Region in a Fuel Rod

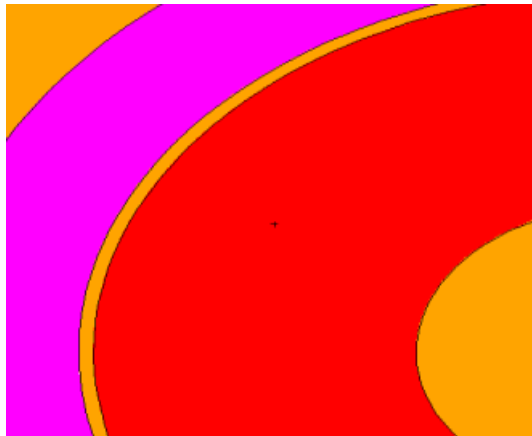


Figure 6.14: Close-up View of Gap Between Fuel and Clad in a Fuel Rod

The second assembly type discussed is the control/shutdown assembly. Because fuel rods that are found within this type of assembly have the same design as the fuel rods in the fuel assemblies, they are not discussed in depth. Figure 6.15 provides a view of a control/shutdown assembly at the elevation of the fueled region of the assembly.

The blue color represents SiC material while the red and dark yellow represent fuel and helium, respectively. The light blue located at the center of the assembly is boron carbide. In the actual MCNP calculations, there are no control rods inserted, and the light blue region and dark blue housing it are dark yellow in order to represent helium flowing through the inner can, which is constantly present. The control rod in Figure 6.15 is present in order to provide the reader with an understanding of the appearance of a control rod insertion. Figure 6.16 presents a close-up view of the control rod in order to show how it is contained within a hexagonal can that rests within the entire assembly.

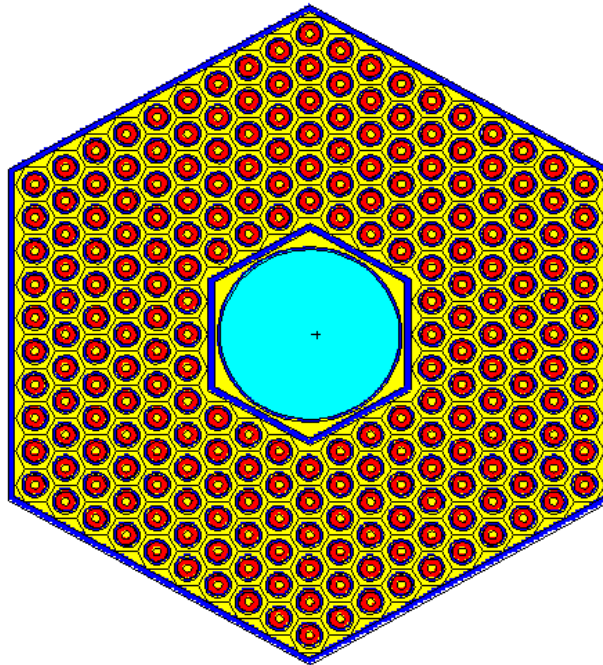


Figure 6.15: Control/Shutdown Assembly Layout at Fuel Elevation

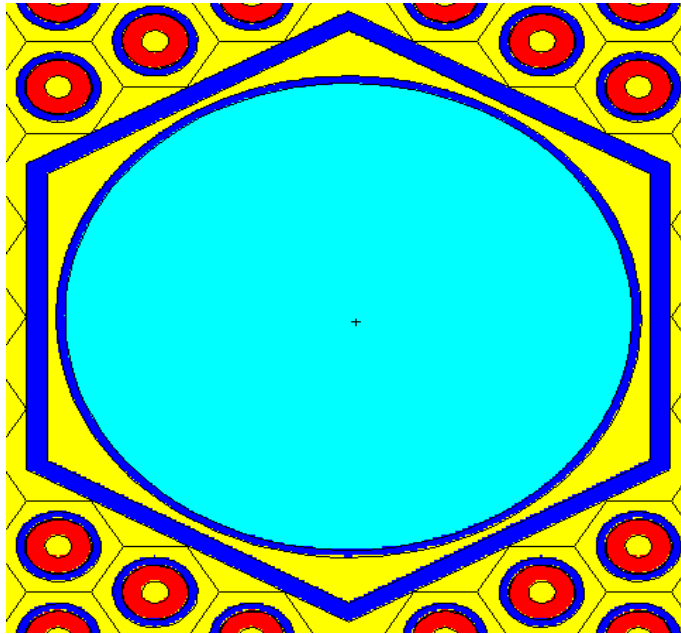


Figure 6.16: Close-up View of Control Rod in Control/Shutdown Assembly

Reflector assemblies have a much simpler design relative to other assembly types present in the reactor core. The lack of cladding, as well as the smaller quantity of rods allows the MCNP user to easily define this assembly type. Figure 6.17 provides visual evidence of this simpler assembly type. Furthermore, Figure 6.18 shows a close-up view of a reflector rod. In both figures, the red symbolizes helium while blue symbolizes Zr_3Si_2 .

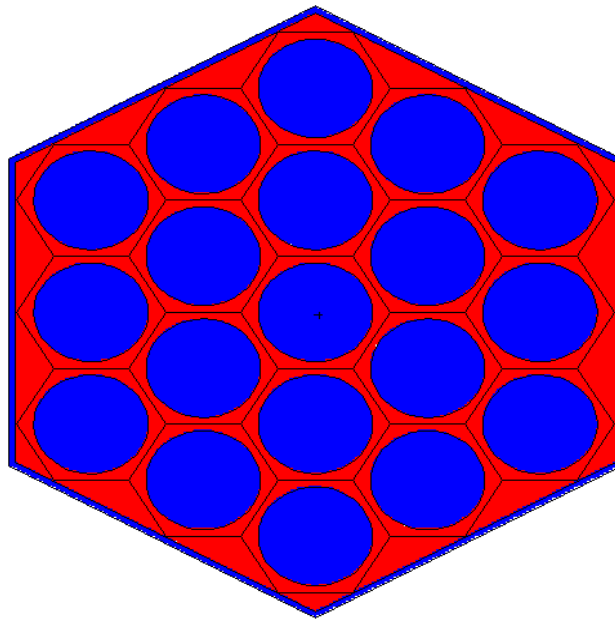


Figure 6.17: Reflector Assembly

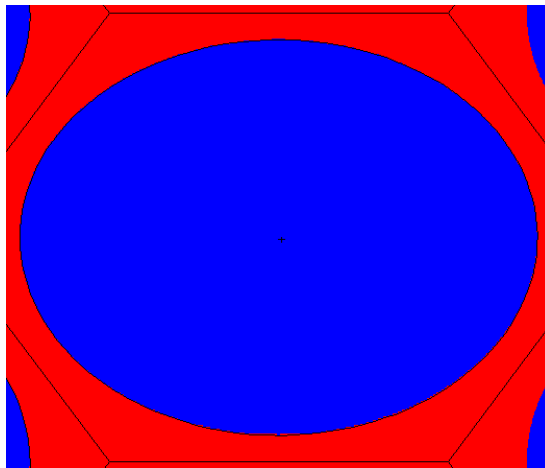


Figure 6.18: Close-up View of Reflector Rod in a Reflector Assembly

Finally, the last assembly type that must be visualized is the borated shield assembly. Figures 6.19 through 6.21 provide visual details of a borated shield assembly.

In these figures, red represents SiC, while blue and yellow represent helium and boron carbide, respectively. The green layer surrounding the shield rods is tungsten. Close-up views are provided in Figures 6.20 and 6.21 in order to provide the reader with a better understanding of the rod structure.

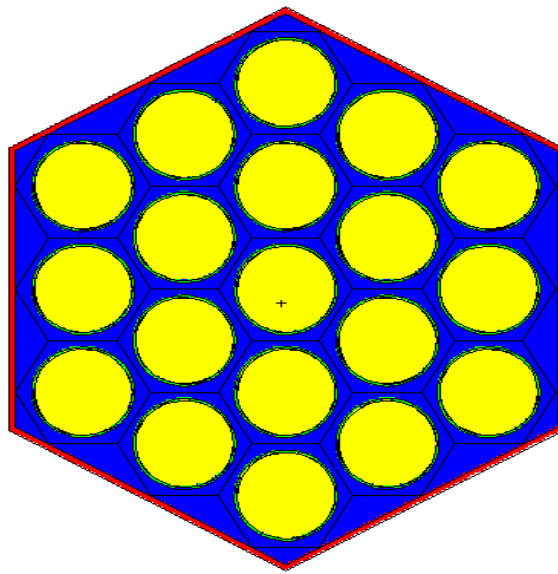


Figure 6.19: Borated Shield Assembly

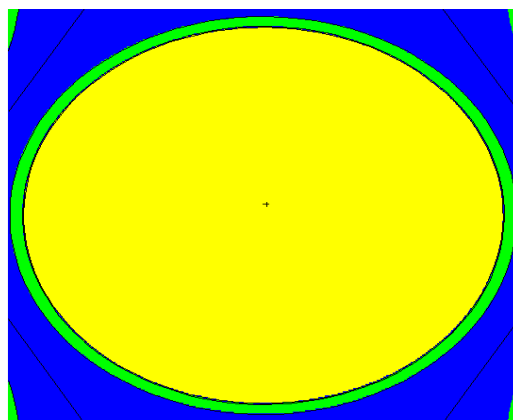


Figure 6.20: Close-up View of a Borated Shield Rod

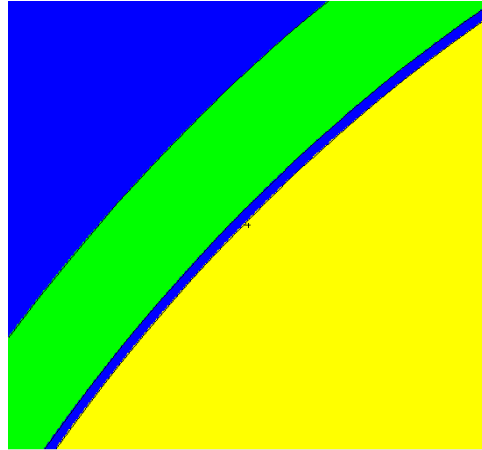


Figure 6.21: Gap Between Boron Carbide and Tungsten Cladding

6.3 Results

Although a larger quantity of data obtained from all work pertaining to this thesis can be found in the next section, MCNP results are still important to acknowledge and assess in order to better understand how the MELCOR deck is created as well as the statistical accuracy of MCNP simulations. This subsection contains the flux data extracted from MCNP which is eventually used in the MELCOR input deck in order to create relative axial and radial power profiles. However, prior to discussing the flux data, it is important for the reader to become familiar with GFR kinetics and fluctuations of its kinetics data. Subsection 6.3.1 documents statistical fluctuations in reactor kinetics properties resulting from varying the number of neutrons sampled found in the kcode card. Data is shown for kinetics values, such as the reactor eigenvalue, standard deviation of the eigenvalue, prompt neutron lifetime, mean generation time, average

number of neutrons produced per fission, and the effective delayed neutron fraction. In order to obtain the effective delayed neutron fraction for the range of neutron populations, input decks where delayed neutron data is turned off are run in order to obtain effective prompt eigenvalues needed in order to calculate effective delayed neutron fractions. Other important data is listed along with the effective prompt eigenvalues as well. Calculations of effective delayed neutron fractions, as well as neutron mean generation times are explained in Subsection 6.3.1.

Tables and graphs shown in Subsections 6.3.2 and 6.3.3 represent the relevant neutron flux data taken from a mesh overlaid upon the active core. Axial levels in the MCNP input deck that contains the axial meshing scheme correspond to the axial levels in the active core region found in the MELCOR input deck. The radial rings present in the MCNP input deck that contains the radial meshing scheme are allocated according to the radial rings created in the MELCOR input deck. While input development contained within this thesis is sequenced so that MCNP input is described prior to MELCOR input, the radial and axial levels planned for use in the MELCOR input deck were known prior to the development of the MCNP meshing schemes. Thus, the meshing schemes found in each MCNP input deck are created according to the axial and radial levels found in the MELCOR input deck.

While the axial meshing scheme found within its respective MCNP input deck represents the axial levels in the MELCOR input deck with a great degree of accuracy, there are minor discrepancies between the radial MCNP mesh and the radial levels in the MELCOR input deck. The radial rings representing the active core region in MELCOR

contain fuel, cladding and canning between axial levels 10 and 19. However, since the active core is not perfectly circular in the MCNP input deck, and the meshing scheme is circular, there is some overlap between the last ring in the active core and the reflector assemblies beyond the active core. In other words, axial levels 10 through 19 in the reflector region may also be taken into account in the neutron flux determination in the last ring of the active core in the MCNP input deck. This discrepancy shows itself in the data regarding the neutron flux distribution; however, it does not significantly affect the necessary conclusions that can be drawn from this thesis. Although there is a lot of data that can be extracted from the MCNP outputs obtained from execution of the MCNP input decks created for this endeavor, key GFR neutronic data is shown Table 6.5. Fuel enrichment values are part of the input; however, they are listed in Table 6.5 because they provide valuable neutronic data. All other values in Table 6.5 are obtained from either outputs or calculations explained later in this section.

Table 6.5: Key GFR Neutronic Data

Parameter	Value(s)
keff	1.0478
Fuel Enrichments (%)	14.8, 15.7, 16.3, 18.1, 20
Neutron Lifetime (sec)	3.4206E-06
Mean Generation Time (sec)	3.2647E-06
Avg. neutrons/fission	2.934
β_{eff}	0.0027

6.3.1 Analysis of US DOE GFR Reactor Kinetics

In order to assess statistical accuracy of the GFR effective eigenvalue, multiple GFR input decks with varying quantities of neutron population are run. Cases are run for neutron populations of 2500, 25000, 250000, and 2500000. Furthermore, since it is desired to obtain the delayed neutron fraction which requires knowledge of the effective prompt eigenvalue, cases are run for the same neutron populations mentioned above with the effect of delayed neutrons neglected. In other words, two cases are run for each of the neutron populations mentioned above. Meshing considerations are ignored for calculations that involve the kinetics parameters mentioned in the first paragraph of this subsection. Tables 6.6 and 6.7 show data for each case with all neutrons and only prompt neutrons considered, respectively. Adjustments to the kcode card in order to obtain the desired number of neutrons for each particular case are not shown in Appendix B. The reader may refer to Subsection 4.2.3 in order to understand adjustments made to the kcode card.

Table 6.6: Reactor Kinetics Parameters (All Neutrons)

Neutrons	keff	Standard Deviation	Neutron Lifetime (sec)	Mean Generation Time (sec)	Avg. Neutrons/Fission
2500	1.0005	1.4320E-02	2.4557E-06	2.4545E-06	2.9020
25000	1.0568	3.9700E-03	3.5545E-06	3.3635E-06	2.9380
250000	1.0491	1.3600E-03	3.4408E-06	3.2797E-06	2.9340
2500000	1.0478	4.1000E-04	3.4206E-06	3.2647E-06	2.9340

Table 6.7: Reactor Kinetics Parameters (Prompt Neutrons Only)

Neutrons	keff	Standard Deviation	Neutron Lifetime (sec)	Mean Generation Time (sec)	Avg. Neutrons/Fission
2500	1.0148	1.3120E-02	3.4751E-06	3.4243E-06	2.9590
25000	1.0424	4.1600E-03	3.2704E-06	3.1374E-06	2.9160
250000	1.0429	1.2500E-03	3.4173E-06	3.2768E-06	2.9190
2500000	1.0450	4.1000E-04	3.4382E-06	3.2902E-06	2.9230

In Tables 6.6 and 6.7, the standard deviation in the eigenvalues decreases as neutron population increases. Thus, there is a greater degree of statistical accuracy as more neutrons are sampled. In both tables, the mean generation is calculated by dividing the neutron lifetime for each case by the effective eigenvalue for that same case. All other values found in both tables are extracted from MCNP outputs. In addition to acknowledging the values observed in Tables 6.6 and 6.7, it is also advisable to calculate the delayed neutron fraction. The delayed neutron fraction, along with the other parameters observed in Tables 6.6 and 6.7 can be used in power oscillation calculations during transient scenarios. Thus, when further research is carried out on the US DOE GFR, researchers may reference this document in order to better understand some of the kinetics parameters involved in fine power control. The effective delayed neutron fraction is calculated using equation 6.25 below where k is the effective eigenvalue and k_p is the effective prompt eigenvalue [20]. Table 6.4 lists all effective delayed neutron

$$\bar{\beta} = 1 - \left(\frac{k_p}{k} \right) \quad (6.25)$$

fraction values along with their corresponding neutron populations. Two important

Table 6.8: Effective Delayed Neutron Fraction Results

neutrons	effective delayed neutron fraction
2500	-0.01431
25000	0.01364
250000	0.00595
2500000	0.00267

conclusions can be drawn from the results presented in Table 6.8. First, statistical fluctuations in the case involving the lowest neutron population drive the effective delayed neutron fraction to an unrealistic value. Therefore, one may surmise that it is unreasonable to perform MCNP calculations for the US DOE GFR with only 2500 neutrons. Second, the final effective delayed neutron value listed in Table 6.8 is relatively close to the delayed neutron fraction for plutonium-239 fuel in a fast reactor, which is 0.0020 [18]. Because the concentration of plutonium-239 fuel throughout the reactor core is relatively high, one can consider the US DOE GFR to be a plutonium-fueled fast reactor system. Therefore, results obtained from a statistically accurate MCNP output display that MCNP calculations present good results.

Although efforts could have been made to increase neutron population even further, calculation time would have eventually been too long. Due to the relatively low standard deviation associated with the final case in Table 6.6, it is decided that 2.5 million particles serves as a high enough neutron population. Further evidence supporting the appropriateness of this neutron population is the fact that the average number of neutrons produced per fission when 2.5 million particles are simulated is equal to the average number of neutrons produced per fission in the case simulating

250000 neutrons. Thus, increasing the neutron population no longer seems to affect neutron production rate, an important factor affecting the reactor eigenvalue.

6.3.2 Axial Meshing Results

Table 6.9 shows the normalized neutron flux data for the axial meshing scheme in MCNP. Figure 6.22 shows a graph of the normalized axial data. One should note that the axial mesh was established at the midway point between the center and the edge of the active core.

Table 6.9: Normalized Axial Neutron Flux Data

Height (cm)	Normalized Axial Flux
6.7	8.1439E-01
20.1	9.3572E-01
33.5	1.0338E+00
46.9	1.1007E+00
60.3	1.1349E+00
73.7	1.1345E+00
87.1	1.0978E+00
100.5	1.0264E+00
113.9	9.2411E-01
127.3	7.9760E-01

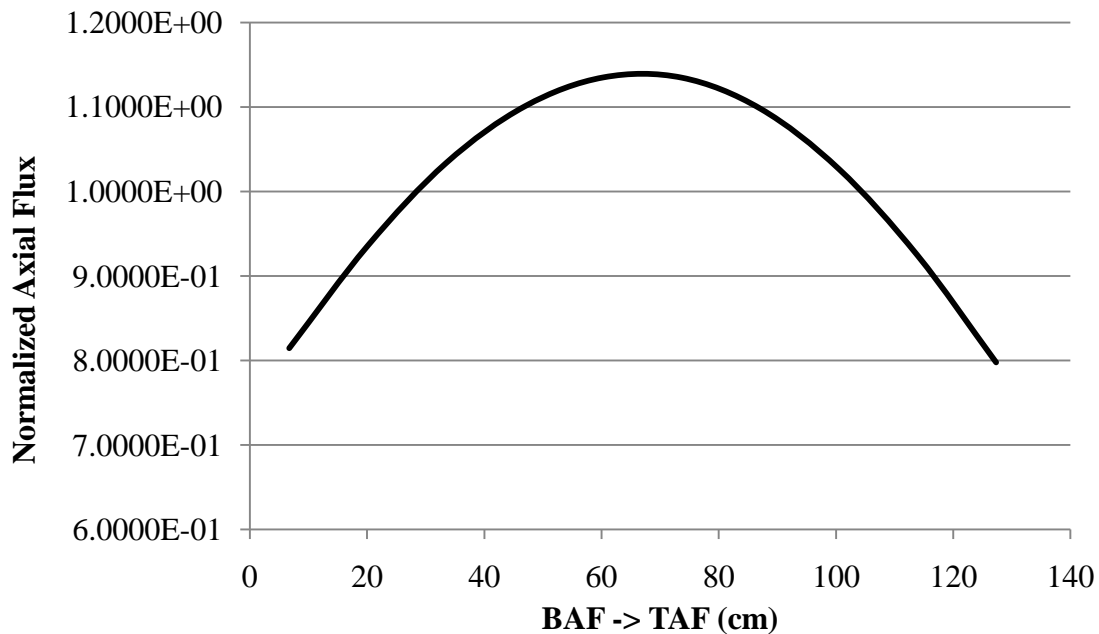


Figure 6.22: Normalized Axial Neutron Flux Profile

The reader should note two important abbreviations present in Figure 6.22. BAF and TAF represent the bottom of the active fuel and the top of the active fuel, respectively.

As one can see from Figure 6.22, an arch in the shape of a cosine function is present along the length of the active fuel region. Thus, the neutron flux is distributed along the length of the active core according to a cosine function. Because the fuel is enriched in a uniform manner along the length of the core, and since there is no neutron moderation originating from either the top or bottom of the reactor core, one would expect the neutron flux profile to assume the cosine shape shown in Figure 6.22. Furthermore, since the reactor power distribution follows the neutron flux profile, the assumption is made that the normalized power distribution follows the same cosine function as the normalized neutron flux distribution. Thus, the values used to create the

axial power profile seen in Figure 6.22 are used in the COR package of the MELCOR input deck in order to create an axial power profile.

6.3.3 Radial Meshing Results

Table 6.10 shows the neutron flux data for the radial meshing scheme in MCNP. Figure 6.23 shows a graph of the normalized radial data. The radial layers are established at the middle axial elevation of the active core, or, midway between the bottom and top of the active fuel region.

Table 6.10: Normalized Radial Neutron Flux Data

Radius (cm)	Normalized Radial Flux
24.085	1.2894E+00
72.255	1.2220E+00
120.420	1.0885E+00
168.600	8.6977E-01
216.800	5.3036E-01

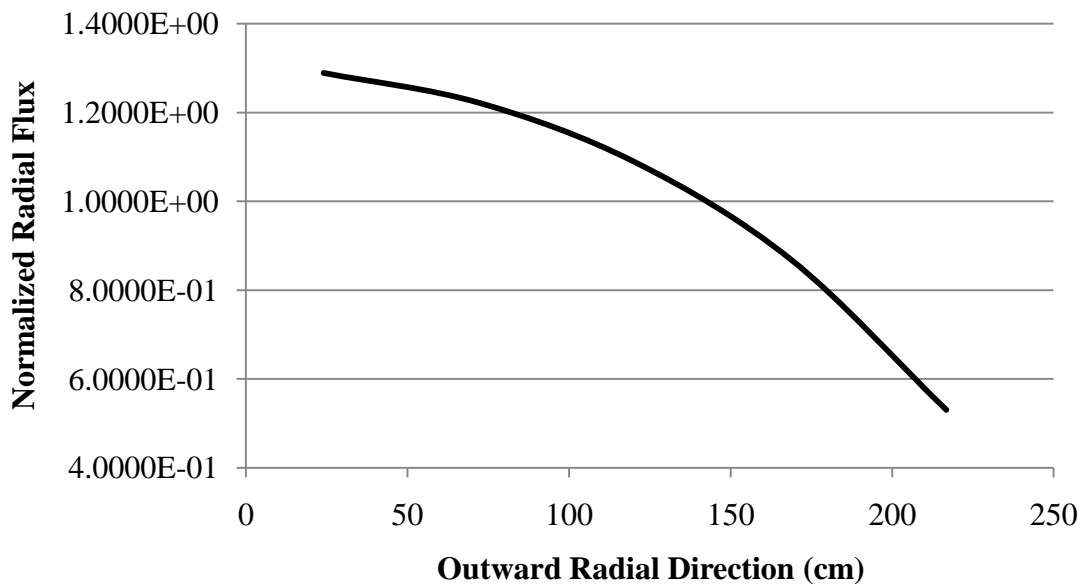


Figure 6.23: Normalized Radial Neutron Flux Profile

Looking at Figure 6.23, one can see that the right half of a cosine function is shown. The neutron flux is at its maximum value at the center of the active core, as expected. Then, the neutron flux profile decreases according to the cosine function as the distance from the center of the core increases, as expected. The results shown in Figure 6.23 indicate that modeling of the radial meshing scheme is accurate except for one detail. The magnitude of the neutron flux at the periphery of the active core seems slightly small. This may be due to the fact that some of the reflector region beyond the active core is being included in the last radial ring of the meshing scheme found within the MCNP input. Because there is no fuel located in the outer reflector region, there is no fission power located in that region. However, when incorporated into the fifth radial level of the radial mesh in MCNP, it becomes a part of the average flux calculation for that region. Thus, the flux is lower as a result of the incorporation of the reflector

region. A lower neutron flux also means a lower power. Therefore, the lower neutron flux in the fifth ring may be a result of the incorporation of the outer reflector region into that particular ring. However, the data is still needed in order to create a power profile in the MELCOR input deck. Because the main focus of this thesis is the development of input techniques for the US DOE GFR, a great amount of attention should not be placed upon perfecting the neutron flux or power distribution. Furthermore, because much of the reactor design had to be inferred from limited data, it is understandable that some of the data may require further analysis. Discrepancies in core power distribution lie beyond the scope of this thesis.

6.3.4 Three-Dimensional Normalized Flux Distribution

For the benefit of the reader, a three-dimensional map of the normalized neutron flux distribution is shown in Figure 6.24. Values in the graph are obtained by multiplying each normalized radial flux by each normalized axial flux. Figure 6.24 that is created by the results provides the reader with a good idea of how flux is distributed throughout the reactor core.

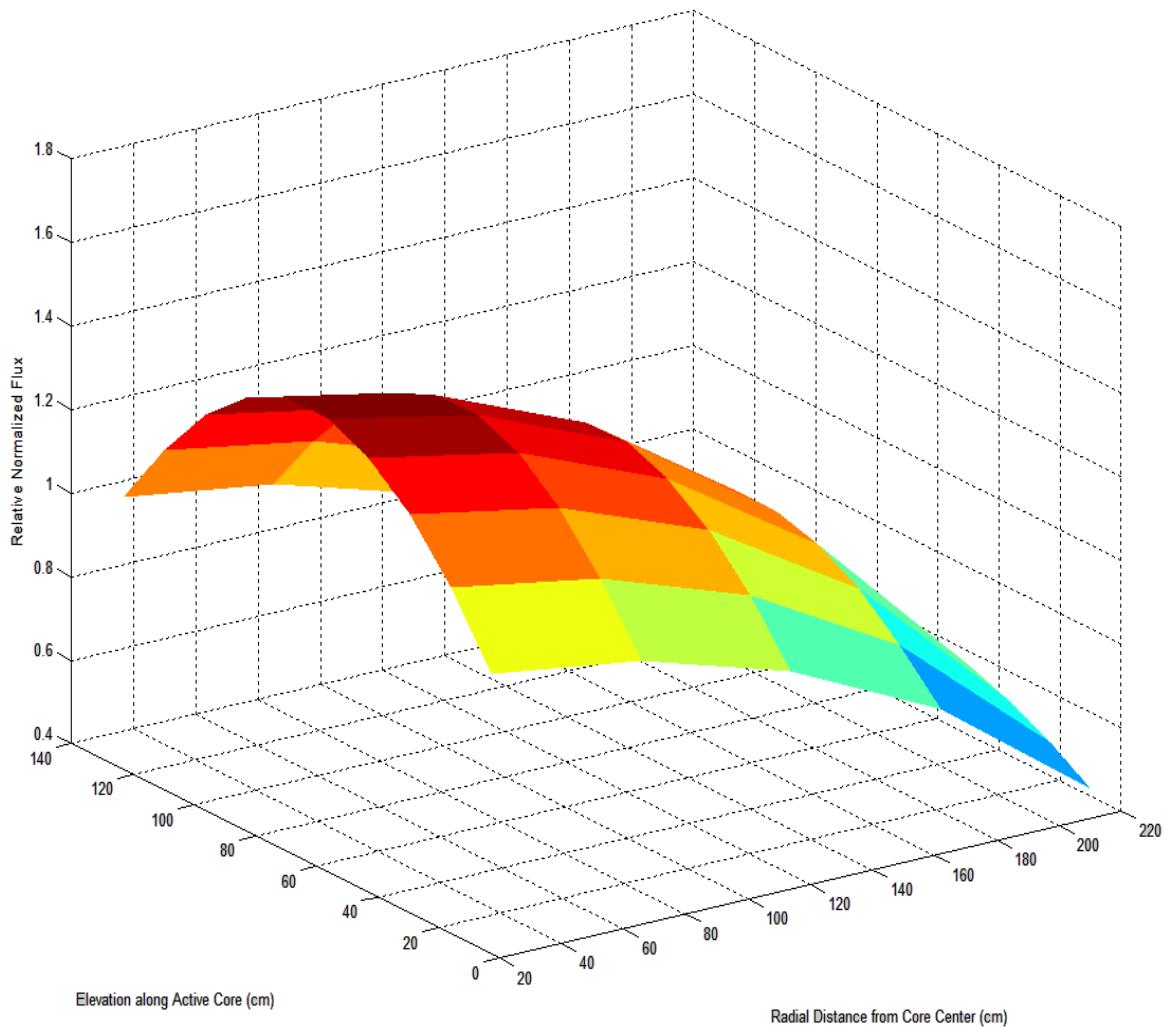


Figure 6.24: 3D Plot of Relative Normalized Neutron Flux Distribution

6.4 MCNP Conclusions

Design specifications regarding the construction of the GFR core are relatively scarce and, at times, conflicting. Therefore, the DOE's intended neutron flux profile may not have been achieved. Further evidence supporting this particular assertion is the fact that the neutron flux at the periphery of the active core was a great deal lower than the neutron flux located at the center of the core. However, for the purposes of

furthering modeling techniques with regard to gas-cooled fast reactor technology, one may state that the objective is fulfilled. A Monte Carlo code input, as opposed to the original deterministic code input, is now established. Furthermore, data obtained from MCNP can be used in MELCOR in order to establish a thermal hydraulic code that differs from the originally used RELAP model.

On a different note, design specifications regarding reactivity control and rod worth are bleak at times. While the DIFF3D and REBUS codes are adequate tools for engineers to use in order to determine GFR reactivity control and control rod worth, MCNP may provide both supporting and diverging information that could prove crucial to the development of the GFR. While running MCNP in order to determine the configurations for which the GFR is either above, at, or below critical conditions, it was determined that the boron-10 concentrations in the control rods were not high enough in order to drive the reactor below criticality. Thus, adjustments are made in order to run an input deck that was capable of establishing a subcritical condition in the reactor core. Therefore, the reactor can be taken supercritical and be dropped to a subcritical state. Conclusive evidence of appropriate boron-10 concentrations for all control rods that can be inserted into the core still does not exist for the type of fuel used for this particular endeavor. However, it is a plausible assertion that data obtained from this MCNP deck can be seen as proof of the advancement of neutronic modeling techniques for the GFR with a Monte Carlo neutronics code.

Meshing techniques used for the extraction of the neutron flux profiles from the MCNP outputs prove valuable towards the development of power profiles required for

input into the MELCOR input deck. Thus, the MCNP input techniques contained in this thesis prove as a valuable resource for acquiring power information for different regions in the GFR core. Furthermore, adjustments made to the MCNP inputs in order to selectively extract prompt neutron data prove useful for ultimately calculating a delayed neutron fraction. Although the delayed neutron fraction is not used in this project, it will prove valuable for all those who seek to analyze GFR power transients. Finally, adjustments to neutron quantity prove useful for assessing the statistical accuracy associated with MCNP calculation. Upon reaching 2.5 million neutrons, it is decided that further increasing the neutron population is no longer necessary due to a very low standard deviation associated with the MCNP input deck containing 2.5 million neutrons. Furthermore, the average number of neutrons did not change relative to the MCNP input deck executed with 250000 neutrons.

7. MELCOR CALCULATIONS

Following the establishment and execution of the MCNP input deck, the MELCOR input deck is then established. Because the MELCOR COR package requires a power profile in order to run, the normalized neutron flux distribution is obtained from MCNP and converted into a normalized power distribution for input to MELCOR. This will be discussed further in Subsection 7.2.1 when the COR package input is discussed. Many reasons are associated with the need for the development of a MELCOR input deck for the GFR. One is that a MELCOR deck has not yet been created for the US DOE GFR. Thermal hydraulic data pertaining to the US DOE GFR design mainly comes from RELAP. Therefore, a MELCOR model could be invaluable either as a code to which data from RELAP may be compared, or possibly as the primary code used for GFR thermal hydraulic design. Furthermore, the MELCOR code was initially intended to be used for thermal reactors only. The MELCOR deck constructed for the purposes of this thesis will lend further insight into the capabilities of MELCOR to handle a fast reactor.

The two primary concerns addressed by the development of a MELCOR input deck are the need to advance modeling techniques for both the MELCOR code and the US DOE GFR, and to obtain a temperature profile along the length of the core during normal operating conditions. Prediction of the temperature profile along the length of the core can only come from a computational model since no experiments exist that can

truly predict core temperatures. This MELCOR deck extends the most recently performed calculations by the US DOE.

7.1 Modeling Approach

The main purpose for the development of this particular MELCOR deck is to develop input techniques for simulating GFR conditions during a steady-state scenario. Development of this particular MELCOR deck is based on the latest design document put forward by the US DOE [3].

All MELGEN and MELCOR input are contained within one file, namely, gfr2400d.inp. The file contains information regarding the execution of both MELGEN and MELCOR. Therefore, information regarding the file types created, as well as the time steps in which to allocate advancement of the problem in time, are included. COR cell, control volume, flow path and heat structure information are also included. These will be discussed further in Subsection 7.2. Also to be discussed further in that subsection are the material, tabular function, noncondensable gas, and control function packages, which are also used in the MELGEN input.

As for the modeling of the actual physical core, all of the assemblies are modeled as they are in MCNP, with the addition of a few components. The commands are different; however, the point being made is that information regarding the physical makeup of the assemblies in MCNP is being translated over to MELCOR input in a consistent manner. Components added in the MELCOR input include the RPV, CB, lower head, LCP, lower nozzles for all assemblies, and the upper head. Components such as the lower and upper head are not given a lot of detail since thermal-hydraulic

behavior in those components is not important to the calculation. However, those components are needed in order to establish a working model. Actual modeling of the added components is discussed in the following subsections. Also present in the following subsections are certain assumptions made about those particular components prior to carrying out the calculations. However, some general assumptions regarding the MELCOR deck are stated as follows:

- The reactor, including the CB, downcomer (DC), and RPV, is azimuthally symmetric about the reactor centerline.
- The coolant flows through an open loop that begins and ends with a source and sink, respectively. The power conversion unit does not need to be modeled.
- It is necessary to model bypass flow due to interassembly gaps.
- Both vertical and horizontal flows are modeled between bypass control volumes.
- The fuel does not melt.
- Material properties for SiC, Zr_3Si_2 , and tungsten are specified.

7.1.1 Reactor Pressure Vessel (RPV)

Although not modeled in MCNP due to its lack of importance for neutronics considerations, the reactor pressure vessel is modeled in MELCOR. It is modeled as stainless steel heat structures. The left hand side of the heat structures, or, the side facing the reactor core, is considered the edge of the last radial ring in the COR package. Its thickness is rounded to 0.28 meters, instead of the design specification of 0.2794 meters. This is done in order to simplify the input. Other information regarding this structure is mentioned in the subsection 7.2.4 when heat structures are described further.

7.1.2 Core Barrel (CB)

Another structure not modeled in MCNP is the core barrel. This structure lies at the edge of the reactor core adjacent to the DC. Like the RPV, it is also modeled with stainless steel. The CB has many more heat structures associated with it relative to the RPV. This is due to the fact that the heat structures for the core barrel serve as the first heat structures seen beyond the active core. Therefore, they must align with the axial COR cells. This will be discussed further in the subsection 7.2.4 during a description of the heat structures.

7.1.3 Reactor Vessel Lower Head

It is assumed that reactor vessel lower head behavior is not important for this model. However, since the MELCOR COR package requires a lower head model, one is constructed. The nodalization of the lower head is kept very simple and is discussed further in the subsection 7.2.1. The material for the lower vessel head is stainless steel. Furthermore, the lower vessel head is modeled as a half sphere. The edge of the modeled half sphere connects to the RPV wall.

7.1.4 Lower Core Plate (LCP)

Of more significant interest to MELCOR calculations, relative to the lower head, is the LCP. As is the case for other structures discussed in this subsection, the LCP is also made of stainless steel. Perhaps one of the most important assumptions regarding the model for the LCP is that it does not fail at any point during the calculation. Furthermore, design specifications do not go into any detail regarding flow paths through the LCP for bypass flow. Thus, another very important assumption is that 25%

of the LCP that rests between assemblies is allocated to bypass flow. Thus, the reader should assume that holes have been drilled through the LCP in order to allow room for helium to flow through the bypass. Modeling of the LCP will be discussed in the subsection when the COR input is defined. Although the LCP does not have any core material in it, it is still considered part of the core package.

7.1.5 Assembly Lower Nozzles

A separate subsection is reserved for the nozzles in the assemblies due to their impact on flow. Due to expansions and contractions that can be seen in Figure 2.2, one can see why it is important to model flow through the nozzle in each of the assemblies. In addition, the nozzles are also made of stainless steel. Therefore, they play a role in conduction heat transfer, as well as convection. Specifications regarding the geometry of the lower nozzle for all assemblies are limited. Thus, two assumptions had to be made. First, all assembly lower nozzles have the same geometry, regardless of assembly type. Second, the throat of the lower nozzle has a cylindrical geometry, while the mouth of the nozzle has hexagonal geometry. Although geometry cannot be directly seen in the MELCOR input, it is important to take these geometries into account since it affects the flow path areas that are input into the MELCOR input deck.

7.1.6 Reactor Vessel Upper Head

Similar to the reactor vessel lower head, the reactor vessel upper head is a large half sphere that is linked to a control volume that is fairly simple in terms of definition. Any sort of fine definition associated with the upper head is not necessary since behavior in the upper head is not important for this calculation. The edge of the half sphere that

makes the upper head is connected to the wall of the RPV. Furthermore, the half sphere is made of stainless steel. The reactor vessel upper head will be discussed in further detail in the subsection 7.2 when the COR input and HS input are discussed.

7.2 Input Description

Included within this subsection is a description of the MELCOR input along with additional details regarding assumptions made in order to clarify and simplify calculations. The input describes the mass calculations for different materials present in the core, hydrodynamic conditions, thermodynamic conditions, structural conditions, etc. One important idea to note is that, in accordance with the control volume-flow path concept, there are no specifications as to how material is shaped in a given volume of space. MELCOR only requires that the user input the amount of mass that occupies a certain amount of space along with the available hydrodynamic volume available to cool the mass.

Throughout the many subsections within this subsection, issues discussed include the formation of COR, CVH, FL, and HS package input for the steady-state calculation. Data represented by the input can be seen in the nodalization diagram represented on the next page. The reader must note that the figure is not drawn to scale, and rounding in excel causes the difference between the inner and outer radius of ring 2 to vary from the width. All numerical input values for the MELCOR input deck can be found in Appendix C.

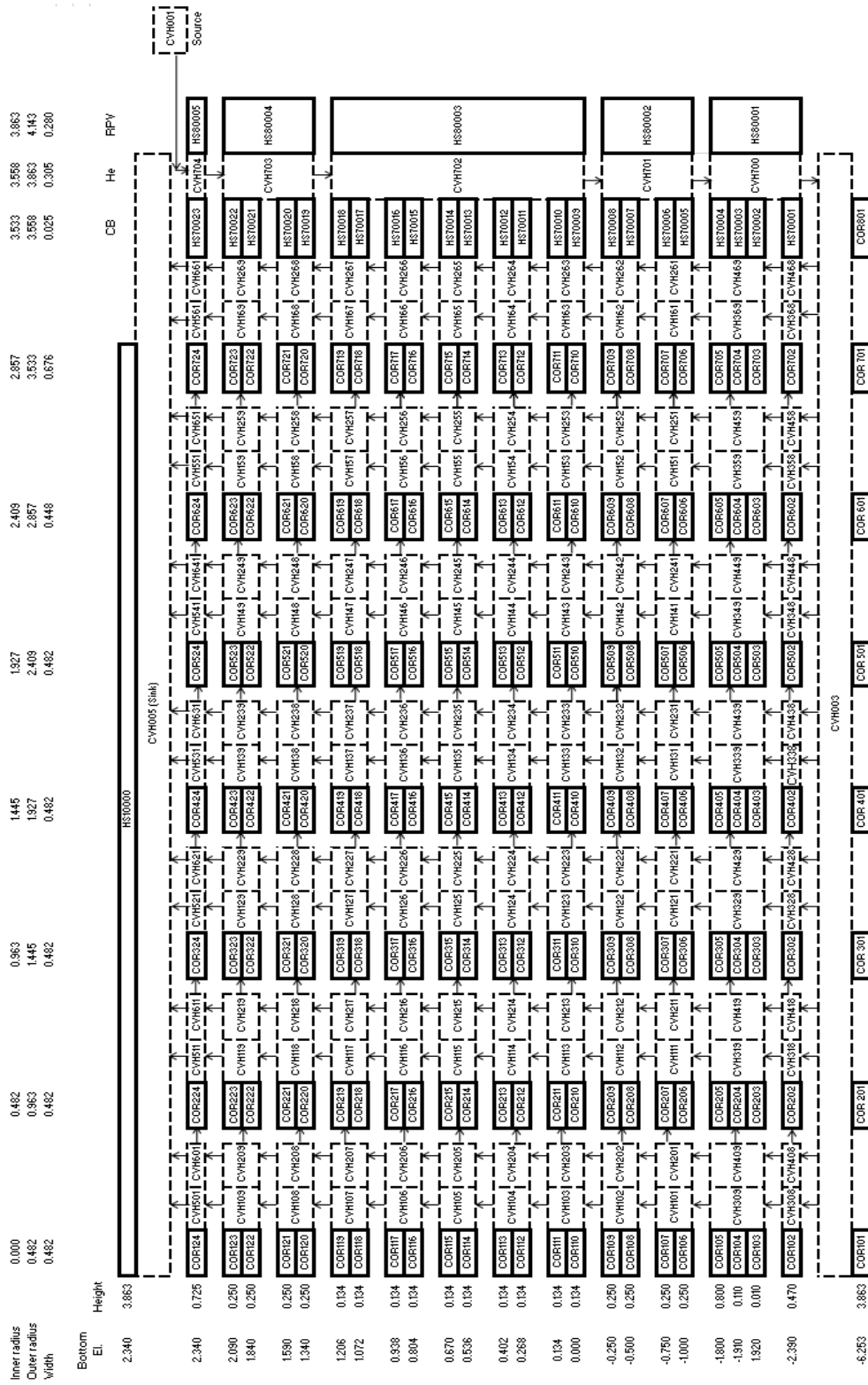


Figure 7.1: MELCOR Input Nodalization Diagram

7.2.1 COR Input

The COR package input contains information regarding the reactor core, LCP and the reactor vessel lower head. The core is divided into 8 radial rings and 24 axial levels, and the entire first axial level represents the lower head. All remaining axial levels in the 8th radial ring are declared empty cells because the CB and DC reside here. Furthermore, the edge of the eighth ring coincides with the inner layer of the RPV. This will be discussed further during the discussion regarding the heat structure package. Axial level 2 in rings 1 through 7 represents the LCP, along with stainless steel used to make a portion of the throat of the lower nozzles for all of the assemblies in the core. Axial level 3 in rings 1 through 7 represents the portion of the throat of the lower nozzles of the assemblies that is above the LCP. Level 4 in rings 1 through 7 represents the mouth of the lower nozzles of the assemblies in the core. Level 5 in rings 1 through 7 is made of the LBS, including the stainless steel plates that lie above and below the actual shield. Axial levels 6 and 7 in rings 1 through 5 consist of the portion of the core where the empty plenum regions of the fuel rods reside. This region also contains other core elements such as can and clad material. Axial levels 6 through 23 in ring 6 contain reflector material, while the same axial levels in ring 7 contain shield material. Can material is also present in those regions; however, only the borated shield region contains cladding, as the reflector rods do not have any cladding. Axial levels 8 and 9 in rings 1 through 5 contain the reflector material that can be found in the fuel rods. Cladding and canning also reside in these regions. Axial levels 10 through 19 in rings 1 through 5 contain the fuel that is found within the active core. Canning and cladding are

also in these regions as well. Continuing in the upward direction, axial levels 20 and 21 in rings 1 through 5 contain the reflector material that is found in the fuel rods along with canning and cladding material. Just beyond the region where the fuel rods contain the reflector is the region where the fuel rods contain the empty plenum region. This is represented in axial levels 22 and 23 in radial rings 1 through 5. Finally, axial level 24 in rings 1 through 7 contains silicon carbide upper support plates, the UBS material, and the upper stainless steel support plates.

The MELCOR code does not contain a built-in reactor type that represents the US DOE GFR. Therefore, that particular reactor type could not be selected. Instead, the BWR reactor type is chosen. One reason as to why this particular type is selected is due to the fact that the BWR type allows the user to define canning material. Although the assembly cans in the GFR are hexagonal as opposed to square, as is the case in the BWR, the intention was to construct the MELCOR input deck so it would be able to account for canning material. No specific geometry is given to the canning material in any MELCOR deck, only the amount of canning mass is input. Thus, the shape of the can does not make a difference. It is necessary to define canning material in order to account for the different modes of heat transfer that occur within those structures. Another reason as to why the BWR reactor type is chosen is because of the type of channel and bypass regions that are represented by the BWR reactor type. The BWR reactor type allows MELCOR to interpret channel flow as flow through assemblies, within the boundary of the assembly cans. Bypass flow is interpreted as flow between assemblies, or, flow that runs along the outside of assembly cans. These definitions of

channel and bypass flow are more representative of the core design specifications than the PWR reactor type, which interprets channel flow as flow through the entire core, while bypass flow is interpreted as flow between the core shroud and CB. This is clearly not representative of the GFR since it does not account for flow between canisters. Furthermore, the GFR does not have a core shroud, according to design specifications. Perhaps it is also important to note that specifying the BWR reactor type allowed for horizontal flow between assemblies without simulating cross flow between assemblies. One of the primary functions of assembly cans is to prevent cross flow between assemblies. However, it is still necessary to simulate the horizontal flow that occurs between assembly cans. All other reactor types that could have been chosen do not need to be considered for the purposes of this thesis. The organization of the COR_RT card is such that the user specifies the reactor type (IRTYP), the control rod poison type (MCRP), and the electric heating element (MATHT). Since no electric heating elements are used, no value is input for MATHT.

Prior to establishing the amount of different materials present in the core, certain parameters must be identified. To begin, the geometric parameter card is established following the card for the reactor type discussed in the preceding paragraph. On the geometric parameters card (COR_GP), the radius of the fuel, radius of the cladding, thickness of the gap between the fuel gap and cladding, as well as the fuel rod pitch are specified. Other important parameters contained within the COR package include the COR_VP card which establishes the vessel parameters. Vessel parameters specified include the outer radius of the active core region, the radius of the inside of the vessel

cylinder, the reactor lower head transition type, the thickness of the cylindrical vessel wall, the thickness of the lower head inside the transition radius that is specified by the reactor lower head transition type, the reactor lower head type, and the radius of curvature of the lower reactor head type. All values pertaining to the vessel parameters can be found in Appendix C. Additional vessel parameters, specified by the COR_AVP card, include the elevation of the BWR baffle plate and the elevation of the core support plate. These values are set equal to each other. Other parameters entered into the COR package prior to declaring all of the masses of core materials include the COR_TP record which specifies how different packages interface with each other along with fission power and gap conductance models. The COR_MS record refers to model switches which control various functions in the core. The only model switch of concern for this thesis is the one which allows for inconsistencies between fluid volumes in the CVH package and COR package to be ignored. Examples of this are seen in MELGEN output when these values differ by relatively small amount, such as on the order of 10^{-3} . In order to prevent failure of various support structures, the COR_SS card is used in order to ensure that specified supporting structures do not fail. This is known as the card for the global loading and failure rule for supporting structures. A similar card is also input for nonsupporting structures.

Although the nodalization of the core is defined in the first paragraph of this subsection, it is still necessary to discuss how the nodalization is established using the COR_ZP and COR_RP records. In the COR_ZP record, the quantities defined are the axial level numbers along with their axial locations and heights. In addition, the porosity

of particulate debris is also defined. However, values for this particular quantity are unimportant since there is no particulate debris modeled in this deck. The boundary heat structures associated with each core level are listed as well as the relative fission power associated with each axial level. Contained within the COR_RP record are values such as the location of the border of each radial ring, as well as the cross-sectional area associated with each ring. Furthermore, the upper level heat structures associated with each core ring are listed. However, since there is only one heat structure at the top of the core, the same heat structure is associated with each ring. Columns are available for various control functions that may be associated with the radial rings. However, since no control functions are associated with the COR_RP record, all of their values are 'NO'. The final column in the COR_RP record is reserved for the relative fission power associated with each ring. Following the construction of the radial and axial levels of the core, each radial and axial level is associated with their respective channel and bypass control volumes in the COR_RBV record.

In order to quantify all major elements present in the reactor core, their mass must be entered into the different MELCOR packages. Beginning with the fuel present in the reactor core, the amount of fuel present in each core cell that holds fuel is calculated considering a (U,TRU)C fuel. Only axial levels 10 through 19 in radial rings 1 through 5 contain the active fuel. The amount of fuel present in each core cell is calculated according to the height of each axial core level along with the quantity of fuel rods present within each core cell. Obviously, the inner and outer radii, as well as the

density of the fuel are taken into account. The process for calculating the amount of fuel present in a core cell is shown in equation 7.1 through 7.3. Equation 7.1 shows how the

$$V_{fuel,cell} = A_{fuel} * h_{cell} * N_{frods} \quad (7.1)$$

volume of fuel in a cell is calculated. The calculation of the area of the fuel rods was done in the previous subsection. h_{cell} represents the height of the core cell being considered, and N_{frods} is the number of fuel rods present in a radial ring. The number of fuel rods present in a ring is calculated using the following equation:

$$N_{frods} = (N_{frods/fasem} * N_{fasem}) + (N_{frods/casem} * N_{casem}) \quad (7.2)$$

In equation 7.2, $N_{frods/fasem}$ accounts for the number of fuel rods present in a fuel assembly, while N_{fasem} accounts for the number of fuel assemblies present within a core cell. $N_{frods/casem}$ accounts for the number of fuel rods present in a control/shutdown assembly, and N_{casem} accounts for the number of control assemblies present in a core cell. The number of fuel and control assemblies per core cell is analogous to the number of fuel and control assemblies per radial ring. Each radial ring is given a certain amount of fuel and control assemblies based on the need to establish rings of equal width in the active core region. The amount of fuel assemblies and control assemblies placed in each ring is based on the allocation of core assemblies seen in the reactor core layout. Finally, the mass of fuel present in a COR cell is calculated using equation 7.3.

$$m_{fuel,cell} = \rho_{fuel} * V_{fuel,cell} * N_{frods} \quad (7.3)$$

In addition to the active fuel that is present in the FU package, the reflector material that is present in the fuel rods is also considered part of the FU package. Thus, all reflector material in the active fuel region is considered part of the FU package.

Reflector material in the 6th ring is not considered part of the FU package. This will be discussed further when nonsupporting structures are discussed. The reflector material that is part of the FU package is found within axial levels 8 and 9, as well as levels 20 and 21, as mentioned earlier. The amount of reflector material present in each COR cell is calculated in the same manner as the amount of fuel that is present in each COR cell. Obviously, the density of the reflector material differs from the density of the fuel material. All other COR cells do not have any FU material.

Another important aspect of the COR input is the cladding present within the core. The cladding component of the COR package allows the user to specify how much cladding is present in the reactor. All cladding considered in the reactor core is located between axial levels 6 and 23 in rings 1 through 5. Although the borated shield rods have a cladding component associated with them, there is no fuel contained in the borated shield. The cladding is reserved for only those rods that contain fuel. The tungsten “cladding” layer that surrounds the boron carbide in the borated shield region is considered part of the nonsupporting structure that makes up that region. This will be discussed further when nonsupporting structures are discussed. The quantity of cladding present in a particular COR cell is calculated in the same manner as the amount of fuel within a fuel cell with obvious adjustments for density and area.

While its material properties may vary depending on core location, canning material can be found between axial levels 5 and 24 in radial rings 1 through 7. SiC canning can be found between axial levels 5 through 24 and within rings 1 through 5 and ring 7. The same axial levels in ring 6 contain Zr_3Si_2 canning. The quantity of mass that

represents the canning material in all rings is calculated in a similar fashion to the manner in which all other materials that reside in a particular COR cell are calculated. Figure 7.1 represents the area considered when calculating the area of an assembly can. The figure is not drawn to scale; however, it does provide the reader with a good idea of the foundation of an assembly can.

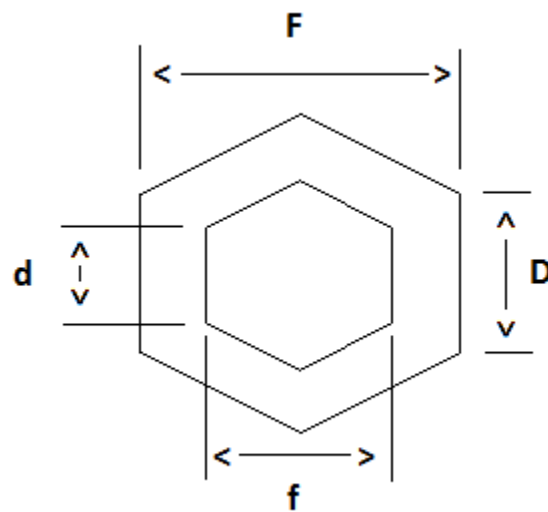


Figure 7.2: Identification of Assembly Canister Parameters

In order to determine the area that makes up the assembly can, the following calculations are performed:

$$D = \frac{F \cdot \sin\left(\frac{\pi}{6}\right)}{\sin\left(\frac{2\pi}{3}\right)} \quad (7.4)$$

Then, the length of an interior side of the hexagonal canister is calculated as:

$$d = \frac{f^* \sin\left(\frac{\pi}{6}\right)}{\sin\left(\frac{2\pi}{3}\right)} \quad (7.5)$$

Next, the area of one of the six wedges that comprise the hexagonal structure in Figure 7.1 can be calculated. First it is necessary to obtain a value for the parameter J , the can thickness:

$$J = \frac{D-d}{2} \quad (7.6)$$

The area of one of these wedges is then calculated as:

$$A_{wedge} = \left(d^* \frac{F-f}{2} \right) + \left(2^* \frac{1}{2}^* \left(J^* \frac{F-f}{2} \right) \right) \quad (7.7)$$

Because an assembly is made of six of these wedges, the area of an assembly is calculated as:

$$A_{can} = 6^* A_{wedge} \quad (7.8)$$

With a calculation scheme for the area of a hexagonal can, the mass of canning material found within a COR cell is then calculated as:

$$m_{can} = \rho_{can}^* A_{can}^* h_{cell}^* N_{can} \quad (7.9)$$

The variable N_{can} represents the total number of assembly cans found within a radial ring. The density of the assembly can (ρ_{can}) is dependent upon the material being considered for the hexagonal can.

Certain materials present within the reactor core are classified as supporting structures. The mass of all supporting structures found in the core are input in the KSS card found within the core package. Perhaps the most obvious supporting structure

present in the reactor is the LCP. The LCP is positioned at axial level 2 in rings 1 through 7. When the mass is input, attention must be paid to the fact that there are two types of holes present within the LCP. Obviously, holes are present where the assemblies could be locked into the LCP. Due to the lower nozzle at the bottom of the assemblies, these holes allow for helium to be passed into the assemblies. The other types of holes present in the LCP are holes that allow for bypass flow to enter into the reactor core. No design specifications were given for how the bypass flow could enter the reactor core. Therefore, it is assumed that 25% of the area occupied between assemblies in the LCP is to be open to bypass flow. The amount of stainless steel comprising the LCP is calculated by first assuming one large steel plate underneath the reactor core. Then, all of the area reserved for coolant flow is subtracted from that mass.

Other supporting structures include the lower nozzles for all of the assemblies, including both the mouth and throat of the nozzles. Furthermore, the SiC cans that provide support to the control rods are also considered supporting structures. The area of these supporting cans is calculated in the same manner as the cans for the assemblies, obviously with different dimensions. These cans are chosen to be support structures rather than canning material because they act in a similar fashion to CRGTs found within a PWR. According to the MELCOR user's guide, control rod guide tubes are better represented as supporting structures in a MELCOR input deck. Finally, all of the support plates, except for the highest stainless steel support plate are considered supporting structures. Because the support plates are comprised of small cylinders that are in line with each of the fuel rods, their volume and mass is calculated in the same

manner as the fuel rods. Although support plates in the final design of the GFR may differ from those assumed for this model, the reader must keep in mind that these types of support plates are chosen in order to simplify the model.

The KNS, or nonsupporting structure, card is the final card in the core package for which mass values must to be entered. Nonsupporting structures refer to a variety of structures, such as the LBS and UBS, the rods in the outer reflector region, the rods in the outer borated shield region, and the highest support plate for all of the assemblies. The reason as to why the highest support plate is chosen as a non supporting structure is because it does not support the weight of other components such as the supporting structures.

Beginning with the LBS and UBS, which have the same geometry, excluding height, as each other, the mass is calculated in the same manner as the mass for the fuel rods. Since the shields are comprised of cylindrical rods, the reader is already familiar with how to calculate the mass. However, attention must be paid to the fact that the rods are made of two different materials. The inner component of the LBS and UBS is made of boron carbide, while the layer surrounding the boron carbide is made of stainless steel. Because the shield is made of two different materials with different densities, the mass must be calculated separately for each material. The volumes are calculated as a solid cylinder and an annular cylinder for the boron carbide and the stainless steel, respectively. Then, each of the volumes is multiplied by their respective densities.

Similar to the LBS and UBS, the rods that make up the outer borated shield assemblies also contain boron carbide along with an outer support layer; however, the

cladding layer for the outer borated shield rods is made of tungsten. Again, the mass of these nonsupporting structures is calculated by obtaining the volume of each of the different materials and then multiplying those volumes by their respective densities. The reflector rods in the outer reflector region of the core are also cylindrical nonsupporting structures whose mass may be calculated in the same manner as well. However, because these rods do not have any cladding associated with them, only one volumetric region is taken into consideration.

Perhaps the smallest of all of the nonsupporting structures are the stainless steel support plates which lie above all of the assemblies. Their mass is also calculated according to the same methodology applied to all of the other cylindrical structures whose mass must be calculated. Because the majority of structures throughout the core are cylindrical in nature, calculations are not provided for all cylindrical structures due to the fact that it would be repetitive.

Prior to executing the MELCOR input deck, initial temperatures are assigned to all core components. All core components are assigned an initial temperature of 763.15 K, which is the inlet temperature of the helium coolant used to cool the reactor core. Setting initial temperatures closer to the steady state value for all core cells has the potential to decrease the amount of time required for the calculation to reach steady state. However, these values were not well known prior to MELCOR calculations. Thus, all structures are assigned the same initial temperature, which is also the coolest coolant temperature that the reactor core experiences.

In order for MELCOR to be able to determine the amount of thermal energy transferred from various core structures to the coolant, the COR_EDR record allows the user to specify the hydraulic diameter of all core components. All hydraulic diameters are calculated using the familiar formula of four times the flow area divided by the wetted perimeter. In the following paragraphs, calculations for a few select hydraulic diameters are shown. This is done in order to provide the reader with an idea of how these particular types of calculations are carried out. Particulate debris in both the channel and bypass region of the core is assigned a random hydraulic diameter since the model is assumed to contain no particulate debris. Therefore, any hydraulic diameter associated with particulate debris is not used. However, a value must be entered in order to satisfy code requirements.

The first hydraulic diameter worthy of further discussion is that of the fuel rod cladding. First, the flow area of the assembly cans for a core cell is calculated as:

$$FA_{can(empty)} = \frac{3*\sqrt{3}*d^2}{2} * (N_{casm} + N_{fasem}) \quad (7.10)$$

Then, in order to calculate how much area around the fuel rods is available for flow, the area occupied by a fuel rod in an assembly is calculated. D_{rod} is the fuel rod diameter.

The total area occupied by the fuel rods in an assembly depends upon the quantity

$$A_{rod} = \pi * \frac{D_{rod}^2}{4} \quad (7.11)$$

of fuel rods present within the assembly. Thus, the area occupied by fuel rods in a fuel assembly is 271 times the area of a single fuel rod. Next, the total fuel rod area is subtracted from the original flow area of the can without any rods in order to determine

the available flow area. This is seen in equation 7.12. The denominator of the equation used for calculating the hydraulic diameter, the wetted perimeter, is obtained by

$$FA_{can} = (N_{asem} * FA_{can(empty)}) - (A_{rod} * N_{frods}) \quad (7.12)$$

calculating the diameter of a fuel rod and multiplying it by the number of fuel rods present in an assembly. Equation 7.13 shows how this procedure is performed. The hydraulic diameter of the cladding within a particular core cell can then be

$$WP_{clad} = N_{frods} * \pi * D_{rod} \quad (7.13)$$

calculated as:

$$EDR_{clad/cell} = \frac{FA_{can}}{WP_{clad}} \quad (7.14)$$

All hydraulic diameters referring to a cylindrical rod structure can be calculated in the same manner. Thus, the reflector rods in the outer reflector region, as well as the boron carbide rods in the outer borated shield region, have hydraulic diameters that are found using the same methodology observed in the equations describing how to calculate the hydraulic diameter of the cladding for the fuel rods. Obviously the quantity of rods per assembly, as well as rod geometries, differs according to assembly type. One important note for the reader to understand about the calculation of the hydraulic diameter of the cladding in the active core is that the flow area in the inner can in the control assemblies is not part of the flow area used in the calculation. Furthermore, the hydraulic diameter of the inner cans of the control/shutdown assemblies are taken into account in the subsection of the COR_EDR record reserved for supporting structures.

Another important hydraulic diameter to consider is that of the assembly cans found throughout the core. The hydraulic diameter for all of the assembly cans is calculated in a very similar fashion to that of the cladding for the rods in a can. The only difference is that the calculation of the hydraulic diameter for the cans includes the wetted perimeter of the assembly can in addition to the wetted perimeter of all of the rods in the assembly. The wetted perimeter of the inside of an assembly canister is calculated with the aid of Figure 7.1 in equation 7.15. This applies to all assembly cans found within the core including the outer reflector cans and the borated shield cans.

$$WP_{can(inside)}=6*d \quad (7.15)$$

The hydraulic diameter for the canisters applies to the hydraulic diameter considered as the channel hydraulic diameter for various regions of the core. On the other hand, the hydraulic diameter for the bypass region of the core is calculated differently. One may consider the hydraulic diameter of the bypass region of the core to be analogous to the hydraulic diameter for the outside of the assembly canisters, regardless of canister type. The calculation of this particular hydraulic diameter involved some creativity. As is seen in the MCNP input deck, all of the assemblies in the reactor core are filled into a hexagonal lattice that spans the entire area of the reactor core. Because the size of each lattice site is slightly larger than the area of an entire assembly, a volume of space occupied by helium lies between edge of the assembly can and the edge of the lattice site. This volume of helium is considered to be bypass flow. Thus, the hydraulic diameter of the canning on the bypass side of the can is calculated using the flow area outside of the can and the wetted perimeter of the outside of the assembly. The wetted

perimeter of the outside of the assembly can is obtained using equation 7.15; however, D is used instead of d . This switch can also be observed in equation 7.18 in Subsection 7.2.3. Equation 7.14 still applies to this situation.

Other important hydraulic diameters that must be input into the COR_EDR record include those for supporting structures, such as the inner cans for the control/shutdown assemblies, the lower assembly nozzles, as well as the bypass region in the LCP. The hydraulic diameters for the inner cans can be calculated using the flow area of the inner can as well as the wetted perimeter of the inside of the can. The flow area can be calculated in a similar fashion as equation 7.10. The wetted perimeter is calculated as 6 times one of the inner sides of the inner can. Then, the hydraulic diameter is once again solved as it was in equation 7.14.

A separate paragraph is reserved for the discussion of the hydraulic diameter of the bypass region found in the LCP. Because no design specifications regarding the core bypass are found in the design report, a bypass flow is inferred. In order to create bypass flow through the LCP, holes through which the gas could flow are created. Considering that the assemblies all fit into a hexagonal lattice that spans the entire core, the area of stainless steel that lies just beyond the outer boundary of the assembly can, yet still within its respective lattice site, is calculated according to the same methodology found in equation 7.4 through 7.8. In other words, the reader can imagine another hexagonal can that lies just beyond the assembly can. However, the hexagonal can in the bypass is made of stainless steel. After calculating the area of the lower core plate outside of the assembly can, it was decided to remove 25% of that area in order to allow for bypass

flow. Flow paths are created in the form of tiny holes drilled through the LCP. The total flow area in the bypass region through the portion of LCP around an assembly is calculated as:

$$FA_{can(LCP)}=0.25*A_{can(LCP)} \quad (7.16)$$

It is also decided that the bypass flow area should be allocated into 12 holes on each side surrounding the assembly. Thus, in total, 72 holes created for the purpose of allowing gas to flow within the bypass of the reactor surround each assembly. Following the same manner in which hydraulic diameters were created earlier, the hydraulic diameter for bypass in the LCP is calculated using equation 7.14, where the flow area is the flow area of all of the holes in particular radial level, and the wetted perimeter is the wetted perimeter of the holes for a particular cell.

Although the boundary flow area for all core cells is a card contained within the COR package, all flow areas are better left for discussion within the subsection concerning the flow path package. Values regarding the COR_BFA record are listed along with other COR input data; however, the values for this particular card are originally derived from the calculation of flow areas, as should be the case in order to maintain consistency. Perhaps one important concept to note about this record at this particular point in the thesis is the fact that there is no bypass flow in the cavity of the reactor core. This concept is a consequence of the fact that all flow in the cavity is classified as channel flow. It did not make sense to model any of the flow as bypass flow since it does not flow in between structures with a decreased He volume.

Calculations for the surface area record card are quite simple and have already been partially solved. The surface area for all components in this card is calculated by multiplying the wetted perimeter of each type of structure by the height of the COR cell in which the component exists. Obviously, there is no wetted perimeter for the fuel since it is not exposed to coolant during normal operation. Therefore, the circumference of the fuel is understood to be analogous to the wetted perimeter and is the value used when calculating the surface area of a fuel component in a COR cell. The calculation of the surface area for a fuel component is presented as follows:

$$SA_{fuel} = (\pi * D_{rod}) * h_{cell} * N_{frods} \quad (7.17)$$

Of particular importance to note is that the wetted perimeter considered for the canister is the wetted perimeter of the inside walls of the canister. The inside walls are chosen as the wetted perimeter due to User Guide specifications. The outside of the canister surfaces are taken into account in the COR_CSA record, which is the next record discussed.

Conveniently, all of the can surface areas concerning the inside of the assemblies are already known from the COR_SA record. However, the COR_CSA record also requires entry of the surface area values for the outer canister walls. Surface area values concerning the bypass side of the can are obtained by multiplying the wetted perimeter of the outer walls of the canisters by the height of the core cell in which that particular component of the canister resides. All entries concerning the surface area of the portion of the canister that lies next to a control blade are 0. This is due to the fact that there are no control blades in the reactor core. Furthermore, one never needs to be concerned with

entering values for these particular surface areas during any kind of transients where reactivity control is needed since all control poisons are entered into the center of the control/shutdown assemblies.

Although LCP behavior is not assessed during the course of this project, the COR_LP record requires entries in order for the MELCOR input deck to run. The axial level at which the LCP resides is level 2. Because there is no in-vessel falling debris, the heat transfer for in-vessel falling debris is 0. Furthermore, a very high pressure is selected as the pressure at which the LCP fails. This is done in order to avoid any sort of possibility that the LCP may fail. Because this input deck is designed with the intention of creating a steady-state run without any structural failure, it is acceptable to place a very high value on the pressure failure criteria. Finally, the velocity of falling debris is set to 0 since there is no falling debris present in the core.

As is the case with the LCP, lower head behavior is also not important for the purposes of this thesis. However, in order to successfully execute the MELCOR calculation, a lower head model is required. The total number of temperature nodes is 2, which is the minimum required value. The total number of insulation mesh layers is set to 0. As one can observe, the lower head structure record is not given a great degree of definition since details of its behavior is not important for this thesis.

Also of rather minor importance with regard to analysis is the lower head segments record, COR_LHD. However, for the purposes of establishing a working model, it is necessary to input data into this record. All temperatures entered are equal to the core inlet helium temperature since this can be considered the initial temperature

of the segments. All radii input into this record correspond to the radii of all rings that are present in the reactor core. Finally, all of the segments are placed in a control volume that is equal in size to the reactor cavity control volume. It is not; however, the same control volume that actually represents the core cavity. MELGEN did not accept the condition where the reactor cavity control volume (CAV-CV003) is used as the lower head. Thus, a “dummy” control volume (LHD-CV004) needed to be created in order to satisfy MELCOR code restrictions. However, only CAV-CV003 is actually used in the MELCOR calculation.

The final card found in the COR package is the COR_FUM card. This card is used to specify extra material included in the fueled region of the core. Zirconium is chosen as the extra fuel material; however, zirconium isn't really the extra fuel material. Later in this section, material substitutions will be discussed. For now, it is important to recognize that silicon carbide is substituted for zirconium. Furthermore, Zr_3Si_2 is substituted for zirconium dioxide. Because the extra fuel material is listed as the oxide for zirconium, which is zirconium dioxide, Zr_3Si_2 is considered as the extra fuel material. Zr_3Si_2 is considered as extra fuel material, rather than nonsupporting structure, in rings one through five since it is contained within the cladding when found in the active core region.

The majority of details concerning input for the COR package have been covered in this subsection. Details concerning flow areas have been left out since they will be covered in the discussion on flow paths. During the discussion of flow paths, mention will be made regarding their connection to the COR package in order to remind the

reader of what types of flow information relate to boundary flow areas found within the COR package. Overall, the COR package is meant to provide the code with information regarding various types of core structures, such as fuel cladding, canning, supporting structures and nonsupporting structures.

7.2.2 CVH Input

Established for the purpose of associating coolant volumes with various core and heat structures, control volumes contain information regarding the coolant used to cool various reactor materials. This subsection contains information regarding the control volumes created for this particular input. The majority of control volumes present in the core are constructed in the same manner. Appendix C contains all of the information regarding the control volumes. Two control volumes differ from the rest, namely, the sink and source control volumes. These are also discussed in this subsection.

Beginning with a description of the general control volumes created, a name and numerical identifier are created first using the CV_ID card. Then, the thermodynamic conditions for the control volume are specified. The first thermodynamic condition set is the fact that the pool temperature is not equal to the atmosphere temperature. The pool is defined as the portion of the control volume that may contain single-phase liquid or two-phase (bubbly) water [2]. Technically, there is no pool in any control volume since there is no liquid. The atmosphere is defined as the portion of the control volume that contains water vapor and/or noncondensable gases. It may also contain suspended water droplets known as fog [2]. Only atmosphere conditions apply since there is only helium gas present in each control volume. Then, the second condition is that fog is

allowed in each control volume. The third field in the thermodynamic conditions card is a switch that is set to ACTIVE. This allows MELCOR to advance the calculation by integrating the conservation equations. The next specification card, CV_PAS, holds the pool and atmosphere switches. The pool and atmosphere are specified to be treated separately and only atmosphere is present in the control volume. Furthermore, the vapor state is declared to be superheated. Next, the pressure conditions are specified on the CV_PTD card followed by the temperature which is specified on the CV_AAD card. All general control volumes also have a noncondensable gas card since helium is present in each control volume. The relative humidity is set to 0 since there is no steam, and the helium fraction is set to 1 since all of the gas present in a control volume is helium. The CV_VAT card is the volume altitude table for all of the control volumes. In this card, the lowest elevation of each segment of a control volume is specified. The final value listed is the height of the whole control volume. Furthermore, the volume of each control volume segment is also listed. All of these values can be found in Appendix C.

Although the majority of the conditions of the source control volume match the initial conditions of the general control volumes, its properties must remain constant. Therefore, this control volume is controlled by various control functions that allow its properties to remain constant. Rather than claiming that the control volume is superheated in the CV_THR card, it is said to be property specified. Then, instead of specifying the pressure, temperature, relative humidity and helium fraction in the source control volume, these properties are linked to control functions that can be found later in the input deck. Control functions will be discussed in a later subsection of this section.

Volume altitude tables are still input for the source control volume in the same manner in which they are input for the general control volumes. The sink control volume is described in the same manner as the source control volume; however, the conditions specified by control functions are different. While the control functions representing the properties of the source and sink control volumes are discussed later, their values can be seen in Appendix C. The following paragraph illustrates how some of the input observed in the control volume package is obtained.

All control volumes established within this input are sized according to the COR cells that are created in this input deck. Their flow areas are dependent upon the flow areas calculated in the flow path package, which is described in the next subsection. The volume altitude table is the element of a control volume that is sized according to the COR cells due to the fact that the elevations in the table are in line with the axial elevations of the COR cells. For example, in the first radial ring of the active core, COR-CV103 has an elevation equal to the height of the first two COR cells with fuel combined. In other words, COR cells 110 and 111 belong to the control volume. The numbers associated with COR cells are interpreted as follows. The first number represents the radial ring, and the next two numbers represent the axial level. Furthermore, the control volume is split into two segments that are divided according to the height of each COR cell. Although the majority of control volumes present in the input deck are divided into two segments and contain two COR cells, some control volumes are split into four segments, and some only contain one segment. The control volume segmentation can be observed in Appendix C. In addition, the reader can

identify which control volumes are associated with which COR cells by observing the COR_RBV data also found in Appendix C. The COR_RBV data allows one to determine how many core cells are associated with a particular control volume. Furthermore, by observing the nodalization scheme outline in the subsection referring to the core nodalization, the reader can deduce the core materials present in a particular control volume.

7.2.3 FL Input

In order to pass He between the control volumes, various flow paths between control volumes are established throughout the input deck. This subsection includes a general description how flow paths are constructed. As was the case in the preceding subsection, general flow paths throughout the input have the same general outline. One flow path in the total flow path input section requires the aid of a control function. Mention of this will be made in the closing paragraph of this subsection.

The first two entries when defining a flow path fall under the FL_ID card, which requires a name and numerical identifier for the flow path. The FL_FT card is used in order to specify the control volumes that the particular flow path being described is connecting. Furthermore, the altitude of the connection between the flow paths is listed for both control volumes. These values are always the same. The FL_GEO card is used to specify geometric parameters, such as the flow area of the flow path, the length of the flow path, as well as the fraction of the flow path that is open. Throughout the entire MELCOR input deck, the fraction of flow path that is open is always 1. Calculation of flow path areas can be found in Subsection 7.1.1 when canister flow areas are discussed.

The FL_JSW switch allows the user to define the flow path orientation. Only two types of flow path orientations are used during the construction of this deck, vertical and horizontal flow paths. The majority of flow paths only consisted of one segment. However, all flow paths that are found in the LCP contain multiple segments. The two entries used in the FL_USL cards observed throughout the input deck are always 0.0. A further discussion of this card will be presented later in this subsection. For now, it is important to realize that it relates to the form losses present in a flow path segment. Each flow path segment entry contains information regarding the flow area, length, hydraulic diameter and surface roughness of the segment. Only the flow path from the control volume source requires an extra entry. The FL_VTM card is used in order to specify the velocity of the fluid as it enters the downcomer. The velocity is defined by a control function. The following paragraph provides some example calculations of how portions of the data for the flow path package are obtained.

Although this paragraph is intended to provide the reader with a description of flow area calculations present in the flow path package, this information is also used to describe the boundary flow areas observed in the COR input. Flow area calculations observed in this subsection are mainly concerned with the channel and bypass flow areas found within the core. However, other flow areas that exist, such as those in the LBS and UBS are based off of the same methodology used to solve for the flow areas in the channel and bypass regions. The flow area within each channel can be calculated using equation 7.12, and the flow path length for each segment is taken to be the distance between the midpoints of the control volume segments being connected by the flow

path. However, the bypass flow must be calculated in a different manner. First, the reader can apply the same mindset applied to the case when the flow area of the bypass region was being considered toward the end of Subsection 7.2.1. Once again, the reader must imagine that each assembly sits in a hexagonal lattice site. Then, the area beyond each assembly, but still within the hexagonal lattice site, is considered as the bypass flow area. The summation of all of these areas within each individual ring accounts for the bypass flow in that particular ring. The flow path area is equal to the bypass area just as the flow path area for a channel is equal to the available area for flow in a channel control volume. The hydraulic diameters are obtained by dividing four times these flow areas by the wetted perimeter of the outside of the assembly canisters. Equation 7.4 is used in equation 7.15 in order to obtain the wetted perimeter for an assembly canister.

$$WP_{can(out)}=6*D \quad (7.18)$$

Perhaps the most difficult values to obtain throughout the entire course of this endeavor are the flow areas for the horizontal flow paths that connect a control volume in a radial ring to its adjacent control volume in the next radial ring. Although the modeling technique used in order to calculate this flow area requires some imagination, it seems to be the most plausible approach towards making an accurate assessment of the horizontal flow area. First, it has already been mentioned that assemblies comprising each active core ring are allocated in such a manner as to establish 5 rings of equal width. Thus, after careful observation of the initial core layout, it is determined that the area available for lateral helium movement is calculated as the combined width of the spacing between the outermost assemblies in a radial ring multiplied by the height of the

axial levels to which the bypass control volumes are attached. The width of the spacing between each fuel assembly is taken to be 7 mm since that is the distance between assembly cans. Next, the number of exit paths is quantified such that only the flow paths that allow escape from the first radial ring to the second radial ring are taken into account. While the radial active core rings are allocated in such a manner that sometimes a fraction of an assembly appears in the calculations, the value for the flow paths is rounded to the next highest number for simplification. Furthermore, it did not seem advisable to take a portion of a horizontal flow area into account. After taking the overall length of the combination of exit path width, it is multiplied by the height of the bypass control volume to which it is connected in order to finally determine the area. Calculation for the methodology on how the horizontal flow path areas are obtained is outlined below. Also seen below are calculations of the wetted perimeter and hydraulic diameters for these flow paths.

As mentioned in the opening paragraph of this subsection, further discussion is required of the FL_USL card. This card is applied to all flow paths that are within the reactor from the LBS up to the UBS. This card is concerned with form losses, or pressure drops that may occur due to possible bending, opening, or closing of a flow path. Because all flow paths between axial levels 5 and 24 do not contain any characteristics that contribute to a form loss, they are assigned a forward and reverse form loss coefficient of 0.0. This same concept applies to all flow paths in the DC. Form losses are not assigned to flow paths in the cavity since the cavity causes the flow to bend. Furthermore, expansions and contractions exist in the LCP that prevent

assignment of a form loss of 0.0 to flow paths in the LCP. Therefore, flow paths concerning the cavity and LCP do not contain the FL_USL card since the default value must be assumed due to lack of information concerning the appropriate form losses for those flow paths. The default form loss value is 1.0.

Another flow path characteristic worthy of further discussion is the surface roughness factor listed on the FL_SEG card. While many of the form losses are set to 0.0 in order to prevent pressure drop calculations due to form losses, pressure drop due to friction is still present throughout the entire core. Surface roughness factors are required in order for MELCOR to be able to calculate the wall friction for a particular surface. The friction factor for single-phase flow is calculated using equation 7.19 if the flow is laminar, or equation 7.20 if the flow is turbulent. Equation 7.20 is known as the Colebrook-White equation and requires an iterative solution [21]. The friction and diameter terms are f_{fric} and D_{fric} . They are shown this way, instead of as f and D in order to differentiate them from f and D in figure 7.1. The diameter in equation 7.20 is not

$$f_{fric} = \frac{16.0}{Re} \quad (7.19)$$

$$\frac{1}{\sqrt{f_{fric}}} = 3.48 - 4.0 \log_{10} \left[\frac{2.0e}{D_{fric}} + \frac{9.35}{Re \sqrt{f_{fric}}} \right] \quad (7.20)$$

necessarily that of a pipe due to the fact that flow paths represent flow channels rather than pipes. However, since all flow paths are represented within radial rings, it is as if a diameter can be assigned. Furthermore, one can consider the diameter to be a hydraulic diameter. Various surface roughness values used in the MELCOR input can be found in

Appendix C. They differ based on the material which accounts of the wall of a channel and/or bypass region. Values for SiC are able to be found. However, difficulties were encountered when trying to obtain surface roughness values for Zr_3Si_2 and tungsten. Thus, it is assumed that they have the same roughness values as stainless steel. Technically, this assumption is somewhat reasonable because one could assume that Zr_3Si_2 and tungsten can be smoothed to the value of stainless steel. However, it is important for the reader to realize that many assumptions had to be made throughout the entire course of this project in order to be able to establish a working model.

7.2.4 HS Input

In order to establish various bounding structures, such as the CB, the RPV wall and the upper head, various heat structures are created. This paragraph addresses the input used in order to create all heat structures found within the input deck. The heat structures representing the CB and the RPV wall have very similar inputs that describe their characteristics. However, the heat structure that covers the top of the reactor takes on a different description. Inputs and descriptions of the various types of heat structures are provided in this subsection.

The first entries for a heat structure fall under the HS_ID card and are the name and number associated with the heat structure. The general heat structure data that is input on the HS_GD card describes the type of geometry as well as the steady state initialization of the heat structure. The heat structure associated with the upper head of the reactor has a TOPHALFSPHERE geometry while all heat structures associated with the CB and the RPV wall are of the cylindrical type. The HS_EOD card refers to the

elevation and orientation data of a heat structure. There is no orientation associated with the upper head heat structure; however, all other heat structures have a vertical orientation. None of the heat structures are considered to have an internal heat source. Therefore, every HS_SRC card has a 'NO' value associated with it. Following the internal heat source card is the HS_ND card which is where the nodalization of the heat structure is input. Values for the nodalization may be found in Appendix C. Following the HS_ND card is the HS_LB card where the left boundary surface data is defined. Such information includes the boundary condition type, the control volume to which the boundary is associated and the mass transfer option. Then, the type of flow associated with the left boundary of the heat structure is input on the HS_LBS record along with the critical pool and atmosphere fractions. The final card describing the left boundary surface is the HS_LBS card which refers to additional data used to describe the surface. The area of the boundary surface is input along with the characteristic length and axial length of the boundary surface. The same features used to describe the left boundary surface are also used to describe the right boundary surface. The last card for every heat structure concerns the film tracking model, which is turned off for all heat structures in this input deck.

The majority of information describing the heat structures present in this MELCOR deck does not require calculations. The only calculations that require explanation are the nodalization for heat structures and the surface area of the boundary of a heat structure. Perhaps it is best to begin with a description of the heat structure linked to the upper head control volume. The heat structure is hemispherical in

geometry since it acts as the dome that covers the top of the reactor vessel. The elevation parameter is listed as 3.0654 meters which is the bottom central location of the hemisphere. Orientation data is not necessary for this type of structure. Because the thickness of the reactor cover is equal to the thickness of the RPV wall, and since the nodalization scheme for a ‘TOPHALFSPHERE’ structure is based on the distance between the inner and outer surfaces of the structure at its right hand side, it has the same nodalization as the heat structure for the RPV wall. Therefore, the first indexed point is located at 3.863 meters, and the second indexed point is located at 4.143 meters. All references to the left boundary layer of this heat structure refer to the inside of the dome, while all references to the right boundary refer to the outside of the dome. The surface area calculation is performed as the surface area of half of a sphere with a radius equal to the radial boundary of the eighth core ring. The eighth core ring is equivalent to the radius of the inner boundary of the RPV wall, which is equal to 3.863 meters, denoted as r_8 .

$$A_{THIS}=(2*\pi*r_8^2) \quad (7.21)$$

All remaining heat structures found within the core are of the cylindrical type and account for the CB and RPV wall. The main difference between the two structures is that the core barrel is nodalized according to the axial levels in the core package while the RPV wall is nodalized according to the control volumes that make up the volume for the downcomer. Furthermore, the core barrel is only 1 in thick, while the RPV wall is 11 in thick. A good example that can be used to illustrate these types of heat structures is the lowest portion of the CB, which has the same axial elevation as the LCP. The heat

structure is cylindrical and is 1 in thick. Therefore, the first indexed point in the HS_ND card is 3.533 meters, which is equivalent to the radius of the third core ring. Because the structure is 1 in (0.254 cm) thick, the second indexed point is 3.5584 meters. Although the left hand boundary requires that a value be input for the upper head, cylindrical geometries do not require an input value. Therefore, a value of 1.0 is selected for all cylindrical heat structures since MELCOR ignores this value.

Finally, it is important to note that the right hand boundaries for both the upper head heat structure and the RPV wall are insulated boundaries. Thus, the HS_RB record for these heat structures has the entry 'SYMMETRY' as opposed to 'CalcCoefHS'. In other words, an insulated boundary condition is applied as opposed to a convective boundary condition where the heat transfer coefficients are calculated by the HS package.

7.2.5 MP Input

This subsection addresses information regarding material property input in the MELCOR input deck. Each material is given a name when the MP_ID card information is listed. Built-in material names already exist in MELCOR. Therefore, when substituting in a new material into the input deck, such as (U,TRU)C for uranium dioxide, the URANIUM-DIOXIDE name is still used even though a different material is used for the fuel. Then, the MP_PRTF card is used to specify the properties that are changed in addition to the names of the data indexes that can be found in the tabular function package, which will be explained in the next subsection. Not all materials listed in the MP package require property substitutions as is seen in Appendix C.

However, some cards do require the MP_PRC card, which allows the user to specify property constant values.

7.2.6 TF Input

While the tabular function package can be used for many different purposes, it is mainly used in this input deck in order to describe the properties in the material package that are being substituted. For example, the enthalpy function being substituted for uranium dioxide is 'ENH-UC'. This function name appears in the TF_ID card which is the first card used to define a tabular function. Then, the TF_TAB card is used in order to show how the enthalpy of the new substance changes as a function of temperature. The same procedure is followed for all materials which have substituted properties that are originally shown in the materials package yet executed in the tabular function package. In other words, the materials package is used in order to declare a function that is being used to substitute property values, and the tabular function package describes the functions originating from the materials package in a tabular format where the property is shown to be dependent upon temperature.

7.2.7 CF Input

Control functions have a wide variety of applications in MELCOR. This subsection discusses some of the control functions used in this input deck. As with the majority of packages already discussed, each control function requires a name and numerical identifier. The CF_ID card is reserved for these two quantities, as well as the type of control function being specified. The control function type specifies how the function is being used. In other words, if a variable is being set equal to a constant

value, then the function is set to the 'EQUALS' type. On the other hand, if there is a division being performed by the control function, then the control function type is 'DIVIDE'. Many other control function types exist; however, these two are mentioned since they are used in the control function package for this input deck. The next control function card is the CF_SAI card which defines the multiplicative and additive scaling constants, as well as an initial value. Finally, the CF_ARG card is used in order to identify equations that are used in order to define how the control function is operating.

Although the control functions can be used in order to create formulas where certain variables are constantly changing according to a specific formula, the majority of control functions used in this input deck are used in order to hold certain properties constant. For example, the first control function mentioned is a function that controls the reactor power level. Because the reactor power remains constant throughout the entire steady state calculation, the control function is of the 'EQUALS' type, and the value of the control function is set, using the CF_SAI and CF_ARG cards, to 2400MWt. Only one control function is classified as being of the 'DIVIDE' type. The control function for the helium velocity is solved by first setting the first argument to obtain the helium density from the highest control volume associated with the left boundary of the heat structure representing the RPV wall and multiplying it by the flow area of that control volume. Then, the second argument consists of calling upon the control function defining the core mass flow rate. Because the control function is of the 'DIVIDE' type, execution of the control function consists of dividing the second argument by the first argument. This is the only true calculation contained in the control function package.

7.2.8 NCG Input

While the noncondensable gas package can be used to identify various properties of different gases, it is only used in this input deck to identify gases that must be identified for the purpose of executing this input deck. Therefore, only the NCG_ID card is used in order to identify the different gases that must be identified in order to allow the input deck to run.

7.3 Results

After successful execution of the MELCOR input deck, pertinent results are plotted. In the following subsections, results regarding pressure drop, temperature change, and core structure temperatures are plotted and discussed. Other important results are shown as well. The results chosen for listing and explanation are chosen because it is felt that they provide the best insight into GFR design aspects. Key thermal hydraulic data for the GFR is listed in Table 7.1. Although some of the data is input, as opposed to values obtained from MELCOR output, all of the data is needed in order to obtain a fundamental understanding of the thermal hydraulic characteristics of the US DOE GFR modeled in MELCOR.

Table 7.1: Key Thermal Hydraulic Data

Parameter	Value
Thermal Power (MWt)	2400
Power Density (MW/m ³)	100
Mass Flow Rate (kg/s)	3022.5
Inlet Coolant Temperature (K)	763.15
Outlet Coolant Temperature (K)	1123.15
Maximum Fuel Temperature (K)	2041.85
Maximum Clad Temperature (K)	1599.85

7.3.1 Coolant Pressure Drop

As seen in Figure 7.3, the core pressure drop is set due to conditions imposed upon the source and sink control volumes. The source control volume, from where the helium coolant originates, is set to 7.24 MPa, and the sink control volume, represented by the upper head, is set to 7.07 MPa. These values are taken from original design criteria for the 2400MWt GFR, where 7.24 MPa represents the pressure of the fluid leaving the compressor, and 7.07 MPa represents the pressure at the inlet to the upper plenum. In addition to the source and sink pressure, the cavity pressure is listed as well

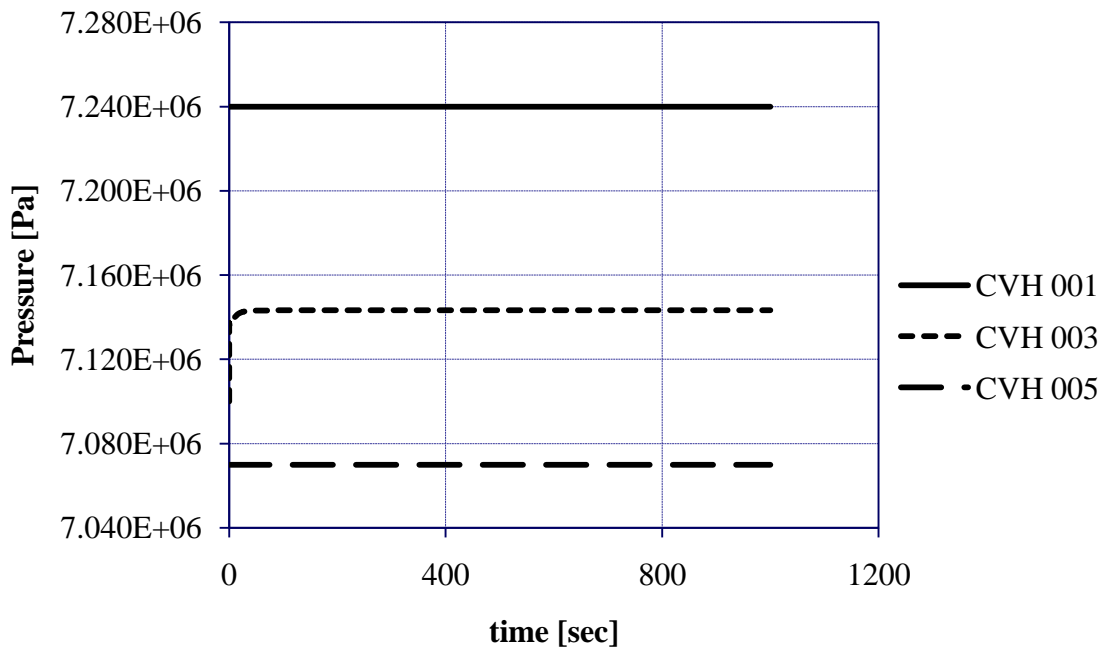


Figure 7.3: Pressure Drop Along Core

in order so that the reader may identify the pressure drop between the core inlet and the upper plenum. This is also considered the pressure drop along the core.

Although the overall core pressure drop is set, pressure still varies between different axial levels and radial rings due to varying degrees of heating and friction in different quadrants of the reactor. Figure 7.4 displays the pressure drop through the channel control volumes associated with the first core radial ring. Pressure drop is taken into account beginning at the bottom of the fuel rod at the elevation of the lower plenum of the fuel rod, continues through the middle elevation of the active fuel, and ends at the axial elevation of the upper rod plenum. The same axial elevations apply to Figures 7.5

and 7.6; however, these results are taken from control volumes present in the fifth and seventh radial core rings, respectively. Figures 7.7, 7.8 and 7.9 also occur at the same

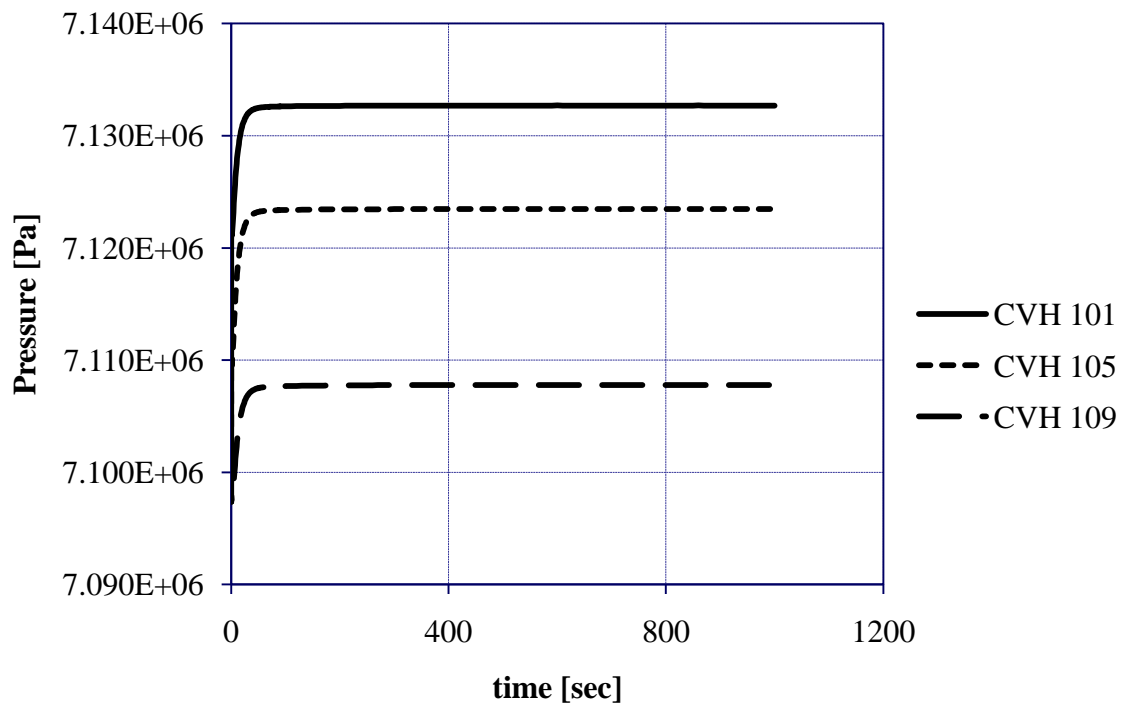


Figure 7.4: Pressure Drop Through Channel Side of Ring 1

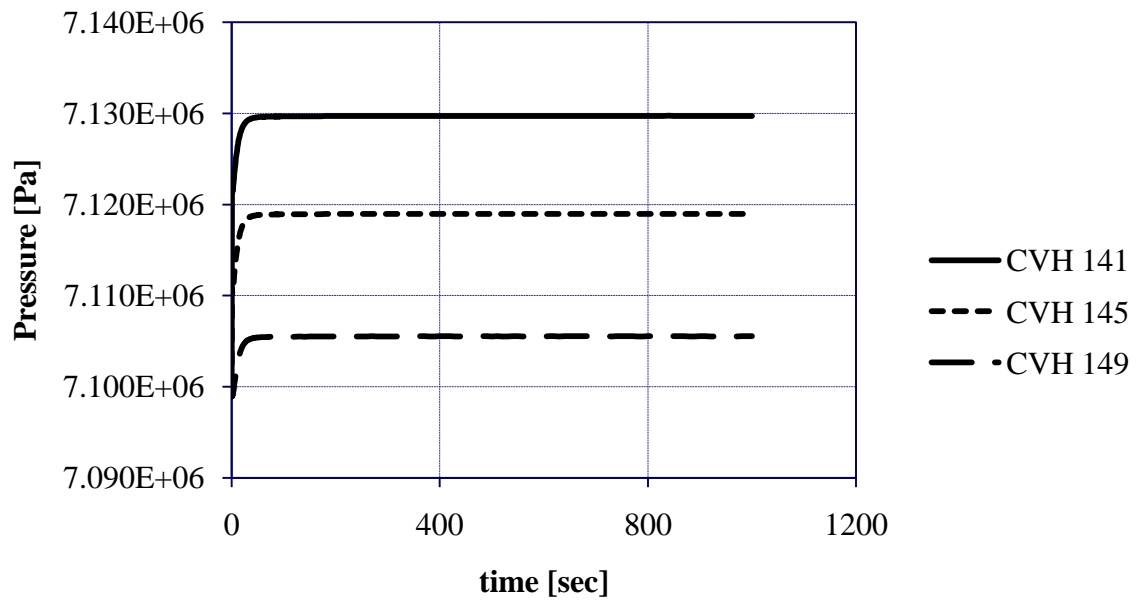


Figure 7.5: Pressure Drop Through Channel Side of Ring 5

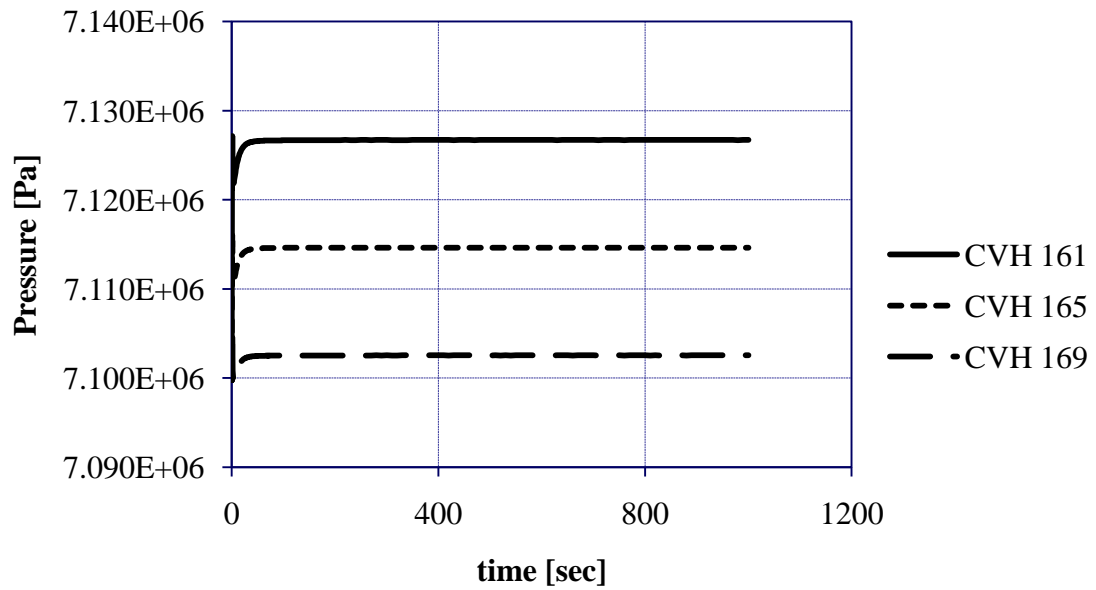


Figure 7.6: Pressure Drop Through Channel Side of Ring 7

elevations; however, these figures are representative of bypass control volumes associated with the control volumes shown in figures 7.3, 7.4 and 7.5.

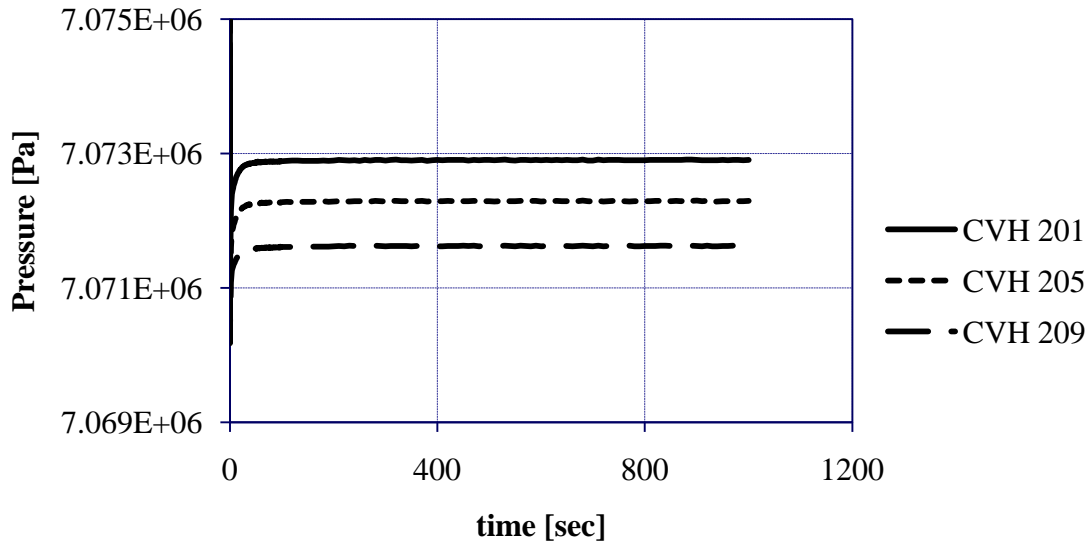


Figure 7.7: Pressure Drop Through Bypass Side of Ring 1

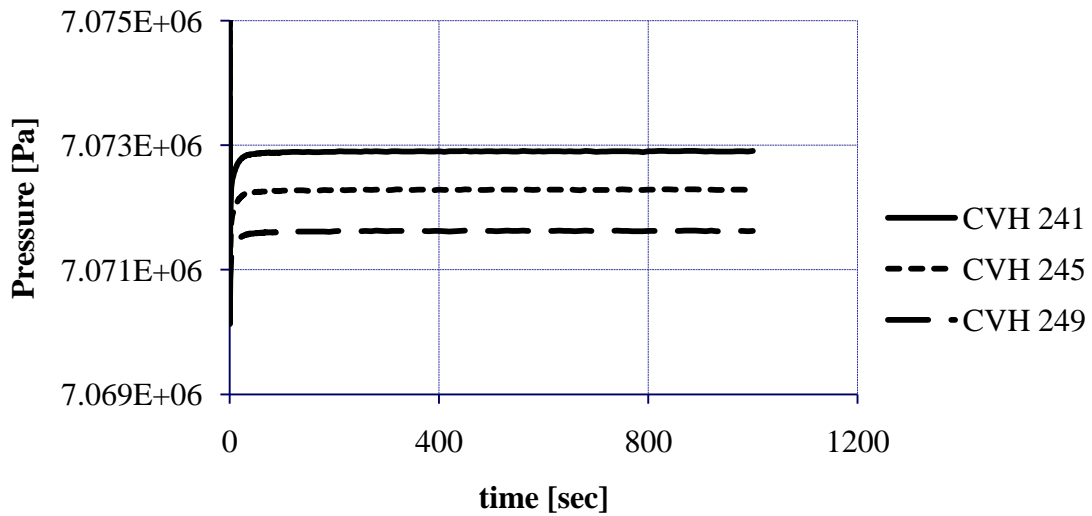


Figure 7.8: Pressure Drop Through Bypass Side of Ring 5

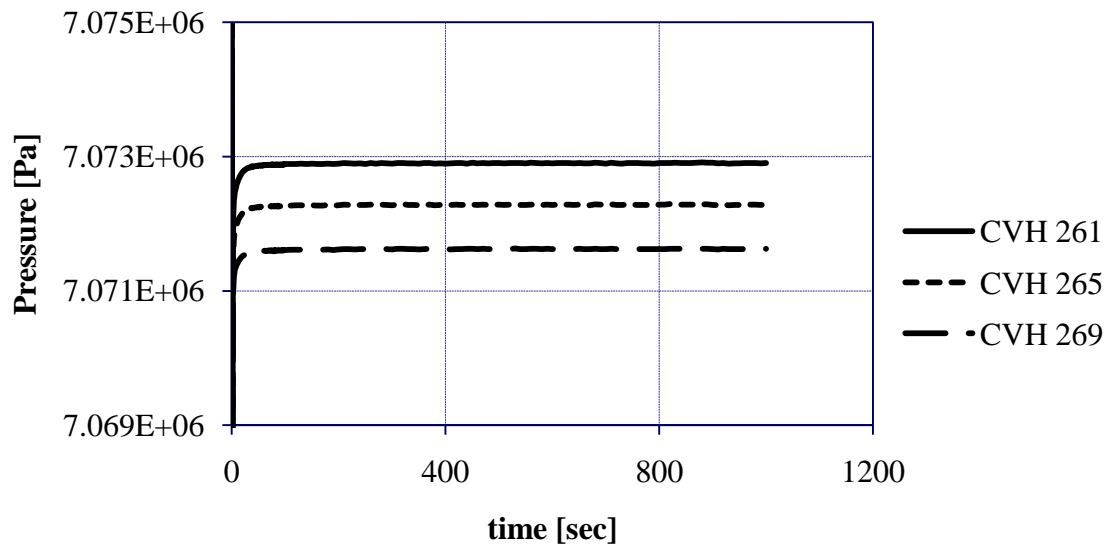


Figure 7.9: Pressure Drop Through Bypass Side of Ring 7

Also of importance is the difference in pressure between different radial rings in the core. Figure 7.10 shows how pressure changes in the radial direction of the core in various channel side control volumes. Each control volume has the same axial location, which is at the middle elevation of the active core. Radial changes in pressure for the bypass control volumes associated with the channel control volumes shown in Figure 7.10 are not shown since they do not change very much with respect to the outward radial direction of the core.

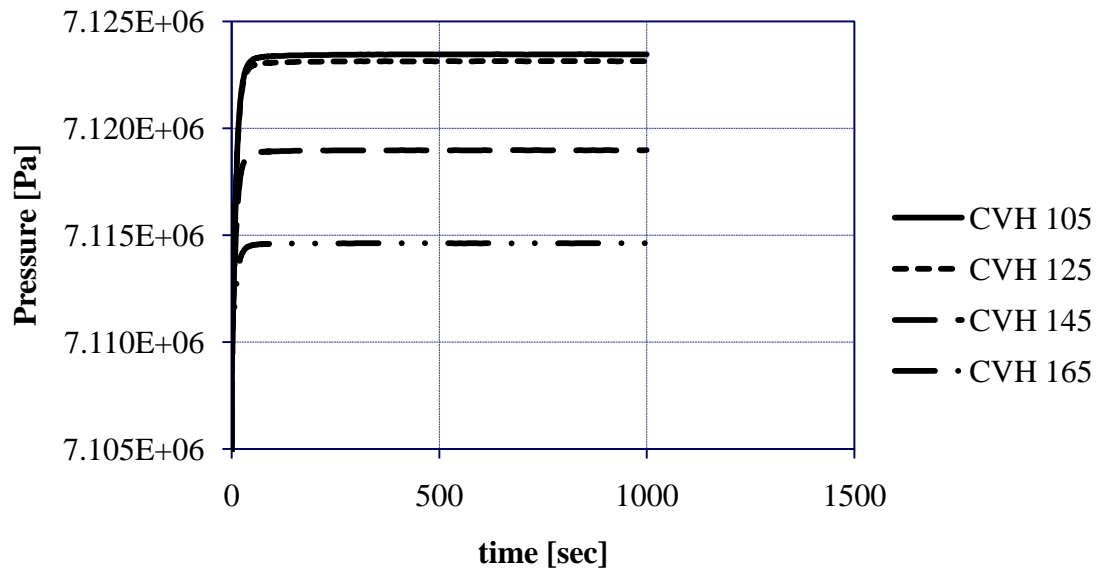


Figure 7.10: Channel Pressure Drop Across Core in Radial Direction

As expected, pressure drops across the core, as well as pressure differences in the radial direction, are relatively small. Small pressure drops are expected since the active core region is relatively short. Furthermore, SiC is a relatively smooth material. Therefore, additional pressure loss caused by friction losses is mitigated by a smooth SiC cladding and canning material [21]. In addition, because there are no expansions, contractions, or bends seen along the length of the entire fuel rod region, form losses do not contribute to pressure drop. Spacer grids and mixing vane grids are not taken into account, so the effect of form losses may be underestimated. However, for the purposes of this thesis, form losses are not of major concern.

7.3.2 Coolant Temperature Changes

Serving as the cornerstone behind any reactor design is the intention to transfer thermal energy to the reactor's coolant in order to ultimately produce useful energy. This subsection addresses changes in the coolant temperature at various locations in the active core. Figures 7.11, 7.12 and 7.13 display how the coolant temperature changes along the length of the channel side of the first, fifth and seventh radial rings, respectively. Furthermore, Figures 7.14, 7.15 and 7.16 provide the reader with temperature profiles for the coolant found in the bypass control volumes associated with the channel control volumes in Figures 7.11, 7.12 and 7.13, respectively. Figure 7.17 shows how the temperature changes at the central axial location of the active core across the radial rings found within the entire core. Finally, Figure 7.18 shows how the bypass control volumes associated with the channel control volumes in Figure 7.17 experience coolant temperature changes. While variations in bypass coolant temperature are not as drastic as those observed for channel coolant temperatures, they are still important for the purposes of this thesis.

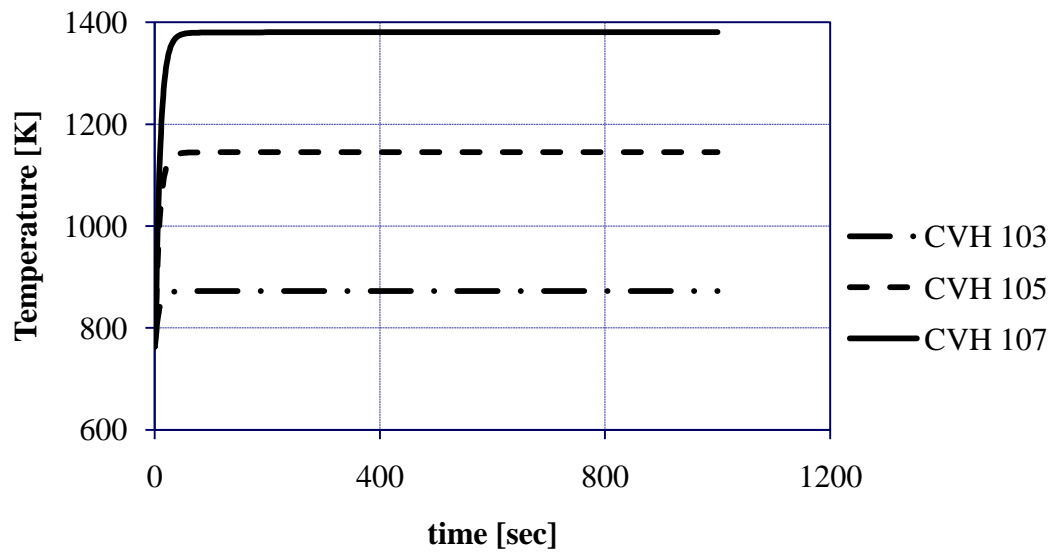


Figure 7.11: Coolant Temperature Rise on Channel Side of Ring 1

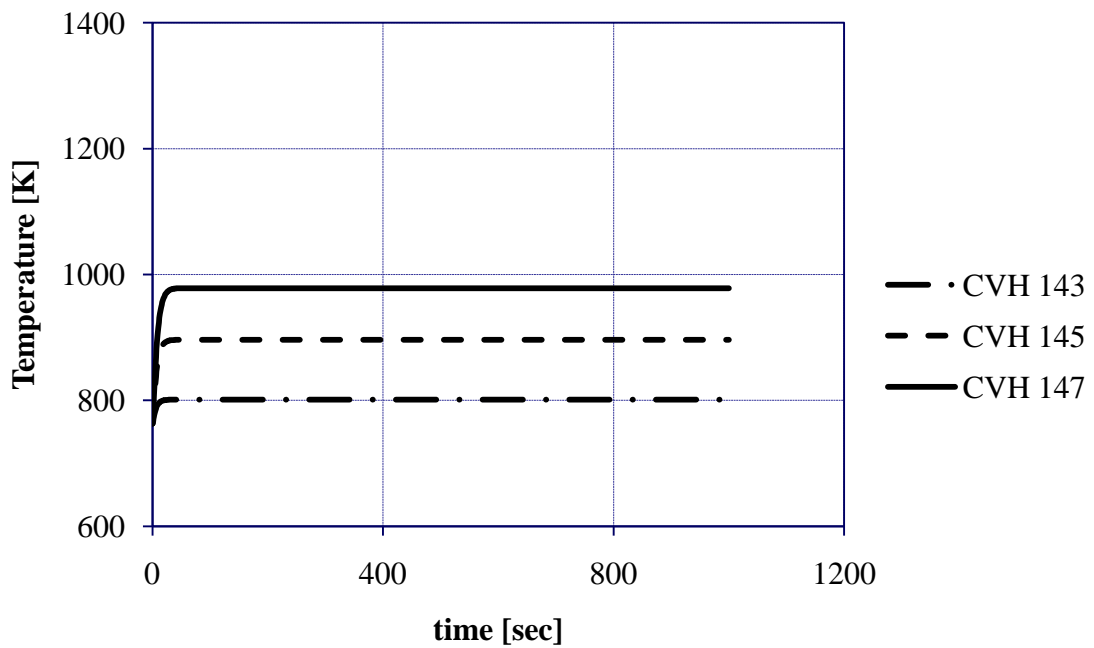


Figure 7.12: Coolant Temperature Rise on Channel Side of Ring 5

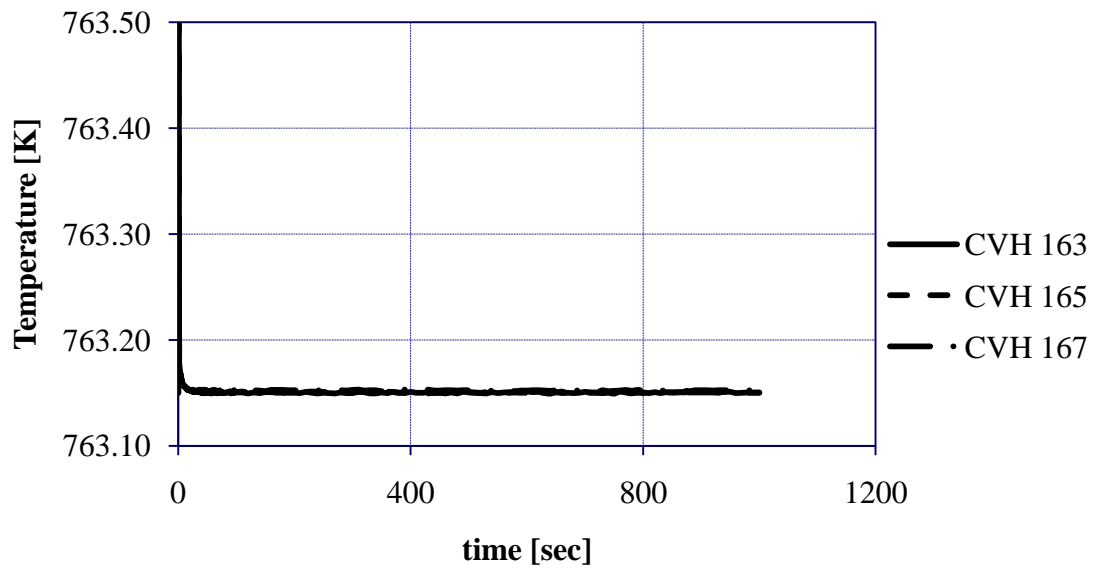


Figure 7.13: Coolant Temperature Rise on Channel Side of Ring 7

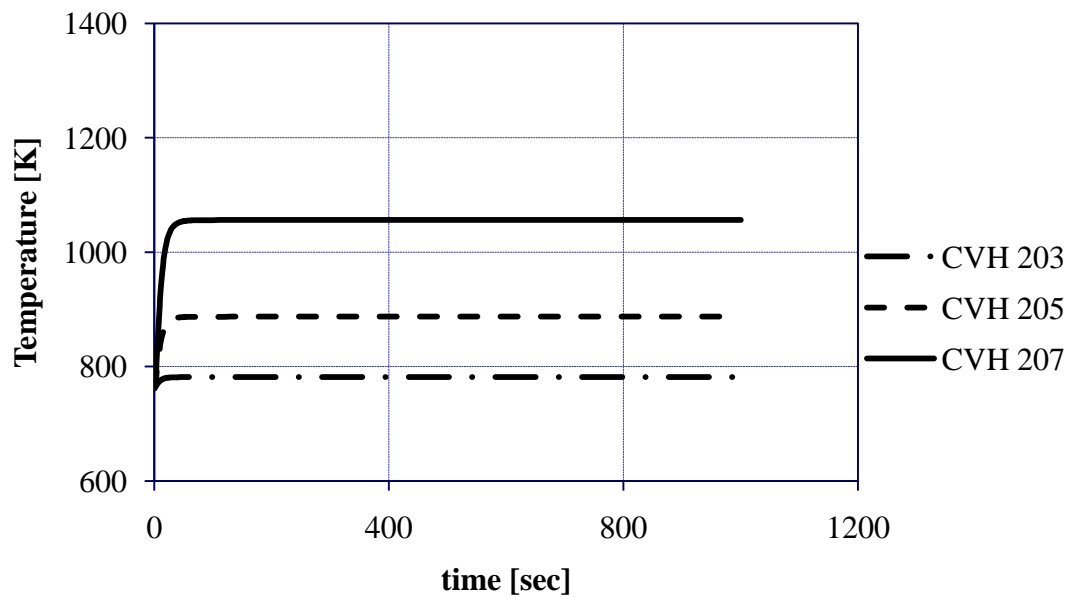


Figure 7.14: Coolant Temperature Rise on Bypass Side of Ring 1

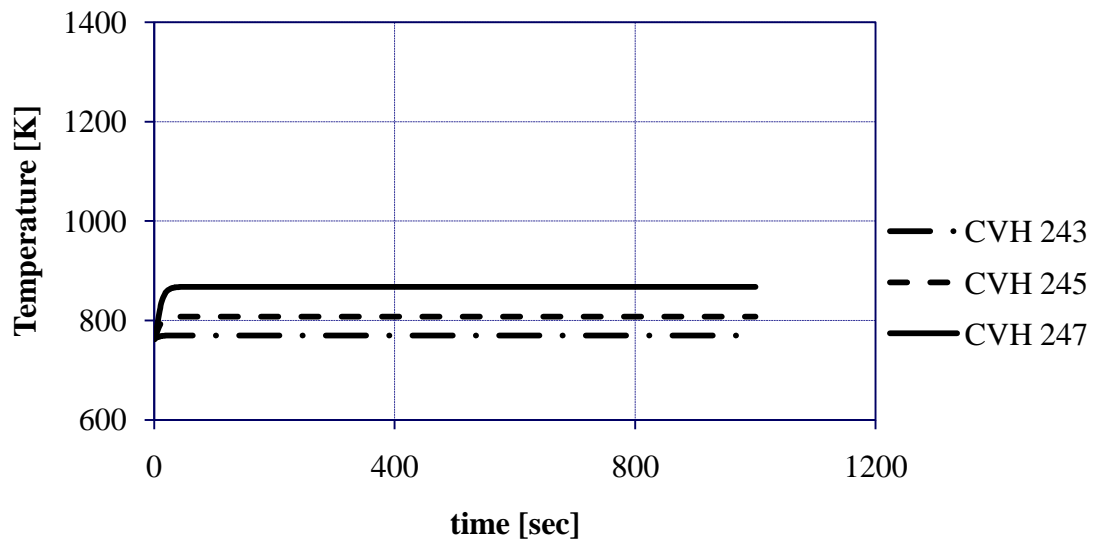


Figure 7.15: Coolant Temperature Rise on Bypass Side of Ring 5

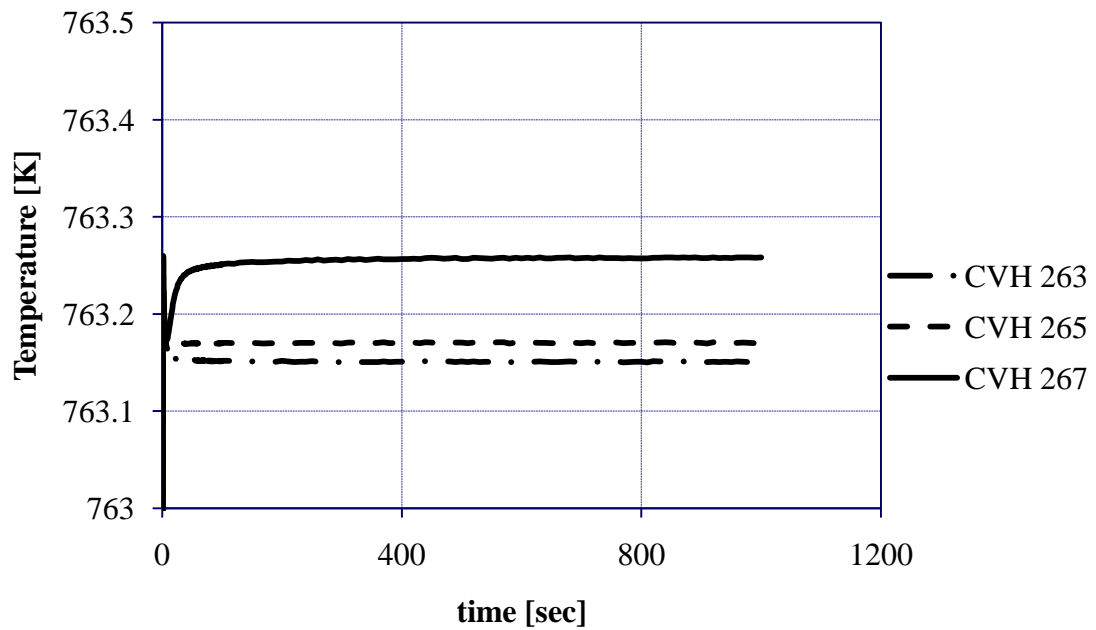


Figure 7.16: Coolant Temperature Rise on Bypass Side of Ring 7

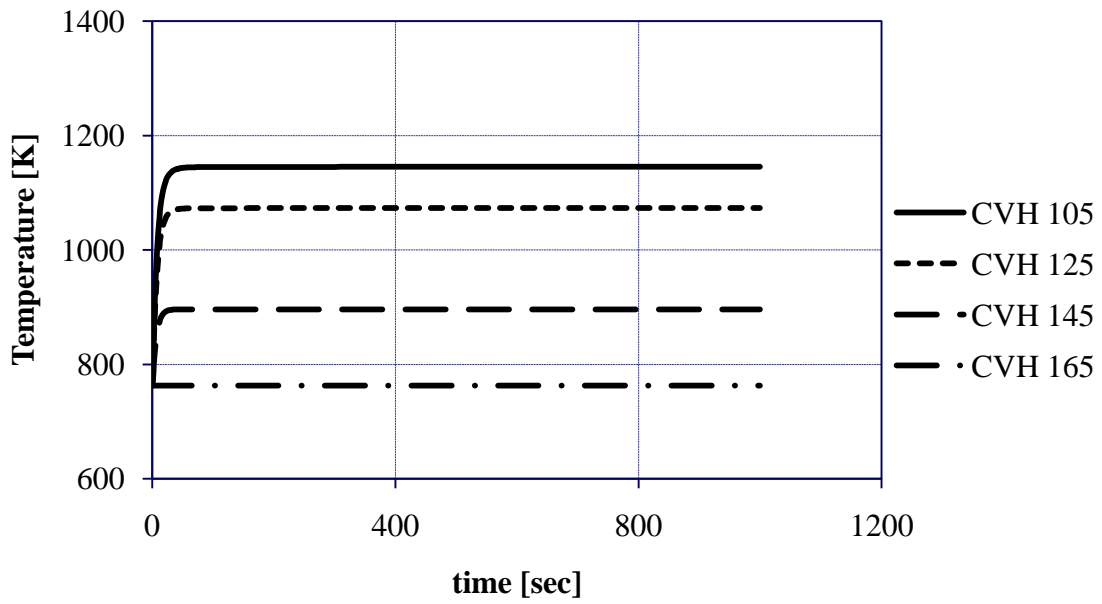


Figure 7.17: Channel Temperature Difference Observed in Radial Direction

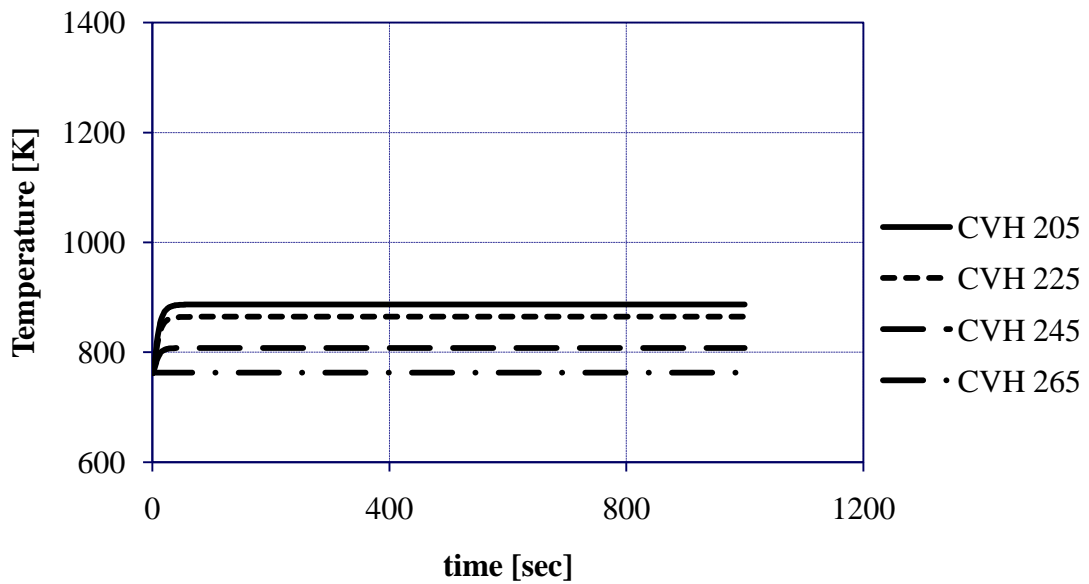


Figure 7.18: Bypass Temperature Difference Observed in Radial Direction

Results observed in Figures 7.11 and 7.12 seem correct considering that the coolant temperature should rise as it gains thermal energy from the fuel while traveling up the length of the active core. Figure 7.13 shows that very little energy is gained from the borated shield rods. This is plausible as well considering that there is no power produced by these rods. The same idea applies to the reflector rods. However, results for the reflector rods are not shown due to their similarity to the results concerning the outer borated shield region. Figures 7.14 and 7.15 show that the bypass coolant temperature also rises along the length of the core in the active fuel region. Interestingly, the bypass coolant temperature in the seventh ring increases slightly. This is most likely due to horizontal flow between assemblies, where some of the bypass flow originating from the center of the core finds its way to the periphery of the core. Furthermore, observations of Figures 7.17 and 7.18 indicate that the coolant temperature decreases as radial distance from the center of the core increases. This also seems correct considering that power drops as distance from the center of the core increases. Temperature profiles will become important during the discussion of the thermionic characteristics of a possible decay heat removal system.

7.3.3 Coolant Velocity Observations

As the coolant moves through various regions of the reactor core, it experiences changes in velocity due to various events such as coolant path expansions and contractions. Furthermore, the velocity may change as a result of changes of direction in the flow. Coolant flow over core structures also induces a certain amount of friction which impedes the flow and also causes changes in coolant velocity [21]. Temperature

changes along the length of the core induce changes in coolant characteristics which also alters flow velocity. Pressure changes observed along the length of the core also vary the coolant velocity. All of these events are observed in the GFR reactor core. Figures 7.19, 7.20 and 7.21 show changes in coolant velocity along the length of the flow paths connecting control volumes on the channel side of the first, fifth and seventh radial rings, respectively. These flow paths are at, approximately, the same elevations used in Subsection 7.3.1. Figures 7.22, 7.23 and 7.24 show velocity changes within the flow paths connecting the bypass control volumes associated with the channel control volumes being connected. Figures 7.25 and 7.26 show how the flow velocity changes in the channel and bypass control volumes, respectively, with respect to radial distance from the center of the core.

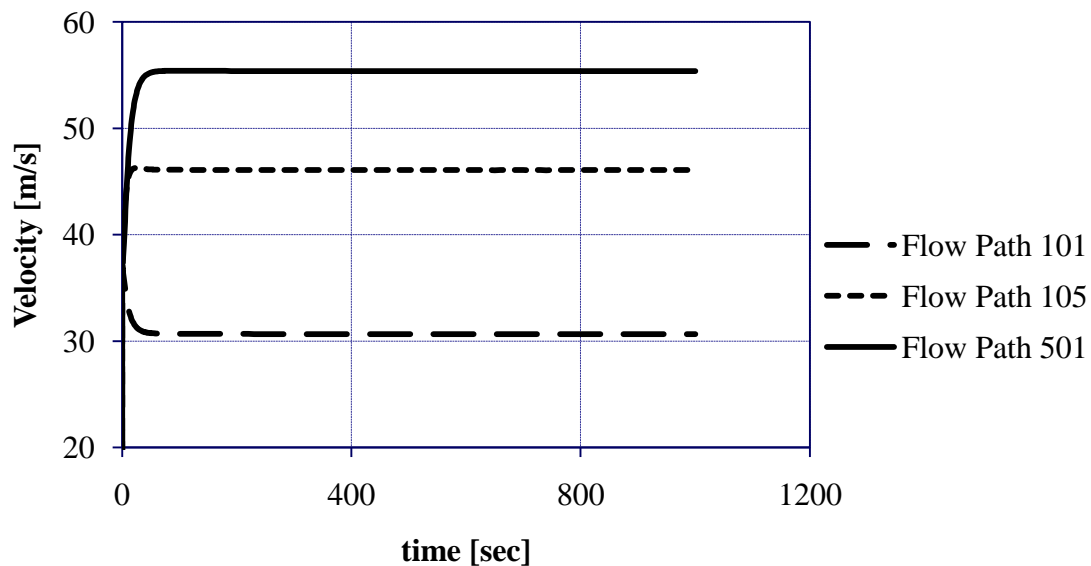


Figure 7.19: Coolant Velocity Through Channel Side of Ring 1

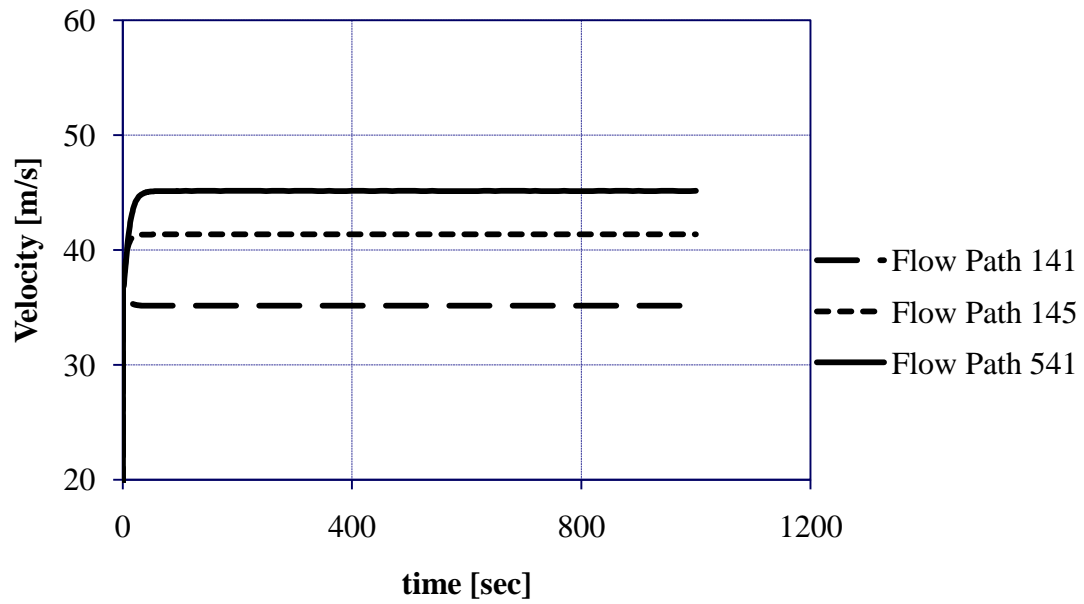


Figure 7.20: Coolant Velocity Through Channel Side of Ring 5

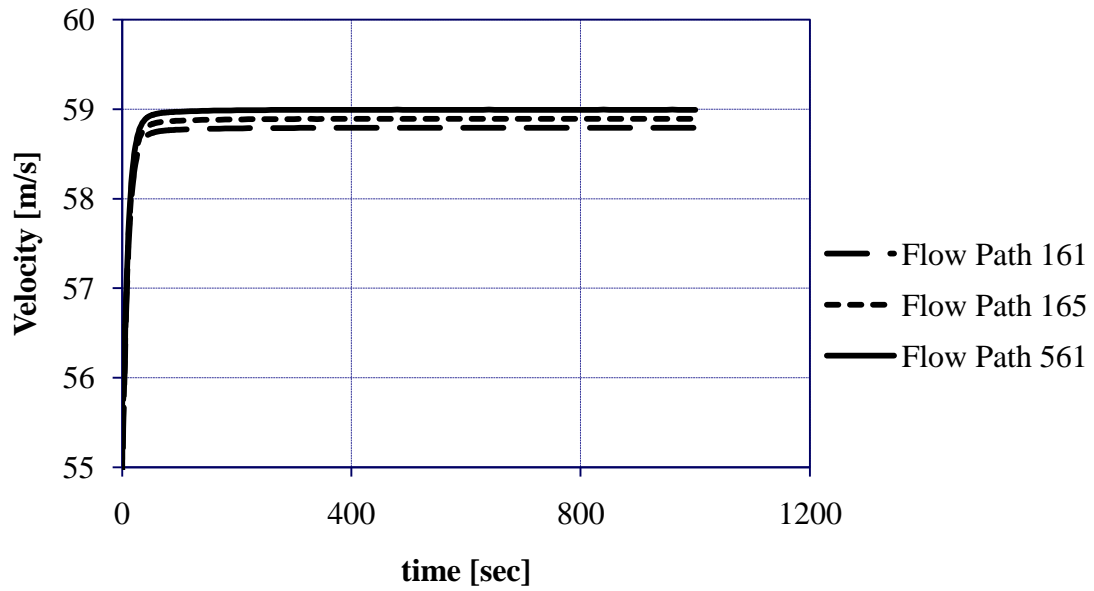


Figure 7.21: Coolant Velocity Through Channel Side of Ring 7

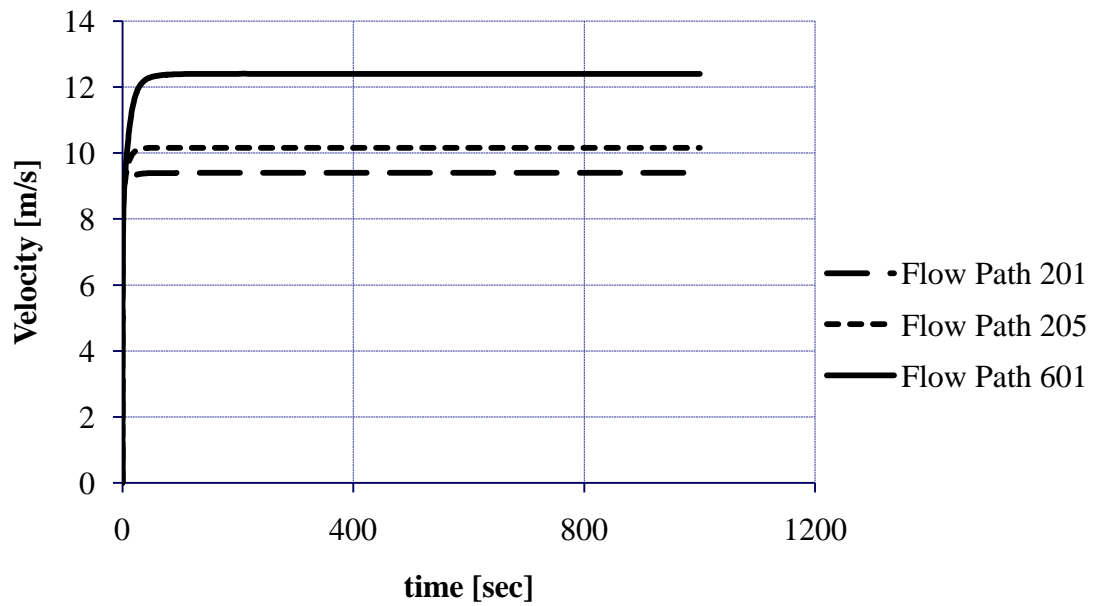


Figure 7.22: Coolant Velocity Through Bypass Side of Ring 1

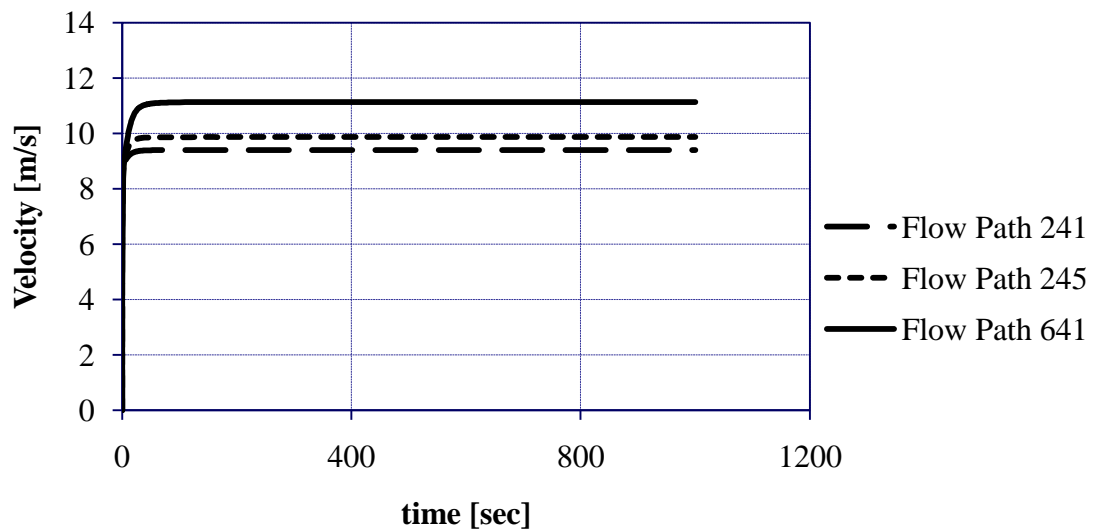


Figure 7.23: Coolant Velocity Through Bypass Side of Ring 5

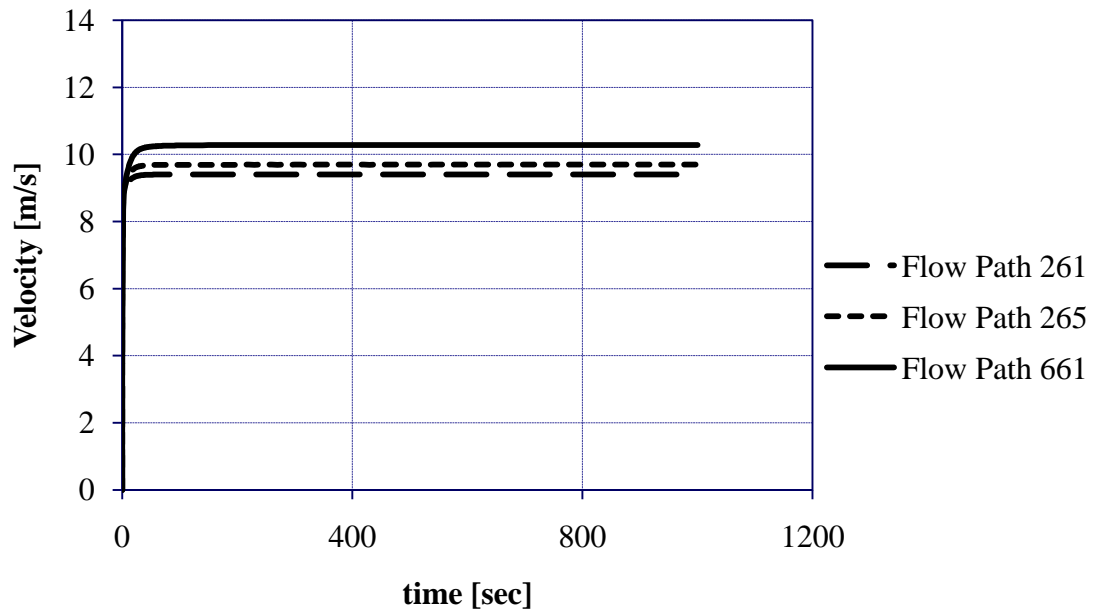


Figure 7.24: Coolant Velocity Through Bypass Side of Ring 7

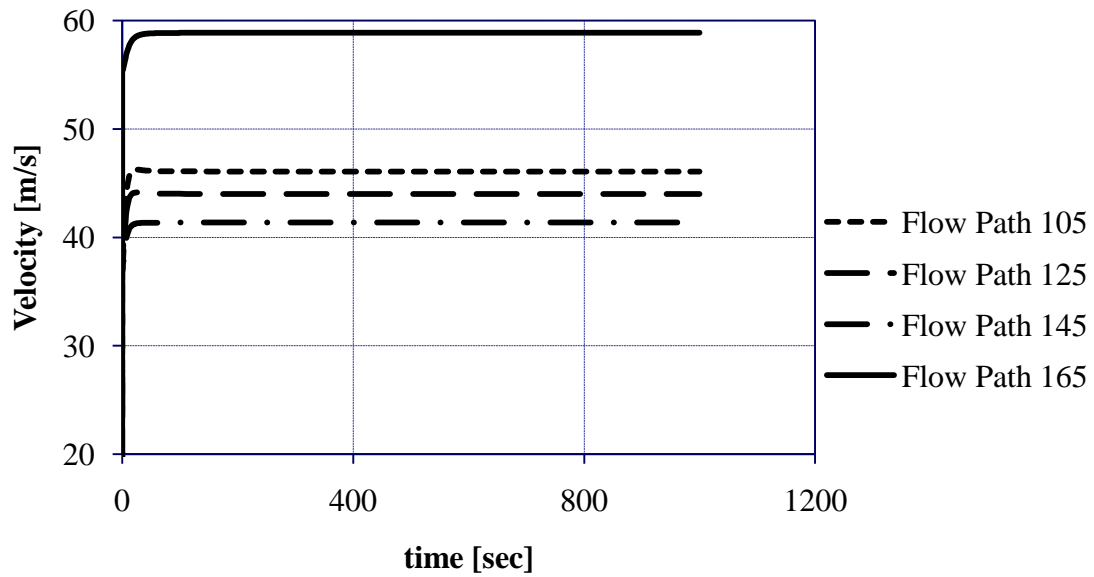


Figure 7.25: Channel Coolant Velocity Variations with Radial Direction

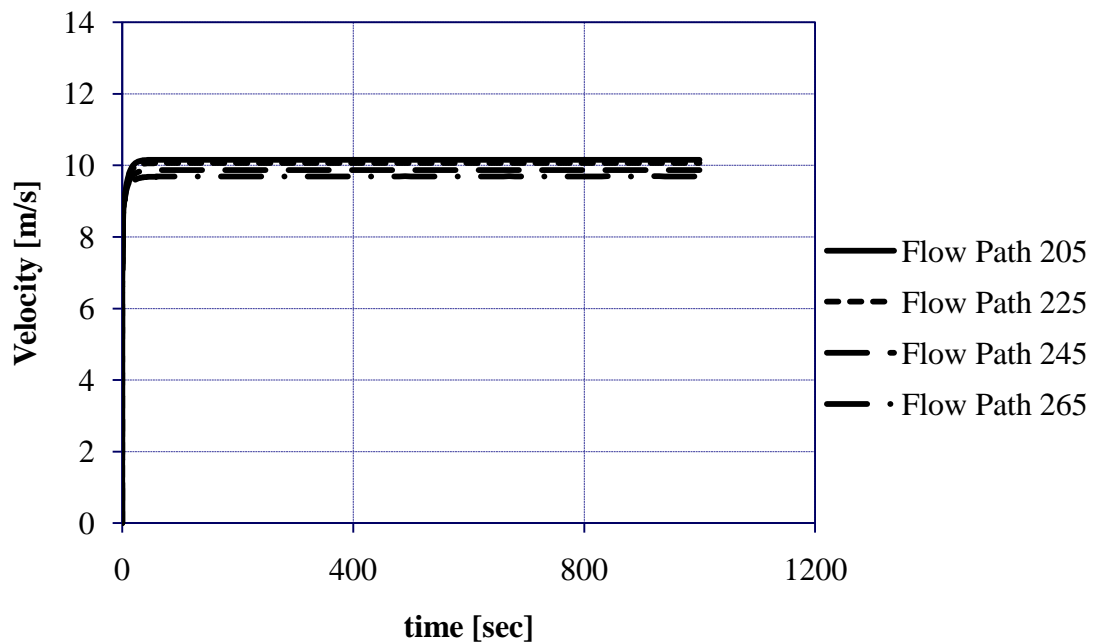


Figure 7.26: Bypass Coolant Velocity Variations in Radial Direction

Also of some concern is the bypass flow in the horizontal direction. The magnitude of the velocity of the horizontal bypass flow is small relative to vertical bypass flow; however, it is still worth assessment. Figure 7.27 shows how velocity in the horizontal direction changes along with location of the flow path along the height of the core. As one can see from Figure 7.27, the horizontal velocity is at a maximum between the first and second rings when it is at the middle elevation of the active core. Figure 7.28 presents flow in the horizontal direction between rings 5 and 6. Once again, horizontal coolant flow is at a maximum at the middle elevation of the core.

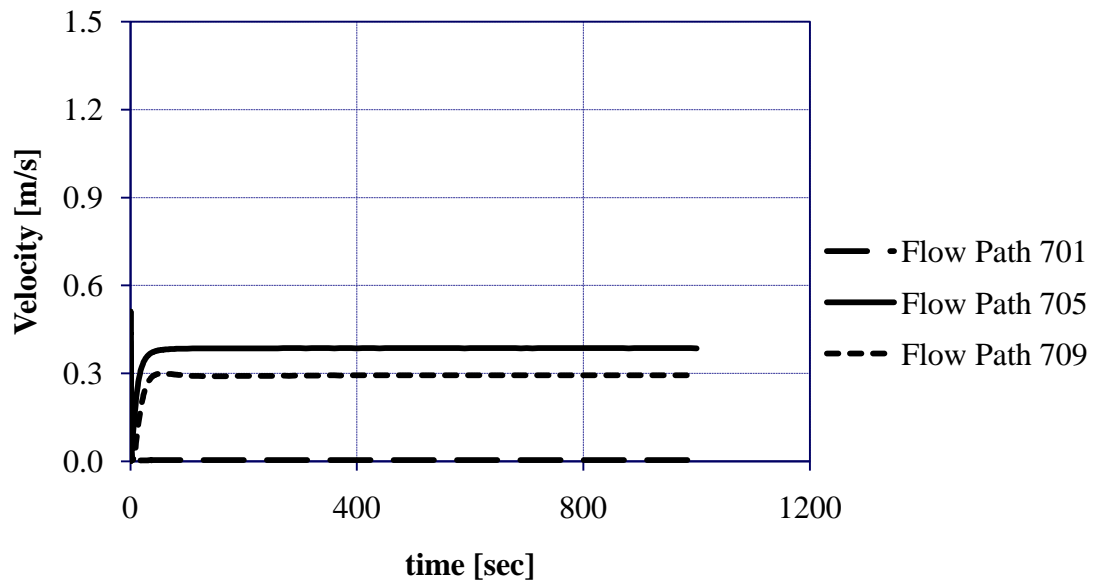


Figure 7.27: Velocity in Horizontal Flow Paths Between Ring 1 and Ring 2

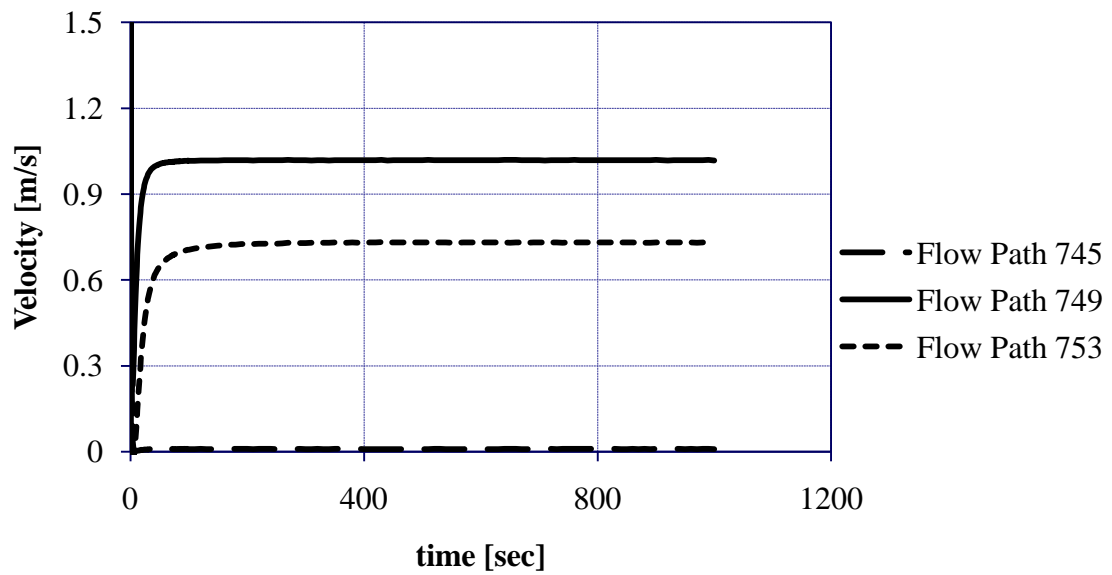


Figure 7.28: Velocity in Horizontal Flow Paths Between Ring 5 and Ring 6

Many important points can be made regarding the figures in this subsection. Thermal energy is absorbed by the gas as it encounters the fuel region. As the gas absorbs thermal energy, it expands and becomes less dense. This helps to accelerate the fluid along the length of the core. This effect can be observed in Figures 7.19 and 7.20, as well as in Figures 7.22 and 7.23. However, this effect is not seen in Figure 7.21 since the borated shield rods do not serve as a heat source. Although there is no fission power present in the outer borated shield region, the reader may observe that Figure 7.24 shows an increase in bypass coolant velocity higher along the core in ring 7. This may be due to heating effects from the bypass flow originating in the center of the core and making its way to the edge of the core. Hotter bypass gas originating from the center of core may be causing bypass gas density in ring 7 to go down, thus accelerating the gas. According to Figure 7.26, vertical bypass flow velocity decreases with increasing radial distance from the center of the core. However, the difference in bypass flow velocity between the center and edge of the core is quite small and may be considered negligible. Figures 7.27 and 7.28 show that differences between horizontal coolant velocities at different elevations are also very small. Perhaps the horizontal coolant velocity is greatest at the middle axial elevation due to greater heat delivery rates to the coolant at that elevation relative to other elevations. Greater heat delivery rates can cause the coolant to expand at a higher rate, thus accelerating the fluid in the horizontal direction.

In the previous paragraph, Figure 7.25 is not mentioned on purpose. Perhaps one of the more interesting observable phenomena throughout this thesis is observed in this figure, and it requires some attention. The reader can notice that the vertical channel

coolant velocity decreases with increasing radial distance from the core except in ring 7. This spike in channel velocity is also observed in ring 6; however, since the coolant velocity in this ring so closely resembles that of the coolant velocity in ring 7, it is not shown. Looking at Figure 7.29, one can observe that coolant velocity in ring 7 is accelerated to a much a greater degree than the coolant velocity in ring 1. The coolant velocity in ring 7 remains, approximately, the same value the rest of length of the core,

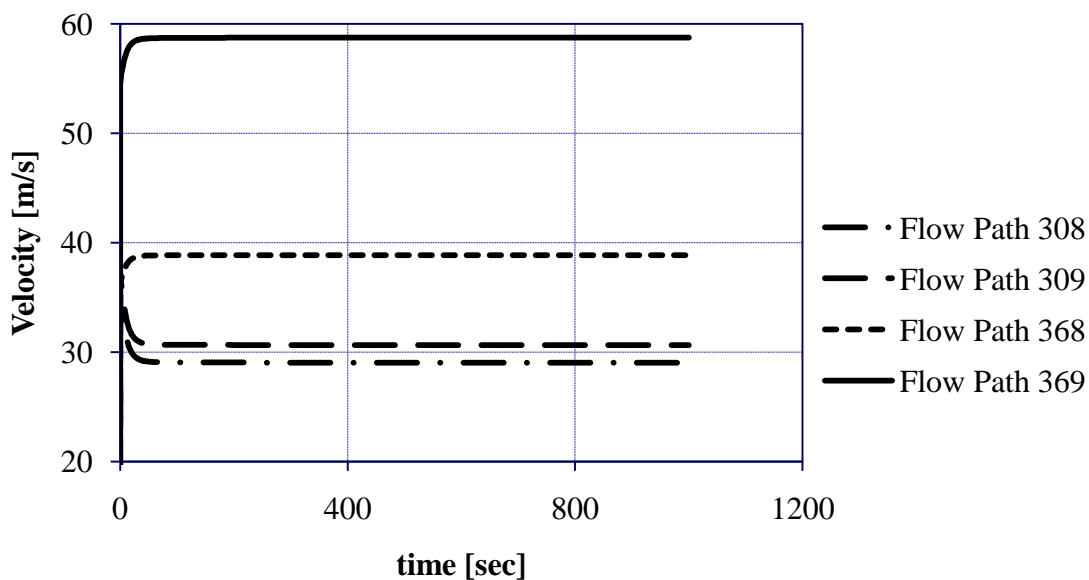


Figure 7.29: Flow Acceleration Through Channel Side of Bottom of Rings 1 and 7

while the coolant velocity in ring 1 increases to, approximately, 45 m/s once it reaches the middle of the core, as is shown in Figure 7.25. As observed in Figure 7.19, the coolant velocity on the channel side of ring 1 does not reach a value comparable to the channel coolant velocity in ring 7 until the top of the channel. Even then, the velocity is

only slightly over 55 m/s, while the coolant velocity on the channel side of ring 7 is constantly around 58 m/s. Thus, one can observe that heating of the gas has a significant impact on increasing its velocity. However, this still begs the question why the velocity in ring 7 is so much higher even though the gas in that channel is receiving much less heat than the gas in ring 1. The effect causing this is explained in the following paragraph.

Although all form loss coefficients in the LCP are taken to be the default values present in MELCOR, which may be inaccurate, the point is that they are all the same. Thus, when treating expansions and contractions, they are all treated similarly. The amount of contraction flow contraction between the LCP and the LBS in ring 1 is less than the amount of contraction observed in the LCP and LBS in ring 7. Support of this argument is evidenced by the fact that the flow area in ring 1 contracts from 0.6548 m^2 to 0.3240 m^2 , while the flow area in ring 7 contracts from 12.190 m^2 to 4.214 m^2 . The ratio of the larger area to the smaller area in ring 1 is 2.021, while the same ratio is 2.893 in ring 7. Thus, one can observe how there is much more contraction, and thus much more acceleration occurring in ring 7 relative to ring 1.

Another interesting phenomena affecting the flow velocity is viscosity variation along the length of the channel. This effect does not have a great deal of impact on the reflector and borated shield regions of rings 6 and 7, respectively, since not a great deal of heat is transferred to the coolant in those regions. However, this effect has the ability to impede flow in the active core. MELCOR uses the Lennard-Jones parameters, presented in equation 7.22, in order to determine the viscosity of a low density gas [2].

In equation 7.22, M is the molecular weight of the gas, T is the temperature, σ is the collision diameter, and Ω_μ is the collision integral for viscosity [22]. σ and Ω_μ can be found in tables. Because the viscosity of the gas increases with increasing temperature, the viscosity of the He towards the center of the core is much higher than the viscosity of

$$\mu = \left(2.6692 \cdot 10^{-5}\right) \frac{\sqrt{MT}}{\sigma^2 \Omega_\mu} \quad (7.22)$$

the He at the edge of the core. Thus, while the velocity of the gas at the center of the core is increasing, the fluid must overcome a greater deal of resistance due to the fact that higher viscosity creates more friction. Overall, it is important for the reader to understand that while thermal energy transferred from the fuel to the coolant works to decrease the density of the gas, thereby accelerating it; resistance to flow is still present due to increasing viscosity.

7.3.4 Fuel Temperature Results

Driving the production of thermal energy in the active core, nuclear fission taking place in the fuel causes fuel temperatures to increase. It is important to understand the fuel temperature profile throughout the active core for multiple reasons. Attention must be paid to fuel temperature in order to make sure that it does not reach its melting point. Furthermore, knowledge of the fuel temperature profile lends insight into how much thermal energy is being transferred to the cladding and gas during operation. In addition, knowledge of the fuel temperature profile may provide further insight into possible ideas towards a decay heat removal system based on thermionic principles. This will be discussed further in the next section.

Figures 7.30 and 7.31 show how the fuel temperature varies in the axial direction within rings 1 and 5, respectively. Figure 7.32 is a display of how the fuel temperature decreases with increasing distance from the core in the radial outward direction. Values displayed in Figure 7.32 are at the middle axial elevation of the fuel and include data from rings 1, 3 and 5.

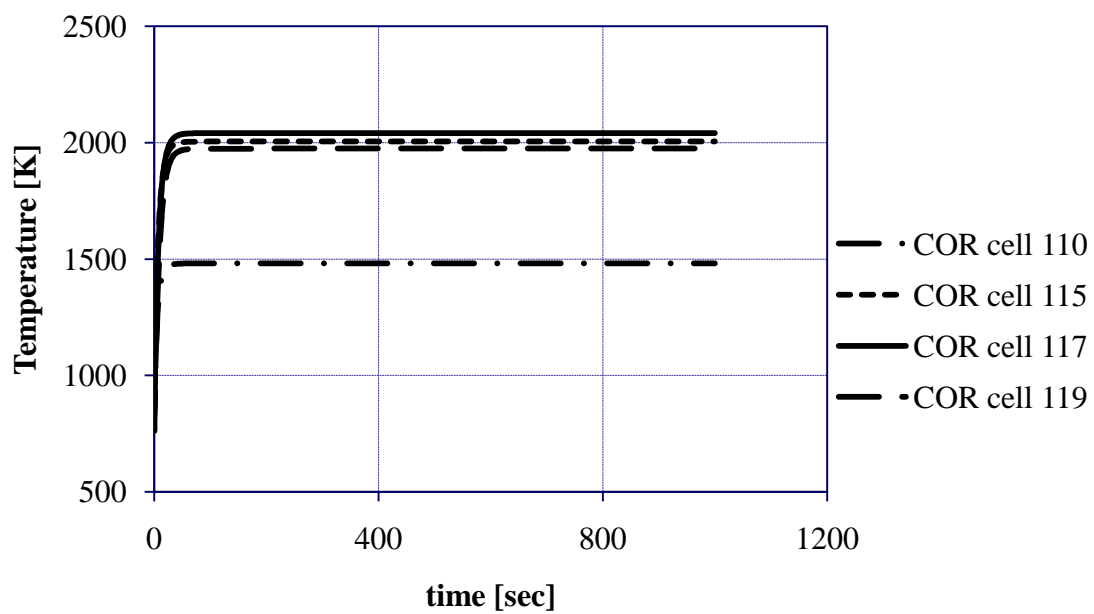


Figure 7.30: Axial Fuel Temperature Variation in Ring 1

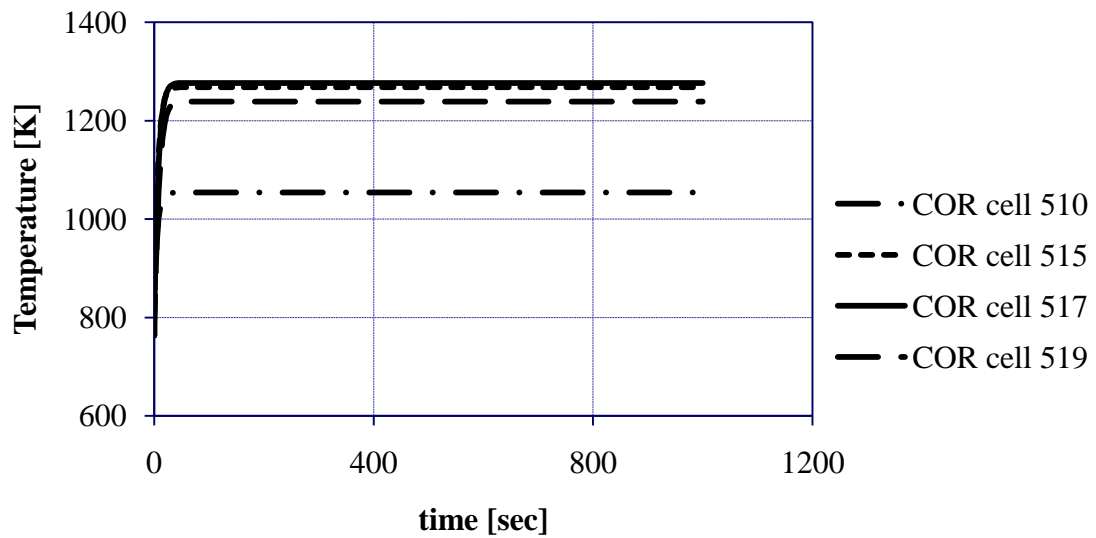


Figure 7.31: Axial Fuel Temperature Variation in Ring 5

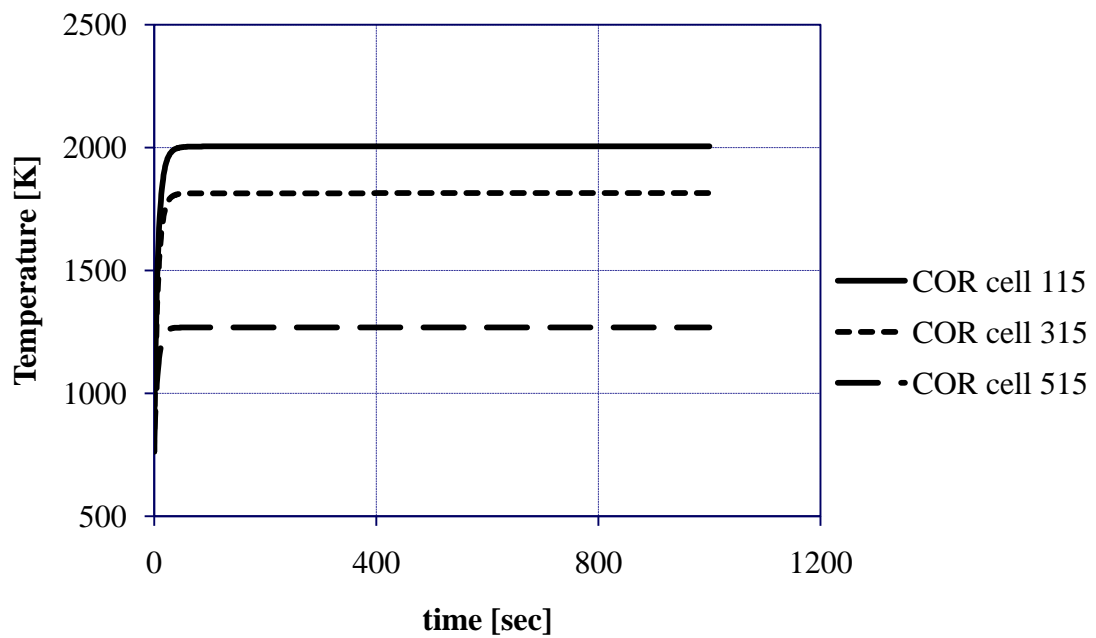


Figure 7.32: Radial Fuel Temperature Variation Across Active Core

Upon observation of Figures 7.30 and 7.31, one can notice that the fuel temperature rises along the length of the active core, as expected. However, upon further observation, one can notice that the fuel temperature is at its highest value above the center of the active core. This, initially, seems strange since power peaks at the center of the core, which should cause the highest temperature to be at the central axial elevation of the active core as well. Two possible explanations may describe why this particular phenomenon is observed. First, axial conduction may cause heat to be transferred axially along the length of the active fuel. Second, He gas has a relatively low volume-specific heat capacity, as do most gases. Volume-specific heat capacity is a measure of how much thermal energy a substance can store. Furthermore, this quantity is a product of density and specific heat capacity [23]. Within the reactor core, the specific heat capacity of the helium does not change very much. However, the density is constantly decreasing as more heat is transferred to the He coolant. Therefore, as the coolant rises along the length of the core, it becomes harder for it to store thermal energy. Thus, more heat remains stored in various regions of the fuel pin, whether it is the fuel or the cladding. More heat may also be stored within the canister walls. Perhaps this better explains why the fuel is hotter above the active core. Less heat is able to be transferred away from the fuel since the coolant can only store a certain amount of thermal energy at a certain rate. Furthermore, the relative fission power at the hottest location is not much lower than the relative fission power at the middle of the core. Eventually, the fuel temperature begins to decrease with increasing core height. This is most likely due to the fact that relative fission power towards the top of the active

core is much less than relative power closer to the center of the active core. Principles concerning specific heat capacity also play a role in heat transfer concerning the cladding, as seen in the next subsection.

Because steady state temperature values are reached during the MELCOR calculation, it seems advisable to present the fuel temperature results in a tabular-like format. For the benefit of the reader, Figure 7.33 lists all of the fuel steady state temperatures within the outline of Figure 7.1. Accompanying the fuel temperature results are the coolant temperature results. Other figures similar to Figure 7.33 are presented at the end of Subsections 7.3.5 and 7.3.6. However, COR cell temperatures in those diagrams represent the steady state cladding and canning temperatures, respectively. All red numbers refer to temperatures that are located in the active fuel region. In figure 7.33, all numbers that can be found within COR cells are red since only the active fuel temperatures are listed. However, the reader must note that other nodalization diagrams with COR cell temperatures show COR cell temperatures that are not in red since there are COR cells that are not in the active fuel region.

7.3.5 Clad Temperature Results

Serving as the barrier between the fuel and the coolant, the fuel rod cladding plays an important role with regard to the transfer of thermal energy to the coolant. Figures 7.34 and 7.35 display how the cladding temperature rises along the length of the active core. Unlike the fuel temperature; however, the highest clad temperature can be found at the top of the active fuel region. This will be explained in the next paragraph. Figure 7.36 shows how the cladding temperature varies along the radial direction of the core at the middle elevation of the active fuel region.

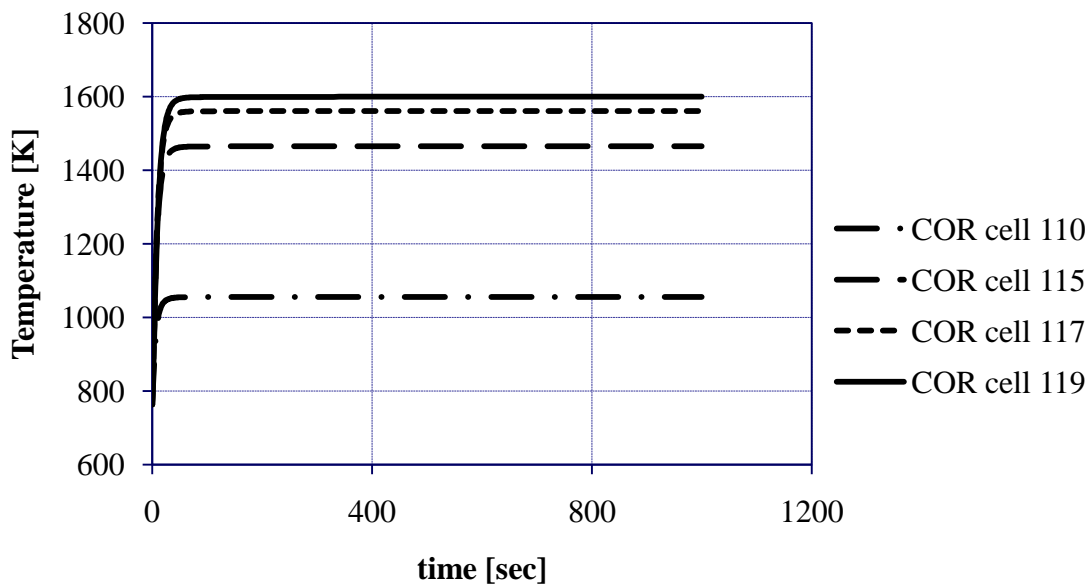


Figure 7.34: Cladding Temperature Along Core in Ring 1

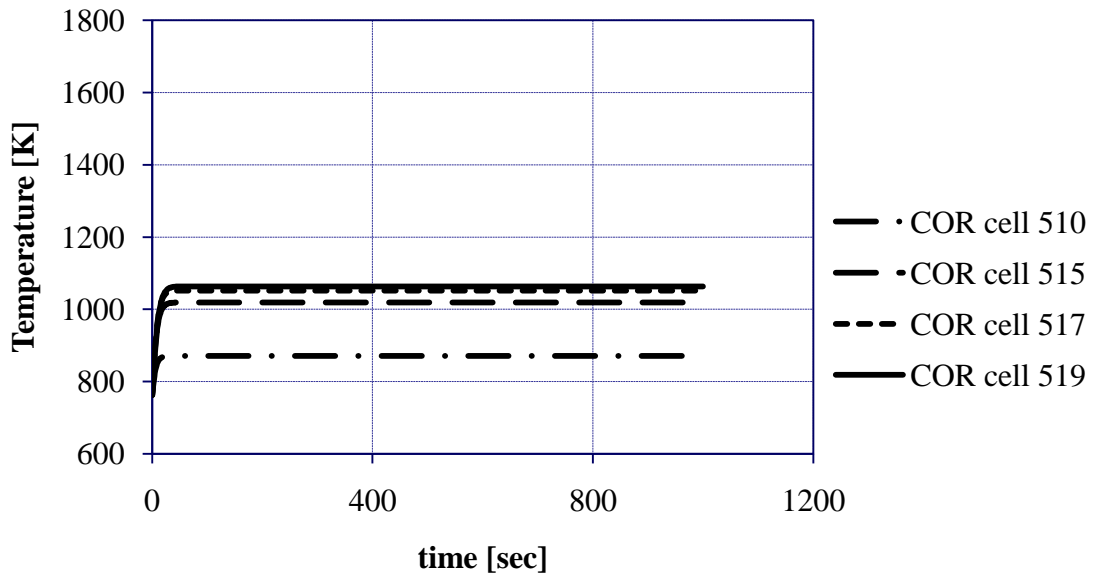


Figure 7.35: Cladding Temperature Along Core in Ring 5

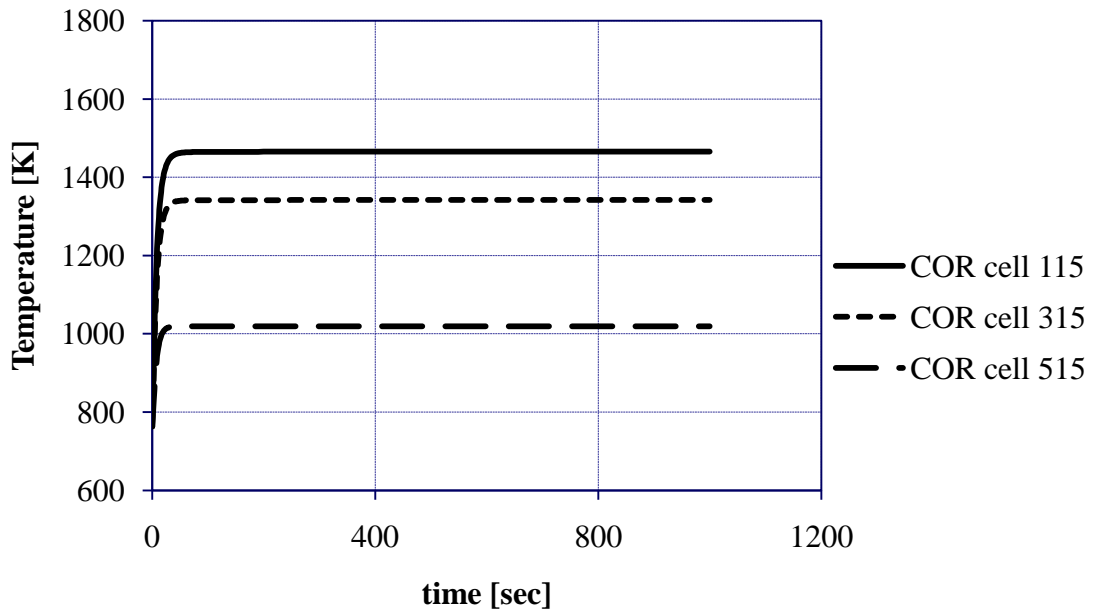
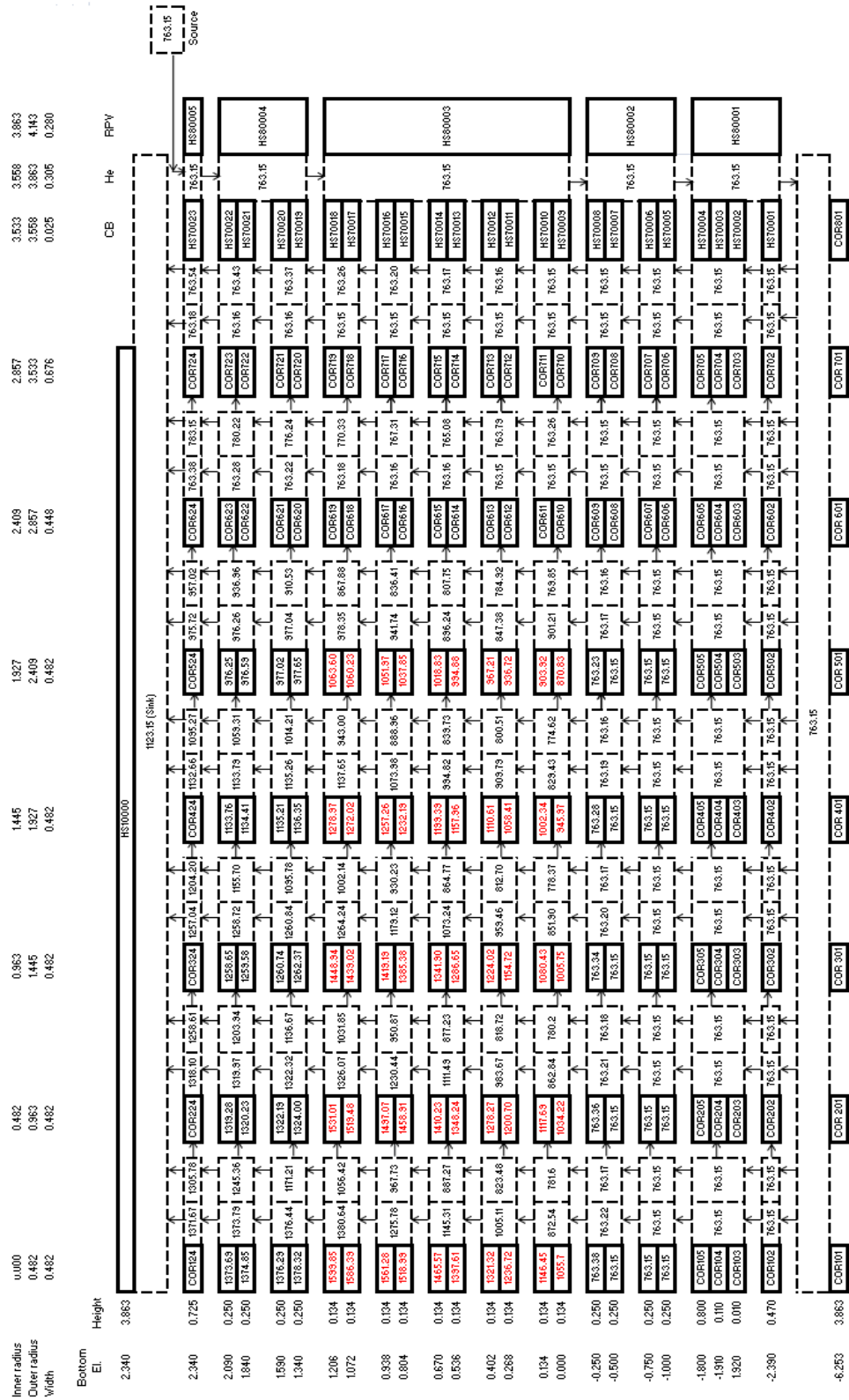


Figure 7.36: Radial Cladding Temperature Profile at Middle Elevation



As expected, the cladding temperature rises with increasing axial elevation along the active core. This is due to the fact that the coolant volume-specific heat capacity is falling and is less able to accept heat as it moves up the core and is expanded. In Figure 7.36, the cladding temperature decreases along with increasing radial distance from the core. This is expected since reactor power decreases away from the center of the core. Figure 7.37 shows a nodalization diagram with the cladding temperatures. Coolant temperatures are also shown for convenience.

7.3.6 Canning Temperature Results

Because temperature variations with elevation are insignificant in the reflector and outer borated shield regions, canning within these regions is not discussed. However, canning temperature variations with elevation and radial distance from the center of the core are discussed for cans contained within the active core. Figures 7.38 and 7.39 show canning temperature variations along the height of the core in rings 1 and 5, respectively. Figure 7.40 shows how the canning temperature changes with radial distance from the center of the core.

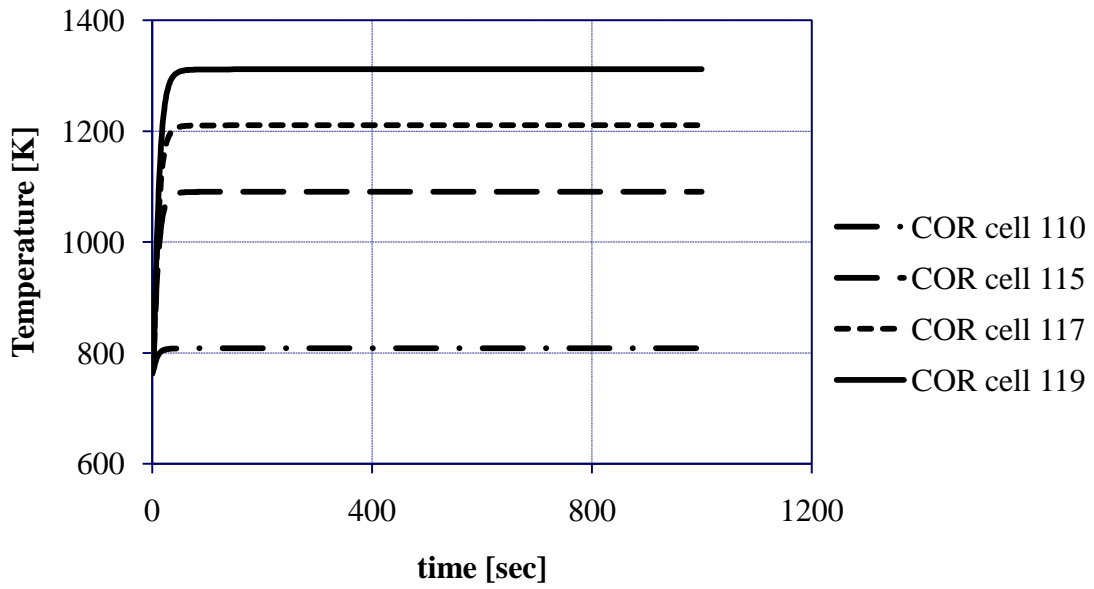


Figure 7.38: Canning Temperature Along Core in Ring 1

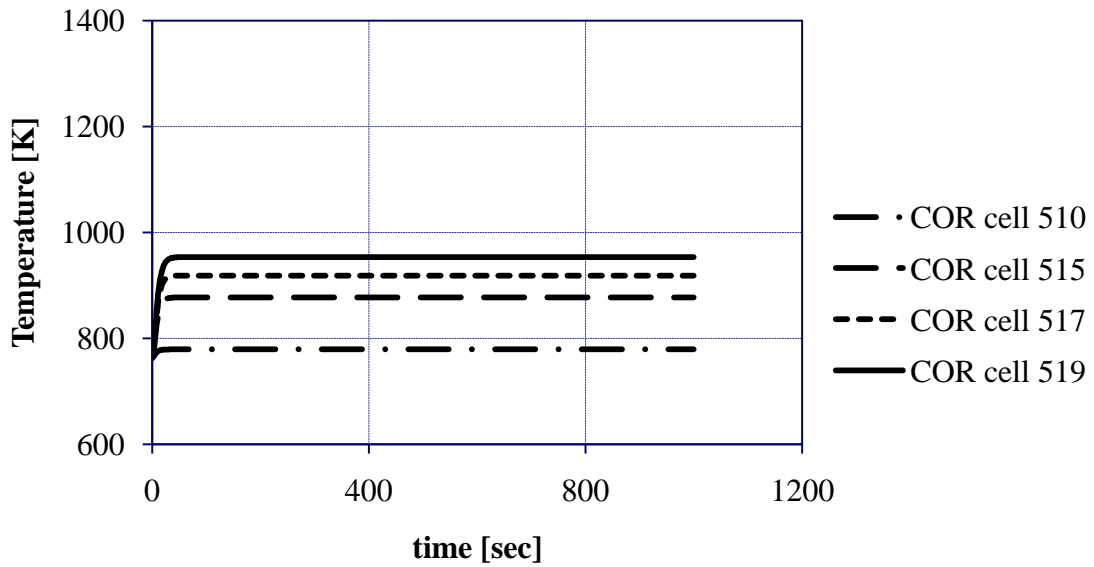


Figure 7.39: Canning Temperature Along Core in Ring 5

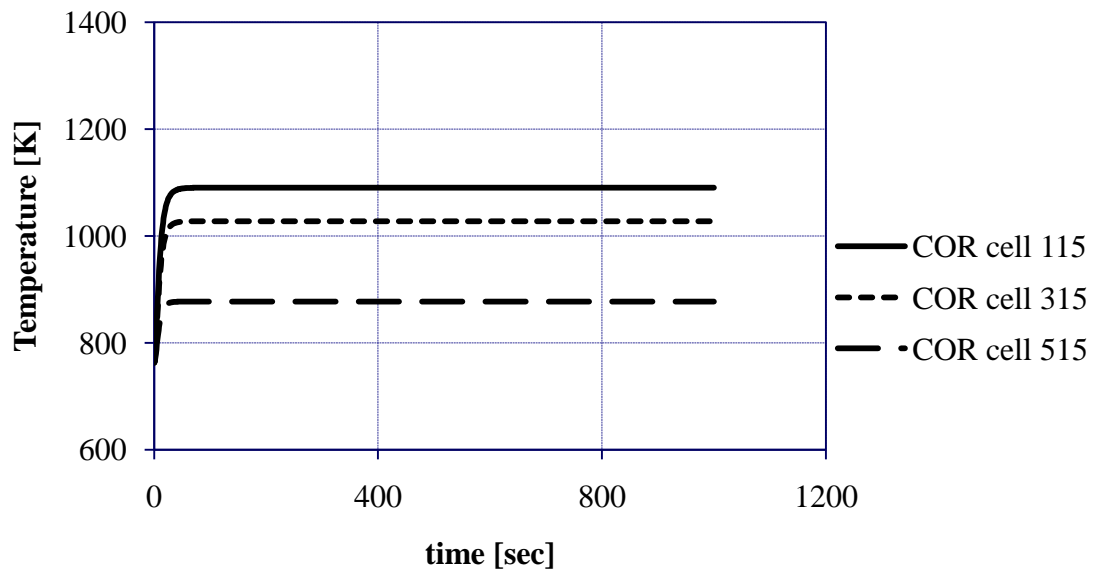


Figure 7.40: Canning Temperature Variations in Radial Direction at Middle Elevation

Figures 7.38 through 7.40 show similar results to those found in Figures 7.34 through 7.36, which represent cladding temperatures at the same core locations. Cladding temperatures are higher since the cladding is much closer to the fuel. Figure 7.41 shows a MELCOR nodalization diagram with temperatures for can material and coolant temperatures throughout the core.

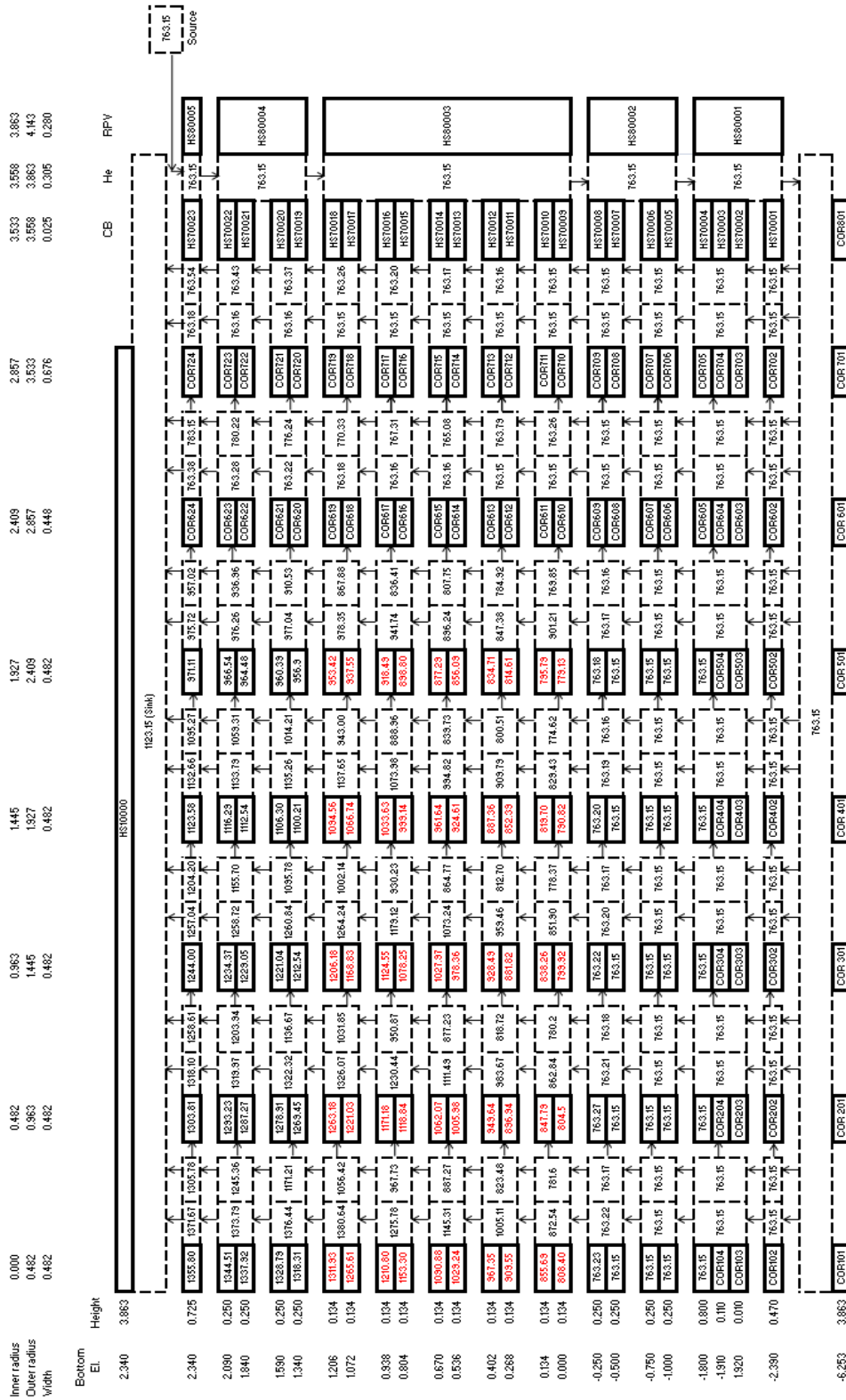


Figure 7.41: MELCOR Nodalization Diagram with Canning and Coolant Temperatures

7.3.7 Fuel-Clad-Coolant Temperature Profile

Although temperature variations in the fuel, coolant, and cladding have already been discussed, it seems advisable to present a profile that traverses all three of those regions. In reality, the reader can observe how the temperature between these regions simply by looking at previous figures. However, it seems advisable to establish one figure which shows an entire profile in order to put multiple concepts together. Figure 7.42 ties these concepts together.

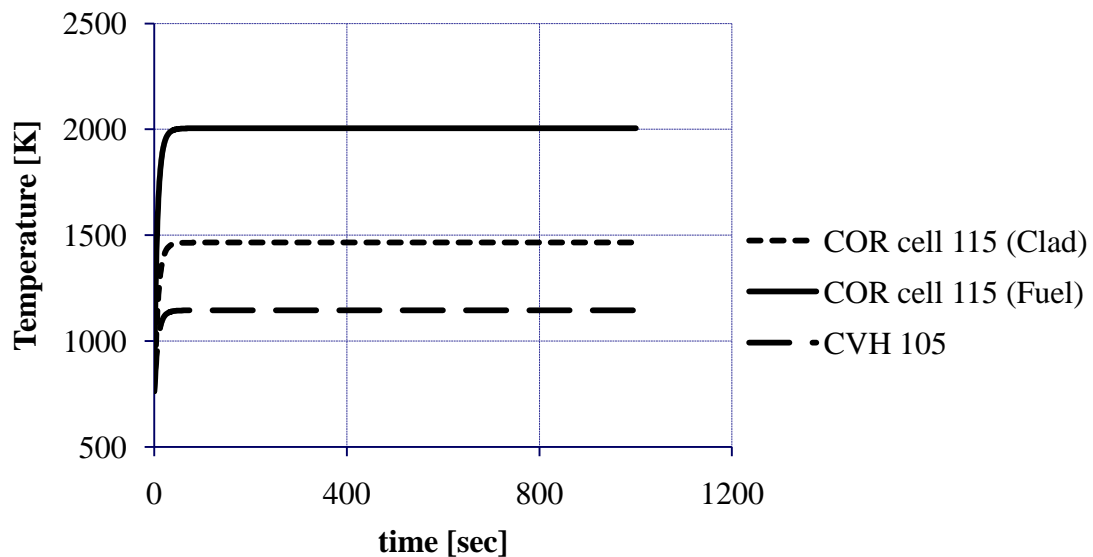


Figure 7.42: Temperature Profile in Center of Active Core

As expected, the fuel temperature is higher than the clad temperature which is higher than the coolant temperature. This graph, along with all of the other graphs presented in this section supports the fact that MELCOR input techniques developed for the purpose of this thesis have much validity. The next section will further discuss how

certain results observed from the MELCOR output provide support for the fact that modeling techniques used throughout the course of this project are quite useful.

7.4 MELCOR Conclusions

Throughout this section, a variety of interesting modeling techniques, as well as results, are observed. As in Section 6, assumptions regarding extended design criteria, as well as the actual input description are put forward in this section. The results of the MELCOR input deck are also shown. With supporting explanations of the observed results, as well as a concluding graph bringing multiple concepts together, one may surmise that inputs for this MELCOR deck seem quite plausible. Observed pressure gradients, temperature profiles, and velocity profiles all seem to hold a great deal of validity. While assumptions regarding form losses may not be totally acceptable at this juncture in time, they do provide a foundation off of which one may draw some basic conclusions as to some important characteristics regarding the US DOE GFR design.

Allocation techniques used in order to achieve the desired nodalization of the GFR in the MELCOR input deck seem to prove valuable. COR cells found within the active core are purposefully created with short axial elevations due to the large thermal power density observed within the GFR core causing the fuel to temperature increase rather quickly over short distances along the length of the core. Each active core cell is chosen to have an axial elevation of 0.134 meters. Two COR cells within the active core are associated with one control volume, thus making the axial elevation of each active core control volume 0.268 meters. This allowed the active core to be allocated into 10 axial COR cell levels along with 5 active core control volumes. Further reduction in

axial elevation per each active core COR cell and control volume would have significantly increased computation time. Fuel temperature increase at the center of the active core among the lower COR cells is rather large, approximately 145K. However, farther up the active core, the cell temperature differences reduce to approximately 6K. The same effect can be seen in the other radial rings; however, temperature differences between COR cells is slightly reduced due to a reduction in power away from the center of the active core. The average reduction in fuel temperature per COR cell does not seem high enough so as to significantly distort temperature calculations. The same may be said regarding temperature calculations for various other components, such as cladding and canning.

Other modeling techniques worthy of discussion include those used for substitution of materials. Locations in the MELCOR input deck representing zircalloy, as those found in the COR_KCL and COR_KCN cards, are substituted with SiC. This is done in order to capture the fact that SiC is meant for use as both cladding and canning in many locations, such as those observed in the active core. Furthermore, Zr_3Si_2 is substituted for zirconium dioxide, and tungsten is substituted for stainless steel oxide. The materials targeted for substitution out of the input deck, such as zircalloy, zirconium dioxide and stainless steel oxide are able to be eliminated since they do not serve a purpose in this input deck. In order to physically represent the materials substituted into the core, the tabular functions package is used to dictate how material properties change as a function of temperature. Results obtained from MELCOR output show that the changes in material properties have an impact upon the calculations performed by

MELCOR. Thus, one can say that substitution techniques displayed in the MELCOR input deck are valuable towards accurately reflecting the behavior of different core components found within the GFR.

Although bypass flow is observed in the MELCOR input deck created for this endeavor, there were no initial bypass specifications provided by the DOE. However, due to the gaps present between each of the assemblies, it is inferred that there must be some bypass flow. The bypass flow is modeled as making its way into the reactor core through small holes surrounding the bottom of each of the assemblies. MELCOR results seem to indicate that the amount of space allocated for bypass flow through the LCP is appropriate. Furthermore, the simulation of horizontal flow between assemblies seems to be modeled appropriately as a mixing effect taking place causes bypass temperatures in the outer core regions to increase slightly. Thus, one may surmise that the bypass flow does have a small impact on temperature calculations.

8. CONCLUSIONS AND FUTURE WORK

Although new modeling techniques for the GFR have been introduced in this thesis, there is still much more work that must be done in order to further develop GFR models. This section discusses some key issues that still require attention in order to facilitate GFR development. While the primary purpose of this thesis is to develop new and improved modeling techniques for the GFR, this thesis is also created with the intention of attracting more attention to the GFR in the US. Recently, efforts to develop modeling techniques for the GFR in the US have been halted. Perhaps these new neutronics and thermal hydraulics models will provide further insight and interest into GFR development as well as spark interest into resolving some of the issues mentioned in this section that require further analysis.

8.1 MCNP Models

The MCNP input decks created during this project were created with the intention of obtaining a neutron flux profile in the active core of the GFR. This neutron flux profile was needed in order to infer a relative power profile that could be entered into the MELCOR input deck. Although obtainment of this profile was a success, there is still a great deal of other information that can be obtained from the MCNP input deck.

Information from the design report regarding control rod boron-10 enrichment in each control/shutdown assembly was not very clear. Further analysis of reactor criticality conditions with control rods containing boron-10 enrichments that differ from design specification seems advisable in order to advance GFR modeling techniques.

Boron-10 enrichment is not discussed in the body of this document since boron-10 enrichment was only manipulated for the purpose of bringing the reactor to subcritical conditions in order to insure that it could be operated safely. When all control rods were in the withdrawn position, the reactor was slightly supercritical. However, this is considered normal since many reactors operate with partially inserted control rods in order to insure safe operation with a reactor eigenvalue of approximately unity. Further development of an MCNP input deck for the GFR should involve gathering information regarding control rod positions at which the reactor can safely operate, as well as boron-10 enrichments for those control rods. DOE design specifications did mention the amount of rod worth needed in order to safely shutdown the reactor; however, no specifics were given as to control rod patterns used during normal operation.

In addition to gathering more information on control rod boron-10 enrichments, perhaps simulations could be performed using other control poisons such as gadolinium, hafnium, erbium, etc. Other reactor designs, such as the BWR, use other control poisons in order to control reactivity or to SCRAM the reactor. Furthermore, certain reactor designs, such as the PWR, contain burnable absorbers in order to assist in reactivity control during reactor startup. Initial reactivity conditions during startup for this reactor do not seem to be available at this point in time.

MCNP5 is the MCNP version of choice for this project. Although it allows one to obtain a neutron flux profile for the reactor, it does not provide information on burnup and changes in isotopic conditions throughout the course of reactor operation. Because variations in isotopes affect the reactivity of a reactor over the course of its operation,

perhaps it is advisable to investigate how burnup affects reactivity and thus the neutron flux profile over the course of the GFR's operating cycle. Furthermore, a script could be written that automatically transfers neutron flux data, and thus power profile data, to the MELCOR deck in order so that it may be continuously updated over the course of its operation. Because this thesis only deals with steady state conditions, reactivity effects are not issues.

While only a limited amount of data is available regarding GFR design aspects, the MCNP code can be validated for GFR modeling upon further definition of the GFR core. Perhaps this MCNP input deck can be compared to input decks for the GFR that were created using the DIFF3D and REBUS codes. Validation of the MCNP code for GFR modeling is crucial towards the advancement of GFR neutronic modeling techniques.

8.2 MELCOR Techniques

The primary reason for creating a MELCOR model of the GFR is to advance current GFR thermal-hydraulic modeling techniques. Although MELCOR is primarily used to model severe accidents in thermal reactors, it is believed that the MELCOR code will provide further insight into GFR thermal-hydraulic issues. A model of the reactor is established in this thesis in order to provide a foundation off of which accident scenarios may be eventually modeled. Furthermore, this model will also prove that MELCOR can be applied to fast reactor technology, as opposed to only thermal reactor technology. The remainder of this section discusses the opportunities that have been presented along with the creation of a MELCOR model for the GFR.

Perhaps one of the most well-known postulated accident scenarios is a loss of coolant accident (LOCA). During such an accident, coolant is lost from the reactor in addition to a loss of pressure. In MELCOR, control functions can be used in order to simulate a LOCA. Furthermore, other accidents such as pressurized loss of flow and depressurized loss of flow accidents can also be modeled. In the event of various transients and accidents in any reactor, the reactor power profile is almost guaranteed to change. Therefore, introduction of the point kinetics model in MELCOR will be of use when transients and accidents are modeled. However, a reactor kinetics profile for the GFR will need to be produced in order to implement it into the MELCOR code. Currently, the MELCOR point reactor kinetics model is only meant to handle power profiles for thermal reactors. Again, the MELCOR model created for this thesis is meant to lay a foundation for MELCOR modeling techniques to be used later for GFR modeling techniques and development. All results observed from MELCOR calculations are meant to provide the reader with an understanding of the temperature distributions observed from MELCOR calculations. While this thesis lays a foundation for further thermal-hydraulic modeling of the GFR with MELCOR, it is performed with the intention of using data from MELCOR in order to create a decay heat removal system. Discussion of such a system is reserved for the final subsection of this section.

Another important concept relating to thermal-hydraulic development of the GFR with MELCOR is the use of view factors. View factors dictate radiation exchange between surfaces depending upon where both surfaces are located in space. Because view factors were not used in this particular MELCOR input deck, default values were

automatically used by the code. The reactor type input at the beginning of the COR package was a BWR. Therefore, the fuel rods radiate heat towards each other as if they are established in a square lattice inside of a square canister. However, the GFR fuel rods exist in a triangular pitch inside of hexagonal assembly cans. Perhaps this may have somewhat of an impact as to how much radiated heat one fuel rod receives from another. Further modeling techniques are required in order to determine the validity of that statement. However, view factors were not available in the design specifications for the GFR.

In due time, more information regarding design aspects of the GFR may become available. With this added information, the MELCOR input deck established for this endeavor can assist in validation of the MELCOR code as a code capable of being used for GFR modeling. Furthermore, comparisons of the MELCOR input deck established for this project can be made with RELAP5 models of the GFR. Validation of the MELCOR code for GFR modeling is crucial towards modeling a GFR capable of safe operation.

8.3 Thermionic Modeling Considerations

Although the creation of an MELCOR-based thermal hydraulic model is necessary in order to advance thermal hydraulic modeling of the GFR, the MELCOR input created for this project is designed with another intention as well. Efforts to create a passive decay heat removal system for the GFR have, to date, been unsuccessful. Without a heat sink, such as graphite, which is intended for use in gas-cooled thermal reactors, the GFR has great difficulty cooling itself naturally without coolant flow.

Furthermore, power density in the reactor core during operation is relatively high. Therefore, if a loss of flow were to occur during 100% power conditions, the consequences could be severe. The MELCOR model is created with the intention of better understanding the temperature profile in order to pave the way for the development of a decay heat removal system based on thermionic principles.

With the aid of MCNP and MELCOR, it seems possible to develop a decay heat removal system capable of using the decay heat to provide electricity to a decay heat removal system. In light of recent events that have transpired in Japan at the Fukushima Daiichi power station, the development of a passive decay heat removal system that does not depend upon diesel generators or an alternative offsite power supply has become crucial in order to ensure that a reactor can be shut down safely. GFR development is dependent upon several factors. Perhaps one of the main factors is the guarantee of being able to shut down the reactor properly and remove decay heat. The MCNP and MELCOR models created during this project help to further understanding of the GFR so that a decay heat removal system can be developed. While improvements to LWR decay heat removal systems may be necessary as well, the GFR is chosen because of its advantages mentioned at the beginning of this document. Events in Fukushima were brought up in order to provide the reader with a level of understanding of how important it truly is to develop a dependable decay heat removal system that does not depend on alternative electricity sources found outside of the actual plant. In addition, our current LWR designs will, most likely, become obsolete. Therefore it is important to advance safety systems related to the GFR for when it becomes a reality.

Initially intended for use in space reactors, thermionic principles can be applied to terrestrial reactors as well. The driving concept behind thermionics is the idea that a plate made of a certain type of metal can be taken to very high temperatures in order so that electrons boil off of its surface. This plate is referred to as the emitter. Then, another plate of a different material is placed a very short distance away from the emitter and kept at a cooler temperature. This plate is referred to as the collector since it collects the electrons that are boiling off of the emitter. As electrons leave the emitter and arrive at the collector, they create an electrical current. Figure 8.1 provides the reader with an illustration of this physical concept. Therefore, if all offsite power is lost, along

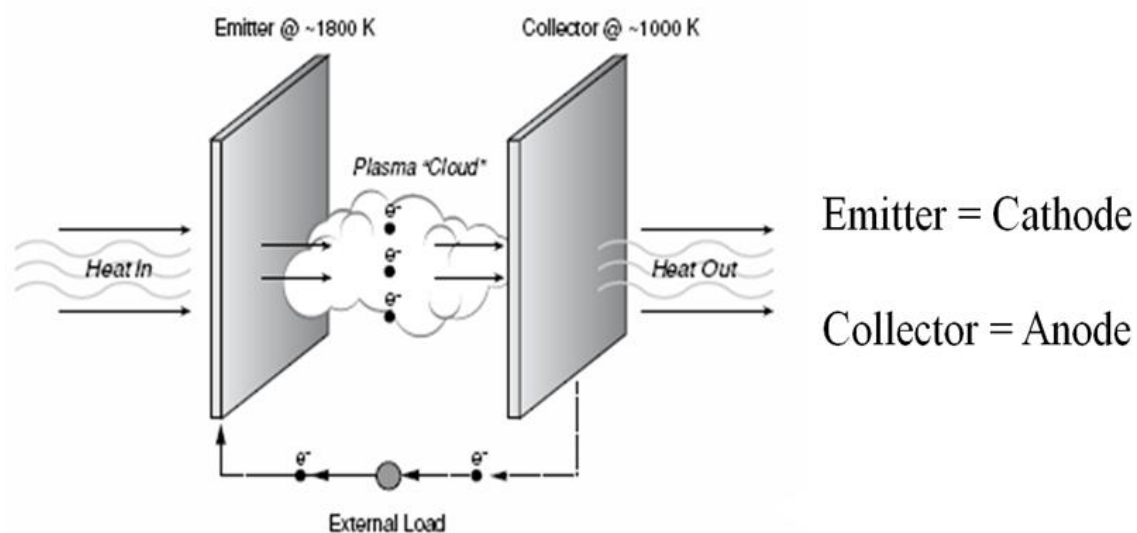


Figure 8.1: Illustration of Thermionic Principles [24]

with the diesel generators, as was the case at Fukushima, electricity may still be harnessed for the reactor cooling system by using the decay heat to create electricity for

the reactor cooling system. This would obviate dependence on diesel generators and offsite power for reactor cooling systems. Consideration has been given to placing thermionic plates between assemblies. However, it may also be worth considering using these materials in the fuel and/or control rods as cylindrical plates, as shown in Figure 8.2. The reader may neglect the liner presented in Figure 8.2, as it is not necessary for use in the GFR. Use of thermionic principles in fuel rods may also increase plant efficiency since thermal energy may be able to supply Balance of Plant systems with

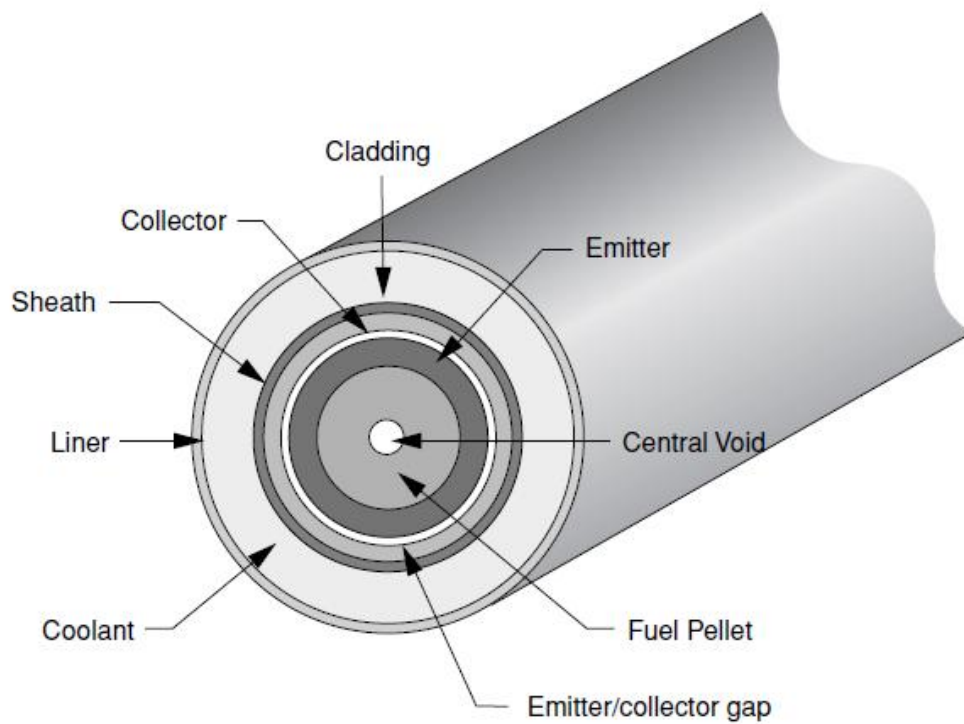


Figure 8.2: Illustration of Thermionic Principles Applied to a Fuel Rod [24]

electricity, thus reducing electricity demand from offsite sources. However, issues concerning the use of cylindrical thermionic elements stem from the fact that they will be present in the reactor core throughout an entire fuel cycle. Thermionic elements may cause certain variations in flux profiles as well experience cracking due to thermal stresses. Fuel rod expansion and bowing could induce thermal stresses upon the cylindrical thermionic elements and ultimately cause them to rupture. Nonetheless, one can still make a strong case for the pursuit of research regarding thermionic elements that are neutron transparent and that can adequately survive the harsh conditions found with the GFR core.

In conclusion, there are many issues which require further attention with regard to GFR modeling development. However, the MCNP and MELCOR models created during this project serve as advancements of current GFR modeling techniques and as good models to use for assessing GFR operating characteristics and safety concerns. With the intention of developing a decay heat removal system based on thermionic principles discussed in the preceding paragraph, these models may be used to advance passive heat removal technology.

REFERENCES

- [1] Answers Corporation, 2011.
http://wiki.answers.com/Q/What_percent_of_the_world's_energy_does_nuclear_fission_supply.
- [2] MELCOR computer code manuals vol. 2: Reference Manual, Technical Report NUREG/CR-6119, Sandia National Laboratories, Sandia, NM, September 2008.
- [3] T.Y.C. Wei. Generation IV Nuclear Energy System Initiative GenIV 2400MWt Direct Cycle GFR Status, Argonne National Laboratory, Argonne, IL, September 2008.
- [4] J.Y. Malo, C. Bassi, T. Cadiou, M. Blanc, A. Messie, A. Tosello and P. Dumaz. Gas- Cooled Fast Reactors – DHR Systems, Preliminary Design and Thermal-Hydraulic Studies, CEA/DEN/DER/CEA Cadarache, February 6, 2006.
- [5] K. D. Weaver, T. Marshall, J. Sterbentz, E. P. Loewen, T. C. Totemeier, D. E. Clark, P. E. MacDonald, T. Y. C. Wei, E. E. Feldman, M. K. Meyer, J. Gan, H. Ludewig, W. F. Gale, M. J. Driscoll, P. Hejzlar, K. Czerwinski, T. Allen. Gas-Cooled Fast Reactor FY03 Annual Report, Generation IV International Forum, 2003.
- [6] K. D. Weaver, T.C. Totemeier, D.E. Clark, E.E. Feldman, E.A. Hoffman, R.B. Vilim, T.Y.C. Wei, J. Gan, M.K. Meyer, W.F. Gale, M.J. Driscoll, M. Golay, G. Apostolakis, K. Czerwinski. Gas-Cooled Fast Reactor FY04 Annual Report, Generation IV International Forum, 2004.
- [7] K.D. Weaver, T. Marshall, T. Totemeier, J. Gan, E.E. Feldman, E.A. Hoffman, R.F. Kulak, I.U. Therios, C.P. Tzanos, T.Y.C. Wei, L-Y. Chung, H. Ludewig, J. Jo, R. Nanstad, W. Corwin, V.G. Krishnardula, W.F. Gale, J.W. Fergus, T. Allen, P. Sabharwall. Gas-Cooled Fast Reactor FY05 Annual Report, Generation IV International Forum, September 30, 2005.
- [8] A. Epiney, K. Mikityuk, and R. Chawla, Heavy Gas Injection in the Generation IV Gas-cooled Fast Reactor to improve decay heat removal under depressurized conditions, in: Proceedings of The 13th International Topical Meeting on Nuclear Thermal Hydraulics (NURETH-13), Kanazawa City, Ishikawa Prefecture, Japan, September 27-October 2, 2009.
- [9] F. Bertrand, F. Bentivoglio, G. Rimpault, F. Audubert, C. Journeau, J.M. Seiler. Preliminary transient analysis and approach of hypothetical scenarios for

- prevention and understanding of severe accidents of the 2400 MWth Gas-cooled Fast Reactor, in: Proceedings of The 13th International Topical Meeting on Nuclear Thermal Hydraulics (NURETH-13), Kanazawa City, Ishikawa Prefecture, Japan, September 27-October 2, 2009.
- [10] A. Epiney, N. Alpy, D. Haubensack, J.Y. Malo, K. Mikityuk, R. Chawla. Preliminary design of a Brayton cycle as a standalone decay heat removal system for the Gas-cooled Fast Reactor, in: Proceedings of The 13th International Topical Meeting on Nuclear Thermal Hydraulics (NURETH-13), Kanazawa City, Ishikawa Prefecture, Japan, September 27-October 2, 2009.
- [11] M. M. Stempniewicz and A. de With. Passive safety design optimization for 600 MWth GCFR, in: Proceedings of The 13th International Topical Meeting on Nuclear Thermal Hydraulics (NURETH-13), Kanazawa City, Ishikawa Prefecture, Japan, September 27-October 2, 2009.
- [12] I. Dor, N. Tauveron, and F. Bentivoglio, B. Mathiue and C. Poette. ALLEGRO project-DHR investigation with the CATHARE2 Code, in: Proceedings of The 13th International Topical Meeting on Nuclear Thermal Hydraulics (NURETH-13), Kanazawa City, Ishikawa Prefecture, Japan, September 27-October 2, 2009.
- [13] A. E. Waltar and Albert B. Reynolds, Fast Breeder Reactors, Pergamon Press, Oxford, UK, 1981.
- [14] MCNP-A General Monte Carlo N-Particle Transport Code, Version 5, vol 1: Overview and Theory, Technical Report LA-UR-03-1987, Los Alamos National Laboratory, Los Alamos, NM, April 2003.
- [15] MCNP-A General Monte Carlo N-Particle Transport Code, Version 5, vol 2: User's Guide, Technical Report LA-UR-03-0245, Los Alamos National Laboratory, Los Alamos, NM, April 2003.
- [16] MELCOR Computer Code Manuals vol.1: Primer and users' guide, version 2.1, Technical Report NUREG/CR-6119, Sandia National Laboratories, Sandia, NM, September 2008.
- [17] J. Corson. Development of MELCOR Input Techniques for High Temperature Gas-cooled Reactor Analysis, Texas A&M University, May 2010.

- [18] J. R. Lamarsh and A. J. Baratta, Introduction to Nuclear Engineering, 3rd ed., Prentice Hall, Upper Saddle River, NJ, 2001.
- [19] J. K. Shultis and R. E. Faw, Fundamentals of Nuclear Science and Engineering, Marcel Dekker, New York, 2002.
- [20] S. Michalek, J. Hascik and G. Farkas, MCNP5 delayed neutron fraction (β_{eff}) calculation in training reactor VR-1, Journal of Electrical Engineering, vol. 59, (2008) 221-224.
- [21] Y. A. Cengel and J. M. Cimbala, Fluid Mechanics: Fundamentals and Applications, McGraw-Hill, New York, 2006.
- [22] R. B. Bird, W. E. Stewart, and E. N. Lightfoot, Transport Phenomena, 2nd ed., John Wiley and Sons, New York, 2002.
- [23] F. P. Incropera, D. P. Dewitt, T. L. Bergman, and A. S. Lavine, Fundamentals of Heat and Mass Transfer, 6th ed., John Wiley and Sons, Hoboken, NJ, 2007.
- [24] Thermionics Quo Vadis? An Assessment of the DTRA's Advanced Thermionics Research and Development Program, National Academy of Sciences, National Academy Press, Washington, DC, 2001.
- [25] Webelements, The periodic table on the web, 1993-2010, <http://webelements.com/silicon/isotopes.html>.
- [26] Webelements, The periodic table on the web, 1993-2010, <http://webelements.com/helium/isotopes.html>.
- [27] Webelements, The periodic table on the web, 1993-2010, <http://webelements.com/zirconium/isotopes.html>.
- [28] Webelements, The periodic table on the web, 1993-2010, <http://webelements.com/boron/isotopes.html>.
- [29] Webelements, The periodic table on the web. 1993-2010, <http://webelements.com/tungsten/isotopes.html>.

- [30] Specs: 316, 316L and 317L, Sandmeyer Steel Company, Philadelphia, PA.
- [31] D.F. Fischer and L. Leibowitz, Enthalpy of Uranium-Plutonium Carbide from 298K to the Melting Point, Argonne National Laboratory, Argonne, IL, 1977.
- [32] H.D. Lewis and J.F. Kerrisk, Electrical and Thermal Transport Properties of Uranium and Plutonium Carbides, Los Alamos Scientific Laboratory of the University of California, Los Alamos, NM, 1975.
- [33] J.F. Andrew and T.W. Latimer, Review of Thermal Expansion and Density of Uranium and Plutonium Carbides, Los Alamos Scientific National Laboratory, Los Alamos, NM, 1975.
- [34] V.I. Koshchenko, Ya. Kh. Grinberg, and R.V. Koshchenko, Thermodynamic Functions of B₆As (5-600K), beta-SiC (5-2000K), and Si₃N₄ (5-4000K), D.I. Mendeleev Moscow Chemical Technology Institute, Moscow, Russia, 1985.
- [35] R.G. Munro, Material properties of a sintered alpha-SiC, Journal of Physical and Chemical Reference Data, vol. 26, (1997) 1195-1203.
- [36] M. Le Flem, J. Canel and S. Urvoy, Processing and Characterization of Zr₃Si₂ for Nuclear Applications, CEA, Saclay, France, 2007.
- [37] V. Ya. Chekhovskoi, The Enthalpy and Heat Capacity of Tungsten in the Temperature Range 400-3500K, High Temperature Res. Inst., Acad. Sci. Russia, Moscow, Russia, 1980.
- [38] B.E. Neimark and L.K. Voronin, Thermal Conductivity, Electrical Resistivity and Emissivity of Refractory Metals at High Temperatures, All-Union Heat Engineering Institute, Moscow, Russia, 1968.

APPENDIX A
PLOT PARAMETERS

Contained within this appendix is the list of MELCOR parameters that are plotted throughout this thesis. Table A.1 contains the list of figures for which plot parameter information is required. Each figure has legend strings of each data set displayed on that particular figure, as well as the MELCOR variables associated with the legend strings.

Table A.1: MELCOR Plot Parameters

Figure	Legend String	MELCOR Variable
7.2	CVH 001	CVH-P.1
	CVH 003	CVH-P.3
	CVH 005	CVH-P.5
7.3	CVH 101	CVH-P.101
	CVH 105	CVH-P.105
	CVH 109	CVH-P.109
7.4	CVH 141	CVH-P.141
	CVH 145	CVH-P.145
	CVH 149	CVH-P.149
7.5	CVH 161	CVH-P.161
	CVH 165	CVH-P.165
	CVH 169	CVH-P.169
7.6	CVH 201	CVH-P.201
	CVH 205	CVH-P.205
	CVH 209	CVH-P.209
7.7	CVH 241	CVH-P.241
	CVH 245	CVH-P.245
	CVH 249	CVH-P.249
7.8	CVH 261	CVH-P.261
	CVH 265	CVH-P.265
	CVH 269	CVH-P.269
7.9	CVH 105	CVH-P.105
	CVH 125	CVH-P.125
	CVH 145	CVH-P.145
	CVH 165	CVH-P.165

Table A.1 (Continued)

Figure	Legend String	MELCOR Variable
7.10	CVH 101	CVH-TVAP.101
	CVH 105	CVH-TVAP.105
	CVH 109	CVH-TVAP.109
7.11	CVH 141	CVH-TVAP.141
	CVH 145	CVH-TVAP.145
	CVH 149	CVH-TVAP.149
7.12	CVH 161	CVH-TVAP.161
	CVH 165	CVH-TVAP.165
	CVH 169	CVH-TVAP.169
7.13	CVH 201	CVH-TVAP.201
	CVH 205	CVH-TVAP.205
	CVH 209	CVH-TVAP.209
7.14	CVH 241	CVH-TVAP.241
	CVH 245	CVH-TVAP.245
	CVH 249	CVH-TVAP.249
7.15	CVH 261	CVH-TVAP.261
	CVH 265	CVH-TVAP.265
	CVH 269	CVH-TVAP.269
7.16	CVH 105	CVH-TVAP.105
	CVH 125	CVH-TVAP.125
	CVH 145	CVH-TVAP.145
	CVH 165	CVH-TVAP.165
7.17	CVH 205	CVH-TVAP.205
	CVH 225	CVH-TVAP.225
	CVH 245	CVH-TVAP.245
	CVH 265	CVH-TVAP.265
7.18	Flow Path 101	FL-VELVAP.101
	Flow Path 105	FL-VELVAP.105
	Flow Path 501	FL-VELVAP.501
7.19	Flow Path 141	FL-VELVAP.141
	Flow Path 145	FL-VELVAP.145
	Flow Path 541	FL-VELVAP.149
7.20	Flow Path 161	FL-VELVAP.161
	Flow Path 165	FL-VELVAP.165
	Flow Path 169	FL-VELVAP.561
7.21	Flow Path 201	FL-VELVAP.201
	Flow Path 205	FL-VELVAP.205
	Flow Path 209	FL-VELVAP.209

Table A.1 (Continued)

Figure	Legend String	MELCOR Variable
7.22	Flow Path 241	FL-VELVAP.241
	Flow Path 245	FL-VELVAP.205
	Flow Path 249	FL-VELVAP.209
7.23	Flow Path 261	FL-VELVAP.261
	Flow Path 265	FL-VELVAP.265
	Flow Path 269	FL-VELVAP.269
7.24	Flow Path 105	FL-VELVAP.105
	Flow Path 125	FL-VELVAP.125
	Flow Path 145	FL-VELVAP.145
	Flow Path 165	FL-VELVAP.165
7.25	Flow Path 205	FL-VELVAP.205
	Flow Path 225	FL-VELVAP.225
	Flow Path 245	FL-VELVAP.245
	Flow Path 265	FL-VELVAP.265
7.26	Flow Path 701	FL-VELVAP.701
	Flow Path 705	FL-VELVAP.705
	Flow Path 709	FL-VELVAP.709
7.27	Flow Path 745	FL-VELVAP.745
	Flow Path 749	FL-VELVAP.749
	Flow Path 753	FL-VELVAP.753
7.28	Flow Path 308	FL-VELVAP.308
	Flow Path 309	FL-VELVAP.309
	Flow Path 368	FL-VELVAP.368
	Flow Path 369	FL-VELVAP.369
7.29	COR cell 110	COR-TFU.110
	COR cell 115	COR-TFU.115
	COR cell 117	COR-TFU.117
	COR cell 119	COR-TFU.119
7.30	COR cell 510	COR-TFU.510
	COR cell 515	COR-TFU.515
	COR cell 517	COR-TFU.517
	COR cell 519	COR-TFU.518
7.31	COR cell 115	COR-TFU.115
	COR cell 315	COR-TFU.315
	COR cell 515	COR-TFU.515
7.32	COR cell 110	COR-TCL.110
	COR cell 115	COR-TCL.115
	COR cell 117	COR-TCL.117
	COR cell 119	COR-TCL.119

Table A.1 (Continued)

Figure	Legend String	MELCOR Variable
7.33	COR cell 510	COR-TCL.510
	COR cell 515	COR-TCL.515
	COR cell 517	COR-TCL.517
	COR cell 519	COR-TCL.519
7.34	COR cell 115	COR-TCL.115
	COR cell 315	COR-TCL.315
	COR cell 515	COR-TCL.515
7.35	COR cell 110	COR-TCN.110
	COR cell 115	COR-TCN.115
	COR cell 117	COR-TCN.117
	COR cell 119	COR-TCN.119
7.36	COR cell 510	COR-TCN.510
	COR cell 515	COR-TCN.515
	COR cell 517	COR-TCN.517
	COR cell 519	COR-TCN.519
7.37	COR cell 115	COR-TCN.115
	COR cell 315	COR-TCN.315
	COR cell 515	COR-TCN.515
7.38	COR cell 115 (Clad)	COR-TCL.115
	COR cell 115 (Fuel)	COR-TFU.115
	CVH 105	COR-TVAP.105

APPENDIX B

MCNP CALCULATION NOTEBOOK FOR US DOE GFR

Contained within this appendix is the calculation notebook for the two MCNP input decks that were constructed for this thesis. Because the input decks contain the same input, except for the meshing, only the input for one of the decks is listed. However, both meshing schemes are listed separately. Therefore, there are two meshing schemes. The input decks represented in this appendix are ftn3.inp and ftnA3.inp. While the majority of all appendices in this thesis are outlined in a tabular format, the cell card data containing outlines of the various types of assemblies are shown in the same format as they are input into the deck. The same is true for the overall layout of the entire core. This is done for the benefit of the reader in order so that he/she may better understand the MCNP input techniques. Furthermore, fill commands associated with the assembly and core layouts that are found above and to the left of the pattern are left out of tabular format as well. This is due to their placement in the input deck. It seems more advisable to leave the fill command for an entire assembly or core with the pattern itself. All material densities are listed in units of atoms/barn-cm.

B.1 GFR Cell Card Data

Table B.1: Core Boundary

Cell Number	Material Number	Material Location	Fill	n importance
701	0	-701 702 -703 704 -705 706 19 -24	75	1

Table B.4: Layer of Void Beyond Core

Cell Number	Material Number	Material Location	n importance
704	0	801:-802:803:- 804:805:-806:-19:24	0

Table B.5: Inner Layer of Can for 20 w/o Fuel Assembly

Cell Number	Material Number	Material Location	Fill	Universe	n importance
501	0	-401 402 -403 404 -405 406 19 -24	99	1	1

Table B.6: 20 w/o Assembly Layout

Cell Number	Material	Material Density	Material Location	Lattice	Universe	n importance
502	7	5.3582E-04	-301 302 -303 304 -305 306	2	99	1

```

fill=-10:10 -10:10 0:0
99 20R
99 9R          50 50 50 50 50 50 50 50 50 50 50 99
99 8R          50 50 50 50 50 50 50 50 50 50 50 99
99 7R          50 50 50 50 50 50 50 50 50 50 50 99
99 6R          50 50 50 50 50 50 50 50 50 50 50 99
99 5R          50 50 50 50 50 50 50 50 50 50 50 99
99 4R          50 50 50 50 50 50 50 50 50 50 50 99
99 3R          50 50 50 50 50 50 50 50 50 50 50 99
99 2R          50 50 50 50 50 50 50 50 50 50 50 99
99 1R          50 50 50 50 50 50 50 50 50 50 50 99
99          50 50 50 50 50 50 50 50 50 50 50 50 50 99
99          50 50 50 50 50 50 50 50 50 50 50 50 50 99 1R
99          50 50 50 50 50 50 50 50 50 50 50 50 50 99 2R
99          50 50 50 50 50 50 50 50 50 50 50 50 50 99 3R
99          50 50 50 50 50 50 50 50 50 50 50 50 50 99 4R
99          50 50 50 50 50 50 50 50 50 50 50 50 50 99 5R
99          50 50 50 50 50 50 50 50 50 50 50 50 50 99 6R
99          50 50 50 50 50 50 50 50 50 50 50 50 50 99 7R
99          50 50 50 50 50 50 50 50 50 50 50 50 50 99 8R
99          50 50 50 50 50 50 50 50 50 50 50 50 50 99 9R
99          50 50 50 50 50 50 50 50 50 50 50 50 50 99 20R
    
```

Figure B.2: 20 w/o Fuel Assembly Configuration

Table B.7: SiC Canning for 20 w/o Fuel Assembly

Cell Number	Material Number	Material Density	Material Location	Universe	n importance
503	6	4.8211E-02	(-501 502 -503 504 -505 506) (401:- 402:403:-404:405: -406) 19 -24	1	1

Table B.11: SiC Canning for 18.1 w/o Fuel Assembly

Cell Number	Material Number	Material Density	Material Location	Universe	n importance
507	6	4.8211E-02	(-501 502 -503 504 -505 506) (401:- 402:403:-404:405: -406) 19 -24	2	1

Table B.12: Helium Beyond 18.1 w/o Fuel Assembly

Cell Number	Material Number	Material Density	Material Location	Universe	n importance
508	7	5.3582E-04	501:-502:503:- 504:505:-506:-19:24	2	1

Table B.13: Inner Layer of Can for 16.3 w/o Fuel Assembly

Cell Number	Material Number	Material Location	Fill	Universe	n importance
509	0	-401 402 -403 404 -405 406 19 -24	97	3	1

Table B.14: 16.3 w/o Fuel Assembly Layout

Cell Number	Material	Material Density	Material Location	Lattice	Universe	n importance
510	7	5.3582E-04	-301 302 -303 304 -305 306	2	97	1

```

fill=-10:10 -10:10 0:0
97 20R
97 9R      42 42 42 42 42 42 42 42 42 42 42 97
97 8R      42 42 42 42 42 42 42 42 42 42 42 97
97 7R      42 42 42 42 42 42 42 42 42 42 42 97
97 6R      42 42 42 42 42 42 42 42 42 42 42 42 97
97 5R      42 42 42 42 42 42 42 42 42 42 42 42 42 97
97 4R      42 42 42 42 42 42 42 42 42 42 42 42 42 42 97
97 3R      42 42 42 42 42 42 42 42 42 42 42 42 42 42 97
97 2R      42 42 42 42 42 42 42 42 42 42 42 42 42 42 42 97
97 1R      42 42 42 42 42 42 42 42 42 42 42 42 42 42 42 97
97      42 42 42 42 42 42 42 42 42 42 42 42 42 42 42 42 97
97      42 42 42 42 42 42 42 42 42 42 42 42 42 42 42 42 97 1R
97      42 42 42 42 42 42 42 42 42 42 42 42 42 42 42 42 97 2R
97      42 42 42 42 42 42 42 42 42 42 42 42 42 42 42 42 97 3R
97      42 42 42 42 42 42 42 42 42 42 42 42 42 42 42 42 97 4R
97      42 42 42 42 42 42 42 42 42 42 42 42 42 42 42 42 97 5R
97      42 42 42 42 42 42 42 42 42 42 42 42 42 42 42 42 97 6R
97      42 42 42 42 42 42 42 42 42 42 42 42 42 42 42 42 97 7R
97      42 42 42 42 42 42 42 42 42 42 42 42 42 42 42 42 97 8R
97      42 42 42 42 42 42 42 42 42 42 42 42 42 42 42 42 97 9R
97      42 42 42 42 42 42 42 42 42 42 42 42 42 42 42 42 97 20R
    
```

Figure B.4: 16.3 w/o Fuel Assembly Configuration

Table B.15: SiC Canning for 16.3 w/o Fuel Assembly

Cell Number	Material Number	Material Density	Material Location	Universe	n importance
511	6	4.8211E-02	(-501 502 -503 504 -505 506) (401:- 402:403:-404:405: -406) 19 -24	3	1

Table B.16: Helium Beyond 16.3 w/o Fuel Assembly

Cell Number	Material Number	Material Density	Material Location	Universe	n importance
512	7	5.3582E-04	501:-502:503:- 504:505:-506:-19:24	3	1

Table B.17: Inner Layer of Can for 15.7 w/o Fuel Assembly

Cell Number	Material Number	Material Location	Fill	Universe	n importance
513	0	-401 402 -403 404 -405 406 19 -24	96	4	1

Table B.18: 15.7 w/o Fuel Assembly Layout

Cell Number	Material	Material Density	Material Location	Lattice	Universe	n importance
514	7	5.3582E-04	-301 302 -303 304 -305 306	2	96	1

```

fill=-10:10 -10:10 0:0
96 20R
96 9R      38 38 38 38 38 38 38 38 38 38 38 96
96 8R      38 38 38 38 38 38 38 38 38 38 38 96
96 7R      38 38 38 38 38 38 38 38 38 38 38 38 96
96 6R      38 38 38 38 38 38 38 38 38 38 38 38 38 96
96 5R      38 38 38 38 38 38 38 38 38 38 38 38 38 96
96 4R      38 38 38 38 38 38 38 38 38 38 38 38 38 38 96
96 3R      38 38 38 38 38 38 38 38 38 38 38 38 38 38 96
96 2R      38 38 38 38 38 38 38 38 38 38 38 38 38 38 38 96
96 1R      38 38 38 38 38 38 38 38 38 38 38 38 38 38 38 96
96      38 38 38 38 38 38 38 38 38 38 38 38 38 38 38 38 96
96      38 38 38 38 38 38 38 38 38 38 38 38 38 38 38 38 96 1R
96      38 38 38 38 38 38 38 38 38 38 38 38 38 38 38 38 96 2R
96      38 38 38 38 38 38 38 38 38 38 38 38 38 38 38 38 96 3R
96      38 38 38 38 38 38 38 38 38 38 38 38 38 38 38 38 96 4R
96      38 38 38 38 38 38 38 38 38 38 38 38 38 38 38 38 96 5R
96      38 38 38 38 38 38 38 38 38 38 38 38 38 38 38 38 96 6R
96      38 38 38 38 38 38 38 38 38 38 38 38 38 38 38 38 96 7R
96      38 38 38 38 38 38 38 38 38 38 38 38 38 38 38 38 96 8R
96      38 38 38 38 38 38 38 38 38 38 38 38 38 38 38 38 96 9R
96      38 38 38 38 38 38 38 38 38 38 38 38 38 38 38 38 96 20R
    
```

Figure B.5: 15.7 w/o Fuel Assembly Configuration

Table B.23: SiC Canning for 14.8 w/o Fuel Assembly

Cell Number	Material Number	Material Density	Material Location	Universe	n importance
519	6	4.8211E-02	(-501 502 -503 504 - 505 506) (401:- 402:403:-404:405: -406) 19 -24	5	1

Table B.24: Helium Beyond 14.8 w/o Fuel Assembly

Cell Number	Material Number	Material Density	Material Location	Universe	n importance
520	7	5.3582E-04	501:-502:503:- 504:505:-506:-19:24	5	1

Table B.25: Inner Layer of Inner Can for 20 w/o Control Assembly

Cell Number	Material Number	Material Location	Fill	Universe	n importance
521	0	-101 102 -103 104 -105 106 19 -24	30	6	1

Table B.26: SiC Canning for Inner Can in 20 w/o Control Assembly

Cell Number	Material Number	Material Density	Material Location	Universe	n importance
522	6	4.8211E-02	(-201 202 -203 204 -205 206) (101: -102:103:-104:105: -106) 19 -24	6	1

Table B.27: Meshing Layout Between Cans of 20 w/o Control Assembly

Cell Number	Material Number	Material Location	Fill	Universe	n importance
523	0	(-401 402 -403 404 -405 406) (201: -202:203:-204:205: -205) 19 -24	94	6	1

Table B.28: 20 w/o Control Assembly Layout

Cell Number	Material Number	Material Location	Lattice	Universe	n importance
524	7	-301 302 -303 304 -305 306	2	94	1

```

fill=-10:10 -10:10 0:0
94 20R
94 9R          50 50 50 50 50 50 50 50 50 50 50 94
94 8R          50 50 50 50 50 50 50 50 50 50 50 94
94 7R          50 50 50 50 50 50 50 50 50 50 50 94
94 6R          50 50 50 50 50 50 50 50 50 50 50 94
94 5R          50 50 50 50 50 50 50 50 50 50 50 94
94 4R          50 50 50 50 50 50 50 50 50 50 50 94
94 3R          50 50 50 50 50 50 94 94 94 94 50 50 50 50 94
94 2R          50 50 50 50 50 50 94 94 94 94 50 50 50 50 94
94 1R          50 50 50 50 50 50 94 94 94 94 94 50 50 50 50 94
94          50 50 50 50 50 50 94 94 94 94 94 50 50 50 50 94 1R
94          50 50 50 50 50 50 94 94 94 94 94 50 50 50 50 94 2R
94          50 50 50 50 50 50 94 94 94 94 50 50 50 50 94 3R
94          50 50 50 50 50 50 50 50 50 50 50 50 50 94 4R
94          50 50 50 50 50 50 50 50 50 50 50 50 94 5R
94          50 50 50 50 50 50 50 50 50 50 50 94 6R
94          50 50 50 50 50 50 50 50 50 94 7R
94          50 50 50 50 50 50 50 50 94 8R
94          50 50 50 50 50 50 50 94 9R
94          50 50 50 50 50 50 50 94 20R
  
```

Figure B.7: 20 w/o Control Assembly Configuration

Table B.29: SiC Canning for Outer Can of 20 w/o Control Assembly

Cell Number	Material Number	Material Density	Material Location	Universe	n importance
525	6	4.8211E-02	(-501 502 -503 504 -505 506) (401:- 402:403:-404:405: -406) 19 -24	6	1

Table B.30: Helium Beyond 20 w/o Control Assembly

Cell Number	Material Number	Material Density	Material Location	Universe	n importance
526	7	5.3582E-04	501:-502:503:- 504:505:-506:-19:24	6	1

Table B.31: Inner Layer of Inner Can for 18.1 w/o Control Assembly

Cell Number	Material Number	Material Location	Fill	Universe	n importance
527	0	-101 102 -103 104 -105 106 19 -24	30	10	1

Table B.35: SiC Canning of Outer Can of 18.1 w/o Control Assembly

Cell Number	Material Number	Material Density	Material Location	Universe	n importance
531	6	4.8211E-02	(-501 502 -503 504 -505 506) (401:- 402:403:-404:405: -406) 19 -24	10	1

Table B.36: Helium Beyond 18.1 w/o Control Assembly

Cell Number	Material Number	Material Density	Material Location	Universe	n importance
532	7	5.3582E-04	501:-502:503:- 504:505:-506:-19:24	10	1

Table B.37: Inner Layer of Inner Can of 14.8 w/o Control Assembly

Cell Number	Material Number	Material Location	Fill	Universe	n importance
533	0	-101 102 -103 104 -105 106 19 -24	30	7	1

Table B.38: SiC Canning for Inner Can of 14.8 w/o Control Assembly

Cell Number	Material Number	Material Density	Material Location	Universe	n importance
534	6	4.8211E-02	(-201 202 -203 204 -205 206) (101: -102:103:-104:105: -106) 19 -24	7	1

Table B.39: Meshing Layout Between Cans of 18.1 w/o Control Assembly

Cell Number	Material Number	Material Location	Fill	Universe	n importance
535	0	(-401 402 -403 404 -405 406) (201: -202:203:-204:205: -205) 19 -24	92	7	1

Table B.40: 14.8 w/o Control Assembly Layout

Cell Number	Material Number	Material Location	Lattice	Universe	n importance
536	7	-301 302 -303 304 -305 306	2	92	1


```

fill=-3:3 -3:3 0:0
89 6R
89 2R      20 20 20      89
89 1R      20 20 20 20   89
89         20 20 20 20 20 89
89         20 20 20 20   89 1R
89         20 20 20     89 2R
89         20 20 20     89 6R

```

Figure B.10: Reflector Assembly Configuration

Table B.45: Zr₃Si₂ Canning for Reflector Assembly

Cell Number	Material Number	Material Density	Material Location	Universe	n importance
541	8	1.0735E-02	(-501 502 -503 504 -505 506) (401:- 402:403:-404:405: -406) 19 -24	8	1

Table B.46: Helium Beyond Reflector Assembly

Cell Number	Material Number	Material Density	Material Location	Universe	n importance
542	7	5.3582E-04	501:-502:503:- 504:505:-506:-19:24	8	1

Table B.47: Inner Layer of Can for Borated Shield Assembly

Cell Number	Material Number	Material Location	Fill	Universe	n importance
543	0	-401 402 -403 404 -405 406 19 -24	88	9	1

Table B.48: Borated Shield Assembly Layout

Cell Number	Material	Material Density	Material Location	Lattice	Universe	n importance
544	7	5.3582E-04	-307 308 -309 310 -311 312	2	88	1

```

fill=-3:3 -3:3 0:0
88 6R
88 2R      16 16 16      88
88 1R      16 16 16 16   88
88         16 16 16 16 16 88
88         16 16 16 16   88 1R
88         16 16 16     88 2R
88         16 16 16     88 6R

```

Figure B.11: Borated Shield Assembly Configuration

Table B.49: SiC Canning for Borated Shield Assembly

Cell Number	Material Number	Material Density	Material Location	Universe	n importance
545	6	4.8211E-02	(-501 502 -503 504 -505 506) (401:- 402:403:-404:405: -406) 5 -12	9	1

Table B.50: Helium Beyond Borated Shield Assembly

Cell Number	Material Number	Material Density	Material Location	Universe	n importance
546	7	5.3582E-04	501:-502:503:- 504:505:-506:-5:12	9	1

Table B.51: 20 w/o Fuel Pin Design

Cell Number	Material Number	Atom Density	Surface Cards	Universe	n importance
201	15	8.6819E-02	-4, -20	50	1
202	11	2.7470E-02	-3, 20, -21	50	1
203	15	8.6819E-02	3, -4, 20, -21	50	1
204	15	8.6819E-02	-4, 21, -5	50	1
1	7	5.3582E-04	-3,5, -6	50	1
2	8	1.0735E-02	-2, 6, -7	50	1
3	7	5.3582E-04	2, -3, 6, -7	50	1
4	7	5.3582E-04	-1, 7, -10	50	1
5	1	3.2726E-02	1, -2, 7, -10	50	1
6	7	5.3582E-04	2, -3, 7, -10	50	1
10	8	1.0735E-02	-2, 10, -11	50	1
11	7	5.3582E-04	2, -3, 10, -11	50	1
12	7	5.3582E-04	-3, 11, -12	50	1
13	6	4.8211E-02	3, -4, 5, -12	50	1
14	7	5.3582E-04	4	50	1
205	6	4.8211E-02	-4, 12, -22	50	1
206	11	2.7470E-02	-3, 22, -23	50	1
207	15	8.6819E-02	3, -4, 22, -23	50	1
208	15	8.6819E-02	-4, 23	50	1

Table B.52: 18.1 w/o Fuel Pin Design

Cell Number	Material Number	Atom Density	Surface Cards	Universe	n importance
209	15	8.6819E-02	-4, -20	46	1
210	11	2.7470E-02	-3, 20, -21	46	1
211	15	8.6819E-02	3, -4, 20, -21	46	1
212	15	8.6819E-02	-4, 21, -5	46	1
21	7	5.3582E-04	-3, 5, -6	46	1
22	8	1.0735E-02	-2, 6, -7	46	1
23	7	5.3582E-04	2, -3, 6, -7	46	1
24	7	5.3582E-04	-1, 7, -10	46	1
25	2	3.2728E-02	1, -2, 7, -10	46	1
26	7	5.3582E-04	2, -3, 7, -10	46	1
30	8	1.0735E-02	-2, 10, -11	46	1
31	7	5.3582E-04	2, -3, 10, -11	46	1
32	7	5.3582E-04	-3, 11, -12	46	1
33	6	4.8211E-02	3, -4, 5, -12	46	1
34	7	5.3582E-04	4	46	1
213	6	4.8211E-02	-4, 12, -22	46	1
214	11	2.7470E-02	-3, 22, -23	46	1
215	15	8.6819E-02	3, -4, 22, -23	46	1
216	15	8.6819E-02	-4, 23	46	1

Table B.53: 16.3 w/o Fuel Pin Design

Cell Number	Material Number	Atom Density	Surface Cards	Universe	n importance
217	15	8.6819E-02	-4, -20	42	1
218	11	2.7470E-02	-3, 20, -21	42	1
219	15	8.6819E-02	3, -4, 20, -21	42	1
220	15	8.6819E-02	-4, 21, -5	42	1
41	7	5.3582E-04	-3, 5, -6	42	1
42	8	1.0735E-02	-2, 6, -7	42	1
43	7	5.3582E-04	2, -3, 6, -7	42	1
44	7	5.3582E-04	-1, 7, -10	42	1
45	3	3.2731E-02	1, -2, 7, -10	42	1
46	7	5.3582E-04	2, -3, 7, -10	42	1
50	8	1.0735E-02	-2, 10, -11	42	1
51	7	5.3582E-04	2, -3, 10, -11	42	1
52	7	5.3582E-04	-3, 11, -12	42	1
53	6	4.8211E-02	3, -4, 5, -12	42	1
54	7	5.3582E-04	4	42	1
221	6	4.8211E-02	-4, 12, -22	42	1
222	11	2.7470E-02	-3, 22, -23	42	1
223	15	8.6819E-02	3, -4, 22, -23	42	1
224	15	8.6819E-02	-4, 23	42	1

Table B.54: 15.7 w/o Fuel Pin Design

Cell Number	Material Number	Atom Density	Surface Cards	Universe	n importance
225	15	8.6819E-02	-4, -20	38	1
226	11	2.7470E-02	-3, 20, -21	38	1
227	15	8.6819E-02	3, -4, 20, -21	38	1
228	15	8.6819E-02	-4, 21, -5	38	1
61	7	5.3582E-04	-3, 5, -6	38	1
62	8	1.0735E-02	-2, 6, -7	38	1
63	7	5.3582E-04	2, -3, 6, -7	38	1
64	7	5.3582E-04	-1, 7, -10	38	1
65	4	3.2732E-02	1, -2, 7, -10	38	1
66	7	5.3582E-04	2, -3, 7, -10	38	1
70	8	1.0735E-02	-2, 10, -11	38	1
71	7	5.3582E-04	2, -3, 10, -11	38	1
72	7	5.3582E-04	-3, 11, -12	38	1
73	6	4.8211E-02	3, -4, 5, -12	38	1
74	7	5.3582E-04	4	38	1
229	6	4.8211E-02	-4, 12, -22	38	1
230	11	2.7470E-02	-3, 22, -23	38	1
231	15	8.6819E-02	3, -4, 22, -23	38	1
232	15	8.6819E-02	-4, 23	38	1

Table B.55: 14.8 w/o Fuel Pin Design

Cell Number	Material Number	Atom Density	Surface Cards	Universe	n importance
233	15	8.6819E-02	-4, -20	34	1
234	11	2.7470E-02	-3, 20, -21	34	1
235	15	8.6819E-02	3, -4, 20, -21	34	1
236	15	8.6819E-02	-4, 21, -5	34	1
81	7	5.3582E-04	-3, 5, -6	34	1
82	8	1.0735E-02	-2, 6, -7	34	1
83	7	5.3582E-04	2, -3, 6, -7	34	1
84	7	5.3582E-04	-1, 7, -10	34	1
85	5	3.2733E-02	1, -2, 7, -10	34	1
86	7	5.3582E-04	2, -3, 7, -10	34	1
90	8	1.0735E-02	-2, 10, -11	34	1
91	7	5.3582E-04	2, -3, 10, -11	34	1
92	7	5.3582E-04	-3, 11, -12	34	1
93	6	4.8211E-02	3, -4, 5, -12	34	1
94	7	5.3582E-04	4	34	1
237	6	4.8211E-02	-4, 12, -22	34	1
238	11	2.7470E-02	-3, 22, -23	34	1
239	15	8.6819E-02	3, -4, 22, -23	34	1
240	15	8.6819E-02	-4, 23	34	1

Table B.56: Reflector Pin Design

Cell Number	Material Number	Atom Density	Surface Cards	Universe	n importance
241	15	8.6819E-02	-15, -20	20	1
242	11	2.7470E-02	-17, 20, -21	20	1
243	15	8.6819E-02	17, -15, 20, -21	20	1
244	15	8.6819E-02	-15, 21, -5	20	1
116	8	1.0735E-02	-15, 5, -12	20	1
117	7	5.3582E-04	15	20	1
245	6	4.8211E-02	-15, 12, -22	20	1
246	11	2.7470E-02	-17, 22, -23	20	1
247	15	8.6819E-02	17, -15, 22, -23	20	1
248	15	8.6819E-02	-15, 23	20	1

Table B.57: Borated Shield Pin Design

Cell Number	Material Number	Atom Density	Surface Cards	Universe	n importance
249	15	8.6819E-02	-15, -20	16	1
250	11	2.7470E-02	-17, 20, -21	16	1
251	15	8.6819E-02	17, -15, 20, -21	16	1
252	15	8.6819E-02	-15, 21, -5	16	1
118	11	2.7470E-02	-16	16	1
119	7	5.3582E-04	16, -17	16	1
120	14	6.3057E-02	17, -15	16	1
121	7	5.3582E-04	15	16	1
253	6	4.8211E-02	-15, 12, -22	16	1
254	11	2.7470E-02	-17, 22, -23	16	1
255	15	8.6819E-02	17, -15, 22, -23	16	1
256	15	8.6819E-02	-15, 23	16	1

B.2 GFR Surface Card Data

Table B.58: Cylindrical Surface (cz) Input

Surface Number	Radius (cm)
1	0.1510
2	0.3685
3	0.3785
4	0.4785
13	3.1900
14	3.2900
15	2.0050
16	1.8950
17	1.9050
18	2.0050

Table B.59: General Plane (p) Input

Surface Number	A	B	C	D
103	1	1.7320508076	0	6.78
104	1	1.7320508076	0	-6.78
105	-1	1.7320508076	0	6.78
106	-1	1.7320508076	0	-6.78
203	1	1.7320508076	0	7.24
204	1	1.7320508076	0	-7.24
205	-1	1.7320508076	0	7.24
206	-1	1.7320508076	0	-7.24
303	1.7320508076	1	0	1.256
304	1.7320508076	1	0	-1.256
305	1.7320508076	-1	0	1.256
306	1.7320508076	-1	0	-1.256
309	1.7320508076	1	0	4.663597
310	1.7320508076	1	0	-4.6636
311	1.7320508076	-1	0	4.663597
312	1.7320508076	-1	0	-4.6636
403	1	1.7320508076	0	21.04
404	1	1.7320508076	0	-21.04
405	-1	1.7320508076	0	21.04
406	-1	1.7320508076	0	-21.04
503	1	1.7320508076	0	21.5
504	1	1.7320508076	0	-21.5
505	-1	1.7320508076	0	21.5

Table B.59 (Continued)

Surface Number	A	B	C	D
506	-1	1.7320508076	0	-21.5
603	1	1.7320508076	0	22.2
604	1	1.7320508076	0	-22.2
605	-1	1.7320508076	0	22.2
606	-1	1.7320508076	0	-22.2
703	1.7320508076	1	0	673.508
704	1.7320508076	1	0	-673.508
705	1.7320508076	-1	0	673.508
706	1.7320508076	-1	0	-673.508
803	1.7320508076	1	0	729.388
804	1.7320508076	1	0	-729.388
805	1.7320508076	-1	0	729.388
806	1.7320508076	-1	0	-729.388

Table B60: Vertical Plane (px) Input

Surface Number	Pitch/2 (cm)
101	3.39
102	-3.39
201	3.62
202	-3.62
401	10.52
402	-10.52
501	10.75
502	-10.75
601	11.1
602	-11.1

Table B.61: Horizontal Plane (py) Input

Surface Number	Pitch/2 (cm)
301	0.628
302	-0.628
307	2.331798599
308	-2.331798599
701	336.7539783
702	-336.7539783
801	364.6939783
802	-364.6939783

Table B.62: Axial Elevation Cutoff Plane (pz) Input

Surface Number	Height (cm)
5	0
6	50
7	100
10	234
11	284
12	334

B.3 GFR Data Card Input

Table B.63: kcode Input

Neutrons per keff cycle	Initial Estimate of keff	keff cycle skipped	Total keff cycles run
10000	1	50	250

Table B.64: ksrc Input

Source	x-coordinate	y-coordinate	z-coordinate
1	0.0035	6.514	167
2	4	0	167
3	137.2	0	167
4	-137.2	0	167

Table B.65: Material Card Input for 20 w/o Fuel (m1)

Isotope Identifier	Cross Section Library	Weight Percentage
92235	72c	5.3315E-03
92238	72c	7.5631E-01
94239	72c	1.8089E-01
94241	72c	5.7123E-03
95242	72c	1.9041E-02
96243	72c	9.5205E-04
96245	72c	9.5205E-04
6000	72c	4.7950E-02

Table B.66: Material Card Input for 18.1 w/o Fuel (m2)

Isotope Identifier	Cross Section Library	Weight Percentage
92235	72c	5.4581E-03
92238	72c	7.7427E-01
94239	72c	1.6370E-01
94241	72c	5.1696E-03
95242	72c	1.7232E-03
96243	72c	8.6160E-04
96245	72c	8.6160E-04
6000	72c	4.7954E-02

Table B.67: Material Card Input for 16.3 w/o Fuel (m3)

Isotope Identifier	Cross Section Library	Weight Percentage
92235	72c	5.5780E-03
92238	72c	7.9128E-01
94239	72c	1.4742E-01
94241	72c	4.6555E-03
95242	72c	1.5518E-03
96243	72c	7.7591E-04
96245	72c	7.7591E-04
6000	72c	4.7958E-02

Table B.68: Material Card Input for 15.7 w/o Fuel (m4)

Isotope Identifier	Cross Section Library	Weight Percentage
92235	72c	5.6180E-03
92238	72c	7.9695E-01
94239	72c	1.4200E-01
94241	72c	4.4841E-03
95242	72c	1.4947E-03
96243	72c	7.4735E-04
96245	72c	7.4735E-04
6000	72c	4.7960E-02

Table B.69: Material Card Input for 14.8 w/o Fuel (m5)

Isotope Identifier	Cross Section Library	Weight Percentage
92235	72c	5.6780E-03
92238	72c	8.0546E-01
94239	72c	1.3386E-01
94241	72c	4.2271E-03
95242	72c	1.4090E-03
96243	72c	7.0451E-04
96245	72c	7.0451E-04
6000	72c	4.7962E-02

Table B.70: Material Card Input for SiC (m6) [25]

Isotope Identifier	Cross Section Library	Atom Percentage
14028	72c	4.6115E-01
14029	72c	2.3416E-02
14030	72c	1.5436E-02
6000	72c	5.0000E-01

Table B.71: Material Card Input for Helium (m7) [26]

Isotope Identifier	Cross Section Library	Atom Percentage
2004	72c	1

Table B.72: Material Card Input for Zr₃Si₂ (m8) [25,27]

Isotope Identifier	Cross Section Library	Atom Percentage
40090	72c	3.0870E-01
40091	72c	6.7320E-02
40092	72c	1.0290E-01
40094	72c	1.0428E-01
40096	72c	1.6800E-02
14028	72c	3.6892E-01
14029	72c	1.8773E-02
14030	72c	1.2349E-02

Table B.73: Material Card Input for Natural Boron (m11) [28]

Isotope Identifier	Cross Section Library	Weight Percentage
5010	72c	1.4427E-01
5011	72c	6.3851E-01
6000	72c	2.1722E-01

B.74: Material Card Input for Tungsten (m14) [29]

Isotope Identifier	Cross Section Library	Atom Percentage
74182	72c	2.6620E-01
74183	72c	1.4310E-01
74184	72c	3.0640E-01
74186	72c	2.8430E-01

Table B.75: Material Card Input for Stainless Steel (m15) [30]

Isotope identifier	Cross Section Library	Weight Percentage
6000	72c	3.0000E-02
25055	72c	2.0000E+00
14028	72c	6.8905E-01
14029	72c	3.6238E-01
14030	72c	2.4711E-02
24050	72c	7.5126E-01
24052	72c	1.5066E+01
24053	72c	1.7412E+00
24054	72c	4.4161E-01
28058	72c	9.4077E+00
28060	72c	3.7486E+00
28061	72c	1.6567E-01
28062	72c	5.3688E-01
28064	72c	1.4114E-01
42092	72c	4.2640E-01
42094	72c	2.7156E-01
42095	72c	4.7235E-01
42096	72c	5.0011E-01
42097	72c	2.8932E-01
42098	72c	7.3858E-01
42100	72c	3.0078E-01
15031	72c	4.5000E-02

Table B.75 (Continued)

Isotope identifier	Cross Section Library	Weight Percentage
16032	72c	2.8396E-02
16033	72c	2.3400E-04
16034	72c	1.3630E-03
16036	72c	6.7302E-06
7014	72c	1.0000E-01
26054	72c	3.5028E+00
26056	72c	5.7020E+01
26057	72c	1.3404E+00
26058	72c	1.8151E-01

B.76: Radial Meshing Criteria

Type	Geometry Command	Origin Command
FMESH4:N	Geom=cyl	origin = 0 0 100

B.77: Radial Mesh Data Input for R-Direction

IMESH (cm)	IINTS
48.17	1
96.34	1
144.5	1
192.7	1
240.9	1

B.78: Radial Mesh Input for Z-Direction

JMESH (cm)	JINTS
134	1

B.79: Radial Mesh Input for Theta-Direction

KMESH (rev)	KINTS
1	1

B.80: Axial Meshing Criteria

Type	Geometry Command	Origin Command
FMESH4:N	Geom=cyl	origin = 0 0 100

B.81: Axial Mesh Input for R-Direction

IMESH (cm)	IINTS
240.9	1

B.82: Axial Mesh Input for Z-Direction

JMESH (cm)	JINTS
13.4	1
26.8	1
40.2	1
53.6	1
67	1
80.4	1
93.8	1
107.2	1
120.6	1
134	1

Table B.83: Axial Mesh Input for Theta-Direction

KMESH (rev)	KINTS
1	1

B.84: Print Table Input

Tables
30
32
110

APPENDIX C

MELCOR CALCULATION NOTEBOOK FOR US DOE GFR

This appendix is the calculation notebook for the US DOE GFR MELCOR input deck. The majority of input is based on Reference 3, with exceptions for necessary assumptions and inferences discussed in this thesis. All input contained within this appendix can be found in the file gfr2400d.inp, which is the steady state calculation performed by MELCOR.

C.1 MELGEN ENVIRONMENTAL DATA

CARD	WORD	VALUE
MEG_DIAGFILE	-	'gfr2400g.dia'
MEL_DIAGFILE	-	'gfr2400.dia'
MEG_OUTPUTFILE	-	'gfr2400g.out'
MEL_OUTPUTFILE	-	'gfr2400.out'
PLOTFILE	-	'gfr2400.ptf'
MEG_RESTARTFILE	-	'gfr2400.rst'
MEL_RESTARTFILE	-	'gfr2400.rst'
	CYCLE	NCYCLE
	NREST	-1
MESSAGEFILE	-	'gfr2400.mes'
STATUSFILE	-	'MELSTT_v2-0'
STOPFILE	-	'MELSTP_v2-0'
WRITENEWINP	-	'gfr2400.txt'

C.2 MELGEN EXEC INPUT

CARD	WORD	VALUE
EXEC_INPUT	-	-
EXEC_TITLE	-	'2400-MWGFR(SS)'
EXEC_JOBID	-	'gfr2400-'

C.3 NCG INPUT

CARD	WORD	VALUE
NCG_ID	MNAME	Table C.1

Table C.1: Names for Noncondensable Gases**MNAME**

HE
H2
CO
O2
CO2
CH4

C.4 COR INPUT

CARD	WORD	VALUE
COR_RT	IRTYP	BWR
	MCRP	B4C
COR_GP	RFUEL	3.685E-03
	RCLAD	4.785E-03
	DRGAP	1.000E-04
	PITCH	1.256E-02
COR_VP	RCOR	3.533E+00
	RVESS	3.863E+00
	ILHTRN	0.000E+00
	DZRV	2.80E-01
	DZLH	2.80E-01
	ILHTYP	HEMISPHERE
COR_AVP	RVLH	3.863
	HLST	-2.39
	HCSP	-2.39
COR_TP	NTPCOR	NO
	RNTPCOR	NO
	ICFGAP	NO
	ICFFIS	FISPOWALL
	CFNAME	CORE-POWER

COR_MS	IEUMOD	0	
	IHSDT	0	
	IDTDZ	0	
	ICORCV	1	
COR_SS	IA	Table C.2	
	IR	Table C.2	
	ISSMOD	Table C.2	
	ISSFAI	Table C.2	
	TSSFAI	Table C.2	
	SSMETAL	Table C.2	
	COR_NS	IA	Table C.3
IR		Table C.3	
INSSUP		Table C.3	
METAL		Table C.3	
TNSMAX		Table C.3	
DRNSMN		Table C.3	
COR_ZP		NAXL	24
	Z	Table C.4	
	DZ	Table C.4	
	PORDP	0.4	
	IHSA	Table C.4	
	FZPOW	Table C.4	
	COR_RP	NRAD	8
RINGR		Table C.5	
ASCELA		Table C.5	
IHSR		UHD	
ICFLHF		NO	
ICFCHN		NO	
ICFBYP		NO	
FRPOW		Table C.5	
COR_RBV		IA	Table C.6
		IR	Table C.6
	IREF	Table C.6	
	JREF	Table C.6	
	ICVHC	Table C.6	
	ICVHB	Table C.6	

COR_KFU	IA	Table C.7
	IR	Table C.7
	XMFUUO	Table C.7
	XMFUHT	0.0
	XMFUXM	0.0
	XMFUXO	Table C.7
COR_KCL	IA	Table C.8
	IR	Table C.8
	XMCLZR	Table C.8
	XMCLZX	0.0
	XMCLIN	0.0
COR_KCN	IA	Table C.9
	IR	Table C.9
	XMCNZR	Table C.9
	XMCNXI	Table C.9
	XMCNXO	0.0
COR_KSS	IA	Table C.10
	IR	Table C.10
	XMSSSS	Table C.10
	XMSSSX	0.0
	XMSSZR	Table C.10
	XMSSZX	0.0
COR_KNS	IA	Table C.11
	IR	Table C.11
	XMNSSS	Table C.11
	XMNSSX	Table C.11
	XMNSCP	Table C.11
	XMNSZR	Table C.11
	XMNSZX	Table C.11
COR_CIT	IA	ALL
	IR	ALL
	TFU	763.15
	TCL	763.15
	TCN	763.15
	TCB	0.0
	TPD	0.0
	TSS	763.15
	TNS	763.15
	TPB	0.0

COR_EDR	IA	Table C.12
	IR	Table C.12
	DHYCL	Table C.12
	DHYPD	0.2
	DHYCNC	Table C.12
	DHYCNB	Table C.12
	DHYSS	Table C.12
	DHYNS	Table C.12
	DHYPB	0.2
COR_BFA	IA	Table C.13
	IR	Table C.13
	ASCELR	Table C.13
	AFLOWC	Table C.13
	AFLOWB	Table C.13
COR_SA	IA	Table C.14
	IR	Table C.14
	ASFU	Table C.14
	ASCL	Table C.14
	ASCN	Table C.14
	ASSS	Table C.14
COR_CSA	ASNS	Table C.14
	IA	Table C.15
	IR	Table C.15
	ASCN	Table C.15
	ASCNB	Table C.15
	ASCB	0.0
	ASCBB	0.0
COR_LP	IAXSUP	2
	HDBH2O	0.0
	PPFAIL	2.0E+07
	VFALL	0.0
COR_LH	NLH	2
	NINSLH	0
COR_LHD	NLHT	8
	NLHTA	8
	TLH	763.15
	RADLH	Table C.16
COR_FUM	ICVCAV	LHD-CV004
	XFUMAT	ZR

Table C.2: Supporting Structure Parameters

IA	IR	ISSMOD	ISSFAI	TSSFAI	SSMETAL
5-24	1-5	COLUMN	TSFAIL	5000.0	ZIRC
24	1-7	PLATEG	TSFAIL	5000.0	ZIRC
5	1-7	PLATEG	TSFAIL	5000.0	STEEL
3-4	1-7	PLATE	TSFAIL	5000.0	STEEL
2	1-7	PLATEB	TSFAIL	5000.0	STEEL

Table C.3: Nonsupporting Structure Parameters

IA	IR	INSSUP	METAL	TNSMAX	DRNSMN
24	1-5	ABOVE	STEEL	5000.00	0.00

Table C.4: Axial Elevation Parameters

LEVEL	Z	DZ	IHSA	FZPOW
1	-6.253E+00	3.863E+00	NO	0.0
2	-2.390E+00	4.700E-01	HS70001	0.0
3	-1.920E+00	1.000E-02	HS70002	0.0
4	-1.910E+00	1.100E-01	HS70003	0.0
5	-1.800E+00	8.000E-01	HS70004	0.0
6	-1.000E+00	2.500E-01	HS70005	0.0
7	-7.500E-01	2.500E-01	HS70006	0.0
8	-5.000E-01	2.500E-01	HS70007	0.0
9	-2.500E-01	2.500E-01	HS70008	0.0
10	0.000E+00	1.340E-01	HS70009	8.14052E-01
11	1.340E-01	1.340E-01	HS70010	9.36322E-01
12	2.680E-01	1.340E-01	HS70011	1.03416
13	4.020E-01	1.340E-01	HS70012	1.10157
14	5.360E-01	1.340E-01	HS70013	1.13576
15	6.700E-01	1.340E-01	HS70014	1.13261
16	8.040E-01	1.340E-01	HS70015	1.09637
17	9.380E-01	1.340E-01	HS70016	1.02584
18	1.072	1.340E-01	HS70017	9.23658E-01
19	1.206	1.300E-01	HS70018	7.99659E-01
20	1.340	2.500E-01	HS70019	0.0
21	1.590	2.500E-01	HS70020	0.0
22	1.840	2.500E-01	HS70021	0.0
23	2.090	2.500E-01	HS70022	0.0
24	2.340	7.254E-01	HS70023	0.0

Table C.5: Radial Ring Parameters

RING	RINGR	ASCELA	FRPOW
1	4.817E-01	7.290E-01	1.30056
2	9.634E-01	2.187	1.23019
3	1.445	3.644	1.08502
4	1.927	5.106	8.59784E-01
5	2.409	6.566	5.24439E-01
6	2.857	7.427	0.0
7	3.533	1.357E+01	0.0
8	3.862	7.667	0.0

Table C.6: Coupling of COR Cells and CVH Volumes

IA	IR	IREF	JREF	ICVHC	ICVHB
1	1	0	0	CAV-CV003	CAV-CV003
2	1	0	0	LCP-CV308	LCP-CV408
3-5	1	0	0	LBS-CV309	LBS-CV409
6-7	1	0	0	LRP-CV101	LRP-CV201
8-9	1	0	0	LRR-CV102	LRR-CV202
10-11	1	0	0	COR-CV103	COR-CV203
12-13	1	0	0	COR-CV104	COR-CV204
14-15	1	0	0	COR-CV105	COR-CV205
16-17	1	0	0	COR-CV106	COR-CV206
18-19	1	0	0	COR-CV107	COR-CV207
20-21	1	0	0	URR-CV108	URR-CV208
22-23	1	0	0	URP-CV109	URP-CV209
24	1	0	0	UBS-CV501	UBS-CV601
1	2	1	1		
2	2	0	0	LCP-CV318	LCP-CV418
3-5	2	0	0	LBS-CV319	LBS-CV419
6-7	2	0	0	LRP-CV111	LRP-CV211
8-9	2	0	0	LRR-CV112	LRR-CV212
10-11	2	0	0	COR-CV113	COR-CV213
12-13	2	0	0	COR-CV114	COR-CV214
14-15	2	0	0	COR-CV115	COR-CV215
16-17	2	0	0	COR-CV116	COR-CV216
18-19	2	0	0	COR-CV117	COR-CV217
20-21	2	0	0	URR-CV118	URR-CV218
22-23	2	0	0	URP-CV119	URP-CV219
24	2	0	0	UBS-CV511	UBS-CV611

Table C.6 (Continued)

IA	IR	IREF	JREF	ICVHC	ICVHB
1	3	1	1		
2	3	0	0	LCP-CV328	LCP-CV428
3-5	3	0	0	LBS-CV329	LBS-CV429
6-7	3	0	0	LRP-CV121	LRP-CV221
8-9	3	0	0	LRR-CV122	LRR-CV222
10-11	3	0	0	COR-CV123	COR-CV223
12-13	3	0	0	COR-CV124	COR-CV224
14-15	3	0	0	COR-CV125	COR-CV225
16-17	3	0	0	COR-CV126	COR-CV226
18-19	3	0	0	COR-CV127	COR-CV227
20-21	3	0	0	URR-CV128	URR-CV228
22-23	3	0	0	URP-CV129	URP-CV229
24	3	0	0	UBS-CV521	UBS-CV621
1	4	1	1		
2	4	0	0	LCP-CV338	LCP-CV438
3-5	4	0	0	LBS-CV339	LBS-CV439
6-7	4	0	0	LRP-CV131	LRP-CV231
8-9	4	0	0	LRR-CV132	LRR-CV232
10-11	4	0	0	COR-CV133	COR-CV233
12-13	4	0	0	COR-CV134	COR-CV234
14-15	4	0	0	COR-CV135	COR-CV235
16-17	4	0	0	COR-CV136	COR-CV236
18-19	4	0	0	COR-CV137	COR-CV237
20-21	4	0	0	URR-CV138	URR-CV238
22-23	4	0	0	URP-CV139	URP-CV239
24	4	0	0	UBS-CV531	UBS-CV631
1	5	1	1		
2	5	0	0	LCP-CV348	LCP-CV448
3-5	5	0	0	LBS-CV349	LBS-CV449
6-7	5	0	0	LRP-CV141	LRP-CV241
8-9	5	0	0	LRR-CV142	LRR-CV242
10-11	5	0	0	COR-CV143	COR-CV243
12-13	5	0	0	COR-CV144	COR-CV244
14-15	5	0	0	COR-CV145	COR-CV245
16-17	5	0	0	COR-CV146	COR-CV246
18-19	5	0	0	COR-CV147	COR-CV247
20-21	5	0	0	URR-CV148	URR-CV248
22-23	5	0	0	URP-CV149	URP-CV249
24	5	0	0	UBS-CV541	UBS-CV641

Table C.6 (Continued)

IA	IR	IREF	JREF	ICVHC	ICVHB
1	6	1	1		
2	6	0	0	LCP-CV358	LCP-CV458
3-5	6	0	0	LBS-CV359	LBS-CV459
6-7	6	0	0	ORF-CV151	ORF-CV251
8-9	6	0	0	ORF-CV152	ORF-CV252
10-11	6	0	0	ORF-CV153	ORF-CV253
12-13	6	0	0	ORF-CV154	ORF-CV254
14-15	6	0	0	ORF-CV155	ORF-CV255
16-17	6	0	0	ORF-CV156	ORF-CV256
18-19	6	0	0	ORF-CV157	ORF-CV257
20-21	6	0	0	ORF-CV158	ORF-CV258
22-23	6	0	0	ORF-CV159	ORF-CV259
24	6	0	0	UBS-CV551	UBS-CV651
1	7	1	1		
2	7	0	0	LCP-CV368	LCP-CV468
3-5	7	0	0	LBS-CV369	LBS-CV469
6-7	7	0	0	OBS-CV161	OBS-CV261
8-9	7	0	0	OBS-CV162	OBS-CV262
10-11	7	0	0	OBS-CV163	OBS-CV263
12-13	7	0	0	OBS-CV164	OBS-CV264
14-15	7	0	0	OBS-CV165	OBS-CV265
16-17	7	0	0	OBS-CV166	OBS-CV266
18-19	7	0	0	OBS-CV167	OBS-CV267
20-21	7	0	0	OBS-CV168	OBS-CV268
22-23	7	0	0	OBS-CV169	OBS-CV269
24	7	0	0	UBS-CV561	UBS-CV661
1	8	1	1		
2-5	8	NULL	NULL		
6-9	8	NULL	NULL		
10-19	8	NULL	NULL		
20-23	8	NULL	NULL		
24	8	NULL	NULL		

Table C.7: Mass of Fuel Materials

IA	IR	XMFUUO	XMFOXO
8-9	1	0.0	2.879E+02
10-19	1	2.970E+02	0.0
20-21	1	0.0	2.879E+02
8-9	2	0.0	8.569E+02
10-19	2	8.839E+02	0.0
20-21	2	0.0	8.569E+02
8-9	3	0.0	1.423E+03
10-19	3	1.468E+03	0.0
20-21	3	0.0	1.423E+03
8-9	4	0.0	2.000E+03
10-19	4	2.063E+03	0.0
20-21	4	0.0	2.000E+03
8-9	5	0.0	2.547E+03
10-19	5	2.627E+03	0.0
20-21	5	0	2.547E+03

Table C.8: Mass of Cladding Material

IA	IR	XMCLZR
6-9	1	9.921E+01
10-19	1	5.318E+01
20-23	1	9.921E+01
6-9	2	2.952E+02
10-19	2	1.582E+02
20-23	2	2.952E+02
6-9	3	4.904E+02
10-19	3	2.629E+02
20-23	3	4.904E+02
6-9	4	6.891E+02
10-19	4	3.694E+02
20-23	4	6.891E+02
6-9	5	8.775E+02
10-19	5	4.703E+02
20-23	5	8.775E+02

Table C.9: Mass of Canning Materials

IA	IR	XMCNZR	XMCNXI
5	1	7.433E+01	0.0
6-9	1	2.323E+01	0.0
10-19	1	1.245E+01	0.0
20-23	1	2.323E+01	0.0
24	1	6.740E+01	0.0
5	2	2.230E+02	0.0
6-9	2	6.969E+02	0.0
10-19	2	3.735E+01	0.0
20-23	2	6.969E+02	0.0
24	2	2.002E+02	0.0
5	3	3.717E+02	0.0
6-9	3	1.161E+02	0.0
10-19	3	6.225E+01	0.0
20-23	3	1.161E+02	0.0
24	3	3.370E+02	0.0
5	4	5.203E+02	0.0
6-9	4	1.627E+02	0.0
10-19	4	8.718E+01	0.0
20-23	4	1.627E+02	0.0
24	4	4.718E+02	0.0
5	5	6.690E+02	0.0
6-9	5	2.090E+02	0.0
10-19	5	1.120E+02	0.0
20-23	5	2.090E+02	0.0
24	5	6.066E+02	0.0
5	6	0.0	1.387E+03
6-9	6	0.0	4.335E+02
10-19	6	0.0	2.323E+02
20-23	6	0.0	4.335E+02
24	6	0.0	1.258E+03
5	7	1.384E+03	0.0
6-9	7	4.325E+02	0.0
10-19	7	2.318E+02	0.0
20-23	7	4.325E+02	0.0
24	7	1.255E+03	0.0

Table C.10: Mass of Supporting Structural Material

IA	IR	XMSSS	XMSSZR
2	1	1.533E+03	0.0
3	1	1.786E+01	0.0
4	1	2.547E+01	0.0
5	1	1.342E+02	1.434E+00
6-9	1	0.0	4.482E-01
10-19	1	0.0	2.402E-01
20-23	1	0.0	4.482E-01
24	1	0.0	2.823E+01
2	2	4.599E+03	0.0
3	2	5.358E+01	0.0
4	2	7.641E+01	0.0
5	2	3.994E+02	8.606E+00
6-9	2	0.0	2.689E+00
10-19	2	0.0	1.441E+00
20-23	2	0.0	2.689E+00
24	2	0.0	8.794E+01
2	3	7.666E+03	0.0
3	3	8.929E+01	0.0
4	3	1.274E+02	0.0
5	3	6.636E+02	1.721E+01
6-9	3	0.0	5.379E+00
10-19	3	0.0	2.883E+00
20-23	3	0.0	5.379E+00
24	3	0.0	1.487E+02
2	4	1.073E+04	0.0
3	4	1.250E+02	0.0
4	4	1.783E+02	0.0
5	4	9.320E+02	2.008E+01
6-9	4	0.0	6.275E+00
10-19	4	0.0	3.363E+00
20-23	4	0.0	6.275E+00
24	4	0.0	2.052E+02
2	5	1.380E+04	0.0
3	5	1.607E+02	0.0
4	5	2.292E+02	0.0
5	5	1.187E+03	4.016E+01
6-9	5	0.0	1.255E+01
10-19	5	0.0	6.727E+00

Table C.10 (Continued)

IA	IR	XMSSS	XMSSZR
20-23	5	0.0	1.255E+01
24	5	0.0	2.747E+02
2	6	1.562E+04	0.0
3	6	1.819E+02	0.0
4	6	2.595E+02	0.0
5	6	1.697E+03	0.0
24	6	0.0	3.404E+02
2	7	2.854E+04	0.0
3	7	3.325E+02	0.0
4	7	4.742E+02	0.0
5	7	3.101E+03	0.0
24	7	0.0	6.222E+02

Table C.11: Mass of Nonsupporting Structural Material

IA	IR	XMNSSS	XMNSSX	XMNSCP	XMNSZR	XMNSZX
5	1	7.410E+02	0.0	3.902E+02	0.0	0.0
24	1	7.343E+02	0.0	3.513E+02	0.0	0.0
5	2	2.205E+03	0.0	1.161E+03	0.0	0.0
24	2	2.185E+03	0.0	1.045E+03	0.0	0.0
5	3	3.663E+03	0.0	1.929E+03	0.0	0.0
24	3	3.630E+03	0.0	1.737E+03	0.0	0.0
5	4	5.145E+03	0.0	2.709E+03	0.0	0.0
24	4	5.099E+03	0.0	2.439E+03	0.0	0.0
5	5	6.555E+03	0.0	3.452E+03	0.0	0.0
24	5	6.496E+03	0.0	3.108E+03	0.0	0.0
5	6	2.434E+03	0.0	7.116E+03	0.0	0.0
6-9	6	0.0	0.0	0.0	0.0	6.138E+03
10-19	6	0.0	0.0	0.0	0.0	3.290E+03
20-23	6	0.0	0.0	0.0	0.0	6.138E+03
24	6	3.040E+03	0.0	6.408E+03	3.404E+02	0.0
5	7	4.448E+03	0.0	1.301E+04	0.0	0.0
6-9	7	0.0	3.572E+03	4.294E+03	0.0	0.0
10-19	7	0.0	1.914E+03	2.302E+03	0.0	0.0
20-23	7	0.0	3.572E+03	4.294E+03	0.0	0.0
24	7	5.556E+03	0.0	1.171E+04	6.222E+02	0.0

Table C.12: Equivalent Diameter Record

IA	IR	DHYCL	DHYCNC	DHYCNB	DHYSS	DHYNS
1	1	0.2	0.2	0.2	0.2	0.2
2	1	0.2	0.2	0.2	6.357E-02	0.2
3	1	0.2	0.2	0.2	7.129E-02	0.2
4	1	0.2	0.2	0.2	1.113E-01	0.2
5	1	0.2	8.583E-03	1.423E-02	9.371E-03	9.271E-03
6-23	1	9.271E-03	8.583E-03	1.423E-02	6.780E-02	0.2
24	1	0.2	8.583E-03	1.423E-02	6.780E-02	9.271E-03
1	2	0.2	0.2	0.2	0.2	0.2
2	2	0.2	0.2	0.2	6.357E-02	0.2
3	2	0.2	0.2	0.2	7.129E-02	0.2
4	2	0.2	0.2	0.2	1.113E-01	0.2
5	2	0.2	8.674E-03	1.423E-02	9.492E-03	9.292E-03
6-23	2	9.292E-03	8.674E-03	1.423E-02	6.780E-02	0.2
24	2	0.2	8.674E-03	1.423E-02	6.780E-02	9.292E-03
1	3	0.2	0.2	0.2	0.2	0.2
2	3	0.2	0.2	0.2	6.357E-02	0.2
3	3	0.2	0.2	0.2	7.129E-02	0.2
4	3	0.2	0.2	0.2	1.113E-01	0.2
5	3	0.2	8.711E-03	1.423E-02	9.541E-03	9.300E-03
6-23	3	9.300E-03	8.711E-03	1.423E-02	6.780E-02	0.2
24	3	0.2	8.711E-03	1.423E-02	6.780E-02	9.300E-03
1	4	0.2	0.2	0.2	0.2	0.2
2	4	0.2	0.2	0.2	6.357E-02	0.2
3	4	0.2	0.2	0.2	7.129E-02	0.2
4	4	0.2	0.2	0.2	1.113E-01	0.2
5	4	0.2	8.674E-03	1.423E-02	9.492E-03	9.292E-03
6-23	4	9.292E-03	8.674E-03	1.423E-02	6.780E-02	0.2
24	4	0.2	8.674E-03	1.423E-02	6.780E-02	9.292E-03
1	5	0.2	0.2	0.2	0.2	0.2
2	5	0.2	0.2	0.2	6.357E-02	0.2
3	5	0.2	0.2	0.2	7.129E-02	0.2
4	5	0.2	0.2	0.2	1.113E-01	0.2
5	5	0.2	8.777E-03	1.423E-02	9.628E-03	9.315E-03
6-23	5	9.315E-03	8.777E-03	1.423E-02	6.780E-02	0.2
24	5	0.2	8.777E-03	1.423E-02	6.780E-02	9.315E-03

Table C.12 (Continued)

IA	IR	DHYCL	DHYCNC	DHYCNB	DHYSS	DHYNS
1	6	0.2	0.2	0.2	0.2	0.2
2	6	0.2	0.2	0.2	6.357E-02	0.2
3	6	0.2	0.2	0.2	7.129E-02	0.2
4	6	0.2	0.2	0.2	1.113E-01	0.2
5	6	0.2	1.669E-02	1.423E-02	2.215E-02	2.215E-02
6-23	6	0.2	1.669E-02	1.423E-02	0.2	2.215E-02
24	6	0.2	1.669E-02	1.423E-02	2.215E-02	2.215E-02
1	7	0.2	0.2	0.2	0.2	0.2
2	7	0.2	0.2	0.2	6.357E-02	0.2
3	7	0.2	0.2	0.2	7.129E-02	0.2
4	7	0.2	0.2	0.2	1.113E-01	0.2
5	7	0.2	1.669E-02	1.423E-02	2.215E-02	2.215E-02
6-23	7	0.2	1.669E-02	1.423E-02	0.2	2.215E-02
24	7	0.2	1.669E-02	1.423E-02	2.215E-02	2.215E-02
1	8	0.2	0.2	0.2	0.2	0.2

Table C.13: Boundary Flow Areas

IA	IR	ASCELR	AFLOWC	AFLOWB
1	1	1.169E+01	7.290E-01	0.0
2	1	1.423E+00	3.417E-01	1.131E-02
3	1	3.027E-02	3.417E-01	4.525E-02
4	1	3.329E-01	6.548E-01	4.525E-02
5	1	2.421E+00	3.240E-01	4.525E-02
6-9	1	7.567E-01	3.240E-01	4.525E-02
10-19	1	4.056E-01	3.240E-01	4.525E-02
20-23	1	7.567E-01	3.240E-01	4.525E-02
24	1	2.196E+00	3.240E-01	4.525E-02
1	2	2.338E+01	2.187E+00	0.0
2	2	2.845E+00	1.025E+00	3.394E-02
3	2	6.053E-02	1.025E+00	1.357E-01
4	2	6.659E-01	1.964E+00	1.357E-01
5	2	4.843E+00	9.782E-01	1.357E-01
6-9	2	1.513E+00	9.782E-01	1.357E-01
10-19	2	8.111E-01	9.782E-01	1.357E-01
20-23	2	1.513E+00	9.782E-01	1.357E-01
24	2	4.391E+00	9.782E-01	1.357E-01

Table C.13 (Continued)

IA	IR	ASCELR	AFLOWC	AFLOWB
1	3	3.507E+01	3.644E+00	0.0
2	3	4.267E+00	1.709E+00	5.656E-02
3	3	9.079E-02	1.709E+00	2.262E-01
4	3	9.987E-01	3.274E+00	2.262E-01
5	3	7.623E+00	1.635E+00	2.262E-01
6-9	3	2.270E+00	1.635E+00	2.262E-01
10-19	3	1.217E+00	1.635E+00	2.262E-01
20-23	3	2.270E+00	1.635E+00	2.262E-01
24	3	6.586E+00	1.635E+00	2.262E-01
1	4	4.677E+01	5.106E+00	0.0
2	4	5.691E+00	2.392E+00	7.918E-02
3	4	1.211E-01	2.392E+00	3.167E-01
4	4	1.332E+00	4.584E+00	3.167E-01
5	4	9.686E+00	2.282E+00	3.167E-01
6-9	4	3.027E+00	2.282E+00	3.167E-01
10-19	4	1.622E+00	2.282E+00	3.167E-01
20-23	4	3.027E+00	2.282E+00	3.167E-01
24	4	8.783E+00	2.282E+00	3.167E-01
1	5	5.847E+01	6.566E+00	0.0
2	5	7.114E+00	3.076E+00	1.018E-01
3	5	1.514E-01	3.076E+00	4.072E-01
4	5	1.665E+00	5.893E+00	4.072E-01
5	5	1.211E+01	2.956E+00	4.072E-01
6-9	5	3.784E+00	2.956E+00	4.072E-01
10-19	5	2.028E+00	2.956E+00	4.072E-01
20-23	5	3.784E+00	2.956E+00	4.072E-01
24	5	1.098E+01	2.956E+00	4.072E-01
1	6	6.934E+01	7.412E+00	0.0
2	6	8.437E+00	3.482E+00	1.152E-01
3	6	1.795E-01	3.482E+00	4.610E-01
4	6	1.975E+00	6.671E+00	4.610E-01
5	6	1.436E+01	2.306E+00	4.610E-01
6-9	6	4.488E+00	2.306E+00	4.610E-01
10-19	6	2.405E+00	2.306E+00	4.610E-01
20-23	6	4.488E+00	2.306E+00	4.610E-01
24	6	1.302E+01	2.306E+00	4.610E-01

Table C.13 (Continued)

IA	IR	ASCELR	AFLOWC	AFLOWB
1	7	8.575E+01	1.357E+01	0.0
2	7	1.043E+01	6.363E+00	2.106E-01
3	7	2.220E-01	6.363E+00	8.424E-01
4	7	2.442E+00	1.219E+01	8.424E-01
5	7	1.776E+01	4.214E+00	8.424E-01
6-9	7	5.550E+00	4.214E+00	8.424E-01
10-19	7	1.610E+01	4.214E+00	8.424E-01
20-23	7	5.550E+00	4.214E+00	8.424E-01
24	7	1.610E+01	4.214E+00	8.424E-01
1	8	9.376E+01	7.668E+00	0.0

Table C.14: Surface Areas

IA	IR	ASFU	ASCL	ASCN	ASSS	ASNS
1	1	0.0	0.0	0.0	0.0	0.0
2	1	0.0	0.0	0.0	1.005E+01	0.0
3	1	0.0	0.0	0.0	1.272E-01	0.0
4	1	0.0	0.0	0.0	1.399E+00	0.0
5	1	0.0	0.0	9.959E+00	7.214E+00	1.034E+02
6-7	1	0.0	3.451E+01	3.112E+00	6.270E-02	0.0
8-9	1	2.658E+01	3.451E+01	3.112E+00	6.270E-02	0.0
10-19	1	1.425E+01	1.850E+01	1.668E+00	3.361E-02	0.0
20-21	1	2.658E+01	3.451E+01	3.112E+00	6.270E-02	0.0
22-23	1	0.0	3.451E+01	3.112E+00	6.270E-02	0.0
24	1	0.0	0.0	9.030E+00	3.688E+00	9.663E+01
1	2	0.0	0.0	0.0	0.0	0.0
2	2	0.0	0.0	0.0	1.771E+01	0.0
3	2	0.0	0.0	0.0	3.816E-01	0.0
4	2	0.0	0.0	0.0	4.198E+00	0.0
5	2	0.0	0.0	2.988E+01	2.207E+01	3.078E+02
6-7	2	0.0	1.027E+02	9.337E+00	3.762E-01	0.0
8-9	2	7.909E+01	1.027E+02	9.337E+00	3.762E-01	0.0
10-19	2	4.239E+01	5.505E+01	5.004E+00	2.016E-01	0.0
20-21	2	7.909E+01	1.027E+01	9.337E+00	3.762E-01	0.0
22-23	2	0.0	1.027E+01	9.337E+00	3.762E-01	0.0
24	2	0.0	0.0	2.709E+01	1.153E+01	2.876E+02

Table C.14 (Continued)

IA	IR	ASFU	ASCL	ASCN	ASSS	ASNS
1	3	0.0	0.0	0.0	0.0	0.0
2	3	0.0	0.0	0.0	2.538E+01	0.0
3	3	0.0	0.0	0.0	6.360E-01	0.0
4	3	0.0	0.0	0.0	6.996E+00	0.0
5	3	0.0	0.0	4.979E+01	3.708E+01	5.113E+02
6-7	3	0.0	1.706E+02	1.556E+01	7.524E-01	0.0
8-9	3	1.314E+02	1.706E+02	1.556E+01	7.524E-01	0.0
10-19	3	7.043E+01	9.145E+01	8.341E+00	4.033E-01	0.0
20-21	3	1.314E+02	1.706E+02	1.556E+01	7.524E-01	0.0
22-23	3	0.0	1.706E+01	1.556E+01	7.524E-01	0.0
24	3	0.0	0.0	4.515E+01	1.952E+01	4.777E+02
1	4	0.0	0.0	0.0	0.0	0.0
2	4	0.0	0.0	0.0	3.306E+01	0.0
3	4	0.0	0.0	0.0	8.908E-01	0.0
4	4	0.0	0.0	0.0	9.798E+00	0.0
5	4	0.0	0.0	6.974E+01	5.152E+01	7.184E+02
6-7	4	0.0	2.397E+02	2.179E+01	8.778E-01	0.0
8-9	4	1.846E+02	2.397E+02	2.179E+01	8.778E-01	0.0
10-19	4	9.895E+01	1.285E+02	1.168E+01	4.705E-01	0.0
20-21	4	1.846E+02	2.397E+02	2.179E+01	8.778E-01	0.0
22-23	4	0.0	2.397E+02	2.179E+01	8.778E-01	0.0
24	4	0.0	0.0	6.323E+01	2.690E+01	6.712E+02
1	5	0.0	0.0	0.0	0.0	0.0
2	5	0.0	0.0	0.0	4.071E+01	0.0
3	5	0.0	0.0	0.0	1.145E+00	0.0
4	5	0.0	0.0	0.0	1.259E+01	0.0
5	5	0.0	0.0	8.961E+01	6.764E+01	9.148E+02
6-7	5	0.0	3.052E+02	2.800E+01	1.756E+00	0.0
8-9	5	2.351E+02	3.052E+02	2.800E+01	1.756E+00	0.0
10-19	5	1.260E+02	1.636E+02	1.501E+01	9.410E-01	0.0
20-21	5	2.351E+02	3.052E+02	2.800E+01	1.756E+00	0.0
22-23	5	0.0	3.052E+02	2.800E+01	1.756E+00	0.0
24	5	0.0	0.0	8.125E+01	3.611E+01	8.547E+02
1	6	0.0	0.0	0.0	0.0	0.0
2	6	0.0	0.0	0.0	4.527E+01	0.0
3	6	0.0	0.0	0.0	1.296E+00	0.0
4	6	0.0	0.0	0.0	1.426E+01	0.0
5	6	0.0	0.0	1.015E+02	2.116E+01	3.120E+02
6-9	6	0.0	0.0	3.170E+01	0.0	1.041E+02
10-19	6	0.0	0.0	1.699E+01	0.0	5.581E+01

Table C.14 (Continued)

IA	IR	ASFU	ASCL	ASCN	ASSS	ASNS
20-23	6	0.0	0.0	3.170E+01	0.0	1.041E+02
24	6	0.0	0.0	9.199E+01	1.058E+01	2.915E+02
1	7	0.0	0.0	0.0	0.0	0.0
2	7	0.0	0.0	0.0	7.758E+01	0.0
3	7	0.0	0.0	0.0	2.368E+00	0.0
4	7	0.0	0.0	0.0	2.605E+01	0.0
5	7	0.0	0.0	1.854E+02	3.867E+01	5.703E+02
6-9	7	0.0	0.0	5.794E+01	0.0	1.903E+02
10-19	7	0.0	0.0	3.106E+01	0.0	1.020E+02
20-23	7	0.0	0.0	5.794E+01	0.0	1.903E+02
24	7	0.0	0.0	1.681E+02	1.933E+01	5.328E+02
1	8	0.0	0.0	0.0	0.0	0.0

Table C.15: Can Surface Areas

IA	IR	ASCN	ASCNB
5	1	9.959E+00	1.018E+01
6-9	1	3.112E+00	3.180E+00
10-19	1	1.668E+00	1.705E+00
20-23	1	3.112E+00	3.180E+00
24	1	9.030E+00	9.228E+00
5	2	2.988E+01	3.053E+01
6-9	2	9.337E+00	9.541E+00
10-19	2	5.004E+00	5.114E+00
20-23	2	9.337E+00	9.541E+00
24	2	2.709E+01	2.768E+01
5	3	4.979E+01	5.088E+01
6-9	3	1.556E+01	1.590E+01
10-19	3	8.341E+00	8.523E+00
20-23	3	1.556E+01	1.590E+01
24	3	4.515E+01	4.614E+01
5	4	6.974E+01	7.126E+01
6-9	4	2.179E+01	2.227E+01
10-19	4	1.168E+01	1.194E+01
20-23	4	2.179E+01	2.227E+01
24	4	6.323E+01	6.462E+01

Table C.15 (Continued)

IA	IR	ASCN	ASCNB
5	5	8.961E+01	9.157E+01
6-9	5	2.800E+01	2.861E+01
10-19	5	1.501E+01	1.534E+01
20-23	5	2.800E+01	2.961E+01
24	5	8.125E+01	8.303E+01
5	6	1.015E+02	1.037E+02
6-9	6	3.170E+01	3.240E+01
10-19	6	1.699E+01	1.737E+01
20-23	6	3.170E+01	3.240E+01
24	6	9.199E+01	9.401E+01
5	7	1.854E+02	1.895E+02
6-9	7	5.794E+01	5.921E+01
10-19	7	3.106E+01	3.174E+01
20-23	7	5.794E+01	5.921E+01
24	7	1.681E+02	1.718E+02

Table C.16: Radial Rings in Lower Head

RING	RADLH
1	4.817E-01
2	9.634E-01
3	1.445
4	1.927
5	2.409
6	2.857
7	3.533
8	3.863

C.5 GENERAL CVH INPUT

CARD	WORD	VALUE
CV_ID	CVNAME	Table C.17
	ICVNUM	Table C.17
CV_THR	ICVTHR	NONEQUIL
	IPFSW	FOG
	ICVACT	ACTIVE

CV_PAS	ITYPTH IPORA VAPORSTATE	SEPARATE ONLYATM SUPERHEATED
CV_PTD	PTDID PVOL	PVOL 7.00E+06
CV_AAD	ATMID TATM	TATM 763.15
CV_NCG	NMMAT NCGID RHUM NAMGAS MLFR	1 RHUM 0 HE 1
CV_VAT	ICVVZP CVZ CVVOL	CV SPECIFIC Table C.17 Table C.17

Table C.17: General CVH Properties

CVNAME	ICVNUM	Bottom El. (m)	Top El. (m)	Volume (m ³)
LCP-CV308	308	-2.390	1.920	1.606E-01
LBS-CV309	309	-1.920	-1.000	3.346E-01
LRP-CV101	101	-1.000	-0.500	1.620E-01
LRR-CV102	102	-0.500	0.000	1.620E-01
COR-CV103	103	0.000	0.268	8.684E-02
COR-CV104	104	0.268	0.536	8.684E-02
COR-CV105	105	0.536	0.804	8.684E-02
COR-CV106	106	0.804	1.072	8.684E-02
COR-CV107	107	1.072	1.340	8.684E-02
URR-CV108	108	1.340	1.840	1.620E-01
URP-CV109	109	1.840	2.340	1.620E-01
UBS-CV501	501	2.340	3.0654	2.350E-01
LCP-CV318	318	-2.390	1.920	4.818E-01
LBS-CV319	319	-1.920	-1.000	1.009E+00
LRP-CV111	111	-1.000	-0.500	4.892E-01
LRR-CV112	112	-0.500	0.000	4.892E-01
COR-CV113	113	0.000	0.268	2.622E-01
COR-CV114	114	0.268	0.536	2.622E-01
COR-CV115	115	0.536	0.804	2.622E-01
COR-CV116	116	0.804	1.072	2.622E-01
COR-CV117	117	1.072	1.340	2.622E-01
URR-CV118	118	1.340	1.840	4.892E-01
URP-CV119	119	1.840	2.340	4.892E-01

Table C.17 (Continued)

CVNAME	ICVNUM	Bottom El. (m)	Top El. (m)	Volume (m ³)
UBS-CV511	511	2.340	3.0654	7.096E-01
LCP-CV328	328	-2.390	1.920	8.032E-01
LBS-CV329	329	-1.920	-1.000	1.685E+00
LRP-CV121	121	-1.000	-0.500	8.176E-01
LRR-CV122	122	-0.500	0.000	8.176E-01
COR-CV123	123	0.000	0.268	4.382E-01
COR-CV124	124	0.268	0.536	4.382E-01
COR-CV125	125	0.536	0.804	4.382E-01
COR-CV126	126	0.804	1.072	4.382E-01
COR-CV127	127	1.072	1.340	4.382E-01
URR-CV128	128	1.340	1.840	8.176E-01
URP-CV129	129	1.840	2.340	8.176E-01
UBS-CV521	521	2.340	3.0654	1.186E+00
LCP-CV338	338	-2.390	1.920	1.124E+00
LBS-CV339	339	-1.920	-1.000	2.354E+00
LRP-CV131	131	-1.000	-0.500	1.141E+00
LRR-CV132	132	-0.500	0.000	1.141E+00
COR-CV133	133	0.000	0.268	6.116E-01
COR-CV134	134	0.268	0.536	6.116E-01
COR-CV135	135	0.536	0.804	6.116E-01
COR-CV136	136	0.804	1.072	6.116E-01
COR-CV137	137	1.072	1.340	6.116E-01
URR-CV138	138	1.340	1.840	1.141E+00
URP-CV139	139	1.840	2.340	1.141E+00
UBS-CV531	531	2.340	3.0654	1.655E+00
LCP-CV348	348	-2.390	1.920	1.446E+00
LBS-CV349	349	-1.920	-1.000	3.044E+00
LRP-CV141	141	-1.000	-0.500	1.478E+00
LRR-CV142	142	-0.500	0.000	1.478E+00
COR-CV143	143	0.000	0.268	7.922E-01
COR-CV144	144	0.268	0.536	7.922E-01
COR-CV145	145	0.536	0.804	7.922E-01
COR-CV146	146	0.804	1.072	7.922E-01
COR-CV147	147	1.072	1.340	7.922E-01
URR-CV148	148	1.340	1.840	1.478E+00
URP-CV149	149	1.840	2.340	1.478E+00
UBS-CV541	541	2.340	3.0654	2.144E+00

Table C.17 (Continued)

CVNAME	ICVNUM	Bottom El. (m)	Top El. (m)	Volume (m ³)
LCP-CV358	358	-2.390	1.920	1.637E+00
LBS-CV359	359	-1.920	-1.000	2.614E+00
ORF-CV151	151	-1.000	-0.500	1.153E+00
ORF-CV152	152	-0.500	0.000	1.153E+00
ORF-CV153	153	0.000	0.268	6.180E-01
ORF-CV154	154	0.268	0.536	6.180E-01
ORF-CV155	155	0.536	0.804	6.180E-01
ORF-CV156	156	0.804	1.072	6.180E-01
ORF-CV157	157	1.072	1.340	6.180E-01
ORF-CV158	158	1.340	1.840	1.153E+00
ORF-CV159	159	1.840	2.340	1.153E+00
UBS-CV551	551	2.340	3.0654	1.673E+00
LCP-CV368	368	-2.390	1.920	2.991E+00
LBS-CV369	369	-1.920	-1.000	4.776E+00
OBS-CV161	161	-1.000	-0.500	2.108E+00
OBS-CV162	162	-0.500	0.000	2.108E+00
OBS-CV163	163	0.000	0.268	1.129E+00
OBS-CV164	164	0.268	0.536	1.129E+00
OBS-CV165	165	0.536	0.804	1.129E+00
OBS-CV166	166	0.804	1.072	1.129E+00
OBS-CV167	167	1.072	1.340	1.129E+00
OBS-CV168	168	1.340	1.840	2.108E+00
OBS-CV169	169	1.840	2.340	2.108E+00
UBS-CV561	561	2.340	3.0654	3.057E+00
LCP-CV408	408	-2.390	1.920	5.316E-03
LBS-CV409	409	-1.920	-1.000	4.706E-02
LRP-CV201	201	-1.000	-0.500	2.262E-02
LRR-CV202	202	-0.500	0.000	2.262E-02
COR-CV203	203	0.000	0.268	1.213E-02
COR-CV204	204	0.268	0.536	1.213E-02
COR-CV205	205	0.536	0.804	1.213E-02
COR-CV206	206	0.804	1.072	1.213E-02
COR-CV207	207	1.072	1.340	1.213E-02
URR-CV208	208	1.340	1.840	2.262E-02
URP-CV209	209	1.840	2.340	2.262E-02
UBS-CV601	601	2.340	3.0654	3.282E-02
LCP-CV418	418	-2.390	1.920	1.595E-02
LBS-CV419	419	-1.920	-1.000	1.412E-01

Table C.17 (Continued)

CVNAME	ICVNUM	Bottom El. (m)	Top El. (m)	Volume (m ³)
LRP-CV211	211	-1.000	-0.500	6.788E-02
LRR-CV212	212	-0.500	0.000	6.788E-02
COR-CV213	213	0.000	0.268	3.638E-02
COR-CV214	214	0.268	0.536	3.638E-02
COR-CV215	215	0.536	0.804	3.638E-02
COR-CV216	216	0.804	1.072	3.638E-02
COR-CV217	217	1.072	1.340	3.638E-02
URR-CV218	218	1.340	1.840	6.788E-02
URP-CV219	219	1.840	2.340	6.788E-02
UBS-CV611	611	2.340	3.0654	9.844E-02
LCP-CV428	428	-2.390	1.920	2.658E-02
LBS-CV429	429	-1.920	-1.000	2.081E-01
LRP-CV221	221	-1.000	-0.500	1.131E-01
LRR-CV222	222	-0.500	0.000	1.131E-01
COR-CV223	223	0.000	0.268	6.064E-02
COR-CV224	224	0.268	0.536	6.064E-02
COR-CV225	225	0.536	0.804	6.064E-02
COR-CV226	226	0.804	1.072	6.064E-02
COR-CV227	227	1.072	1.340	6.064E-02
URR-CV228	228	1.340	1.840	1.131E-01
URP-CV229	229	1.840	2.340	1.131E-01
UBS-CV621	621	2.340	3.0654	1.641E-01
LCP-CV438	438	-2.390	1.920	3.721E-02
LBS-CV439	439	-1.920	-1.000	2.914E-01
LRP-CV231	231	-1.000	-0.500	1.584E-01
LRR-CV232	232	-0.500	0.000	1.584E-01
COR-CV233	233	0.000	0.268	8.488E-02
COR-CV234	234	0.268	0.536	8.488E-02
COR-CV235	235	0.536	0.804	8.488E-02
COR-CV236	236	0.804	1.072	8.488E-02
COR-CV237	237	1.072	1.340	8.488E-02
URR-CV238	238	1.340	1.840	1.584E-01
URP-CV239	239	1.840	2.340	1.584E-01
UBS-CV631	631	2.340	3.0654	2.297E-01
LCP-CV448	448	-2.390	1.920	4.785E-02
LBS-CV449	449	-1.920	-1.000	3.747E-01
LRP-CV241	241	-1.000	-0.500	2.036E-01
LRR-CV242	242	-0.500	0.000	2.036E-01
COR-CV243	243	0.000	0.268	1.091E-01

Table C.17 (Continued)

CVNAME	ICVNUM	Bottom El. (m)	Top El. (m)	Volume (m ³)
COR-CV244	244	0.268	0.536	1.091E-01
COR-CV245	245	0.536	0.804	1.091E-01
COR-CV246	246	0.804	1.072	1.091E-01
COR-CV247	247	1.072	1.340	1.091E-01
URR-CV248	248	1.340	1.840	2.036E-01
URP-CV249	249	1.840	2.340	2.036E-01
UBS-CV641	641	2.340	3.0654	2.954E-01
LCP-CV458	459	-2.390	1.920	5.414E-02
LBS-CV459	459	-1.920	-1.000	4.241E-01
ORF-CV251	251	-1.000	-0.500	2.304E-01
ORF-CV252	252	-0.500	0.000	2.304E-01
ORF-CV253	253	0.000	0.268	1.235E-01
ORF-CV254	254	0.268	0.536	1.235E-01
ORF-CV255	255	0.536	0.804	1.235E-01
ORF-CV256	256	0.804	1.072	1.235E-01
ORF-CV257	257	1.072	1.340	1.235E-01
ORF-CV258	258	1.340	1.840	2.304E-01
ORF-CV259	259	1.840	2.340	2.304E-01
UBS-CV651	651	2.340	3.0654	3.344E-01
LCP-CV468	468	-2.390	1.920	9.898E-02
LBS-CV469	469	-1.920	-1.000	7.750E-01
OBS-CV261	261	-1.000	-0.500	4.212E-01
OBS-CV262	262	-0.500	0.000	4.212E-01
OBS-CV263	263	0.000	0.268	2.258E-01
OBS-CV264	264	0.268	0.536	2.258E-01
OBS-CV265	265	0.536	0.804	2.258E-01
OBS-CV266	266	0.804	1.072	2.258E-01
OBS-CV267	267	1.072	1.340	2.258E-01
OBS-CV268	268	1.340	1.840	4.212E-01
OBS-CV269	269	1.840	2.340	4.212E-01
UBS-CV661	661	2.340	3.0654	6.111E-01
HS-CV700	700	-2.390	-1.000	9.872E+00
HS-CV701	701	-1.000	0.000	7.102E+00
HS-CV702	702	0.000	1.340	9.517E+00
HS-CV703	703	1.340	2.340	7.102E+00
HS-CV704	704	2.340	3.0654	5.152E+00
CAV-CV003	003	-6.253	-2.390	1.811E+02
LHD-CV004	004	-6.253	-2.390	1.811E+02

C.6 SOURCE CVH INPUT

CARD	WORD	VALUE
CV_ID	CVNAME	SRC-CV001
	ICVNUM	001
CV_THR	ICVTHR	NONEQUIL
	IPFSW	FOG
	ICVACT	PROP-SPECIFIED
CV_PAS	ITYPTH	SEPARATE
	IPORA	ONLYATM
	VAPORSTATE	SUPERHEATED
CV_PTD	PTDID	PVOL
	PVOL	CF 'COOL-SOURCE-P'
CV_AAD	ATMID	TATM
	TATM	CF 'COOL-SOURCE-T'
CV_NCG	NMMAT	1
	NCGID	RHUM
	RHUM	CF 'COOL-SOURCE-RHUM'
	NAMGAS	HE
	MLFR	CF 'COOL-SOURCE-HE-FRACTION'
CV_VAT	ICVVZP	2
	CVZ	Table C.18
	CVVOL	Table C.18

Table C.18: CVH Source Volume Altitude Parameters

Bottom El. (m)	Top El. (m)	Volume (m³)
3.0654	3.5654	3.551

C.7 SINK CVH INPUT

CARD	WORD	VALUE
CV_ID	CVNAME	UHD-CV005
	ICVNUM	005
CV_THR	ICVTHR	NONEQUIL
	IPFSW	FOG
	ICVACT	PROP-SPECIFIED
CV_PAS	ITYPTH	SEPARATE
	IPORA	ONLYATM
	VAPORSTATE	SUPERHEATED

CV_PTD	PTDID	PVOL
	PVOL	CF 'COOL-SINK-P'
CV_AAD	ATMID	TATM
	TATM	CF 'COOL-SINK-T'
CV_NCG	NMMAT	1
	NCGID	RHUM
	RHUM	CF 'COOL-SINK-RHUM'
	NAMGAS	HE
	MLFR	CF 'COOL-SINK-HE-FRACTION'
CV_VAT	ICVVZP	2
	CVZ	Table C.19
	CVVOL	Table C.19

Table C.19: CVH Sink Volume Altitude Parameters

Bottom El. (m)	Top El. (m)	Volume (m³)
3.0654	6.9284	1.81E+02

C.8 GENERAL FLOW PATH INPUT

CARD	WORD	VALUE
FL_ID	FPNAME	Table C.20
	IFPNUM	Table C.20
FL_FT	KCVFM	Table C.20
	KCVTO	Table C.20
	ZFM	Table C.21
	ZTO	Table C.21
FL_GEO	FLARA	Table C.22
	FLEN	Table C.22
	FLOPO	1.0
FL_JSW	KFLGFL	Table C.21
FL_USL	FRICFO	Table C.22
	FRICRO	Table C.22
FL_SEG	INPSG	Table C.23
	NSEG	Table C.23
	SAREA	Table C.23
	SLEN	Table C.23
	SHYD	Table C.23
	SRGH	Table C.23

Table C.20: Flow Path Definitions and Connections

FPNAME	IFPNUM	KCVFM	KCVTO
LCP-FL308	308	LCP-CV308	LBS-CV309
LBS-FL309	309	LBS-CV309	LRP-CV101
LRP-FL101	101	LRP-CV101	LRR-CV102
LRR-FL102	102	LRR-CV102	COR-CV103
COR-FL103	103	COR-CV103	COR-CV104
COR-FL104	104	COR-CV104	COR-CV105
COR-FL105	105	COR-CV105	COR-CV106
COR-FL106	106	COR-CV106	COR-CV107
COR-FL107	107	COR-CV107	URR-CV108
URR-FL108	108	URR-CV108	URP-CV109
UBS-FL501	501	URP-CV109	UBS-CV501
LCP-FL318	318	LCP-CV318	LBS-CV319
LBS-FL319	319	LBS-CV319	LRP-CV111
LRP-FL111	111	LRP-CV111	LRR-CV112
LRR-FL112	112	LRR-CV112	COR-CV113
COR-FL113	113	COR-CV113	COR-CV114
COR-FL114	114	COR-CV114	COR-CV115
COR-FL115	115	COR-CV115	COR-CV116
COR-FL116	116	COR-CV116	COR-CV117
COR-FL117	117	COR-CV117	URR-CV118
URR-FL118	118	URR-CV118	URP-CV119
UBS-FL511	511	URP-CV119	UBS-CV511
LCP-FL328	328	LCP-CV328	LBS-CV329
LBS-FL329	329	LBS-CV329	LRP-CV121
LRP-FL121	121	LRP-CV121	LRR-CV122
LRR-FL122	122	LRR-CV122	COR-CV123
COR-FL123	123	COR-CV123	COR-CV124
COR-FL124	124	COR-CV124	COR-CV125
COR-FL125	125	COR-CV125	COR-CV126
COR-FL126	126	COR-CV126	COR-CV127
COR-FL127	127	COR-CV127	URR-CV128
URR-FL128	128	URR-CV128	URP-CV129
UBS-FL521	521	URP-CV129	UBS-CV521
LCP-FL338	338	LCP-CV338	LBS-CV339
LBS-FL339	339	LBS-CV339	LRP-CV131
LRP-FL131	131	LRP-CV131	LRR-CV132
LRR-FL132	132	LRR-CV132	COR-CV133
COR-FL133	133	COR-CV133	COR-CV134

Table C.20 (Continued)

FPNAME	IFPNUM	KCVFM	KCVTO
COR-FL134	134	COR-CV134	COR-CV135
COR-FL135	135	COR-CV135	COR-CV136
COR-FL136	136	COR-CV136	COR-CV137
COR-FL137	137	COR-CV137	URR-CV138
URR-FL138	138	URR-CV138	URP-CV139
UBS-FL531	531	URP-CV139	UBS-CV531
LCP-FL348	348	LCP-CV348	LBS-CV349
LBS-FL349	349	LBS-CV349	LRP-CV141
LRP-FL141	141	LRP-CV141	LRR-CV142
LRR-FL142	142	LRR-CV142	COR-CV143
COR-FL143	143	COR-CV143	COR-CV144
COR-FL144	144	COR-CV144	COR-CV145
COR-FL145	145	COR-CV145	COR-CV146
COR-FL146	146	COR-CV146	COR-CV147
COR-FL147	147	COR-CV147	URR-CV148
URR-FL148	148	URR-CV148	URP-CV149
UBS-FL541	541	URP-CV149	UBS-CV541
LCP-FL358	358	LCP-CV358	LBS-CV359
LBS-FL359	359	LBS-CV359	ORF-CV151
ORF-FL151	151	ORF-CV151	ORF-CV152
ORF-FL152	152	ORF-CV152	ORF-CV153
ORF-FL153	153	ORF-CV153	ORF-CV154
ORF-FL154	154	ORF-CV154	ORF-CV155
ORF-FL155	155	ORF-CV155	ORF-CV156
ORF-FL156	156	ORF-CV156	ORF-CV157
ORF-FL157	157	ORF-CV157	ORF-CV158
ORF-FL158	158	ORF-CV158	ORF-CV159
UBS-FL551	551	ORF-CV159	UBS-CV551
LCP-FL368	368	LCP-CV368	LBS-CV369
LBS-FL369	369	LBS-CV369	OBS-CV161
OBS-FL161	161	OBS-CV161	OBS-CV162
OBS-FL162	162	OBS-CV162	OBS-CV163
OBS-FL163	163	OBS-CV163	OBS-CV164
OBS-FL164	164	OBS-CV164	OBS-CV165
OBS-FL165	165	OBS-CV165	OBS-CV166
OBS-FL166	166	OBS-CV166	OBS-CV167
OBS-FL167	167	OBS-CV167	OBS-CV168
OBS-FL168	168	OBS-CV168	OBS-CV169

Table C.20 (Continued)

FPNAME	IFPNUM	KCVFM	KCVTO
OBS-FL561	561	OBS-CV169	UBS-CV561
LCP-FL408	408	LCP-CV408	LBS-CV409
LBS-FL409	409	LBS-CV409	LRP-CV101
LRP-FL201	201	LRP-CV201	LRR-CV202
LRR-FL202	202	LRR-CV202	COR-CV203
COR-FL203	203	COR-CV203	COR-CV204
COR-FL204	204	COR-CV204	COR-CV205
COR-FL205	205	COR-CV205	COR-CV206
COR-FL206	206	COR-CV206	COR-CV207
COR-CV207	207	COR-CV207	URR-CV208
URR-CV208	208	URR-CV208	URP-CV209
UBS-CV601	601	URP-CV209	UBS-CV601
LCP-FL418	418	LCP-CV418	LBS-CV419
LBS-FL419	419	LBS-CV419	LRP-CV111
LRP-FL211	211	LRP-CV211	LRR-CV212
LRR-FL212	212	LRR-CV212	COR-CV213
COR-FL213	213	COR-CV213	COR-CV214
COR-FL214	214	COR-CV214	COR-CV215
COR-FL215	215	COR-CV215	COR-CV216
COR-FL216	216	COR-CV216	COR-CV217
COR-CV217	217	COR-CV217	URR-CV218
URR-CV218	218	URR-CV218	URP-CV219
UBS-CV611	611	URP-CV219	UBS-CV611
LCP-FL428	428	LCP-CV428	LBS-CV429
LBS-FL429	429	LBS-CV429	LRP-CV121
LRP-FL221	221	LRP-CV221	LRR-CV222
LRR-FL222	222	LRR-CV222	COR-CV223
COR-FL223	223	COR-CV223	COR-CV224
COR-FL224	224	COR-CV224	COR-CV225
COR-FL225	225	COR-CV225	COR-CV226
COR-FL226	226	COR-CV226	COR-CV227
COR-CV227	227	COR-CV227	URR-CV228
URR-CV228	228	URR-CV228	URP-CV229
UBS-CV621	621	URP-CV229	UBS-CV621
LCP-FL438	438	LCP-CV438	LBS-CV439
LBS-FL439	439	LBS-CV439	LRP-CV131
LRP-FL231	231	LRP-CV231	LRR-CV232
LRR-FL232	232	LRR-CV232	COR-CV233

Table C.20 (Continued)

FPNAME	IFPNUM	KCVFM	KCVTO
COR-FL233	233	COR-CV233	COR-CV234
COR-FL234	234	COR-CV234	COR-CV235
COR-FL235	235	COR-CV235	COR-CV236
COR-FL236	236	COR-CV236	COR-CV237
COR-CV237	237	COR-CV237	URR-CV238
URR-CV238	238	URR-CV238	URP-CV239
UBS-CV631	631	URP-CV239	UBS-CV631
LCP-FL448	448	LCP-CV448	LBS-CV449
LBS-FL449	449	LBS-CV449	LRP-CV141
LRP-FL241	241	LRP-CV241	LRR-CV242
LRR-FL242	242	LRR-CV242	COR-CV243
COR-FL243	243	COR-CV243	COR-CV244
COR-FL244	244	COR-CV244	COR-CV245
COR-FL245	245	COR-CV245	COR-CV246
COR-FL246	246	COR-CV246	COR-CV247
COR-CV247	247	COR-CV247	URR-CV248
URR-CV248	248	URR-CV248	URP-CV249
UBS-CV641	641	URP-CV249	UBS-CV641
LCP-FL458	458	LCP-CV458	LBS-CV459
LBS-FL459	459	LBS-CV459	ORF-CV151
ORF-FL251	251	ORF-CV251	ORF-CV252
ORF-FL252	252	ORF-CV252	ORF-CV253
ORF-FL253	253	ORF-CV253	ORF-CV254
ORF-FL254	254	ORF-CV254	ORF-CV255
ORF-FL255	255	ORF-CV255	ORF-CV256
ORF-FL256	256	ORF-CV256	ORF-CV257
ORF-CV257	257	ORF-CV257	ORF-CV258
ORF-CV258	258	ORF-CV258	ORF-CV259
UBS-CV651	651	ORF-CV259	UBS-CV651
LCP-FL468	468	LCP-CV468	LBS-CV469
LBS-FL469	469	LBS-CV469	OBS-CV161
OBS-FL261	261	OBS-CV261	OBS-CV262
OBS-FL262	262	OBS-CV262	OBS-CV263
OBS-FL263	263	OBS-CV263	OBS-CV264
OBS-FL264	264	OBS-CV264	OBS-CV265
OBS-FL265	265	OBS-CV265	OBS-CV266
OBS-FL266	266	OBS-CV266	OBS-CV267
OBS-CV267	267	OBS-CV267	OBS-CV268

Table C.20 (Continued)

FPNAME	IFPNUM	KCVFM	KCVTO
OBS-CV268	268	OBS-CV268	OBS-CV269
UBS-CV661	661	OBS-CV269	UBS-CV661
LBS-FL700	700	LBS-CV409	LBS-CV419
LRP-FL701	701	LRP-CV201	LRP-CV211
LRR-FL702	702	LRR-CV202	LRR-CV212
COR-FL703	703	COR-CV203	COR-CV213
COR-FL704	704	COR-CV204	COR-CV214
COR-FL705	705	COR-CV205	COR-CV215
COR-FL706	706	COR-CV206	COR-CV216
COR-FL707	707	COR-CV207	COR-CV217
URR-FL708	708	URR-CV208	URR-CV218
URP-FL709	709	URP-CV209	URP-CV219
UBS-FL710	710	UBS-CV601	UBS-CV611
LBS-FL711	711	LBS-CV419	LBS-CV429
LRP-FL712	712	LRP-CV211	LRP-CV221
LRR-FL713	713	LRR-CV212	LRR-CV222
COR-FL714	714	COR-CV213	COR-CV223
COR-FL715	715	COR-CV214	COR-CV224
COR-FL716	716	COR-CV215	COR-CV225
COR-FL717	717	COR-CV216	COR-CV226
COR-FL718	718	COR-CV217	COR-CV227
URR-FL719	719	URR-CV218	URR-CV228
URP-FL720	720	URP-CV219	URP-CV229
UBS-FL721	721	UBS-CV611	UBS-CV621
LBS-FL722	722	LBS-CV429	LBS-CV439
LRP-FL723	723	LRP-CV221	LRP-CV231
LRR-FL724	724	LRR-CV222	LRR-CV232
COR-FL725	725	COR-CV223	COR-CV233
COR-FL726	726	COR-CV224	COR-CV234
COR-FL727	727	COR-CV225	COR-CV235
COR-FL728	728	COR-CV226	COR-CV236
COR-FL729	729	COR-CV227	COR-CV237
URR-FL730	730	URR-CV228	URR-CV238
URP-FL731	731	URP-CV229	URP-CV239
UBS-FL732	732	UBS-CV621	UBS-CV631
LBS-FL733	733	LBS-CV439	LBS-CV449
LRP-FL734	734	LRP-CV231	LRP-CV241
LRR-FL735	735	LRR-CV232	LRR-CV242

Table C.20 (Continued)

FPNAME	IFPNUM	KCVFM	KCVTO
COR-FL736	736	COR-CV233	COR-CV243
COR-FL737	737	COR-CV234	COR-CV244
COR-FL738	738	COR-CV235	COR-CV245
COR-FL739	739	COR-CV236	COR-CV246
COR-FL740	740	COR-CV237	COR-CV247
URR-FL741	741	URR-CV238	URR-CV248
URP-FL742	742	URP-CV239	URP-CV249
UBS-FL743	743	UBS-CV631	UBS-CV641
LBS-FL744	744	LBS-CV449	LBS-CV459
LRP-FL745	745	LRP-CV241	LRP-CV251
LRR-FL746	746	LRR-CV242	LRR-CV252
COR-FL747	747	COR-CV243	COR-CV253
COR-FL748	748	COR-CV244	COR-CV254
COR-FL749	749	COR-CV245	COR-CV255
COR-FL750	750	COR-CV246	COR-CV256
COR-FL751	751	COR-CV247	COR-CV257
URR-FL752	752	URR-CV248	URR-CV258
URP-FL753	753	URP-CV249	URP-CV259
UBS-FL754	754	UBS-CV641	UBS-CV651
LBS-FL755	755	LBS-CV459	LBS-CV469
LRP-FL756	756	LRP-CV251	LRP-CV261
LRR-FL757	757	LRR-CV252	LRR-CV262
COR-FL758	758	COR-CV253	COR-CV263
COR-FL759	759	COR-CV254	COR-CV264
COR-FL760	760	COR-CV255	COR-CV265
COR-FL761	761	COR-CV256	COR-CV266
COR-FL762	762	COR-CV257	COR-CV267
URR-FL763	763	URR-CV258	URR-CV268
URP-FL764	764	URP-CV259	URP-CV269
UBS-FL765	765	UBS-CV651	UBS-CV661
HS-FL800	800	HS-CV704	HS-CV703
HS-FL801	801	HS-CV703	HS-CV702
HS-FL802	802	HS-CV702	HS-CV701
HS-FL803	803	HS-CV701	HS-CV700
CAV-FL003	003	CAV-CV003	LCP-CV308
CAV-FL004	004	CAV-CV003	LCP-CV408
CAV-FL005	005	CAV-CV003	LCP-CV318
CAV-FL006	006	CAV-CV003	LCP-CV418
CAV-FL007	007	CAV-CV003	LCP-CV328

Table C.20 (Continued)

FPNAME	IFPNUM	KCVFM	KCVTO
CAV-FL008	008	CAV-CV003	LCP-CV428
CAV-FL009	009	CAV-CV003	LCP-CV338
CAV-FL010	010	CAV-CV003	LCP-CV438
CAV-FL011	011	CAV-CV003	LCP-CV348
CAV-FL012	012	CAV-CV003	LCP-CV448
CAV-FL013	013	CAV-CV003	LCP-CV358
CAV-FL014	014	CAV-CV003	LCP-CV458
CAV-FL015	015	CAV-CV003	LCP-CV368
CAV-FL016	016	CAV-CV003	LCP-CV468
UHD-FL017	017	UHD-CV005	UBS-CV501
UHD-FL018	018	UHD-CV005	UBS-CV601
UHD-FL019	019	UHD-CV005	UBS-CV511
UHD-FL020	020	UHD-CV005	UBS-CV611
UHD-FL021	021	UHD-CV005	UBS-CV521
UHD-FL022	022	UHD-CV005	UBS-CV621
UHD-FL023	023	UHD-CV005	UBS-CV531
UHD-FL024	024	UHD-CV005	UBS-CV631
UHD-FL025	025	UHD-CV005	UBS-CV541
UHD-FL026	026	UHD-CV005	UBS-CV641
UHD-FL027	027	UHD-CV005	UBS-CV551
UHD-FL028	028	UHD-CV005	UBS-CV651
UHD-FL029	029	UHD-CV005	UBS-CV561
UHD-FL030	030	UHD-CV005	UBS-CV661
CNC-FL050	050	HS-CV700	CAV-CV003

Table C.21: Flow Path Connection Heights and Orientations

IFPNUM	ZFM (m)	ZTO (m)	KFLGFL
308	-1.920	-1.920	0
309	-1.000	-1.000	0
101	-5.000E-01	-5.000E-01	0
102	0.000	0.000	0
103	2.680E-01	2.680E-01	0
104	5.360E-01	5.360E-01	0
105	8.040E-01	8.040E-01	0
106	1.072	1.072	0
107	1.340	1.340	0

Table C.21 (Continued)

IFPNUM	ZFM (m)	ZTO (m)	KFLGFL
108	1.840	1.840	0
501	2.340	2.340	0
318	-1.920	-1.920	0
319	-1.000	-1.000	0
111	-5.000E-01	-5.000E-01	0
112	0.000	0.000	0
113	2.680E-01	2.680E-01	0
114	5.360E-01	5.360E-01	0
115	8.040E-01	8.040E-01	0
116	1.072	1.072	0
117	1.340	1.340	0
118	1.840	1.840	0
511	2.340	2.340	0
328	-1.920	-1.920	0
329	-1.000	-1.000	0
121	-5.000E-01	-5.000E-01	0
122	0.000	0.000	0
123	2.680E-01	2.680E-01	0
124	5.360E-01	5.360E-01	0
125	8.040E-01	8.040E-01	0
126	1.072	1.072	0
127	1.340	1.340	0
128	1.840	1.840	0
521	2.340	2.340	0
338	-1.920	-1.920	0
339	-1.000	-1.000	0
131	-5.000E-01	-5.000E-01	0
132	0.000	0.000	0
133	2.680E-01	2.680E-01	0
134	5.360E-01	5.360E-01	0
135	8.040E-01	8.040E-01	0
136	1.072	1.072	0
137	1.340	1.340	0
138	1.840	1.840	0
531	2.340	2.340	0
348	-1.920	-1.920	0
349	-1.000	-1.000	0
141	-5.000E-01	-5.000E-01	0
142	0.000	0.000	0

Table C.21 (Continued)

IFPNUM	ZFM (m)	ZTO (m)	KFLGFL
143	2.680E-01	2.680E-01	0
144	5.360E-01	5.360E-01	0
145	8.040E-01	8.040E-01	0
146	1.072	1.072	0
147	1.340	1.340	0
148	1.840	1.840	0
541	2.340	2.340	0
358	-1.920	-1.920	0
359	-1.000	-1.000	0
151	-5.000E-01	-5.000E-01	0
152	0.000	0.000	0
153	2.680E-01	2.680E-01	0
154	5.360E-01	5.360E-01	0
155	8.040E-01	8.040E-01	0
156	1.072	1.072	0
157	1.340	1.340	0
158	1.840	1.840	0
551	2.340	2.340	0
368	-1.920	-1.920	0
369	-1.000	-1.000	0
161	-5.000E-01	-5.000E-01	0
162	0.000	0.000	0
163	2.680E-01	2.680E-01	0
164	5.360E-01	5.360E-01	0
165	8.040E-01	8.040E-01	0
166	1.072	1.072	0
167	1.340	1.340	0
168	1.840	1.840	0
561	2.340	2.340	0
408	-1.920	-1.920	0
409	-1.000	-1.000	0
201	-5.000E-01	-5.000E-01	0
202	0.000	0.000	0
203	2.680E-01	2.680E-01	0
204	5.360E-01	5.360E-01	0
205	8.040E-01	8.040E-01	0
206	1.072	1.072	0
207	1.340	1.340	0
208	1.840	1.840	0

Table C.21 (Continued)

IFPNUM	ZFM (m)	ZTO (m)	KFLGFL
601	2.340	2.340	0
418	-1.920	-1.920	0
419	-1.000	-1.000	0
211	-5.000E-01	-5.000E-01	0
212	0.000	0.000	0
213	2.680E-01	2.680E-01	0
214	5.360E-01	5.360E-01	0
215	8.040E-01	8.040E-01	0
216	1.072	1.072	0
217	1.340	1.340	0
218	1.840	1.840	0
611	2.340	2.340	0
428	-1.920	-1.920	0
429	-1.000	-1.000	0
221	-5.000E-01	-5.000E-01	0
222	0.000	0.000	0
223	2.680E-01	2.680E-01	0
224	5.360E-01	5.360E-01	0
225	8.040E-01	8.040E-01	0
226	1.072	1.072	0
227	1.340	1.340	0
228	1.840	1.840	0
621	2.340	2.340	0
438	-1.920	-1.920	0
439	-1.000	-1.000	0
231	-5.000E-01	-5.000E-01	0
232	0.000	0.000	0
233	2.680E-01	2.680E-01	0
234	5.360E-01	5.360E-01	0
235	8.040E-01	8.040E-01	0
236	1.072	1.072	0
237	1.340	1.340	0
238	1.840	1.840	0
631	2.340	2.340	0
448	-1.920	-1.920	0
449	-1.000	-1.000	0
241	-5.000E-01	-5.000E-01	0
242	0.000	0.000	0
243	2.680E-01	2.680E-01	0

Table C.21 (Continued)

IFPNUM	ZFM (m)	ZTO (m)	KFLGFL
244	5.360E-01	5.360E-01	0
245	8.040E-01	8.040E-01	0
246	1.072	1.072	0
247	1.340	1.340	0
248	1.840	1.840	0
641	2.340	2.340	0
458	-1.920	-1.920	0
459	-1.000	-1.000	0
251	-5.000E-01	-5.000E-01	0
252	0.000	0.000	0
253	2.680E-01	2.680E-01	0
254	5.360E-01	5.360E-01	0
255	8.040E-01	8.040E-01	0
256	1.072	1.072	0
257	1.340	1.340	0
258	1.840	1.840	0
651	2.340	2.340	0
468	-1.920	-1.920	0
469	-1.000	-1.000	0
261	-5.000E-01	-5.000E-01	0
262	0.000	0.000	0
263	2.680E-01	2.680E-01	0
264	5.360E-01	5.360E-01	0
265	8.040E-01	8.040E-01	0
266	1.072	1.072	0
267	1.340	1.340	0
268	1.840	1.840	0
661	2.340	2.340	0
700	-1.460	-1.460	3
701	-7.500E-01	-7.500E-01	3
702	-2.500E-01	-2.500E-01	3
703	1.340E-01	1.340E-01	3
704	4.020E-01	4.020E-01	3
705	6.700E-01	6.700E-01	3
706	9.380E-01	9.380E-01	3
707	1.206	1.206	3
708	1.590	1.590	3
709	2.090	2.090	3
710	2.703	2.703	3

Table C.21 (Continued)

IFPNUM	ZFM (m)	ZTO (m)	KFLGFL
711	-1.460	-1.460	3
712	-7.500E-01	-7.500E-01	3
713	-2.500E-01	-2.500E-01	3
714	1.340E-01	1.340E-01	3
715	4.020E-01	4.020E-01	3
716	6.700E-01	6.700E-01	3
717	9.380E-01	9.380E-01	3
718	1.206	1.206	3
719	1.590	1.590	3
720	2.090	2.090	3
721	2.703	2.703	3
722	-1.460	-1.460	3
723	-7.500E-01	-7.500E-01	3
724	-2.500E-01	-2.500E-01	3
725	1.340E-01	1.340E-01	3
726	4.020E-01	4.020E-01	3
727	6.700E-01	6.700E-01	3
728	9.380E-01	9.380E-01	3
729	1.206	1.206	3
730	1.590	1.590	3
731	2.090	2.090	3
732	2.703	2.703	3
733	-1.460	-1.460	3
734	-7.500E-01	-7.500E-01	3
735	-2.500E-01	-2.500E-01	3
736	1.340E-01	1.340E-01	3
737	4.020E-01	4.020E-01	3
738	6.700E-01	6.700E-01	3
739	9.380E-01	9.380E-01	3
740	1.206	1.206	3
741	1.590	1.590	3
742	2.090	2.090	3
743	2.703	2.703	3
744	-1.460	-1.460	3
745	-7.500E-01	-7.500E-01	3
746	-2.500E-01	-2.500E-01	3
747	1.340E-01	1.340E-01	3
748	4.020E-01	4.020E-01	3
749	6.700E-01	6.700E-01	3
750	9.380E-01	9.380E-01	3

Table C.21 (Continued)

IFPNUM	ZFM (m)	ZTO (m)	KFLGFL
751	1.206	1.206	3
752	1.590	1.590	3
753	2.090	2.090	3
754	2.703	2.703	3
755	-1.460	-1.460	3
756	-7.500E-01	-7.500E-01	3
757	-2.500E-01	-2.500E-01	3
758	1.340E-01	1.340E-01	3
759	4.020E-01	4.020E-01	3
760	6.700E-01	6.700E-01	3
761	9.380E-01	9.380E-01	3
762	1.206	1.206	3
763	1.590	1.590	3
764	2.090	2.090	3
765	2.703	2.703	3
800	2.340	2.340	0
801	1.340	1.340	0
802	0.000	0.000	0
803	-1.000	-1.000	0
003	-2.390	-2.390	0
004	-2.390	-2.390	0
005	-2.390	-2.390	0
006	-2.390	-2.390	0
007	-2.390	-2.390	0
008	-2.390	-2.390	0
009	-2.390	-2.390	0
010	-2.390	-2.390	0
011	-2.390	-2.390	0
012	-2.390	-2.390	0
013	-2.390	-2.390	0
014	-2.390	-2.390	0
015	-2.390	-2.390	0
016	-2.390	-2.390	0
017	3.065	3.065	0
018	3.065	3.065	0
019	3.065	3.065	0
020	3.065	3.065	0
021	3.065	3.065	0
022	3.065	3.065	0

Table C.21 (Continued)

IFPNUM	ZFM (m)	ZTO (m)	KFLGFL
023	3.065	3.065	0
024	3.065	3.065	0
025	3.065	3.065	0
026	3.065	3.065	0
027	3.065	3.065	0
028	3.065	3.065	0
029	3.065	3.065	0
030	3.065	3.065	0
050	-2.390	-2.390	0

Table C.22: Flow Path Lengths and Form Loss Coefficients

IFPNUM	FLARA	FLEN	FRICFO	FRICRO
308	3.417E-01	6.950E-01		
309	3.240E-01	7.100E-01	0.0	0.0
101	3.240E-01	5.000E-01	0.0	0.0
102	3.240E-01	3.840E-01	0.0	0.0
103	3.240E-01	2.680E-01	0.0	0.0
104	3.240E-01	2.680E-01	0.0	0.0
105	3.240E-01	2.680E-01	0.0	0.0
106	3.240E-01	2.680E-01	0.0	0.0
107	3.240E-01	3.480E-01	0.0	0.0
108	3.240E-01	5.000E-01	0.0	0.0
501	3.240E-01	6.127E-01	0.0	0.0
318	1.025E+00	6.950E-01		
319	9.782E-01	7.100E-01	0.0	0.0
111	9.782E-01	5.000E-01	0.0	0.0
112	9.782E-01	3.840E-01	0.0	0.0
113	9.782E-01	2.680E-01	0.0	0.0
114	9.782E-01	2.680E-01	0.0	0.0
115	9.782E-01	2.680E-01	0.0	0.0
116	9.782E-01	2.680E-01	0.0	0.0
117	9.782E-01	3.480E-01	0.0	0.0
118	9.782E-01	5.000E-01	0.0	0.0
511	9.782E-01	6.127E-01	0.0	0.0
328	1.709E+00	6.950E-01		
329	1.635E+00	7.100E-01	0.0	0.0
121	1.635E+00	5.000E-01	0.0	0.0

Table C.22 (Continued)

IFPNUM	FLARA	FLEN	FRICFO	FRICRO
122	1.635E+00	3.840E-01	0.0	0.0
123	1.635E+00	2.680E-01	0.0	0.0
124	1.635E+00	2.680E-01	0.0	0.0
125	1.635E+00	2.680E-01	0.0	0.0
126	1.635E+00	2.680E-01	0.0	0.0
127	1.635E+00	3.480E-01	0.0	0.0
128	1.635E+00	5.000E-01	0.0	0.0
521	1.635E+00	6.127E-01	0.0	0.0
338	2.392E+00	6.950E-01		
339	2.282E+00	7.100E-01	0.0	0.0
131	2.282E+00	5.000E-01	0.0	0.0
132	2.282E+00	3.840E-01	0.0	0.0
133	2.282E+00	2.680E-01	0.0	0.0
134	2.282E+00	2.680E-01	0.0	0.0
135	2.282E+00	2.680E-01	0.0	0.0
136	2.282E+00	2.680E-01	0.0	0.0
137	2.282E+00	3.480E-01	0.0	0.0
138	2.282E+00	5.000E-01	0.0	0.0
531	2.282E+00	6.127E-01	0.0	0.0
348	3.076E+00	6.950E-01		
349	2.956E+00	7.100E-01	0.0	0.0
141	2.956E+00	5.000E-01	0.0	0.0
142	2.956E+00	3.840E-01	0.0	0.0
143	2.956E+00	2.680E-01	0.0	0.0
144	2.956E+00	2.680E-01	0.0	0.0
145	2.956E+00	2.680E-01	0.0	0.0
146	2.956E+00	2.680E-01	0.0	0.0
147	2.956E+00	3.480E-01	0.0	0.0
148	2.956E+00	5.000E-01	0.0	0.0
541	2.956E+00	6.127E-01	0.0	0.0
358	3.482E+00	6.950E-01		
359	2.306E+00	7.100E-01	0.0	0.0
151	2.306E+00	5.000E-01	0.0	0.0
152	2.306E+00	3.840E-01	0.0	0.0
153	2.306E+00	2.680E-01	0.0	0.0
154	2.306E+00	2.680E-01	0.0	0.0
155	2.306E+00	2.680E-01	0.0	0.0
156	2.306E+00	2.680E-01	0.0	0.0

Table C.22 (Continued)

IFPNUM	FLARA	FLEN	FRICFO	FRICRO
157	2.306E+00	3.480E-01	0.0	0.0
158	2.306E+00	5.000E-01	0.0	0.0
551	2.306E+00	6.127E-01	0.0	0.0
368	6.363E+00	6.950E-01		
369	4.214E+00	7.100E-01	0.0	0.0
161	4.214E+00	5.000E-01	0.0	0.0
162	4.214E+00	3.840E-01	0.0	0.0
163	4.214E+00	2.680E-01	0.0	0.0
164	4.214E+00	2.680E-01	0.0	0.0
165	4.214E+00	2.680E-01	0.0	0.0
166	4.214E+00	2.680E-01	0.0	0.0
167	4.214E+00	3.480E-01	0.0	0.0
168	4.214E+00	5.000E-01	0.0	0.0
561	4.214E+00	6.127E-01	0.0	0.0
408	1.131E-02	6.950E-01		
409	4.525E-02	7.100E-01	0.0	0.0
201	4.525E-02	5.000E-01	0.0	0.0
202	4.525E-02	3.840E-01	0.0	0.0
203	4.525E-02	2.680E-01	0.0	0.0
204	4.525E-02	2.680E-01	0.0	0.0
205	4.525E-02	2.680E-01	0.0	0.0
206	4.525E-02	2.680E-01	0.0	0.0
207	4.525E-02	3.480E-01	0.0	0.0
208	4.525E-02	5.000E-01	0.0	0.0
601	4.525E-02	6.127E-01	0.0	0.0
418	3.394E-02	6.950E-01		
419	1.357E-01	7.100E-01	0.0	0.0
211	1.357E-01	5.000E-01	0.0	0.0
212	1.357E-01	3.840E-01	0.0	0.0
213	1.357E-01	2.680E-01	0.0	0.0
214	1.357E-01	2.680E-01	0.0	0.0
215	1.357E-01	2.680E-01	0.0	0.0
216	1.357E-01	2.680E-01	0.0	0.0
217	1.357E-01	3.480E-01	0.0	0.0
218	1.357E-01	5.000E-01	0.0	0.0
611	1.357E-01	6.127E-01	0.0	0.0
428	5.656E-02	6.950E-01		
429	2.262E-01	7.100E-01	0.0	0.0

Table C.22 (Continued)

IFPNUM	FLARA	FLEN	FRICFO	FRICRO
221	2.262E-01	5.000E-01	0.0	0.0
222	2.262E-01	3.840E-01	0.0	0.0
223	2.262E-01	2.680E-01	0.0	0.0
224	2.262E-01	2.680E-01	0.0	0.0
225	2.262E-01	2.680E-01	0.0	0.0
226	2.262E-01	2.680E-01	0.0	0.0
227	2.262E-01	3.480E-01	0.0	0.0
228	2.262E-01	5.000E-01	0.0	0.0
621	2.262E-01	6.127E-01	0.0	0.0
438	7.918E-02	6.950E-01		
439	3.167E-01	7.100E-01	0.0	0.0
231	3.167E-01	5.000E-01	0.0	0.0
232	3.167E-01	3.840E-01	0.0	0.0
233	3.167E-01	2.680E-01	0.0	0.0
234	3.167E-01	2.680E-01	0.0	0.0
235	3.167E-01	2.680E-01	0.0	0.0
236	3.167E-01	2.680E-01	0.0	0.0
237	3.167E-01	3.480E-01	0.0	0.0
238	3.167E-01	5.000E-01	0.0	0.0
631	3.167E-01	6.127E-01	0.0	0.0
448	1.018E-01	6.950E-01		
449	4.072E-01	7.100E-01	0.0	0.0
241	4.072E-01	5.000E-01	0.0	0.0
242	4.072E-01	3.840E-01	0.0	0.0
243	4.072E-01	2.680E-01	0.0	0.0
244	4.072E-01	2.680E-01	0.0	0.0
245	4.072E-01	2.680E-01	0.0	0.0
246	4.072E-01	2.680E-01	0.0	0.0
247	4.072E-01	3.480E-01	0.0	0.0
248	4.072E-01	5.000E-01	0.0	0.0
641	4.072E-01	6.127E-01	0.0	0.0
458	1.152E-01	6.950E-01		
459	4.610E-01	7.100E-01	0.0	0.0
251	4.610E-01	5.000E-01	0.0	0.0
252	4.610E-01	3.840E-01	0.0	0.0
253	4.610E-01	2.680E-01	0.0	0.0
254	4.610E-01	2.680E-01	0.0	0.0
255	4.610E-01	2.680E-01	0.0	0.0

Table C.22 (Continued)

IFPNUM	FLARA	FLEN	FRICFO	FRICRO
256	4.610E-01	2.680E-01	0.0	0.0
257	4.610E-01	3.480E-01	0.0	0.0
258	4.610E-01	5.000E-01	0.0	0.0
651	4.610E-01	6.127E-01	0.0	0.0
468	2.106E-01	6.950E-01		
469	8.424E-01	7.100E-01	0.0	0.0
261	8.424E-01	5.000E-01	0.0	0.0
262	8.424E-01	3.840E-01	0.0	0.0
263	8.424E-01	2.680E-01	0.0	0.0
264	8.424E-01	2.680E-01	0.0	0.0
265	8.424E-01	2.680E-01	0.0	0.0
266	8.424E-01	2.680E-01	0.0	0.0
267	8.424E-01	3.480E-01	0.0	0.0
268	8.424E-01	5.000E-01	0.0	0.0
661	8.424E-01	6.127E-01	0.0	0.0
700	1.159E-01	1.894E-02		
701	6.300E-02	1.894E-02		
702	6.300E-02	1.894E-02		
703	3.377E-02	1.894E-02		
704	3.377E-02	1.894E-02		
705	3.377E-02	1.894E-02		
706	3.377E-02	1.894E-02		
707	3.377E-02	1.894E-02		
708	6.300E-02	1.894E-02		
709	6.300E-02	1.894E-02		
710	9.140E-02	1.894E-02		
711	2.190E-01	2.391E-02		
712	1.190E-01	2.391E-02		
713	1.190E-01	2.391E-02		
714	6.378E-02	2.391E-02		
715	6.378E-02	2.391E-02		
716	6.378E-02	2.391E-02		
717	6.378E-02	2.391E-02		
718	6.378E-02	2.391E-02		
719	1.190E-01	2.391E-02		
720	1.190E-01	2.391E-02		
721	1.726E-01	2.391E-02		
722	2.962E-01	2.574E-02		

Table C.22 (Continued)

IFPNUM	FLARA	FLEN	FRICFO	FRICRO
722	2.962E-01	2.574E-02		
723	1.610E-01	2.574E-02		
724	1.610E-01	2.574E-02		
725	8.630E-02	2.574E-02		
726	8.630E-02	2.574E-02		
727	8.630E-02	2.574E-02		
728	8.630E-02	2.574E-02		
729	8.630E-02	2.574E-02		
730	1.610E-01	2.574E-02		
731	1.610E-01	2.574E-02		
732	2.336E-01	2.574E-02		
733	3.993E-01	2.670E-02		
734	2.170E-01	2.670E-02		
735	2.170E-01	2.670E-02		
736	1.163E-01	2.670E-02		
737	1.163E-01	2.670E-02		
738	1.163E-01	2.670E-02		
739	1.163E-01	2.670E-02		
740	1.163E-01	2.670E-02		
741	2.170E-01	2.670E-02		
742	2.170E-01	2.670E-02		
743	3.148E-01	2.670E-02		
744	5.023E-01	2.643E-02		
745	2.730E-01	2.643E-02		
746	2.730E-01	2.643E-02		
747	1.463E-01	2.643E-02		
748	1.463E-01	2.643E-02		
749	1.463E-01	2.643E-02		
750	1.463E-01	2.643E-02		
751	1.463E-01	2.643E-02		
752	2.730E-01	2.643E-02		
753	2.730E-01	2.643E-02		
754	3.961E-01	2.643E-02		
755	5.796E-01	3.197E-02		
756	3.150E-01	3.197E-02		
757	3.150E-01	3.197E-02		
758	1.688E-01	3.197E-02		
759	1.688E-01	3.197E-02		
760	1.688E-01	3.197E-02		

Table C.22 (Continued)

IFPNUM	FLARA	FLEN	FRICFO	FRICRO
761	1.688E-01	3.197E-02		
762	1.688E-01	3.197E-02		
763	3.150E-01	3.197E-02		
764	3.150E-01	3.197E-02		
765	4.570E-01	3.197E-02		
800	7.102E+00	8.625E-01	0.0	0.0
801	7.102E+00	1.170E+00	0.0	0.0
802	7.102E+00	1.170E+00	0.0	0.0
803	7.102E+00	9.600E-01	0.0	0.0
003	3.417E-01	2.167E+00		
004	1.131E-02	2.167E+00		
005	1.025E+00	2.167E+00		
006	3.394E-02	2.167E+00		
007	1.709E+00	2.167E+00		
008	5.656E-02	2.167E+00		
009	2.392E+00	2.167E+00		
010	7.918E-02	2.167E+00		
011	3.076E+00	2.167E+00		
012	1.018E-01	2.167E+00		
013	3.482E+00	2.167E+00		
014	1.152E-01	2.167E+00		
015	6.363E+00	2.167E+00		
016	2.106E-01	2.167E+00		
017	3.240E-01	2.294E+00		
018	4.525E-02	2.294E+00		
019	9.782E-01	2.294E+00		
020	1.357E-01	2.294E+00		
021	1.635E+00	2.294E+00		
022	2.262E-01	2.294E+00		
023	2.282E+00	2.294E+00		
024	3.167E-01	2.294E+00		
025	2.956E+00	2.294E+00		
026	4.072E-01	2.294E+00		
027	2.306E+00	2.294E+00		
028	4.610E-01	2.294E+00		
029	4.214E+00	2.294E+00		
030	8.424E-01	2.294E+00		
050	7.102E+00	1.932E+00		

Table C.23: Flow Path Segment Parameters

IFPNUM	INPSG	NSEG	SAREA	SLEN	SHYD	SRGH
308	3	1	3.417E-03	2.450E-01	1.520E-01	2.000E-06
		2	6.548E-01	1.100E-01	2.104E-01	2.000E-06
		3	3.240E-01	3.400E-01	8.583E-03	2.000E-06
309	2	1	3.240E-01	4.600E-01	8.583E-03	2.000E-06
		2	3.240E-01	2.500E-01	8.583E-03	1.230E-06
101	1	1	3.240E-01	5.000E-01	8.583E-03	1.230E-06
102	1	1	3.240E-01	3.840E-01	8.583E-03	1.230E-06
103	1	1	3.240E-01	2.680E-01	8.583E-03	1.230E-06
104	1	1	3.240E-01	2.680E-01	8.583E-03	1.230E-06
105	1	1	3.240E-01	2.680E-01	8.583E-03	1.230E-06
106	1	1	3.240E-01	2.680E-01	8.583E-03	1.230E-06
107	1	1	3.240E-01	3.480E-01	8.583E-03	1.230E-06
108	1	1	3.240E-01	5.000E-01	8.583E-03	1.230E-06
501	2	1	3.240E-01	2.500E-01	8.583E-03	1.230E-06
		2	3.240E-01	3.627E-01	8.583E-03	2.000E-06
318	3	1	1.025	2.450E-01	1.520E-01	2.000E-06
		2	1.964	1.100E-01	2.104E-01	2.000E-06
		3	9.782E-01	3.400E-01	8.674E-03	2.000E-06
319	2	1	9.782E-01	4.600E-01	8.674E-03	2.000E-06
		2	9.782E-01	2.500E-01	8.674E-03	1.230E-06
111	1	1	9.782E-01	5.000E-01	8.674E-03	1.230E-06
112	1	1	9.782E-01	3.840E-01	8.674E-03	1.230E-06
113	1	1	9.782E-01	2.680E-01	8.674E-03	1.230E-06
114	1	1	9.782E-01	2.680E-01	8.674E-03	1.230E-06
115	1	1	9.782E-01	2.680E-01	8.674E-03	1.230E-06
116	1	1	9.782E-01	2.680E-01	8.674E-03	1.230E-06
117	1	1	9.782E-01	3.480E-01	8.674E-03	1.230E-06
118	1	1	9.782E-01	5.000E-01	8.674E-03	1.230E-06
511	2	1	9.782E-01	2.500E-01	8.674E-03	1.230E-06
		2	9.782E-01	3.627E-01	8.674E-03	2.000E-06
328	3	1	1.709	2.450E-01	1.520E-01	2.000E-06
		2	3.274	1.100E-01	2.104E-01	2.000E-06
		3	1.635	3.400E-01	8.711E-03	2.000E-06
329	2	1	1.635E+00	4.600E-01	8.711E-03	2.000E-06
		2	1.635E+00	2.500E-01	8.711E-03	1.230E-06
121	1	1	1.635E+00	5.000E-01	8.711E-03	1.230E-06
122	1	1	1.635E+00	3.840E-01	8.711E-03	1.230E-06
123	1	1	1.635E+00	2.680E-01	8.711E-03	1.230E-06

Table C.23 (Continued)

IFPNUM	INPSG	NSEG	SAREA	SLEN	SHYD	SRGH
124	1	1	1.635E+00	2.680E-01	8.711E-03	1.230E-06
125	1	1	1.635E+00	2.680E-01	8.711E-03	1.230E-06
126	1	1	1.635E+00	2.680E-01	8.711E-03	1.230E-06
127	1	1	1.635E+00	3.480E-01	8.711E-03	1.230E-06
128	1	1	1.635E+00	5.000E-01	8.711E-03	1.230E-06
521	2	1	1.635E+00	2.500E-01	8.711E-03	1.230E-06
		2	1.635E+00	3.627E-01	8.711E-03	2.000E-06
338	3	1	2.392	2.450E-01	1.520E-01	2.000E-06
		2	4.584	1.100E-01	2.104E-01	2.000E-06
		3	2.282	3.400E-01	8.674E-03	2.000E-06
339	2	1	2.282E+00	4.600E-01	8.674E-03	2.000E-06
		2	2.282E+00	2.500E-01	8.674E-03	1.230E-06
131	1	1	2.282E+00	5.000E-01	8.674E-03	1.230E-06
132	1	1	2.282E+00	3.840E-01	8.674E-03	1.230E-06
133	1	1	2.282E+00	2.680E-01	8.674E-03	1.230E-06
134	1	1	2.282E+00	2.680E-01	8.674E-03	1.230E-06
135	1	1	2.282E+00	2.680E-01	8.674E-03	1.230E-06
136	1	1	2.282E+00	2.680E-01	8.674E-03	1.230E-06
137	1	1	2.282E+00	3.480E-01	8.674E-03	1.230E-06
138	1	1	2.282E+00	5.000E-01	8.674E-03	1.230E-06
531	2	1	2.282E+00	2.500E-01	8.674E-03	1.230E-06
		2	2.282E+00	3.627E-01	8.674E-03	2.000E-06
348	3	1	3.076	2.450E-01	1.520E-01	2.000E-06
		2	5.893	1.100E-01	2.104E-01	2.000E-06
		3	2.956	3.400E-01	8.773E-03	2.000E-06
349	2	1	2.956E+00	4.600E-01	8.773E-03	2.000E-06
		2	2.956E+00	2.500E-01	8.773E-03	1.230E-06
141	1	1	2.956E+00	5.000E-01	8.773E-03	1.230E-06
142	1	1	2.956E+00	3.840E-01	8.773E-03	1.230E-06
143	1	1	2.956E+00	2.680E-01	8.773E-03	1.230E-06
144	1	1	2.956E+00	2.680E-01	8.773E-03	1.230E-06
145	1	1	2.956E+00	2.680E-01	8.773E-03	1.230E-06
146	1	1	2.956E+00	2.680E-01	8.773E-03	1.230E-06
147	1	1	2.956E+00	3.480E-01	8.773E-03	1.230E-06
148	1	1	2.956E+00	5.000E-01	8.773E-03	1.230E-06
541	2	1	2.956E+00	2.500E-01	8.773E-03	1.230E-06
		2	2.956E+00	3.627E-01	8.773E-03	2.000E-06

Table C.23 (Continued)

IFPNUM	INPSG	NSEG	SAREA	SLEN	SHYD	SRGH
358	3	1	3.482	2.450E-01	1.520E-01	2.000E-06
		2	6.671	1.100E-01	2.104E-01	2.000E-06
		3	2.306	3.400E-01	1.669E-02	2.000E-06
359	1	1	2.306E+00	7.100E-01	1.669E-02	2.000E-06
151	1	1	2.306E+00	5.000E-01	1.669E-02	2.000E-06
152	1	1	2.306E+00	3.840E-01	1.669E-02	2.000E-06
153	1	1	2.306E+00	2.680E-01	1.669E-02	2.000E-06
154	1	1	2.306E+00	2.680E-01	1.669E-02	2.000E-06
155	1	1	2.306E+00	2.680E-01	1.669E-02	2.000E-06
156	1	1	2.306E+00	2.680E-01	1.669E-02	2.000E-06
157	1	1	2.306E+00	3.480E-01	1.669E-02	2.000E-06
158	1	1	2.306E+00	5.000E-01	1.669E-02	2.000E-06
551	1	1	2.306E+00	6.127E-01	1.669E-02	2.000E-06
368	3	1	6.363	2.450E-01	1.520E-01	2.000E-06
		2	1.219E+01	1.100E-01	2.104E-01	2.000E-06
		3	4.214	3.400E-01	1.669E-02	2.000E-06
369	1	1	4.214E+00	7.100E-01	1.669E-02	2.000E-06
161	1	1	4.214E+00	5.000E-01	1.669E-02	2.000E-06
162	1	1	4.214E+00	3.840E-01	1.669E-02	2.000E-06
163	1	1	4.214E+00	2.680E-01	1.669E-02	2.000E-06
164	1	1	4.214E+00	2.680E-01	1.669E-02	2.000E-06
165	1	1	4.214E+00	2.680E-01	1.669E-02	2.000E-06
166	1	1	4.214E+00	2.680E-01	1.669E-02	2.000E-06
167	1	1	4.214E+00	3.480E-01	1.669E-02	2.000E-06
168	1	1	4.214E+00	5.000E-01	1.669E-02	2.000E-06
561	1	1	4.214E+00	6.127E-01	1.669E-02	2.000E-06
408	2	1	1.131E-02	2.350E-01	3.422E-03	2.000E-06
		2	4.525E-02	4.600E-01	1.423E-02	1.230E-06
409	1	1	4.525E-02	7.100E-01	1.423E-02	1.230E-06
201	1	1	4.525E-02	5.000E-01	1.423E-02	1.230E-06
202	1	1	4.525E-02	3.840E-01	1.423E-02	1.230E-06
203	1	1	4.525E-02	2.680E-01	1.423E-02	1.230E-06
204	1	1	4.525E-02	2.680E-01	1.423E-02	1.230E-06
205	1	1	4.525E-02	2.680E-01	1.423E-02	1.230E-06
206	1	1	4.525E-02	2.680E-01	1.423E-02	1.230E-06
207	1	1	4.525E-02	3.480E-01	1.423E-02	1.230E-06
208	1	1	4.525E-02	5.000E-01	1.423E-02	1.230E-06
601	1	1	4.525E-02	6.127E-01	1.423E-02	1.230E-06

Table C.23 (Continued)

IFPNUM	INPSG	NSEG	SAREA	SLEN	SHYD	SRGH
418	2	1	3.394E-02	2.350E-01	3.422E-03	2.000E-06
		2	1.357E-01	4.600E-01	1.423E-02	1.230E-06
419	1	1	1.357E-01	7.100E-01	1.423E-02	1.230E-06
211	1	1	1.357E-01	5.000E-01	1.423E-02	1.230E-06
212	1	1	1.357E-01	3.840E-01	1.423E-02	1.230E-06
213	1	1	1.357E-01	2.680E-01	1.423E-02	1.230E-06
214	1	1	1.357E-01	2.680E-01	1.423E-02	1.230E-06
215	1	1	1.357E-01	2.680E-01	1.423E-02	1.230E-06
216	1	1	1.357E-01	2.680E-01	1.423E-02	1.230E-06
217	1	1	1.357E-01	3.480E-01	1.423E-02	1.230E-06
218	1	1	1.357E-01	5.000E-01	1.423E-02	1.230E-06
611	1	1	1.357E-01	6.127E-01	1.423E-02	1.230E-06
428	2	1	5.656E-02	2.350E-01	3.422E-03	2.000E-06
		2	2.262E-01	4.600E-01	1.423E-02	1.230E-06
429	1	1	2.262E-01	7.100E-01	1.423E-02	1.230E-06
221	1	1	2.262E-01	5.000E-01	1.423E-02	1.230E-06
222	1	1	2.262E-01	3.840E-01	1.423E-02	1.230E-06
223	1	1	2.262E-01	2.680E-01	1.423E-02	1.230E-06
224	1	1	2.262E-01	2.680E-01	1.423E-02	1.230E-06
225	1	1	2.262E-01	2.680E-01	1.423E-02	1.230E-06
226	1	1	2.262E-01	2.680E-01	1.423E-02	1.230E-06
227	1	1	2.262E-01	3.480E-01	1.423E-02	1.230E-06
228	1	1	2.262E-01	5.000E-01	1.423E-02	1.230E-06
621	1	1	2.262E-01	6.127E-01	1.423E-02	1.230E-06
438	2	1	7.918E-02	2.350E-01	3.422E-03	2.000E-06
		2	3.167E-01	4.600E-01	1.423E-02	1.230E-06
439	1	1	3.167E-01	7.100E-01	1.423E-02	1.230E-06
231	1	1	3.167E-01	5.000E-01	1.423E-02	1.230E-06
232	1	1	3.167E-01	3.840E-01	1.423E-02	1.230E-06
233	1	1	3.167E-01	2.680E-01	1.423E-02	1.230E-06
234	1	1	3.167E-01	2.680E-01	1.423E-02	1.230E-06
235	1	1	3.167E-01	2.680E-01	1.423E-02	1.230E-06
236	1	1	3.167E-01	2.680E-01	1.423E-02	1.230E-06
237	1	1	3.167E-01	3.480E-01	1.423E-02	1.230E-06
238	1	1	3.167E-01	5.000E-01	1.423E-02	1.230E-06
631	1	1	3.167E-01	6.127E-01	1.423E-02	1.230E-06
448	2	1	1.018E-01	2.350E-01	3.422E-03	2.000E-06
		2	4.072E-01	4.600E-01	1.423E-02	1.230E-06

Table C.23 (Continued)

IFPNUM	INPSG	NSEG	SAREA	SLEN	SHYD	SRGH
449	1	1	4.072E-01	7.100E-01	1.423E-02	1.230E-06
241	1	1	4.072E-01	5.000E-01	1.423E-02	1.230E-06
242	1	1	4.072E-01	3.840E-01	1.423E-02	1.230E-06
243	1	1	4.072E-01	2.680E-01	1.423E-02	1.230E-06
244	1	1	4.072E-01	2.680E-01	1.423E-02	1.230E-06
245	1	1	4.072E-01	2.680E-01	1.423E-02	1.230E-06
246	1	1	4.072E-01	2.680E-01	1.423E-02	1.230E-06
247	1	1	4.072E-01	3.480E-01	1.423E-02	1.230E-06
248	1	1	4.072E-01	5.000E-01	1.423E-02	1.230E-06
641	1	1	4.072E-01	6.127E-01	1.423E-02	1.230E-06
458	2	1	1.152E-01	2.350E-01	3.422E-03	2.000E-06
		2	4.610E-01	4.600E-01	1.423E-02	2.000E-06
459	1	1	4.610E-01	7.100E-01	1.423E-02	2.000E-06
251	1	1	4.610E-01	5.000E-01	1.423E-02	2.000E-06
252	1	1	4.610E-01	3.840E-01	1.423E-02	2.000E-06
253	1	1	4.610E-01	2.680E-01	1.423E-02	2.000E-06
254	1	1	4.610E-01	2.680E-01	1.423E-02	2.000E-06
255	1	1	4.610E-01	2.680E-01	1.423E-02	2.000E-06
256	1	1	4.610E-01	2.680E-01	1.423E-02	2.000E-06
257	1	1	4.610E-01	3.480E-01	1.423E-02	2.000E-06
258	1	1	4.610E-01	5.000E-01	1.423E-02	2.000E-06
651	1	1	4.610E-01	6.127E-01	1.423E-02	2.000E-06
468	2	1	2.106E-01	2.350E-01	3.422E-03	2.000E-06
		2	8.424E-01	4.600E-01	1.423E-02	1.230E-06
469	1	1	8.424E-01	7.100E-01	1.423E-02	1.230E-06
261	1	1	8.424E-01	5.000E-01	1.423E-02	1.230E-06
262	1	1	8.424E-01	3.840E-01	1.423E-02	1.230E-06
263	1	1	8.424E-01	2.680E-01	1.423E-02	1.230E-06
264	1	1	8.424E-01	2.680E-01	1.423E-02	1.230E-06
265	1	1	8.424E-01	2.680E-01	1.423E-02	1.230E-06
266	1	1	8.424E-01	2.680E-01	1.423E-02	1.230E-06
267	1	1	8.424E-01	3.480E-01	1.423E-02	1.230E-06
268	1	1	8.424E-01	5.000E-01	1.423E-02	1.230E-06
661	1	1	8.424E-01	6.127E-01	1.423E-02	1.230E-06
700	1	1	1.159E-01	1.894E-02	1.400E-02	1.230E-06
701	1	1	6.300E-02	1.894E-02	1.400E-02	1.230E-06
702	1	1	6.300E-02	1.894E-02	1.400E-02	1.230E-06
703	1	1	3.377E-02	1.894E-02	1.400E-02	1.230E-06

Table C.23 (Continued)

IFPNUM	INPSG	NSEG	SAREA	SLEN	SHYD	SRGH
704	1	1	3.377E-02	1.894E-02	1.400E-02	1.230E-06
705	1	1	3.377E-02	1.894E-02	1.400E-02	1.230E-06
706	1	1	3.377E-02	1.894E-02	1.400E-02	1.230E-06
707	1	1	3.377E-02	1.894E-02	1.400E-02	1.230E-06
708	1	1	6.300E-02	1.894E-02	1.400E-02	1.230E-06
709	1	1	6.300E-02	1.894E-02	1.400E-02	1.230E-06
710	1	1	9.140E-02	1.894E-02	1.400E-02	1.230E-06
711	1	1	2.190E-01	2.391E-02	1.400E-02	1.230E-06
712	1	1	1.190E-01	2.391E-02	1.400E-02	1.230E-06
713	1	1	1.190E-01	2.391E-02	1.400E-02	1.230E-06
714	1	1	6.378E-02	2.391E-02	1.400E-02	1.230E-06
715	1	1	6.378E-02	2.391E-02	1.400E-02	1.230E-06
716	1	1	6.378E-02	2.391E-02	1.400E-02	1.230E-06
717	1	1	6.378E-02	2.391E-02	1.400E-02	1.230E-06
718	1	1	6.378E-02	2.391E-02	1.400E-02	1.230E-06
719	1	1	1.190E-01	2.391E-02	1.400E-02	1.230E-06
720	1	1	1.190E-01	2.391E-02	1.400E-02	1.230E-06
721	1	1	1.726E-01	2.391E-02	1.400E-02	1.230E-06
722	1	1	2.962E-01	2.574E-02	1.400E-02	1.230E-06
723	1	1	1.610E-01	2.574E-02	1.400E-02	1.230E-06
724	1	1	1.610E-01	2.574E-02	1.400E-02	1.230E-06
725	1	1	8.630E-02	2.574E-02	1.400E-02	1.230E-06
726	1	1	8.630E-02	2.574E-02	1.400E-02	1.230E-06
727	1	1	8.630E-02	2.574E-02	1.400E-02	1.230E-06
728	1	1	8.630E-02	2.574E-02	1.400E-02	1.230E-06
729	1	1	8.630E-02	2.574E-02	1.400E-02	1.230E-06
730	1	1	1.610E-01	2.574E-02	1.400E-02	1.230E-06
731	1	1	1.610E-01	2.574E-02	1.400E-02	1.230E-06
732	1	1	2.336E-01	2.574E-02	1.400E-02	1.230E-06
733	1	1	3.993E-01	2.670E-02	1.400E-02	1.230E-06
734	1	1	2.170E-01	2.670E-02	1.400E-02	1.230E-06
735	1	1	2.170E-01	2.670E-02	1.400E-02	1.230E-06
736	1	1	1.163E-01	2.670E-02	1.400E-02	1.230E-06
737	1	1	1.163E-01	2.670E-02	1.400E-02	1.230E-06
738	1	1	1.163E-01	2.670E-02	1.400E-02	1.230E-06
739	1	1	1.163E-01	2.670E-02	1.400E-02	1.230E-06
740	1	1	1.163E-01	2.670E-02	1.400E-02	1.230E-06
741	1	1	2.170E-01	2.670E-02	1.400E-02	1.230E-06

Table C.23 (Continued)

IFPNUM	INPSG	NSEG	SAREA	SLEN	SHYD	SRGH
742	1	1	2.170E-01	2.670E-02	1.400E-02	1.230E-06
743	1	1	3.148E-01	2.670E-02	1.400E-02	1.230E-06
744	1	1	5.023E-01	2.643E-02	1.400E-02	2.000E-06
745	1	1	2.730E-01	2.643E-02	1.400E-02	2.000E-06
746	1	1	2.730E-01	2.643E-02	1.400E-02	2.000E-06
747	1	1	1.463E-01	2.643E-02	1.400E-02	2.000E-06
748	1	1	1.463E-01	2.643E-02	1.400E-02	2.000E-06
749	1	1	1.463E-01	2.643E-02	1.400E-02	2.000E-06
750	1	1	1.463E-01	2.643E-02	1.400E-02	2.000E-06
751	1	1	1.463E-01	2.643E-02	1.400E-02	2.000E-06
752	1	1	2.730E-01	2.643E-02	1.400E-02	2.000E-06
753	1	1	2.730E-01	2.643E-02	1.400E-02	2.000E-06
754	1	1	3.961E-01	2.643E-02	1.400E-02	2.000E-06
755	1	1	5.796E-01	3.197E-02	1.400E-02	2.000E-06
756	1	1	3.150E-01	3.197E-02	1.400E-02	1.230E-06
757	1	1	3.150E-01	3.197E-02	1.400E-02	1.230E-06
758	1	1	1.688E-01	3.197E-02	1.400E-02	1.230E-06
759	1	1	1.688E-01	3.197E-02	1.400E-02	1.230E-06
760	1	1	1.688E-01	3.197E-02	1.400E-02	1.230E-06
761	1	1	1.688E-01	3.197E-02	1.400E-02	1.230E-06
762	1	1	1.688E-01	3.197E-02	1.400E-02	1.230E-06
763	1	1	3.150E-01	3.197E-02	1.400E-02	1.230E-06
764	1	1	3.150E-01	3.197E-02	1.400E-02	1.230E-06
765	1	1	4.570E-01	3.197E-02	1.400E-02	1.230E-06
800	1	1	7.102E+00	8.625E-01	6.092E-02	2.000E-06
801	1	1	7.102E+00	1.170E+00	6.092E-02	2.000E-06
802	1	1	7.102E+00	1.170E+00	6.092E-02	2.000E-06
803	1	1	7.102E+00	9.600E-01	6.092E-02	2.000E-06
003	1	1	3.417E-01	2.167E+00	1.520E-01	2.000E-06
004	1	1	1.131E-02	2.167E+00	3.422E-02	2.000E-06
005	1	1	1.025E+00	2.167E+00	1.520E-01	2.000E-06
006	1	1	3.394E-02	2.167E+00	3.422E-02	2.000E-06
007	1	1	1.709E+00	2.167E+00	1.520E-01	2.000E-06
008	1	1	5.656E-02	2.167E+00	3.422E-02	2.000E-06
009	1	1	2.392E+00	2.167E+00	1.520E-01	2.000E-06
010	1	1	7.918E-02	2.167E+00	3.422E-02	2.000E-06
011	1	1	3.076E+00	2.167E+00	1.520E-01	2.000E-06
012	1	1	1.018E-01	2.167E+00	3.422E-02	2.000E-06

Table C.23 (Continued)

IFPNUM	INPSG	NSEG	SAREA	SLEN	SHYD	SRGH
013	1	1	3.482E+00	2.167E+00	1.520E-01	2.000E-06
014	1	1	1.152E-01	2.167E+00	3.422E-02	2.000E-06
015	1	1	6.363E+00	2.167E+00	1.520E-01	2.000E-06
016	1	1	2.106E-01	2.167E+00	3.422E-02	2.000E-06
017	1	1	3.240E-01	2.294E+00	8.583E-03	2.000E-06
018	1	1	4.525E-02	2.294E+00	1.423E-02	1.230E-06
019	1	1	9.782E-01	2.294E+00	8.674E-03	2.000E-06
020	1	1	1.357E-01	2.294E+00	1.423E-02	1.230E-06
021	1	1	1.635E+00	2.294E+00	8.711E-03	2.000E-06
022	1	1	2.262E-01	2.294E+00	1.423E-02	1.230E-06
023	1	1	2.282E+00	2.294E+00	8.674E-03	2.000E-06
024	1	1	3.167E-01	2.294E+00	1.423E-02	1.230E-06
025	1	1	2.956E+00	2.294E+00	8.777E-03	2.000E-06
026	1	1	4.072E-01	2.294E+00	1.423E-02	1.230E-06
027	1	1	2.306E+00	2.294E+00	1.669E-02	2.000E-06
028	1	1	4.610E-01	2.294E+00	1.423E-02	1.230E-06
029	1	1	4.214E+00	2.294E+00	1.669E-02	2.000E-06
030	1	1	8.424E-01	2.294E+00	1.423E-02	1.230E-06
050	1	1	7.102E+00	1.932E+00	6.092E-01	2.000E-06

C.9 SOURCE FLOW PATH INPUT

CARD	WORD	VALUE
FL_ID	FPNAME	SRC-FL001
	IFPNUM	001
FL_FT	KCVFM	SRC-CV001
	KCVTO	HS-CV704
	ZFM	3.0654
	ZTO	3.0654
FL_GEO	FLARA	7.102E+00
	FLEN	6.125E-01
	FLOPO	1.0
FL_JSW	KFLGFL	0
FL_USL	FRICFO	0.0
	FRICRO	0.0

FL_SEG	INPSG	1
	NSEG	1
	SAREA	7.102E+00
	SLEN	6.125E-01
	SHYD	6.092E-01
	SRGH	2.000E-06

C.10 HS INPUT FOR TOPHALFSPHERE

CARD	WORD	VALUE
HS_ID	HSNAME	'UHD'
	IHSNUM	10000
HS_GD	IGEOM	TOPHALFSPHERE
	ISS	SS
HS_EOD	HSALT	3.0654
	ALPHA	no value
HS_SRC	ISRC	NO
HS_ND	NP	2
	XI	3.863/4.143
	TEMPIN	-
	MATNAM	STAINLESS-STEEL
HS_LB	IBCL	CalcCoefHS
	IBVL	UHD-CV005
	MTEVAL	NO
HS_LBP	IFLOWL	INT
	CPFPL	0.5
	CPFAL	0.5
HS_LBS	ASURFL	9.376E+01
	CLNL	2.800E-01
	BNDZL	2.800E-01
HS_RB	IBCR	SYMMETRY
	IBVR	NO
	MTEVAR	NO
HS_RBP	IFLOWR	EXT
	CPFPR	0.0
	CPFAR	0.0
HS_RBS	ASURFR	1.0
	CLNR	2.800E-01
	BNDZR	2.800E-01
HS_FT	IFTNUM	OFF

C.11 HS INPUT FOR BARREL

CARD	WORD	VALUE
HS_ID	HSNAME	Table C.24
	IHSNUM	Table C.24
HS_GD	IGEOM	CYLINDRICAL
	ISS	SS
HS_EOD	HSALT	Table C.24
	ALPHA	1.0
HS_SRC	ISRC	NO
HS_ND	NP	2
	XI	3.533/3.5584
	TEMPIN	-
	MATNAM	STAINLESS-STEEL
HS_LB	IBCL	CalcCoef
	IBVL	Table C.24
	MTEVAL	NO
HS_LBP	IFLOWL	INT
	CPFL	0.5
	CPFAL	0.5
HS_LBS	ASURFL	1.0
	CLNL	Table C.24
	BNDZL	Table C.24
HS_RB	IBCR	CalcCoefHS
	IBVR	Table C.24
	MTEVAR	NO
HS_RBP	IFLOWR	INT
	CPFPR	0.5
	CPFAR	0.5
HS_RBS	ASURFR	1.0
	CLNR	Table C.24
	BNDZR	Table C.24
HS_FT	IFTNUM	OFF

Table C.24: Barrel Heat Structure Parameters

HSNAME	IHSNUM	HSALT	IBVL	CLNL	BNDZL	IBVR	CLNR	BNDZR
HS70001	70001	-2.390	LCP-CV468	4.700E-01	4.700E-01	HS-CV700	4.700E-01	4.700E-01
HS70002	70002	-1.920	LBS-CV469	1.000E-02	1.000E-02	HS-CV700	1.000E-02	1.000E-02
HS70003	70003	-1.910	LBS-CV469	1.100E-01	1.100E-01	HS-CV700	1.100E-01	1.100E-01
HS70004	70004	-1.800	LBS-CV469	8.000E-01	8.000E-01	HS-CV700	8.000E-01	8.000E-01
HS70005	70005	-1.000	OBS-CV261	2.500E-01	2.500E-01	HS-CV701	2.500E-01	2.500E-01
HS70006	70006	-7.500E-01	OBS-CV261	2.500E-01	2.500E-01	HS-CV701	2.500E-01	2.500E-01
HS70007	70007	-5.000E-01	OBS-CV262	2.500E-01	2.500E-01	HS-CV701	2.500E-01	2.500E-01
HS70008	70008	-2.500E-01	OBS-CV262	2.500E-01	2.500E-01	HS-CV701	2.500E-01	2.500E-01
HS70009	70009	0.000	OBS-CV263	1.340E-01	1.340E-01	HS-CV702	1.340E-01	1.340E-01
HS70010	70010	1.340E-01	OBS-CV263	1.340E-01	1.340E-01	HS-CV702	1.340E-01	1.340E-01
HS70011	70011	2.680E-01	OBS-CV264	1.340E-01	1.340E-01	HS-CV702	1.340E-01	1.340E-01
HS70012	70012	4.020E-01	OBS-CV264	1.340E-01	1.340E-01	HS-CV702	1.340E-01	1.340E-01
HS70013	70013	5.360E-01	OBS-CV265	1.340E-01	1.340E-01	HS-CV702	1.340E-01	1.340E-01
HS70014	70014	6.700E-01	OBS-CV265	1.340E-01	1.340E-01	HS-CV702	1.340E-01	1.340E-01
HS70015	70015	8.040E-01	OBS-CV266	1.340E-01	1.340E-01	HS-CV702	1.340E-01	1.340E-01
HS70016	70016	9.380E-01	OBS-CV266	1.340E-01	1.340E-01	HS-CV702	1.340E-01	1.340E-01
HS70017	70017	1.072	OBS-CV267	1.340E-01	1.340E-01	HS-CV702	1.340E-01	1.340E-01
HS70018	70018	1.206	OBS-CV267	1.340E-01	1.340E-01	HS-CV702	1.340E-01	1.340E-01
HS70019	70019	1.340	OBS-CV268	2.500E-01	2.500E-01	HS-CV703	2.500E-01	2.500E-01
HS70020	70020	1.590	OBS-CV268	2.500E-01	2.500E-01	HS-CV703	2.500E-01	2.500E-01
HS70021	70021	1.840	OBS-CV269	2.500E-01	2.500E-01	HS-CV703	2.500E-01	2.500E-01
HS70022	70022	2.090	OBS-CV269	2.500E-01	2.500E-01	HS-CV703	2.500E-01	2.500E-01
HS70023	70023	2.340	UBS-CV661	7.254E-01	7.254E-01	HS-CV704	7.254E-01	7.254E-01

C.12 HS INPUT FOR RPV WALL

CARD	WORD	VALUE
HS_ID	HSNAME	Table C.25
	IHSNUM	Table C.25
HS_GD	IGEOM	CYLINDRICAL
	ISS	SS
HS_EOD	HSALT	Table C.25
	ALPHA	1.0
HS_SRC	ISRC	NO
HS_ND	NP	2
	XI	3.863/4.143
	TEMPIN	-
	MATNAM	STAINLESS-STEEL

HS_LB	IBCL	CalcCoefHS
	IBVL	Table C.25
	MTEVAL	NO
HS_LBP	IFLOWL	INT
	CPFL	0.5
	CPFAL	0.5
HS_LBS	ASURFL	1.0
	CLNL	Table C.25
	BNDZL	Table C.25
HS_RB	IBCR	SYMMETRY
	IBVR	NO
	MTEVAR	NO
HS_RBP	IFLOWR	EXT
	CPFPR	0.0
	CPFAR	0.0
HS_FT	IFTNUM	OFF

Table C.25: RPV Wall Characteristics

HSNAME	IHSNUM	HSALT	IBVL	CLNL	BNDZL
HS80001	80001	-2.390	HS-CV700	1.390E+00	1.390E+00
HS80002	80002	-1.000	HS-CV701	1.000	1.000
HS80003	80003	0.000	HS-CV702	1.340	1.340
HS80004	80004	1.340	HS-CV703	1.000	1.000
HS80005	80005	2.340	HS-CV704	7.254E-01	7.254E-01

C.13 MATERIAL INPUT

CARD	WORD	VALUE
MP_ID	MATNAM	URANIUM-DIOXIDE
MP_PRTF	NPRPAR	4
	NPAR	Table C.26
	PROP	Table C.26
	ITBPRP	Table C.26
	CFKEY	TF
MP_ID	MATNAM	ZIRCALOY
MP_PRTF	NPRPAR	4

	NPAR	Table C.27
	PROP	Table C.27
	ITBPRP	Table C.27
	CFKEY	TF
MP_PRC	RHOM	3.210E+03
	TMLT	3003.0
	LHF	1.787E+06
MP_ID	MATNAM	ZIRCONIUM-DIOXIDE
MP_PRTF	NPRPAR	4
	NPAR	Table C.28
	PROP	Table C.28
	ITBPRP	Table C.28
	CFKEY	TF
MP_ID	MATNAM	STAINLESS-STEEL-OXIDE
MP_PRTF	NPRPAR	4
	NPAR	Table C.29
	PROP	Table C.29
	ITBPRP	Table C.29
	CFKEY	TF
MP_PRC	RHOM	1.925E+04
	TMLT	3695.0
	LHF	1.920E+05

Table C.26: Material Functions for Fuel

NPAR	PROP	ITBPRP
1	ENH	'ENH-UC'
2	CPS	'CPS-UC'
3	THC	'THC-UC'
4	RHO	'RHO-UC'

Table C.27: Material Functions for SiC

NPAR	PROP	ITBPRP
1	ENH	'ENH-SiC'
2	CPS	'CPS-SiC'
3	THC	'THC-SiC'
4	RHO	'RHO-SiC'

Table C.28: Material Functions for Zr_3Si_2

NPAR	PROP	ITBPRP
1	ENH	'ENH-ZSI'
2	CPS	'CPS-ZSI'
3	THC	'THC-ZSI'
4	RHO	'RHO-ZSI'

Table C.29: Material Functions for Tungsten

NPAR	PROP	ITBPRP
1	ENH	'ENH-W'
2	CPS	'CPS-W'
3	THC	'THC-W'
4	RHO	'RHO-W'

C.14 TABULAR FUNCTION INPUT

CARD	WORD	VALUE
TF_ID	TFNAME	ENH-UC
	TFSCAL	1
	TFADCN	0
TF_TAB	NTFPAR	25
	NPAR	Table C.30
	X	Table C.30
	Y	Table C.30
TF_ID	TFNAME	CPS-UC
	TFSCAL	1
	TFADCN	0
TF_TAB	NTFPAR	25
	NPAR	Table C.31
	X	Table C.31
	Y	Table C.31
TF_ID	TFNAME	THC-UC
	TFSCAL	1
	TFADCN	0
TF_TAB	NTFPAR	13
	NPAR	Table C.32
	X	Table C.32
	Y	Table C.32

TF_ID	TFNAME	RHO-UC
	TFSCAL	1
	TFADCN	0
TF_TAB	NTFPAR	12
	NPAR	Table C.33
	X	Table C.33
	Y	Table C.33
TF_ID	TFNAME	ENH-SIC
	TFSCAL	1
	TFADCN	0
TF_TAB	NTFPAR	26
	NPAR	Table C.34
	X	Table C.34
	Y	Table C.34
TF_ID	TFNAME	CPS-SIC
	TFSCAL	1
	TFADCN	0
TF_TAB	NTFPAR	7
	NPAR	Table C.35
	X	Table C.35
	Y	Table C.35
TF_ID	TFNAME	THC-SIC
	TFSCAL	1
	TFADCN	0
TF_TAB	NTFPAR	7
	NPAR	Table C.36
	X	Table C.36
	Y	Table C.36
TF_ID	TFNAME	RHO-SIC
	TFSCAL	1
	TFADCN	0
TF_TAB	NTFPAR	7
	NPAR	Table C.37
	X	Table C.37
	Y	Table C.37
TF_ID	TFNAME	ENH-ZSI
	TFSCAL	1
	TFADCN	0
TF_TAB	NTFPAR	23
	NPAR	Table C.38
	X	Table C.38
	Y	Table C.38

TF_ID	TFNAME	CPS-ZSI
	TFSCAL	1
	TFADCN	0
TF_TAB	NTFPAR	23
	NPAR	Table C.39
	X	Table C.39
	Y	Table C.39
TF_ID	TFNAME	THC-ZSI
	TFSCAL	1
	TFADCN	0
TF_TAB	NTFPAR	23
	NPAR	Table C.40
	X	Table C.40
	Y	Table C.40
TF_ID	TFNAME	RHO-ZSI
	TFSCAL	1
	TFADCN	0
TF_TAB	NTFPAR	2
	NPAR	Table C.41
	X	Table C.41
	Y	Table C.41
TF_ID	TFNAME	ENH-W
	TFSCAL	1
	TFADCN	0
TF_TAB	NTFPAR	26
	NPAR	Table C.42
	X	Table C.42
	Y	Table C.42
TF_ID	TFNAME	CPS-W
	TFSCAL	1
	TFADCN	0
TF_TAB	NTFPAR	24
	NPAR	Table C.43
	X	Table C.43
	Y	Table C.43
TF_ID	TFNAME	THC-W
	TFSCAL	1
	TFADCN	0
TF_TAB	NTFPAR	22
	NPAR	Table C.44
	X	Table C.44
	Y	Table C.44

TF_ID	TFNAME	RHO-W
	TFSCAL	1
	TFADCN	0
TF_TAB	NTFPAR	2
	NPAR	Table C.45
	X	Table C.45
	Y	Table C.45

Table C.30: Fuel Enthalpy [31]

NPAR	X (K)	Y (J/kg)
1	298.0	0.0
2	300.0	3.677E+02
3	400.0	2.100E+04
4	500.0	4.296E+04
5	600.0	6.590E+04
6	700.0	8.960E+04
7	800.0	1.138E+05
8	900.0	1.384E+05
9	1000.0	1.631E+05
10	1100.0	1.879E+05
11	1200.0	2.128E+05
12	1300.0	2.376E+05
13	1400.0	2.625E+05
14	1500.0	2.875E+05
15	1600.0	3.128E+05
16	1700.0	3.384E+05
17	1800.0	3.646E+05
18	1900.0	3.916E+05
19	2000.0	4.196E+05
20	2100.0	4.492E+05
21	2200.0	4.804E+05
22	2300.0	5.139E+05
23	2400.0	5.499E+05
24	2500.0	5.891E+05
25	2548.0	6.090E+05

Table C.31: Fuel Specific Heat Capacity [31]

NPAR	X (K)	Y (J/kg-K)
1	298.0	1.983E+02
2	300.0	1.986E+02
3	400.0	2.135E+05
4	500.0	2.250E+02
5	600.0	2.337E+02
6	700.0	2.399E+02
7	800.0	2.440E+02
8	900.0	2.465E+02
9	1000.0	2.479E+02
10	1100.0	2.484E+02
11	1200.0	2.485E+02
12	1300.0	2.488E+02
13	1400.0	2.495E+02
14	1500.0	2.511E+02
15	1600.0	2.540E+02
16	1700.0	2.586E+02
17	1800.0	2.654E+02
18	1900.0	2.748E+02
19	2000.0	2.872E+02
20	2100.0	3.030E+02
21	2200.0	3.227E+02
22	2300.0	3.466E+02
23	2400.0	3.751E+02
24	2500.0	4.088E+02
25	2548.0	4.268E+02

Table C.32: Fuel Thermal Conductivity [32]

NPAR	X (K)	Y (W/m-K)
1	298.0	17.4
2	373.0	17.0
3	573.0	16.5
4	773.0	16.7
5	973.0	17.9
6	1173.0	19.1

Table C.32 (Continued)

NPAR	X (K)	Y (W/m-K)
7	1373.0	20.1
8	1573.0	20.9
9	1773.0	21.6
10	1973.0	22.1
11	2173.0	22.5
12	2373.0	22.8
13	2573.0	22.9

Table C.33: Fuel Density [33]

NPAR	X (K)	Y (kg/m³)
1	298.0	1.346E+04
2	473.0	1.340E+04
3	673.0	1.331E+04
4	873.0	1.320E+04
5	1073.0	1.311E+04
6	1273.0	1.298E+04
7	1473.0	1.290E+04
8	1673.0	1.281E+04
9	1873.0	1.271E+04
10	2073.0	1.261E+04
11	2273.0	1.251E+04
12	2473.0	1.241E+04

Table C.34: SiC Enthalpy [34]

NPAR	X (K)	Y (J/kg)
1	298.1	8.097E+04
2	300.0	8.222E+04
3	400.0	1.596E+05
4	500.0	2.504E+05
5	600.0	3.501E+05
6	700.0	4.559E+05
7	800.0	5.666E+05

Table C.34 (Continued)

NPAR	X (K)	Y (J/kg)
8	900.0	6.813E+05
9	1000.0	7.990E+05
10	1100.0	9.197E+05
11	1200.0	1.042E+06
12	1300.0	1.167E+06
13	1400.0	1.293E+06
14	1500.0	1.420E+06
15	1600.0	1.549E+06
16	1700.0	1.676E+06
17	1800.0	1.805E+06
18	1900.0	1.938E+06
19	2000.0	2.067E+06
20	2100.0	2.197E+06
21	2200.0	2.329E+06
22	2300.0	2.459E+06
23	2400.0	2.591E+06
24	2500.0	2.723E+06
25	3003.0	3.423E+06
26	3003.01	5.000E+06

Table C.35: SiC Specific Heat Capacity [35]

NPAR	X (K)	Y (J/kg-K)
1	293.0	7.150E+02
2	773.0	1.086E+03
3	1273.0	1.240E+03
4	1473.0	1.282E+03
5	1673.0	1.318E+03
6	1773.0	1.336E+03
7	2500.0	1.465E+03

Table C.36: SiC Thermal Conductivity [35]

NPAR	X (K)	Y (W/m-K)
1	293.0	1.140E+02
2	773.0	5.510E+01
3	1273.0	3.570E+01

Table C.36 (Continued)

NPAR	X (K)	Y (W/m-K)
4	1473.0	3.130E+01
5	1673.0	2.780E+01
6	1773.0	2.630E+01
7	2500.0	2.040E+01

Table C.37: SiC Density [35]

NPAR	X (K)	Y (kg/m³)
1	293.0	3.160E+03
2	773.0	3.140E+03
3	1273.0	3.110E+03
4	1473.0	3.100E+03
5	1673.0	3.090E+03
6	1773.0	3.080E+03
7	2500.0	3.044E+03

Table C.38: Zr₃Si₂ Enthalpy [36]

NPAR	X (K)	Y (J/kg)
1	373.0	0.0
2	473.0	4.330E+04
3	573.0	8.660E+04
4	673.0	1.299E+05
5	773.0	1.732E+05
6	873.0	2.165E+05
7	973.0	2.598E+05
8	1073.0	3.031E+05
9	1173.0	3.464E+05
10	1273.0	3.897E+05
11	1373.0	4.330E+05
12	1473.0	4.763E+05
13	1573.0	5.196E+05
14	1673.0	5.629E+05
15	1773.0	6.062E+05
16	1873.0	6.495E+05

Table C.38 (Continued)

NPAR	X (K)	Y (J/kg)
17	1973.0	6.928E+05
18	2073.0	7.361E+05
19	2173.0	7.794E+05
20	2273.0	8.227E+05
21	2373.0	8.660E+05
22	2473.0	9.093E+05
23	2573.0	9.526E+05

Table C.39: Zr_3Si_2 Specific Heat Capacity [36]

NPAR	X (K)	Y (J/kg-K)
1	373.0	3.834E+02
2	473.0	3.980E+02
3	573.0	4.049E+02
4	673.0	4.085E+02
5	773.0	4.104E+02
6	873.0	4.113E+02
7	973.0	4.118E+02
8	1073.0	4.119E+02
9	1173.0	4.119E+02
10	1273.0	4.118E+02
11	1373.0	4.116E+02
12	1473.0	4.115E+02
13	1573.0	4.114E+02
14	1673.0	4.113E+02
15	1773.0	4.113E+02
16	1873.0	4.114E+02
17	1973.0	4.115E+02
18	2073.0	4.118E+02
19	2173.0	4.121E+02
20	2273.0	4.125E+02
21	2373.0	4.130E+02
22	2473.0	4.135E+02
23	2573.0	4.142E+02

Table C.40: Zr₃Si₂ Thermal Conductivity [36]

NPAR	X (K)	Y (W/m-K)
1	373.0	19.019
2	473.0	19.112
3	573.0	19.253
4	673.0	19.417
5	773.0	19.591
6	873.0	19.773
7	973.0	19.958
8	1073.0	20.146
9	1173.0	20.336
10	1273.0	20.527
11	1373.0	20.718
12	1473.0	20.911
13	1573.0	21.104
14	1673.0	21.297
15	1773.0	21.490
16	1873.0	21.684
17	1973.0	21.878
18	2073.0	22.072
19	2173.0	22.266
20	2273.0	22.461
21	2373.0	22.655
22	2473.0	22.849
23	2573.0	23.044

Table C.41: Zr₃Si₂ Density [36]

NPAR	X (K)	Y (kg/m³)
1	373.0	5880.0
2	2800.0	5880.0

Table C.42: Tungsten Enthalpy [37]

NPAR	X (K)	Y (J/kg)
1	298.1	0.0
2	300.0	2.458E+02
3	400.0	1.365E+04

Table C.42 (Continued)

NPAR	X (K)	Y (J/kg)
4	500.0	2.731E+04
5	600.0	4.121E+04
6	700.0	5.536E+04
7	800.0	6.971E+04
8	900.0	8.439E+04
9	1000.0	9.924E+04
10	1100.0	1.144E+05
11	1200.0	1.297E+05
12	1300.0	1.454E+05
13	1400.0	1.612E+05
14	1500.0	1.774E+05
15	1600.0	1.937E+05
16	1700.0	2.103E+05
17	1800.0	2.272E+05
18	1900.0	2.443E+05
19	2000.0	2.616E+05
20	2100.0	2.792E+05
21	2200.0	2.971E+05
22	2300.0	3.152E+05
23	2400.0	3.336E+05
24	2500.0	3.523E+05
25	3695.0	5.503E+05
26	3695.1	7.423E+05

Table C.43: Tungsten Specific Heat Capacity [37]

NPAR	X (K)	Y (J/kg-K)
1	298.1	1.328E+02
2	300.0	1.328E+02
3	400.0	1.353E+02
4	500.0	1.377E+02
5	600.0	1.402E+02
6	700.0	1.427E+02
7	800.0	1.451E+02
8	900.0	1.476E+02
9	1000.0	1.501E+02
10	1100.0	1.525E+02

Table C.43 (Continued)

NPAR	X (K)	Y (J/kg-K)
11	1200.0	1.550E+02
12	1300.0	1.574E+02
13	1400.0	1.599E+02
14	1500.0	1.624E+02
15	1600.0	1.648E+02
16	1700.0	1.673E+02
17	1800.0	1.698E+02
18	1900.0	1.722E+02
19	2000.0	1.747E+02
20	2100.0	1.772E+02
21	2200.0	1.798E+02
22	2300.0	1.825E+02
23	2400.0	1.854E+02
24	2500.0	1.885E+02

Table C.44: Tungsten Thermal Conductivity [38]

NPAR	X (K)	Y (W/m-K)
1	373.2	1.852E+02
2	473.2	1.683E+02
3	573.2	1.547E+02
4	673.2	1.440E+02
5	773.2	1.357E+02
6	873.2	1.296E+02
7	973.2	1.248E+02
8	1073.0	1.210E+02
9	1173.0	1.180E+02
10	1273.0	1.155E+02
11	1373.0	1.135E+02
12	1473.0	1.117E+02
13	1573.0	1.101E+02
14	1673.0	1.087E+02
15	1773.0	1.073E+02
16	1873.0	1.062E+02
17	1973.0	1.051E+02
18	2073.0	1.041E+02
19	2173.0	1.032E+02

Table C.44 (Continued)

NPAR	X (K)	Y (W/m-K)
20	2273.0	1.022E+02
21	2373.0	1.014E+02
22	2473.0	1.007E+02

Table C.45: Tungsten Density [38]

NPAR	X (K)	Y (kg/m³)
1	373.2	19350.0
2	2800.0	19350.0

C.15 CONTROL FUNCTION INPUT

CARD	WORD	VALUE
CF_ID	CFNAME	'CORE-POWER'
	ICFNUM	001
	CFTYPE	EQUALS
CF_SAI	CFSCAL	1.0
	CFADCN	2.400E+09
	CFVALR	2.400E+09
CF_ARG	NCFARG	1
	NARG	1
	CHARG	EXEC-TIME
	ARSCAL	0.0
	ARADCN	0.0
CF_ID	CFNAME	'COOL-SOURCE-P'
	ICFNUM	002
	CFTYPE	EQUALS
CF_SAI	CFSCAL	1.0
	CFADCN	7.240E+06
	CFVALR	7.240E+06
CF_ARG	NCFARG	1
	NARG	1
	CHARG	'EXEC-TIME'
	ARSCAL	0.0
	ARADCN	0.0

CF_ID	CFNAME	'COOL-SOURCE-T'
	ICFNUM	003
	CFTYPE	EQUALS
CF_SAI	CFSCAL	1.0
	CFADCN	763.15
	CFVALR	763.15
CF_ARG	NCFARG	1
	NARG	1
	CHARG	'EXEC-TIME'
	ARSCAL	0.0
	ARADCN	0.0
CF_ID	CFNAME	'COOL-SOURCE-RHUM'
	ICFNUM	004
	CFTYPE	EQUALS
CF_SAI	CFSCAL	1.0
	CFADCN	0
	CFVALR	0
CF_ARG	NCFARG	1
	NARG	1
	CHARG	'EXEC-TIME'
	ARSCAL	0.0
	ARADCN	0.0
CF_ID	CFNAME	'COOLSOURCE-HE-FRACTION'
	ICFNUM	005
	CFTYPE	EQUALS
CF_SAI	CFSCAL	1.0
	CFADCN	1.0
	CFVALR	1.0
CF_ARG	NCFARG	1
	NARG	1
	CHARG	'EXEC-TIME'
	ARSCAL	0.0
	ARADCN	0.0
CF_ID	CFNAME	'SS-MFR'
	ICFNUM	006
	CFTYPE	EQUALS
CF_SAI	CFSCAL	1
	CFADCN	3022.50
	CFVALR	3022.50

CF_ARG	NCFARG	1
	NARG	1
	CHARG	EXEC-TIME
	ARSCAL	0.0
	ARADCN	0.0
CF_ID	CFNAME	'HEVELOCITY'
	ICFNUM	007
	CFTYPE	DIVIDE
CF_SAI	CFSCAL	1.0
	CFADCN	no value
	CFVALR	no value
CF_ARG	NCFARG	2
	NARG	Table C.46
	CHARG	Table C.46
	ARSCAL	Table C.46
	ARADCN	Table C.46
CF_ID	CFNAME	'COOL-SINK-P'
	ICFNUM	008
	CFTYPE	EQUALS
CF_SAI	CFSCAL	1.0
	CFADCN	7.070E+06
	CFVALR	7.070E+06
CF_ARG	NCFARG	1
	NARG	1
	CHARG	EXEC-TIME
	ARSCAL	0.0
	ARADCN	0.0
CF_ID	CFNAME	'COOL-SINK-T'
	ICFNUM	009
	CFTYPE	EQUALS
CF_SAI	CFSCAL	1.0
	CFADCN	1123.15
	CFVALR	1123.15
CF_ARG	NCFARG	1
	NARG	1
	CHARG	EXEC-TIME
	ARSCAL	0.0
	ARADCN	0.0
CF_ID	CFNAME	'COOL-SINK-RHUM'
	ICFNUM	010

	CFTYPE	EQUALS
CF_SAI	CFSCAL	1.0
	CFADCN	0.0
	CFVALR	0.0
CF_ARG	NCFARG	1
	NARG	1
	CHARG	EXEC-TIME
	ARSCAL	0.0
	ARADCN	0.0
CF_ID	CFNAME	'COOL-SINK-HE-FRACTION'
	ICFNUM	011
	CFTYPE	EQUALS
CF_SAI	CFSCAL	1.0
	CFADCN	1.0
	CFVALR	1.0
CF_ARG	NCFARG	1
	NARG	1
	CHARG	EXEC-TIME
	ARSCAL	0.0
	ARADCN	0.0

Table C.46: Control Function for Helium Velocity

NARG	CHARG	ARSCAL	ARADCN
1	CVH-RHO(HS-CV704,HE)	7.107E+00	0
2	CF-VALU('SS-MFR')	1	0

C.16: MELCOR ENVIRONMENTAL DATA

CARD	WORD	VALUE
MEG_DIAGFILE	-	'gfr2400g.dia'
MEL_DIAGFILE	-	'gfr2400.dia'
MEG_OUTPUTFILE	-	'gfr2400g.out'
MEL_OUTPUTFILE	-	'gfr2400.out'
PLOTFILE	-	'gfr2400.ptf'
MEG_RESTARTFILE	-	'gfr2400.rst'
MEL_RESTARTFILE	-	'gfr2400.rst'
	CYCLE	NCYCLE
	NREST	-1

MESSAGEFILE	-	'gfr2400.mes'
STATUSFILE	-	'MELSTT_v2-0'
STOPFILE	-	'MELSTP_v2-0'
WRITENEWINP	-	'gfr2400.txt'

C.17 MELCOR EXEC INPUT

CARD	WORD	VALUE
EXEC_INPUT	-	-
EXEC_TITLE	-	'2400-MWGFR(SS)'
EXEC_JOBID	-	'gfr2400-'
EXEC_TEND	TEND	1000.0
EXEC_TIME	NTMINV	3
	N	Table C.47
	TIME	Table C.47
	DTMAX	Table C.47
	DTMIN	Table C.47
	DTEDIT	Table C.47
	DTPLOT	Table C.47
	DTREST	Table C.47
	DCREST	Table C.47
EXEC_CPULEFT	-	3.000E+01
EXEC_CPULIM	-	1.000E+05
EXEC_CYMESF	NCYEDD	100
	NCYEDP	10000
EXEC_EXACTTIME	NXTIME	1
	N	1
	TIME	1000.0

Table C.47: Executive Time Step Data

N	TIME	DTMAX	DTMIN	DTEDIT	DTPLOT	DTREST	DCREST
1	0.0	0.5	1.00E-05	500.0	1.0	1000.0	1.00E+10
2	10.0	0.5	1.00E-05	500.0	1.0	1000.0	1.00E+10
3	100.0	2.0	1.00E-05	2000.0	10.0	5000.0	1.00E+10

VITA

Name: Andrew Steven Dercher

Address: Department of Nuclear Engineering, Texas A&M University,
3133 TAMU, College Station, TX 77843-3133

Email Address: adercher@gmail.com

Education: B.S. Nuclear Engineering, The Pennsylvania State University, 2009